Validation des performances des gyroscopes MEMS en utilisant des modèles incertains et temps-variant

Jorge Ayala-Cuevas

N° d'ordre NNT : **2021LYSEC45**

Thèse de Doctorat de L'Université de Lyon
opérée au sein de l'Ecole Centrale de Lyon

Ecole Doctorale N° 160 Electronique, Electrotechnique et Automatique (EEA)

Spécialité de doctorat : Automatique

préparée au Laboratoire Ampère, UMR CNRS 5005

Performance Validation of MEMS Gyroscopes using Uncertain and Time-Varying Models

---

par Jorge Ivan AYALA CUEVAS

Date de soutenance prévue le 07/12/2021 devant le jury composé de :

Rapporteur	M. Matthew C. TURNER	Professor, University of Southampton
Rapporteur	M. Fabrice DEMOURANT	Ingénieur de Recherche HDR, ONERA
Examinatrice	Mme. Suzanne LESECQ	Directrice de Recherche, CEA LETI
Président du Jury	M. Jérôme JUILLARD	Professeur des Universités, Centrale Supélec
Examinateur (invité)	M. Christophe LE BLANC	Ingénieur de Recherche, ASYGN
Directeur de thèse	M. Gérard SCORLETTI	Professeur des Universités, École Centrale de Lyon
Co-Encadrant	M. Anton KORNIIENKO	Maître de Conférences, École Centrale de Lyon

"Uncertainty is an uncomfortable position. But certainty is an absurd one."

Voltaire

UNIVERSITÉ DE LYON - ECOLE CENTRALE DE LYON

Abstract

Laboratoire Ampère, UMR CNRS 5005
Ecole Doctorale Electronique, Electrotechnique et Automatique (EEA)

PhD in Automatic Control

Performance Validation of MEMS Gyroscopes using Uncertain and Time-Varying Models

by Jorge Ivan AYALA CUEVAS

MEMS gyroscopes are micro sensors that measure the angular rate of an object with respect to a reference frame, by estimating the Coriolis force. The estimation is obtained thanks to the feedback control of the poorly damped spring-mass system oscillations coupled to synchronous demodulation. In spite of their attractive advantages, they suffer of manufacturing dispersion and an important sensitivity to temperature changes. The controllers are designed using strongly simplified models, without a certified performance level. This PhD work focuses on the pre-experimental performance validation of the designed control, using models that are more realistic, that is, approaching the validation as a dynamical system analysis problem. Due to synchronous demodulation, the system is modeled as linear system with Harmonically Time-Varying (HTV) parameters, i.e. parameters that are time-domain sinusoidal functions of a given frequency. We address the analysis of Linear Harmonically Time-Varying (LHTV) systems by adopting an Integral Quadratic Constraints (IQC) approach. A key step to apply the IQC framework is to characterize HTV parameters by IQCs defined by a set of functions named multipliers. In this work, we introduce new classes of HTV multipliers which dramatically reduce the conservatism of the analysis results. Commercialized MEMS gyroscope must verify accuracy and output noise specifications, defined by standards. We propose model-based performance criteria in order to evaluate these specifications. Most of the proposed tools are given in the form of convex optimization problems. The most important accuracy specification is the Scale Factor Nonlinearity (SFNL), which is recast as robust optimization problem. The standard procedure to evaluate the output noise of MEMS gyroscopes is the Allan variance which is a time-domain statistical tool computed from long-term measures of the gyroscope output. This signal-based method is recast as a model-based analysis tool by adopting a generator filter approach. Different cases are investigated, from LTI models to classes of LHTV models that are relevant for the MEMS gyroscope application, including uncertainties. The proposed approaches are validated using experimental results. Finally, the proposed systems analysis tools are applied to the validation of alternative control strategies that require more complex architectures than the classical LTI control.

UNIVERSITÉ DE LYON - ECOLE CENTRALE DE LYON

Résumé

Laboratoire Ampère, UMR CNRS 5005
Ecole Doctorale Electronique, Electrotechnique et Automatique (EEA)

Doctorat en Automatique

Validation des Performances des Gyroscopes MEMS en utilisant des Modèles Incertains et Temps-Variants

par Jorge Ivan AYALA CUEVAS

Les gyroscopes MEMS sont des micro-capteurs qui mesurent la vitesse angulaire d'un objet par rapport à un référentiel en estimant la force de Coriolis. L'estimation est obtenue grâce à la commande en boucle fermée des oscillations du système ressort-masse peu amorti couplé à une démodulateur synchrone. Malgré leurs avantages attractifs, ils subissent une dispersion de fabrication et d'une sensibilité importante aux changements de température. Les correcteurs sont conçus à partir de modèles fortement simplifiés, sans niveau de performance certifié. Ce travail de thèse se concentre sur la validation pré-expérimentale des performances de la commande conçue en utilisant des modèles plus réalistes, c'est-à-dire, en abordant la validation comme un problème d'analyse de système dynamique. En raison de la démodulation synchrone, le système est modélisé comme un système linéaire avec des paramètres à temps-variants harmoniques (HTV), c'est-à-dire, des paramètres qui sont des fonctions sinusoïdales dans le domaine temporel d'une fréquence particulière. Nous abordons l'analyse des systèmes LHTV (Linear Harmonically Time-Varying) en adoptant une approche de type IQC (Integral Quadratic Constraints). Une étape clé pour appliquer le cadre IQC est de caractériser les paramètres HTV par des IQC définies par un ensemble de fonctions appelées multiplieurs. Dans ce travail, nous introduisons de nouvelles classes de multiplieurs HTV qui réduisent considérablement le conservatisme des résultats de l'analyse. Un gyroscope MEMS commercialisé doit vérifier les spécifications de précision et de bruit de sortie, définies par des normes. Nous proposons des critères de performance basés sur des modèles afin d'évaluer ces spécifications. La plupart des outils proposés sont donnés sous la forme de problèmes d'optimisation convexe. La spécification de précision la plus importante est la non-linéarité du facteur d'échelle (SFNL), qui est reformulée comme un problème d'optimisation robuste. La procédure standard pour évaluer le bruit de sortie des gyroscopes MEMS est la variance d'Allan qui est un outil statistique dans le domaine temporel calculé à partir de mesures à long terme de la sortie du gyroscope. Cette méthode basée sur le signal est reformulée comme un outil d'analyse basé sur le modèle en adoptant une approche de filtre générateur. Différents cas sont étudiés, des modèles LTI aux classes de modèles LHTV qui sont pertinents pour l'application du gyroscope MEMS, y compris les incertitudes. Les approches proposées sont validées à l'aide de résultats expérimentaux. Enfin, les outils d'analyse de systèmes proposés sont appliqués à la validation de stratégies de commande alternatives qui nécessitent des architectures plus complexes que la commande LTI classique.

Acknowledgements

This thesis manuscript is the result of four years of work at the Ampère laboratory, Ecole Centrale de Lyon, within the framework of the Next4MEMS project. However, this achievement would not have been possible without the support and collaboration of many people to whom I would like to express my gratitude in the following paragraphs. As a disclaimer: these acknowledgements are written in three different languages so that I can express them in the most sincere way to the people to whom they are addressed.

First of all, I would like to thank BPI France for funding the PSPC Next4MEMS project, as well as the collaborators from the different institutions and companies that put their efforts in the launch and development of the project. It is thanks to this funding that the achievement of this PhD program was possible, as well as the attendance to summer schools and international conferences that allowed me to broaden my perspectives on my field of research.

I would like to thank the members of my thesis defence jury who accepted to evaluate my doctoral work, even though this can involve a significant investment of time and energy. I would like to thank the reviewers: Mr Mathew C. Turner and Mr Fabrice Demourant, whose important comments and suggestions were very helpful. I also thank the reviewers, whose questions were highly pertinent and allowed to enrich the discussion, both in purely theoretical perspectives and in technical applications: Mrs Suzanne Lesecq, Mr Christophe Le Blanc, as well as Mr Jérôme Juillard who accepted to be president of the jury. The jury is completed by Mr Gérard Scorletti (thesis director) and Mr Anton Korniienko (co-supervisor) whom I thank in the following paragraph (passing to the French part).

Je tiens à adresser un grand merci à mes encadrants : Anton Korniienko et Gérard Scorletti, qui m'ont guidé et soutenu tout au long de ce parcours pour faire aboutir ce travail. Tout d'abord, je vous remercie de m'avoir accordé votre confiance pour mener à bien ce projet de doctorat. Je vous remercie pour votre patience, vos conseils, votre soutien, votre disponibilité et votre gentillesse qui ont permis d'avoir une réunion chaque semaine malgré les nombreuses responsabilités que vous aviez en parallèle. Je dois dire que chaque réunion a été une grande expérience d'apprentissage, grâce à la méticulosité avec laquelle vous avez examiné chaque détail de mon travail, à votre volonté de partager votre excellente connaissance du sujet et à l'enthousiasme que vous m'avez transmis pour l'automatique. Merci car tout cela m'a permis d'atteindre une qualité dans mon travail qui n'aurait pas été possible sans vous. Je me souviendrai toujours de vous comme d'un exemple de professionnalisme, de passion pour la recherche et, surtout, d'une grande qualité humaine.

Je tiens également à remercier d'autres personnes qui ont été impliquées dans mon programme de doctorat et mes activités d'enseignement. Tout d'abord, merci encore à Anton Korniienko pour avoir organisé et surveillé le bon déroulement du projet Next4MEMS au sein du Laboratoire Ampère. Je remercie Xavier Bombois, qui a participé à l'examen de mon dossier et aux entretiens pour ma candidature à ce projet de doctorat, ainsi que pour m'avoir gentiment invité à la Spring School qu'il a organisée. Je tiens à remercier Hassan Omran, mon encadrant pour mon travail de Master, pour m'avoir initié à la commande robuste et pour m'avoir parlé du projet Next4MEMS pour la première fois. Merci à Laurent Bako, membre du projet Next4MEMS, qui a été le premier à me proposer de rejoindre l'équipe d'enseignement du traitement du signal. Dans le même esprit, je remercie Juilien

Huillery et Eric Blanco qui m'ont formé et conseillé pour mener à bien les activités d'enseignement. Je tiens également à remercier les membres de mon comité de suivi de thèse : M. Olivier Sename, M. Vincent Andrieu et M. Julien Huillery pour le temps qu'ils ont consacré à évaluer mon travail et à discuter de son évolution. Et pour la troisième fois (bien que pour une raison différente), merci à Julien Huillery pour son temps et sa disponibilité pour discuter de certains éléments du chapitre 5 de ce document. Merci également à Edith Bergeroux qui s'est occupée de la partie administrative de mon doctorat, qui avec sa grande gentillesse et sa bonne humeur, ainsi qu'un chaleureux "Buenos días", m'a presque fait oublier qu'il s'agissait de démarches administratives. Merci également à Marie-Christine Havgoudoukian qui s'est très gentiment et efficacement occupée de l'administration au nom de l'école doctorale.

Un grand merci aussi pour le reste des permanents du laboratoire Ampère et de l'Ecole Centrale de Lyon, avec lesquels j'ai eu l'opportunité des discuter et passer des moments agréables tout au long de ce parcours. Merci à Christian Vollaire, Alice, Richard, Arnaud Bréard, Giacomo Casadei, Laure Franqueville, Eric Vagnon, Emmanuel Boutleux, Gilles Galboud, Sébastien Cecillon, Jérôme. Je remercie également toutes et tous les doctorants, post-docs, ATERs que j'ai pu rencontrer et avec lesquels j'ai pu passer des agréables repas (au moins au RU) et des pauses café super sympas où on discutait plein des sujets en cherchant les mots croisés : Alexandre, Yanis, Hussein, Ouassim, François, Jérémy, Quentin, Ayyoub, Wided, Fatma, Abdelghani, Grégory, Marion, Benoît, Concepcion, Maxime, Debou, Bassem, Azariel, Jesus.

Bon, je crois que j'ai fini avec les gens du laboratoire, passons maintenant à ... pas vrai, je plaisante. Bien sûr, je ne peux m'empêcher de remercier tous mes collègues de la famille Next4MEMS (élargie à NextJeNeSaisPlusQuelChiffreMEMS), avec votre gentillesse, votre bonne humeur et vos grands talents culinaires, ce fut un vrai bonheur de partager ces années avec vous : les blagues au bureau, les dîners, les sorties pour boire un verre, les journées vertes, les voyages (excusez les ronflements), les anniversaires (espérons que pour les 35/40 ans de Fabrício la surprise sera meilleure), la chasse au trésor organisée pour mon anniversaire (merci pour l'arrivée la plus joyeuse au laboratoire malgré le baby shark et la confession forcée sur l'identification), les playlists du confinement, bref, la liste pourrait s'allonger encore et encore, et je suis convaincu qu'elle continuera à s'allonger.

Je remercie Kévin de m'avoir donné un modèle MEMS qui m'a servi d'excuse pour les limites de mes résultats (je plaisante, il a en fait donné des résultats tout à fait satisfaisants). Et je pense qu'après toutes ces années, même si ma confession sur le fait que l'identification est une science a été obtenue par des moyens peu éthiques, c'était le début d'une sympathie pour cette branche de l'automatique, donc, maintenant je le dis sincèrement : "l'identification semble être une science" (je ne suis pas encore prêt à l'accepter carrément XD). Je remercie Federico pour les excellents discussions, tant sur les mathématiques autour de l'automatique que sur des sujets plus philosophiques, ainsi que sur la manière d'appliquer les problèmes d'optimisation à sa vie personnelle. Malheureusement, le sujet de la cuisine italienne a été délicat étant donné certains dogmes (et la peur qu'il me casse sur la tête un ananas ou des spaghettis qu'il n'ose pas casser dans la casserole). Je remercie Fabrício qui a été à mon côté (littéralement, aussi bien au bureau que dans les réunions hebdomadaires) pendant une bonne partie de ce voyage, qui m'a aidé dans beaucoup de choses et qui m'a toujours écouté quand je bloquais sur une subtilité théorique ou simplement quand nous avions envie de parler longuement de n'importe quelle absurdité. Je te remercie même si maintenant que je suis seul au bureau, je suis encore traumatisé

et je continue à mettre mon ordinateur en veille chaque fois que je dois aller aux toilettes. Je tiens également à remercier Priscila pour les grands moments, et merci à vous deux de nous avoir invités à passer Noël avec vous. Je remercie Eva, dont le dynamisme a donné un nouvel élan de camaraderie à notre groupe et au laboratoire en général. J'apprécie et j'admire tes initiatives pour améliorer la vie des doctorants, et tout cela pour le petit prix de mettre de l'eau à bouillir chaque fois que j'allais à la cafétéria (bien sûr, en baissant la tête et en répondant "oui votre majesté"). Merci à Cécile d'être devenue ma professeur pour la partie expérimentale de mon travail et d'avoir apporté son subtil et extraordinaire sens de l'humour, combiné à d'excellents points de vue sur de nombreux sujets, et merci aussi d'avoir contribué à abaisser la moyenne d'âge du groupe. Merci à Arthur (le post-doc de quelques mois autorise administrativement à te considérer dans le projet) pour ton aide à trouver mes multiplieurs, pour nous aider à nous intégrer dans le labo et pour me recommander les meilleurs tielles. Je remercie également à Julie et à toi pour tous ces bons moments et pour nous avoir si bien accueillis à Sète.

Je tiens également à remercier les autres personnes qui m'ont soutenu en dehors du contexte du laboratoire. D'une part, merci à mes colocataires, avec qui j'ai passé les confinements du 2020 : Anthony, avec qui j'ai pu avoir des conversations amusantes sur des films, des séries, des histoires créatives, mais aussi sur un plan personnel, ce qui nous a permis de nous encourager mutuellement. Juan Carlos, grand ami depuis presque 14 ans, merci pour les conseils concernant le doctorat et la vie professionnelle et personnelle, et merci pour toutes les discussions, les blagues et les rires. Jocelyn, qui avec son dynamisme et sa bienveillance me laisse toujours de bonne humeur après une conversation. Merci également aux ex-colocs qui sont passés par l'appartement et avec qui j'ai pu partager d'agréables moments : Rémi, Marine, Kike, Luisa. D'autre part, je tiens à remercier l'équipe "SGI-Montpellier" (bien que nous ne soyons jamais allés à Montpellier) pour tous les bons moments, les rires et le soutien : Coline, Diego, Sirine, Rayane, William, Cécile, Lara, Guilherme. Enfin, merci à Isaac, un autre ami de longue date, et à Désirée, pour son amitié, pour les moments drôles et pour m'avoir aidé dans cette transition après mon doctorat.

Gracias a los amigos de San Luis Potosí que siguen ahí de forma constante después de casi 8 años que me embarqué en esta aventura: a mi primo Luis (Kuerdo), Adrián (Pelón), Juan José (Wero), Chuy Macías, Miguel, Larissa, Oscar (Pichi), Iván (Pollo), Carlos Ornelas, Kika y Adolfo. Los quiero canijos.

Y he dejado para el final a aquellos con los que estoy infinitamente agradecido. No hay palabras para expresar lo agradecido que estoy con mis padres: Leticia y Jorge, y con mi hermana Claudia. Ustedes son el motor que me ha empujado a lo largo de mi vida. Gracias por todo el esfuerzo y todo el amor que han puesto en mi crianza, mi educación y en hacerme una persona que intenta ser mejor cada día, en lo profesional, pero sobre todo tratando de mantener siempre los pies sobre la tierra, siendo agradecido y tratando de tener una buena calidad humana, tratando a los demás siempre con respeto, empatía y solidaridad. Gracias por los valores que me han inculcado, por haberme apoyado en mis estudios y en todos los proyectos que he emprendido (aun cuando parecen una locura). Y, sobre todo, gracias por estar siempre ahí, aconsejándome y contagiándome de su buen humor. La lista sería interminable. Solo me queda decirles que este logro es también suyo, sin ustedes nada de esto hubiera sido posible. Los amo infinitamente. Gracias también a mi cuñado César, que ha integrado la familia desde hace 8 años, pero lo ha hecho con gran cariño y dándonos siempre su apoyo. Y un agradecimiento especial y con mucho amor a mi sobrina y ahijada Valeria (aunque nos tenemos que esperar unos años antes de que pueda leer esto) que ha traído mucha luz a nuestras vidas con toda su alegría y

esa sonrisa tan hermosa. Y aunque es un poco complicado, quiero agradecer al resto de mi familia que, afortunadamente, es muy numerosa y unida, lo cual vuelve difícil el mencionarlos uno por uno a todos en este párrafo (se me harían tres páginas). Gracias por todo el apoyo y todo el ánimo que me brindan cada vez que nos vemos, ustedes me llenan el corazón de alegría y entusiasmo en cada visita a San Luis.

Y, obviamente, mi más especial agradecimiento va dirigido a quien ha estado incondicionalmente a mi lado a cada instante y de forma constante a lo largo de toda esta aventura, la que cada día me saca una sonrisa al ver un "holi", a la que esta bimbonita, a la mejor compañera de aventuras: Anaïs. Primero, como paréntesis, quiero agradecer a tu mami Pepita y a la familia Postel Carles por todas las atenciones que habéis tenido para conmigo durante mis visitas a Jávea, Alcalá y Valencia, me he sentido como en casa y me ha ayudado mucho para retomar la motivación. Ahora para ti, creo que no hay forma de agradecerte sin quedarme corto de palabras. Gracias por alegrarme cada día con tus stickers, bromas, recomendaciones de canciones, libros y videos, por tus melodías que salen de un rincón de tu memoria que no sabemos identificar pero que me hacen reír. Gracias por empujarme a intentar nuevas cosas a pesar de mi espíritu monótono: escalar y dormir en la cima de un monte, ir en bici hasta la orilla del mar, ir en canoa por el río (por cierto, gracias por acompañarme a revisar mi dedo), hacer snorckel, saltar al agua, etc. Mil gracias, al final lo he disfrutado muchísimo y me ha dejado recuerdos que no voy a olvidar. Y también gracias por acompañarme, escucharme y apoyarme en los momentos difíciles, sobre todo en la pandemia y la redacción. Gracias por ayudarme a atenuar los momentos de estrés y angustia invitándome a ir a caminar, tomar un café o una limonada, ir a la librería, ir al parque, ver una serie, hablarme de plantitas o de tus autoras preferidas. Simplemente, gracias infinitamente por cada momento compartido, por hacerme la vida más feliz, más fácil y más luminosa y, sobre todo, gracias por tanto amor. ¡Te amo pequeña!

Contents

Abstract iii

Acknowledgements vii

List of Abbreviations xxiii

List of Symbols xxv

1 General introduction 1
- 1.1 Context and motivations . . . 1
  - 1.1.1 MEMS gyroscopes . . . 1
  - 1.1.2 The Next4MEMS project . . . 2
  - 1.1.3 The control design process . . . 3
- 1.2 Research approach and contributions . . . 4
  - 1.2.1 Analysis of LHTV systems . . . 5
  - 1.2.2 Model-based performance specifications . . . 6
  - 1.2.3 Control design validation . . . 8
- 1.3 Structure of the manuscript . . . 9
- 1.4 Publications . . . 10

2 Performance validation of MEMS gyroscopes 11
- 2.1 System description . . . 11
  - 2.1.1 Mechanical principle . . . 12
  - 2.1.2 Actuation and detection . . . 14
  - 2.1.3 Feedback control loop . . . 17
    - Drive mode . . . 17
    - Sense mode . . . 18
    - Some control strategies of the NEXT4MEMS project . . . 19
  - 2.1.4 Synchronous demodulation . . . 20
    - Ideal synchronous demodulation . . . 21
    - Extraction of Coriolis force . . . 22
- 2.2 From gyroscope output to measured angular rate . . . 23
- 2.3 Gyroscope Performance Specifications . . . 24
- 2.4 Nonidealities in MEMS gyroscopes: sources of uncertainty . . . 26
  - 2.4.1 Manufacturing dispersion . . . 26
  - 2.4.2 Anisoelasticity . . . 26
  - 2.4.3 Non-ideal Damping . . . 27
  - 2.4.4 Environmental sensitivity . . . 28
  - 2.4.5 Noise . . . 29
  - 2.4.6 Electronic phase-shift . . . 29
  - 2.4.7 Other non-idealities . . . 30
- 2.5 Validation of the control design . . . 30
- 2.6 MEMS gyroscope model and uncertainty . . . 32

2.7 Research problem formulation . . . 34

3 Analysis of Uncertain and Harmonically Time-Varying Systems 37
3.1 Input-output stability and performance . . . 37
3.2 Representation of uncertain systems . . . 38
3.2.1 Linear Fractional Transformation . . . 39
3.3 Robust stability and robust performance . . . 41
3.3.1 Robust stability . . . 41
3.3.2 Robust performance . . . 42
3.4 Analysis of LFT systems . . . 43
3.4.1 Integral Quadratic Constraints (IQC) approach . . . 44
3.4.2 Multiple uncertainties . . . 47
3.4.3 Classes of multipliers . . . 48
3.4.4 Finite dimensional conditions . . . 51
3.5 Uncertain Harmonically Time-Varying Systems . . . 54
3.5.1 System description . . . 56
3.5.2 IQC multiplier for one repeated harmonic parameter . . . 57
Frequency domain solution . . . 63
State-space solution . . . 66
Example . . . 68
3.5.3 Multiplier for coupled harmonic parameters . . . 71
State-space resolution . . . 72
3.5.4 Extension to full-block harmonic operators . . . 74
3.6 Chapter conclusion . . . 77

4 Analysis of Bias and Scale Factor Nonlinearity 79
4.1 MEMS standard specifications and tests . . . 79
4.1.1 Accuracy specifications . . . 79
Sensitivity specifications . . . 81
4.2 From standard specifications to analysis criteria . . . 82
4.3 Scale factor nonlinearity LMI condition . . . 85
4.4 Thermal sensitivity LMI condition . . . 87
4.5 Worst-case SFNL for models obtained by model prediction error identification . . . 89
4.6 Numerical example: SFNL and thermal sensitivity of a controlled MEMS gyroscope model . . . 93
4.7 Application case: study of the experimental SFNL . . . 95
4.7.1 Test platform: AS3125-SDK . . . 95
4.7.2 Model, controllers and uncertainty . . . 96
4.7.3 Result . . . 98
4.8 Chapter conclusion . . . 99

5 Analysis of Output Noise Level 101
5.1 Noise in MEMS gyroscopes and the Allan Variance method . . . 101
5.2 Allan variance in the frequency domain . . . 105
5.3 LTI Model-based Allan variance . . . 108
5.3.1 Allan variance and the $\mathcal{H}_2$ system performance . . . 109
5.3.2 Rational Allan filter design using Padé approximation . . . 112
5.3.3 Example . . . 113
5.4 Worst-case Allan variance of uncertain systems . . . 116
5.5 Model-based Allan variance of demodulated signals . . . 120

5.5.1 Approach 1: IQC approach with harmonic multipliers 120
5.5.2 Approach 2: Equivalent LTI system 122
5.5.3 Example 125
5.6 Application to MEMS gyroscope 126
5.7 Chapter conclusion 128

6 Analysis methods for alternative control strategies 129
6.1 Stability analysis of a phasor-based control strategy with non-ideal synchronous demodulation 130
6.1.1 Phasor-based control with ideal synchronous demodulation . . 130
6.1.2 Analysis with non-ideal synchronous demodulation 133
6.2 Analysis of the discrete-time implementation of a parameter dependent adaptative controller 136
6.2.1 Analysis of the discrete-time implementation of parameter dependent controller with non-ideal resonance frequency estimation 138
6.2.2 Example 145
6.3 Chapter conclusion 146

7 Conclusions and perspectives 149
7.1 Conclusions 149
7.2 Future work 151
7.2.1 Model-based evaluation of MEMS gyroscopes 152
7.2.2 Analysis of LHTV systems 153

A Proofs of Chapter 3 155
A.1 Proof of Theorem 3.6 155
A.2 Proof of Lemma 3.5 158
A.3 Proof of Theorem 3.8 158
A.4 Proof of Theorem 3.9 162

B Proofs and elements of chapter 4 167
B.1 Least Square linear regression and relationship with scale factor error . 167
B.1.1 LFT model of MEMS gyroscope 168
B.2 Relationships between the control design objectives and the global performance specifications 170

C Proofs of chapter 5 173
C.1 Proof of Theorem 5.6 173

D Résumé étendu : Chapitre 1. Introduction générale 179
D.1 Contexte et motivations 179
D.1.1 Gyroscopes MEMS 179
D.1.2 Le projet Next4MEMS 179
D.1.3 Le processus de conception de la commande 180
D.2 Approche de la recherche et contributions 180
D.2.1 Analyse des systèmes LHTV 180
D.2.2 Spécifications de performance basées sur des modèles 181
D.2.3 Validation de la conception de la commande 181

E Résumé étendu : Chapitre 2. Validation des performances des gyroscopes MEMS **183**
E.1 Description du système . . . 183
E.1.1 Principe mécanique . . . 183
E.1.2 Actionnement et détection . . . 185
E.1.3 Commande en boucle fermée . . . 185
Mode Drive . . . 185
Mode sense . . . 185
Quelques stratégies de commande du projet NEXT4MEMS . . . 186
E.1.4 Démodulation synchrone . . . 186
Démodulation synchrone idéale . . . 186
Extraction de la force de Coriolis . . . 187
E.2 De la sortie du gyroscope à la vitesse angulaire mesurée . . . 188
E.3 Spécifications des performances du gyroscope . . . 188
E.4 Non-idéalités dans les gyroscopes MEMS : sources d'incertitude . . . 189
E.4.1 Dispersion de fabrication . . . 189
E.4.2 Aniso élasticité . . . 189
E.4.3 Amortissement non idéal . . . 189
E.4.4 Sensibilité à l'environnement . . . 189
E.4.5 Bruit . . . 189
E.5 Validation de la conception de la commande . . . 190
E.6 Formulation du problème de recherche . . . 190

F Résumé étendu : Chapitre 3. Analyse des systèmes incertains et temps-variants harmoniques **191**
F.1 Stabilité et performance entrée-sortie . . . 191
F.2 Représentation des systèmes incertains . . . 192
F.2.1 Transformation linéaire fractionaire (LFT) . . . 192
F.3 Stabilité robuste et performance robuste . . . 193
F.3.1 Stabilité robuste . . . 193
F.3.2 Performance robuste . . . 193
F.4 Analyse des systèmes LFT . . . 194
F.4.1 Approche des contraintes quadratiques intégrales (IQC) . . . 194
F.4.2 Conditions de dimension finie . . . 195
F.5 Systèmes incertains et temps-variants harmoniques . . . 197
F.5.1 Description du système . . . 197
F.5.2 Multiplicateur IQC pour un paramètre HTV répété . . . 198
Solution dans le domaine fréquentiel . . . 200
Solution dans l'espace d'état . . . 201
F.5.3 Multiplieur pour des paramètres harmoniques couplés . . . 202
F.6 Conclusion du chapitre . . . 203

G Résumé étendu : Chapitre 4. Analyse du Biais et de la Non-linéarité du Facteur d'Échelle **205**
G.1 Spécifications standard et tests des MEMS . . . 205
G.1.1 Spécifications de précision . . . 205
Spécifications de sensibilité . . . 206
G.2 Des spécifications standard aux critères d'analyse . . . 206
G.3 Condition LMI de la nonlinearité du facteur d'échelle . . . 208
G.4 SFNL pire-cas pour les modèles obtenus par identification en utilisant la méthode des erreurs de prédiction de modèle . . . 209

G.5 Cas d'application : étude de la SFNL expérimentale 210
G.5.1 Résultat 211
G.6 Conclusion du chapitre 212

H Résumé étendu : Chapitre 5. Analyse du Niveau de Bruit de Sortie 213
H.1 Le bruit dans les gyroscopes MEMS et la méthode de la Variance d'Allan 213
H.2 Variance d'Allan dans le domaine fréquentiel 214
H.3 Variance d'Allan basée sur le modèle LTI 215
H.3.1 La variance d'Allan et la performance $\mathcal{H}_2$ des systèmes. 215
H.4 Variance d'Allan des signaux démodulés basée sur un modèle 216
H.4.1 Approche 1 : Approche IQC avec multiplieurs harmoniques . . 217
H.4.2 Approche 2 : Système LTI équivalent 218
H.5 Application au gyroscope MEMS 219
H.6 Conclusion du chapitre 220

I Résumé étendu : Chapitre 6. Méthodes d'analyse pour des stratégies de commande alternatives 221
I.1 Analyse de stabilité d'une commande basée-phaseurs avec démodulation non-idéale 221
I.2 Analyse de l'implémentation en temps discret d'un correcteur adaptatif dépendant d'un paramètre 225
I.3 Conclusion du chapitre 228

J Résumé étendu : Chapitre 7. Conclusions et perspectives 231
J.1 Conclusions 231
J.2 Travaux futurs 232
J.2.1 Évaluation des gyroscopes MEMS basée sur des modèles 232
J.2.2 Analyse des systèmes LHTV 233

List of Figures

1.1 Control design process (Next4MEMS project) . . . 4
1.2 LHTV systems: a) open-loop configuration; b) closed-loop configuration 5

2.1 Representation of Coriolis effect . . . 12
2.2 Schematic representation of MEMS drive and sense modes . . . 13
2.3 Bode diagram of the drive mode transfer function . . . 13
2.4 Schematic representation of a comb drive actuator . . . 15
2.5 AGC + PLL drive mode control . . . 18
2.6 Direct control of drive mode . . . 18
2.7 Force to rebalance sense mode control . . . 19
2.8 PSD of a modulated signal z . . . 21
2.9 Schematic representation of the ideal synchronous demodulation . . . 22
2.10 Input-output relationship of a MEMS gyroscope . . . 25
2.11 Schematic representation of anisoelasticity . . . 27
2.12 Identified model with cross-couplings . . . 28
2.13 Effect of a parametric uncertainty on the drive mode resonator . . . 33

3.1 Representation of a set of models . . . 39
3.2 LFT representation $\Delta \star G$ . . . 40
3.3 Feedback interconnection (G_{qp}, Δ) . . . 41
3.4 Equivalent representation of δI_{n_q} . . . 49
3.5 Schematic representation of sets of uncertainties and multipliers . . . 58
3.6 Representation of the exponential form of $\cos(\omega_0 t + \phi)$ . . . 59
3.7 Equivalent representation of θ_{up} . . . 60
3.8 Frequency gridding . . . 64
3.9 Construction of $X_D(j\omega)$ . . . 65
3.10 Construction of $X_G(j\omega)$ . . . 65
3.11 Stability domain of Mathieu-Hill equation with $b = 0$ . . . 70
3.12 Stability domain of Mathieu-Hill equation with $b = 0.75$ . . . 71

4.1 Closed-loop MIMO direct control . . . 83
4.2 Extraction of the in-phase component . . . 84
4.3 LFT for the computation of the output error ε_z . . . 85
4.4 Interconnection associated to the output error . . . 86
4.5 LFT model for thermal sensitivity . . . 88
4.6 Ellipsoidal set $\boldsymbol{U}$ . . . 90
4.7 Comparative of LMI model-based SFNL versus Monte Carlo . . . 94
4.8 MEMS gyroscope packaging . . . 96
4.9 Bode of black-box identified model (normalized) . . . 97
4.10 Closed-loop responses: drive mode tracking error(left) and sense mode Coriolis rejection (right) . . . 97
4.11 Comparison of experimental, Monte Carlo and LMI worst-case errors . 99

5.1 Noise of output angular rate . . . 102
5.2 Computed angular position . . . 102
5.3 Allan deviation plot (adapted from [IEE06]) . . . 104
5.4 Impulse response of h_{Ave_T} . . . 106
5.5 Impulse response . . . 106
5.6 Frequency responses of Allan filter h_{All} . . . 108
5.7 Extended system G_e for Allan variance computation . . . 109
5.8 Frequency response of Allan filter and approximated Allan filters . . . 113
5.9 Absolute error of the approximated Allan filters . . . 113
5.10 Relative error of the approximated Allan filters . . . 114
5.11 Allan deviation plot for an white noise . . . 115
5.12 Allan deviation plot for an white noise for a rate random walk noise . . . 116
5.13 Computation of the Allan variance. a) Allan variance from a noise. b) Allan variance from a nominal system model. c) Worst-case Allan variance from an uncertain system model. . . . 117
5.14 IQC H_2 performance virtual experiment . . . 119
5.15 Comparison of simulation and estimation of Allan variance . . . 125
5.16 Equivalent system . . . 126
5.17 Measured output . . . 126
5.18 Compensated output . . . 127
5.19 Comparison of Allan deviation results . . . 127

6.1 Implementation of $s2p$: synchronous demodulation . . . 133
6.2 Ideal closed-loop phasor control . . . 133
6.3 Non-ideal closed-loop phasor control . . . 136
6.4 Impact of resonance frequency variations on the tracking error . . . 137
6.5 Analysis model in normalized pseudo-continuous time . . . 140
6.6 Variation of performance with respect to $\omega_{m_{max}}$. . . . 146

A.1 Representation of the exponential form of $\theta^{\omega_0}(t)$ . . . 155
A.2 Equivalent representation of θ_{up} . . . 156
A.3 Equivalent representation of θ_{up} . . . 159
A.4 Representation of the exponential form of $\theta^{\omega_0}(t)$ . . . 163
A.5 Representation of the decomposed exponential form of $\theta^{\omega_0}(t)$ . . . 163
A.6 Equivalent representation of θ_{up} . . . 163
A.7 Second commutation of θ_{up} . . . 164

B.1 LFT of the MEMS closed-loop system . . . 169
B.2 LFT for the computation of the output z . . . 170

C.1 DSP $S_l(\omega)$ . . . 177

E.1 Représentation schématique des modes drive et sense du MEMS. . . . 184
E.2 Représentation schématique de la démodulation synchrone idéale . . . 187

F.1 Représentation LFT $\Delta \star G$ . . . 192
F.2 Interconnexion de rétroaction (G_{qp}, Δ) . . . 193
F.3 Construction of $X_G(j\omega)$ . . . 201

G.1 Extraction of the in-phase component . . . 207
G.2 Comparaison des erreurs expérimentales, de Monte Carlo et de LMI pire-cas . . . 211

H.1 Tracé de l'écart d'Allan (adapté de [IEE06]) 214
H.2 Système étendu G_e 215
H.3 Système équivalent 220
H.4 Comparaison des résultats de l'écart d'Allan 220

I.1 Boucle de commande par phaseurs non-idéale 224
I.2 Analysis model in normalized pseudo-continuous time 227

List of Tables

3.1 Classes of multipliers 51

4.1 Results of the SFN thermal sensitivity (LMI versus Monte Carlo) 95

5.1 Table of different order Padé approximants 112

6.1 Results of the non-ideal phasor closed-loop analysis 136

I.1 Résultats de l'analyse de la commande basée phaseur non-idéale . . . 225

List of Abbreviations

AGC	**A**utomatic **G**ain **C**ontrol
ARW	**A**ngular **R**andom **W**alk
IQC	**I**ntegral **Q**uadratic **C**onstraint
LFT	**L**inear **F**ractional **T**ransformation
LHTV	**L**inear **H**armonically **T**ime-**V**arying
LMI	**L**inear **M**atrix **I**nequality
LPTV	**L**inear **P**eriodically **T**ime-**V**arying
LTI	**L**inear **T**ime **I**nvariant
LTV	**L**inear **T**ime-**V**arying
MEMS	**M**icro **E**lectro-**M**echanical **S**ystem
MIMO	**M**ulti-**I**nput **M**ulti-**O**utput
PLL	**P**hase-**L**ocked **L**oop
PSD	**P**ower **S**pectral **D**ensity
RRW	**R**ate **R**andom **W**alk
SFNL	**S**cale **F**actor **N**on**L**inearity
SISO	**S**ingle-**I**nput **S**ingle-**O**utput
SNR	**S**ignal to **N**oise **R**atio

List of Symbols

$\mathbb{R}$	Set of real numbers
$\overline{\mathbb{R}}$	Extended real line, i.e. $\overline{\mathbb{R}} = \mathbb{R} \cup \{-\infty\} \cup \{\infty\}$
$\mathbb{C}$	Set of complex numbers
$\mathbb{C}^0$	Extended imaginary axis $j\mathbb{R}$
j	Imaginary unit, i.e. $j^2 = -1$.
$\widehat{x}$	Fourier transform of x.
A^T	Transpose of A.
$G(j\omega)^*$	Hermitian conjugate of $G(j\omega)$, i.e. $G(j\omega) = G(-j\omega)^T$.
I_n	Identity matrix of dimension n.
I	Identity matrix whose dimension is given by the context.
$0_{m\times n}$	Zero matrix of dimension $m \times n$.
0 (in matrix operations)	Zero matrix whose dimension is given by the context.
$\mathbb{S}^n$	Set of real symmetric matrices of dimension $n \times n$.
$\mathrm{diag}(A_1, ..., A_n)$	Diagonal concatenation of a finite set of matrices A_i, with $i \in \{1, ..., n\}$.
$\mathrm{col}(A, ..., B)$	Column concatenation of a finite set of matrices with compatible dimensions A_i, with $i \in \{1, ..., n\}$.
$\otimes$	Kronecker product
$A \succ (\succeq)\, 0$	It denotes that the matrix A is positive definite (positive semi-definite).
$\overline{\sigma}(A)$	Maximal singular value of A.
$\lvert\cdot\rvert$	Euclidean norm on $\mathbb{R}^n$ is given by $\lvert x\rvert = \sqrt{x^T x}$. On $\mathbb{C}^n$ (also called modulus) is given by $\lvert x\rvert = \sqrt{x^* x}$.
$\mathcal{L}_2^n$	Space of square integrable $\mathbb{R}^n$-valued functions.
$\mathcal{L}_{2e}^n$	Space of $\mathbb{R}^n$-valued functions whose truncation at a time T is square integrable.
$\lVert\cdot\rVert_{\mathcal{L}_2}$	$\mathcal{L}_2$-norm of a signal, i.e. $\lVert x\rVert = \left(\int_{-\infty}^{\infty} \lvert x(t)\rvert^2 dt\right)^{1/2}$.
$\lVert G\rVert_{\mathcal{L}_2}$	$\mathcal{L}_2$-gain of G, i.e. $\lVert G\rVert_{\mathcal{L}_2} = \sup_{w\in\mathcal{L}_{2e}{}^{n_w}} \frac{\lVert G(w)\rVert}{\lVert w\rVert}$.
$\lVert G\rVert_2$	$\mathcal{H}_2$-norm of the linear operator G, i.e. $\lVert G\rVert_2 = \left(\frac{1}{2\pi} G(j\omega)^* G(j\omega)\right)^{1/2}$.
$\lVert G\rVert_\infty$	$\mathcal{H}_\infty$-norm of G.
$\mathcal{H}_\infty^{m\times n}$	Space of complex-valued transfer functions (of dimension $m \times n$) with finite $\mathcal{H}_\infty$ norm
$\mathcal{RL}_\infty^{m\times n}$	Space of real rational transfer functions (of dimension $m \times n$) without poles on the extended imaginary axis $\mathbb{C}^0$.
$\mathcal{RH}_\infty^{m\times n}$	Subset of $\mathcal{RL}_\infty^{m\times n}$ without poles on the closed right-half complex plane

Dedicated to Anaïs and my beloved family

Chapter 1

General introduction

1.1 Context and motivations

1.1.1 MEMS gyroscopes

A gyroscope is a device that measures the angular velocity (or angular rate) of an object with respect to a frame of reference. The acronym MEMS stands for Micro Electro-Mechanical Systems. The MEMS technology is the result of a long progress in the field of microelectronics and semiconductor manufacturing methods [Sau08a]. MEMS devices are generally manufactured by employing photolithography processes that allow the production of microscale structures that are directly integrated in a silicon chip. The term electro-mechanical systems describes the fact that, in contrast to classical microelectronic devices, MEMS sensors exploit simultaneously mechanical and electrical principles. This development made possible the extension of classical microelectronics applications to the measurement of physical magnitudes such as acceleration, angular rate, pressure, flow, etc.

The first large scale applications of MEMS gyroscopes dates from the 1990s, with the implementation of the first automobile electronic stability control that employs MEMS gyroscopes [GBKN91, ES98, MG99, PB16]. A major milestone in the development of the MEMS inertial sensor industry comes with their introduction in consumer electronics applications, most notably in motion-based video-game controllers and smart phones [PB16, Kem11, Sau08a, Apo06]. Nowadays, MEMS inertial industry becomes a rapidly growing market, with MEMS gyroscopes being integrated in medical applications, wearable devices, automobile navigation systems, among other applications. The evolution of the MEMS market is periodically reported by some market research groups, for instance [Dev20].

MEMS gyroscopes employ the Coriolis effect to estimate the angular rate. The mechanical structure consists in two microscopic proof masses that are linked to a fixed platform through silicon beams. The proof masses are then forced to vibrate in orthogonal directions by applying electrostatic forces. Then, in the presence of angular motion, a Coriolis force is induced in the rotating body. Since the Coriolis force is proportional to the oscillations of the mass and the angular rate, we can indirectly measure the angular rate by maintaining the oscillations and detecting the amplitude of the Coriolis force. The MEMS mechanical system is designed to be poorly-damped in order to provoke a resonating effect. The motivation to use a resonator is that it allows to radically improve the Signal to Noise Ratio (SNR). The use of two vibrating masses, generally named modes, is required since one is employed to generate and maintain the oscillations (the drive mode) and the other one is used to detect the Coriolis force (the sense mode). The accuracy and reliability of the measured angular rate is then directly affected by the quality of the mechanisms driving the oscillations and estimating the Coriolis force. Hence, in order to ensure

the proper operation of MEMS gyroscopes, i.e., of the drive and sense modes, it is necessary to implement feedback control loops.

MEMS gyroscopes microscopic size make them suitable for their integration in compact and light embedded systems. Other advantageous features are their considerably lower energy consumption and lower prices with respect to macro-size gyroscopes, such as the ring-laser gyroscopes or the fiber optic gyroscopes. Nevertheless, the implementation of MEMS gyroscopes in applications that demand high-performance specifications, such as defense and aeronautic/aerospace navigation, remains rather limited. While the micro-size of MEMS gyroscopes can be advantageous in some cases, it still implies several drawbacks, such as manufacturing imperfections, high sensitivity to environmental conditions, lower SNR, etc. These limitations, in general, make not possible to achieve the performance levels that are required by the regulations of many delicate applications.

In order to increase the application field of MEMS gyroscopes, their accuracy and reliability must be improved. However, it is desirable that they keep one of their main advantages: an attractive price. One way to achieve the envisaged improvements is to enhance the mechanical features and manufacturing processes. Nevertheless, up to this date, the scale of MEMS gyroscopes and the available technology represent important limitations to reach radical manufacturing improvements in the short-term. In this sense, it is necessary to accept that the produced MEMS gyroscopes can have a relatively high uncertainty, related to the dispersion and environmental sensitivity, which increases the requirements of robustness, that is, the need of ensuring a certain accuracy in spite of the gyroscope imperfections.

Since robustness is a crucial point to be considered, feedback control loops play a crucial role as an alternative to achieve important performance improvements. Indeed, control loops can be designed in order to specifically ensure some accuracy while minimizing the sensibility (improving the robustness) with respect to the system uncertainty. Moreover, the improvement of the implemented control loops does not demand a significant modification of the material features of MEMS gyroscopes, allowing to properly address the trade-off between performance and low-cost. However, in spite of the fact that in modern Robust Control there exist methods that appear suitable candidates to finely address this compromise, the most of the nowadays implemented control methods and architectures are still not adapted to met these challenges.

In this context, the development of MEMS gyroscopes is still an active and interdisciplinary field of research, going from mechanical design to microlectronics and automatic control engineering. This PhD program is part of a large scale research and development project: the Next4MEMS project. Its main ambition is to combine the efforts of the main French players in microelectronics and the inertial sensor industry to provide new solutions for the development of new generations of MEMS gyroscopes, achieving high precision at reasonable cost.

1.1.2 The Next4MEMS project

The Next4MEMS is an initiative of several French players in the microelectronics and inertial sensor industry. The challenge of the Next4MEMS project is to establish a competitive, sustainable French Silicon Inertial MEMS industry that responds to most of the high performance needs. This project is supported by BPI France (the French public investment bank) as part of the competitiveness cluster "Minalogic PSPC" (Structuring Research and Development Project for Competitiveness).

The Next4MEMS project counts with the collaboration of private companies and public research laboratories. Tronics/TDK is a company that manufactures MEMS gyroscopes as well as the associated electronics. Asygn is a company that develops solutions for electronics, signal processing and computer-sensor interfaces. iXblue manufactures Inertial Measurement Units (IMUs), mainly focused on aerospace and marine applications. ONERA is a laboratory involved in the research of both the electro-mechanics of MEMS gyroscopes and their application in the aerospace sector.

Last but not least, this PhD program is carried out within the Ampère Laboratory, whose objective is to propose a systematic methodology for the control design process. The purpose of such a process is to systematically provide control solutions that improve the global performance and robustness specifications of MEMS gyroscopes. As aforementioned, MEMS gyroscopes, given their microscale, present some drawbacks such as manufacturing dispersion, environmental sensitivity, low SNR, etc. The operation in feedback-loop is then essential to ensure some desired properties, for instance robust performance, mitigation of non-ideal phenomena, an appropriate bandwidth, etc. Then, the development of optimal control strategies is crucial for the design of modern MEMS gyroscopes.

1.1.3 The control design process

The control design process adopted for the Next4MEMS is represented in Figure 1.1. The first step is to derive a model (a mathematical representation) that describes the behavior of the real system. This model has to be as accurate as possible while keeping a relatively simple structure, adapted for control design purposes. The PhD work of Kevin Colin, supervised by Xavier Bombois, Laurent Bako and Anton Korniienko [Col20], focuses on proposing and developing system identification (data-based) methods to obtain reliable models of MEMS gyroscopes. The control design step develops control strategies to achieve the required specifications. The PhD program carried out by Fabricio Saggin, and supervised by Gerard Scorletti, Xavier Bombois and Anton Korniienko [Sag21], provides systematic control design tools that allows to optimize the MEMS gyroscopes performance while offering formal guarantees of robustness. Next, adaptative control techniques can be necessary to compensate the effect of the temperature on the system behavior. The PhD work of Federico Morelli, supervised by Xavier Bombois, Laurent Bako and Anton Korniienko [Mor21], proposes the methods to detect in real-time the effect of the temperature.

Finally, the objective of the validation step is to evaluate if the closed-loop system can ensure some desired properties (stability, performance, robustness) when it is implemented on the real system. If the controlled system verifies all the requirements, then the control design is successfully achieved. If this is not the case, it is necessary to detect the causes and to look for a better control solution. In this sense, the design of an optimal control strategy is an iterative process. This implies a major motivation to make the different control design steps as efficient as possible, including the performance validation process. The objective of this work is to propose efficient methods to carry out the system validation step within the control design process. This memoir focuses in the pre-experimental model-based performance validation problem rather than on the experimental validation procedure that usually requires important time and resources investment. The adopted validation approach is discussed in the following sections.

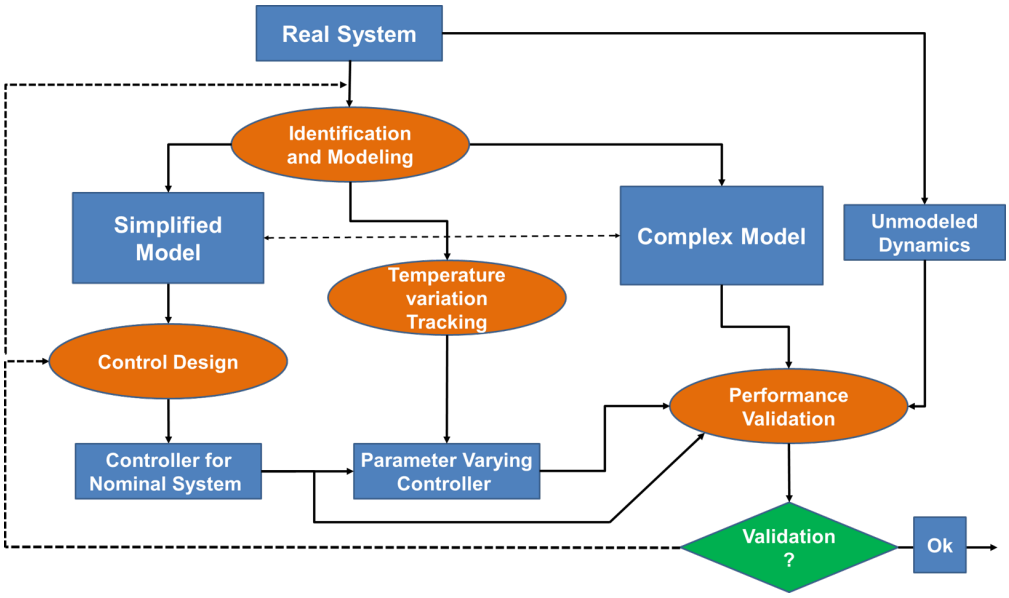

FIGURE 1.1: Control design process (Next4MEMS project)

1.2 Research approach and contributions

In the MEMS gyroscope community, the efforts in automatic control have been mainly focused on the design of control strategies. Performance validation has therefore been mainly approached as a step to be addressed once the product is finalized, commonly through experimental tests. However, in many cases, the experimental validation requires a considerable investment of time and resources, which can be in contradiction with the need of efficiently testing a variety of proposed control solutions. In this context, it is necessary to develop complementary pre-experimental validation methods so that we can enhance the efficiency of the control design process. To this purpose, it is necessary to adopt a model-based approach that, from the control theory perspective, is related to the system analysis problem.

The objective of the system analysis problem is to verify if a given dynamical system ensures some properties: a given notion of stability, a certain number of performance objectives to be met, robustness with respect to modeling errors, etc. A solid framework for the analysis of Linear Time-Invariant (LTI) systems has been established and successfully implemented in many applications. However, in many other applications, the LTI framework does not allow to provide formal guarantees of stability and performance. This is the actual case of MEMS gyroscopes, which can be considered as a particular class of uncertain and time-varying systems.

As aforementioned, the MEMS drive mode generates harmonic oscillations of its mass in order to allow the occurrence of the Coriolis force. Therefore, independently of the adopted control strategy, the MEMS gyroscope closed-loop, partially or completely, work with modulated signals. Then, in order to obtain the measured angular rate, related to the amplitude of some of these modulated signals, it is necessary to implement synchronous demodulation. Synchronous demodulation consists in multiplying by sinusoidal functions and filtering an input signal in order to extract the component of the modulated signal that contains the information of interest. The presence of synchronous demodulation in the system appears as the introduction of one or several Harmonically Time-Varying (HTV) parameters, i.e. parameters that vary as sinusoidal functions of the time.

Then, considering the main control strategies that are studied and developed in the Next4MEMS project, and depending on the localization of the synchronous demodulation in the system, we can distinguish two main classes of Linear Harmonically Time-Varying (LHTV) systems to be analyzed, represented in Figure 1.2. The first configuration considers the so-called direct control strategies [DA09, Sag21], which consists in designing an LTI feedback control loop whose output is sent to the synchronous demodulator in an open-loop configuration. The second case considers the control strategies that require the implementation of the synchronous demodulation inside the closed-loop, such as the phasor-based control [SSK20]; the system is then represented by the interconnection of the LTI part of the system and a set of HTV parameters, which are the effect of the synchronous demodulator in the loop.

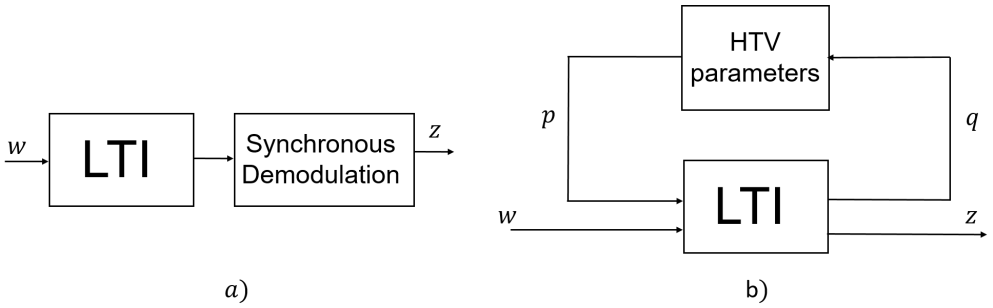

FIGURE 1.2: LHTV systems: a) open-loop configuration; b) closed-loop configuration

Strictly speaking, the open-loop configuration can be addressed as a particular case of the feedback configuration, this by simply reconfiguring the system interconnection. Hence, the analysis tools that are derived to analyze the closed-loop configuration can be also applied to the analysis of the first configuration. This implies a major motivation to formally address the analysis of LHTV systems and to develop a set efficient and general analysis tools. Nevertheless, in some cases, taking into account the particular characteristics of the open-loop configuration allows us to derive accurate analysis criteria for the performance evaluation.

1.2.1 Analysis of LHTV systems

We define an LHTV system as a linear system that contains one or several parameters that are Harmonically Time-Varying (HTV) i.e. that vary as sinusoidal functions of the time. To formally address the analysis of LHTV systems, we adopt the Integral Quadratic Constraints (IQC) approach [MR97, Sei14, VSK16, CS15]. The IQC framework merges several concepts and results of the nonlinear and the robust control theories, which allows to naturally extend the analysis of uncertain systems to the analysis of time-varying and nonlinear systems. Some of the attractive features of this approach are: 1) its generality to test the stability of many classes of systems, as well as a variety performance criteria; 2) its modular structure, offering an important flexibility to easily adapt the analysis tools to different cases; 3) its efficiency by systematically establishing many of the analysis tests in the form of convex optimization problems under Linear Matrix Inequality (LMI) constraints [BEGFB94], a class of optimization problems that can be efficiently solved. This theoretical framework is then adapted to the analysis of MEMS gyroscopes, allowing to simultaneously consider its uncertain and time-varying nature, as well as to study the accuracy, sensitivity and output noise specifications.

A key step to apply the IQC framework is to characterize the input-output relationships of the problematic element, belonging to an uncertain set, through an integral quadratic constraint that is defined by a set of Hermitian matrix functions, referred to as *multipliers*. Different sets of multipliers can satisfy an IQC for a given uncertain set, then, the choice of a set of multipliers to perform the system analysis is not unique. However, if the selected set of multipliers does not imply a sufficiently rich characterization of the uncertain set, we can then obtain a sufficient conditions that could be conservative.

To tackle the analysis of LHTV systems, reducing the conservatism of the results, two results are useful as a starting point: 1) the sets of frequency dependent IQC multipliers for parametric uncertainties (or $D-G$ scalings[1]) [FTD91, MIF00, LTVD00], which can be considered as a particular case of a THV parameter. 2) The frequency dependent multiplier for a repeated HTV parameter, proposed in [MR97]. The motivation is that the $D-G$ scalings allow to obtain sufficient and necessary analysis conditions for systems with a repeated parametric uncertainty, being the introduction of the G scaling which radically reduces the conservatism of the results. In contrast, the harmonic multiplier of [MR97] only has a D scaling. Therefore, a major objective of this work is to extend the multiplier proposed by Rantzer and Megretski, which is only block diagonal (or D Scaling), to a full-block multiplier containing off-diagonal functions (or $D-G$ scaling).

Moreover, some extensions need to be developed to the cases of systems containing multiple HTV parameters that oscillate at the same frequency, but with a phase-shift between them. The idea is to introduce the information about the phase-shift and the structure of the HTV parameters in the new classes of multipliers. Finally, an implicit but important contribution regards the tractable solutions for the analysis of LHTV systems, developing state-space and frequency domain solutions that are particularly adapted to the application of harmonic multipliers.

1.2.2 Model-based performance specifications

The performance specifications allow to characterize the expected behaviour of a given application and to determine at which point the system meets (or not) the required performance indicators. In the case of MEMS gyroscopes, there exists an set of quantitative performance specifications that have been defined and standardized [IEE04, IEE06, IEE18]. Hence, in order to be commercialized, any developed MEMS gyroscope must verify a certain level of performance specifications, defined in terms of the corresponding standards. Among the standard performance specifications, we can list three main classes: the accuracy specifications, the sensitivity specifications and the output noise specifications.

At this point, it is important to underline that we can distinguish two levels of performance specifications, which do not always have a direct relationship between them. On the one hand, we have the closed-loop specifications that are used to constraint the design of a controller. These specifications are usually defined in terms of closed-loop objectives, such as tracking errors or disturbance rejection. On the other hand, the standard specifications are defined in terms that are user-oriented and do not necessarily have a direct interpretation with respect to the closed-loop specifications. A major challenge is then to determine how these different specifications can be reinterpreted as standard mathematical criteria that can be efficiently tested through appropriate analysis tools.

[1]The terminology $D-G$ scaling is commonly employed in the μ-analysis framework but not in the IQC framework. However, for the sake of clarity, we allow this imprecision in the current chapter

From the system point of view, the performance specifications can be interpreted as the relationship between the input and output signals of the system model, that is, to verify some properties of the output signals with respect to a certain class of input signals. Hence, the key issue is the translation of the standard performance indicators, related to some particular properties of the output signal, to the analysis of the properties of the system model that, excited by a particular class of input signals, generates the output signal. The question is, using the particular properties of the system and the performance criteria, it is possible to compute the performance indicators by using the available system analysis tools?

Scale Factor Nonlinearity

The most important accuracy specification is the Scale Factor Nonlinearity (SFNL). The SFNL quantifies the maximal gyroscope measurement error over the whole range of angular rates under which the gyroscope operates. The gyroscope output error, related to the SFNL, is determined as the distance between the measured angular rate and a function that is obtained by fitting some sampled measurements to a linear input-output relationship. The fitting is computed through regression methods, such as the least squares. The fitting is only indirectly affected by the control design constraints, making necessary an interpretation between closed-loops and standard specifications.

The model-based computation of the SFNL, given the particular class of input signals and the application of the synchronous demodulation at the output, is reduced to a robust optimization problem i.e. an optimization problem of a constant function (not a dynamic system) depending on a parameter that can takes values in an interval. Then, a part of our contribution focused on visiting and adapting the available analysis tools, mainly derived from the Robust Control theory, to efficiently compute the SFNL of MEMS gyroscopes. The methods are then extended to the evaluation of the thermal sensitivity and the worst-case SFNL of uncertain models obtained by system identification methods.

Output noise and Allan variance

The standard method to evaluate the output noise of MEMS gyroscopes is the Allan variance method [All66, SHC+12]. The Allan variance is a time-domain statistical procedure that is applied on long-term measurements of the gyroscope output. This method allow to classify and quantify the different stochastic processes that are contained in the gyroscope output noise.

Our ultimate objective is then to provide a set of model-based methods to compute the Allan variance of MEMS gyroscopes. To this purpose, it is necessary to step back and to address some prior problems. First, we need to determine the relationship between the Allan variance and the signal properties that it describes. Then, in order to recast the evaluation of the Allan variance, which is a property of the noisy output signal, into a model-based mathematical criteria, we adopt a generator filter approach, which consists in characterizing the properties of the output signal through the properties of the system model that generates it, which is in turn excited by a particular class of well-behaved signals, for instance, a white noise signal. The first problem consisted in studying the case of a noisy output signal generated by an LTI model. This already implies an interesting contribution for two reasons since the Allan variance is an important indicator of the signal processing theory, having applications beyond the MEMS gyroscopes scope. However, to our best knowledge,

the Allan variance has not been addressed from a system point of view, offering an important opportunity to exploit concepts of the signal processing and control theories to offer efficient and accurate model-based computation methods.

Then, to orient the model-based Allan variance computation to the context of MEMS gyroscopes, it is necessary to consider the problem where the signal is generated by an LTI system, representing the controlled closed-loop, followed by a synchronous demodulator. This requires to determine which is the effect of the synchronous demodulation in the Power Spectral Density (PSD) of the closed-loop output signal. Exploiting the particular structure of the considered system, and based on some results related to the concepts of modulated random signals [Lat70, Pap83], we provide an alternative approach that allows to recast the computation of the model-based Allan variance of this particular LHTV system into the computation of the model-based Allan variance of an equivalent LTI system, allowing a simple and efficient computation of the exact Allan variance. In order to generalize these results, we also address the problem of computing the worst-case Allan variance of uncertain systems by introducing an analysis method based on the Integral Quadratic Constraints method. The problem of a MEMS model consisting on an LTI system and a synchronous demodulation is also analyzed under an IQC perspective, allowing to compare it with the equivalent LTI method. An interesting advantage of the IQC-based method is its natural extension to other cases such as the analysis of systems where the closed-loop is not LTI, for instance, the control strategies that implement the synchronous demodulation inside the closed-loop.

1.2.3 Control design validation

A major interest in the development of our system analysis tools is the validation of alternative control strategies that require more complex architectures than the classical LTI control. Indeed, given the complexity of the control design in such architectures, some strong assumptions and simplifications need to be adopted in order to efficiently design the controllers. However, when we take into account the implementation issues, the adopted assumptions are not necessarily verified, making not possible to provide formal guarantees of stability and performance.

We addressed the analysis of a phasor-based control that requires the implementation of modulators and demodulators in the closed-loop [SSK20]. The control design is carried out by assuming an ideal synchronous demodulation. Considering an ideal synchronous demodulation allows to recast the control design model, which is originally LHTV, into an equivalent LTI control design problem. However, this can be a strong assumption. In an implementation case, where the actual synchronous demodulation is non-ideal, it is not longer possible to assume the system as LTI but as an LHTV one. Such a scenario can compromise the stability of the closed-loop system, making necessary to perform an *a posteriori* analysis with a more approrpiate model. We then investigate the stability of the phasor-based control with non-ideal synchronous demodulation by applying the set of tools that we develop for the analysis of LHTV systems.

Other control strategy of the Next4MEMS consists on the discrete-time implementation of a parameter-dependent controller [SACKS20]. This control strategy employs continuous-time control methods and consists in estimating a system parameter in real-time and then use this estimation to update the parameterization of the controller. However, the implementation in discrete-time and the parameter estimation errors make arise some issues that are neglected in the control design process. This problem leads us to analyze an uncertain system that has a non-rational

dependency on the uncertain parameters, which can be tackled using a proposed Taylor-based approximation and robustness analysis tools.

As a final note, all the analysis methods proposed in this memoir are developed so that its numerical solution is implemented in the form of LMI optimization problems, for which several efficient solvers are available. In this work, we mainly employ the solves SeDumi [Stu99] and Mosek [ApS19], as well as the interpreter Yalmip [Lof04].

1.3 Structure of the manuscript

This manuscript is divided in five chapters (going from 2 to 6). Let us briefly described their content.

Chapter 2: The first chapter is dedicated to the presentation of MEMS gyroscopes. We begin by describing their main features as well as the work principle that allows to obtain a measure of the angular rate at the output. We discuss some of the most common control strategies that are found in the literature and those that have been proposed during the project, followed by the introduction of synchronous demodulation, an element that is present in most of the architectures. Then, we review some of the observed non-ideal phenomena that can be found in MEMS gyroscopes. Later, we introduce the standard performance specifications for MEMS gyroscopes. We continue by discussing the performance validation problem and the pertinence of proposing efficient model-based methods. The chapter finalizes by formalizing the main research questions.

Chapter 3: The first part of the chapter is devoted to introduce the theoretical concepts for the analysis of uncertain systems. First, we introduce some formal definitions of stability, performance and robustness. Afterwards, we review some results of the analysis of systems under Linear Fractional Transformation (LFT) representations, followed by the presentation of the IQC approach, which conforms the fundamental framework of the proposed analysis tools. The second part of the chapter focuses in the analysis of Linear Harmonically Time-Varying Systems (LHTV), proposing theoretical tools to explicitly take into account the effects of the synchronous demodulation. This is a major contribution of this work: first, it enlarges the catalog of available IQC multipliers to several classes of systems containing harmonic oscillations, second: tractable analysis conditions for LHTV systems are proposed both in frequency domain and in state-space. The proposed approach is illustrated through a numerical example: the Mathieu-Hill equations.

Chapter 4: Based on the theoretical concepts introduced in the previous chapter, we tackle the analysis of the first performance specifications: the bias and the scale factor nonlinearity (SFNL), as well as their thermal sensitivity. First, we formally define the performance specifications. In the following, we introduce the closed-loop MEMS gyroscope model, followed by the derivation of an LFT model depending on the angular rate, modeled as an uncertain parameter. We then formalize the worst-case measurement error, presented as an LMI condition depending on the angular rate and we propose a method to efficiently compute the SFNL. The same approach is then extended to other two cases: first, the computation of the thermal sensitivity; second: the computation of the SFNL when the model is obtained by system identification, which implies the inclusion of vector uncertainties. We finalize the chapter

by presenting a numerical example and an application case.

Chapter 5: In this chapter, we continue the development of performance analysis tools, this time focusing on the output noise. At first, we introduce the standard performance tool to evaluate the noise of MEMS gyroscopes: the Allan variance method. Later, the Allan variance is translated into a model-based mathematical criterion: the $\mathcal{H}_2$ performance of an extended system including the so-called Allan filter. Since the aforementioned Allan filter in infinite-dimensional, we propose an similar version based on the Padé approximation. In the following, we introduce the worst-case Allan variance and its computation by using the IQC approach. We then tackle the problem of computing the model-based Allan variance of demodulated signals, proposing two methods: an IQC-based method and an LTI method based on an equivalent system. The last part of the chapter illustrates the approach through a numerical example and an experimental case.

Chapter 6: The last chapter focuses on the analysis of MEMS gyroscopes employing non classical control strategies. The first part of the chapter investigates the stability of a phasor-based control, which implies the presence of synchronous demodulation in the loop. We then discuss how the phasor-based control with non-ideal synchronous demodulation leads to an LHTV system. Hence, we apply the results of Chapter 3 to perform the analysis and we draw some conclusions about the relevance of the proposed IQC multipliers. The second part of the chapter studies the tracking performance of a parameter-dependent controller that is implemented in discrete-time. We derive the analysis system, obtaining an uncertain system that has a non-rational dependency on the uncertainties, making not possible to exploit the analysis tools. We then propose a Taylor-based approximation of the non-rational functions, modeling the approximation error as an uncertainty, which allows to derive sufficient analysis conditions. The approach is illustrated through a numerical example.

1.4 Publications

Conference papers:

- **J. Ayala-Cuevas**, F. Saggin, A. Korniienko, G. Scorletti. Stability Analysis of Time-Varying Systems with Harmonic Oscillations Using IQC Frequency Domain Multipliers. Proceedings of the IEEE 58th Conference on Decision and Control (CDC), pages 5193–5198, Dec 2019.
- F. Saggin, **J. Ayala-Cuevas**, A. Korniienko, G. Scorletti. On the Parameter-dependent H_∞ control for MEMS gyroscopes: synthesis and analysis. Proceedings of the 21th IFAC world congress, Jul 2020.

Journal paper (to be submitted):

- **J. Ayala-Cuevas**, A. Korniienko, G. Scorletti, A. Perodou, F. Saggin. A Frequency Domain Integral Quadratic Constraints Approach for Robustness Analysis of Harmonically Time-Varying Systems.

Chapter 2

Performance validation of MEMS gyroscopes

This chapter introduces the operation principle of a MEMS gyroscope measuring the angular rate with respect to a fixed frame of reference, this by considering an ideal operation. Then, the control strategies used to meet the operation requirements of MEMS gyroscopes are reviewed. The standard specifications that indicate the quality of a gyroscope are then introduced. In the following sections, we will present some of the principal non-idealities that are found in micro gyroscopes and their effects. Finally, we present the system validation process, which allows to state the main objectives and problems that are addressed in this work.

2.1 System description

Gyroscopes are devices that measure the angular rate of an object subject to rotational motion with respect to a given axis. The acronym MEMS stands for Micro Electro-Mechanical Systems. Referring to each elements, micro indicates the scale size of the devices, which is found around the range micrometers. Electro-Mechanical refers to the physical nature of this fascinating devices, involving simultaneously mechanical and electrical effects to its operation. Finally, system means that the different parts of the system, including the associated electronic circuits and control loops work as a whole single system.

Among the MEMS gyroscopes, here we will introduce the known as vibratory (resonating) MEMS gyroscopes, which is probably the most common type of micro gyroscope. The motivation to employ this architecture is that the resonance allows to radically improve the signal to noise ratio (SNR), which becomes critical at the microscale.

The principle on which rely MEMS vibratory gyroscopes is the Coriolis effect, first introduced by the french physicist Gaspard-Gustave Coriolis [Cor35]. This effect describes the appearance of a fictitious force, known as the Coriolis force, that is observed on a moving object only when the observer and the object are in a rotating frame of reference. To explain it into details, please see Figure 2.1. Let us consider the frame of reference rotating around the z-axis at an angular rate Ω_z. Then, an object moves along the x-axis with a linear velocity $\dot{x}$. This object will be subjected to a force that pushes him along the y direction (orthogonal to the direction of displacement and the axis of rotation), with a magnitude that is proportional to the mass of the object, to the velocity $\dot{x}$ and to the angular rate Ω_z.

With the previous background presented, the following sections will introduce the working principle of MEMS vibratory gyroscopes, as well as the main components allowing its proper operation. For the curious reader, the general aspects

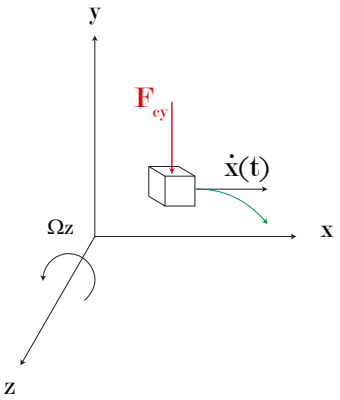

FIGURE 2.1: Representation of Coriolis effect

here addressed and many other topics concerning MEMS inertial sensors are widely detailed in the literature. For instance, in [Kem11, AS08, Apo06, You11, Sau08a, YAN98].

2.1.1 Mechanical principle

The core of MEMS gyroscopes is a micro-mechanical structure composed of two orthogonal spring-mass systems that are poorly damped. The mass m_x can only be linearly displaced on the direction x by applying a force F_x, this is called the drive mode. Similarly, the mass m_y is only displaced on an orthogonal direction y of the drive mode by applying a force F_y, which is known as the sense mode.

Both masses are linked to a fixed structure by the means of silicon cantilever beams. There then exists some stiffness and damping elements between the masses and the fixed structure Figure 2.2. Then, the system can be modeled as two independent mass-spring-damper systems as follows:

$$\begin{aligned} m_x\ddot{x}(t) + d_{xx}\dot{x}(t) + k_{xx}x(t) &= F_x(t) \\ m_y\ddot{y}(t) + d_{yy}\dot{y}(t) + k_{yy}y(t) &= F_y(t) \end{aligned} \tag{2.1}$$

with k_{xx} and k_{yy} respectively the stiffness constants of drive and sense mode, while d_{xx} and d_{yy} are the corresponding damping coefficients.

Now, the transfer function of the drive mode $G_D(s)$ between the applied force F_x and the displacement x is given by

$$G_D(s) = \frac{X(s)}{F_x(s)} = \frac{1}{m_x s^2 + D_{xx}s + k_{xx}} \tag{2.2}$$

We can also write this expression in terms of frequency response variables (the most common representation in the MEMS community) as follows:

$$G_D(s) = \frac{X(s)}{F_x(s)} = \frac{1/m_x}{s^2 + \frac{\omega_{0x}}{Q_x}s + \omega_{0x}^2} \tag{2.3}$$

where $Q_x = \sqrt{m_x k_{xx}}/D_{xx}$ and $\omega_{0x} = \sqrt{k_{xx}/m_x}$ are respectively the *Quality factor* and *resonance frequency* of drive mode.

Let us consider the example of a MEMS drive mode with $Q_x = 60000$ and $\omega_{0x} = 10200$ Hz. The Bode diagram of transfer function (2.3) for this gyroscope is presented

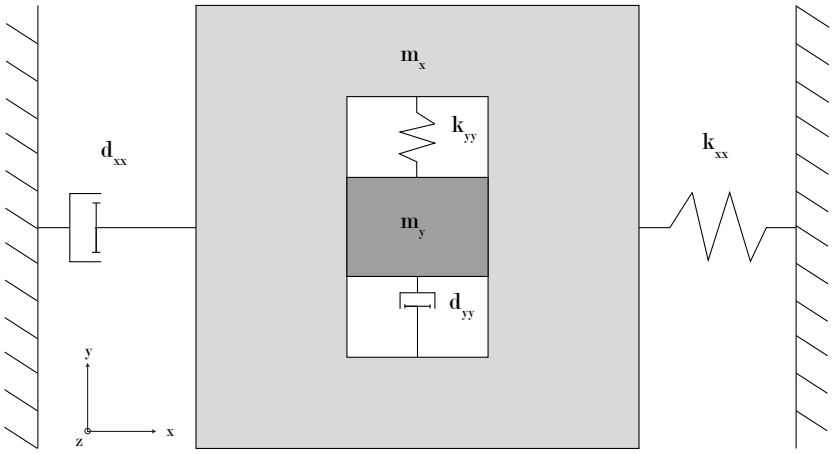

FIGURE 2.2: Schematic representation of MEMS drive and sense modes

in Figure 2.3. We can observe that the gain of the system at the resonance frequency with respect to its static gain is proportional to Q_x. This important amplification allows to obtain an important signal to noise ratio (SNR).

Now, when this mechanical structure is subject to rotational movement with respect to the z-axis (orthogonal to both modes) at an angular rate Ω_z, if we apply a force F_x to induce an oscillatory movement on the mass m_x, the Coriolis effect arises transferring energy from drive to sense mode. This makes appear on the sense mode a Coriolis force F_{cy} proportional to the angular rate Ω_z, and then coupling the drive and the sense mode. There exists as well a Coriolis force F_{cx} that can disturb the vibrations of drive mode. The two described Coriolis forces are defined as follows:

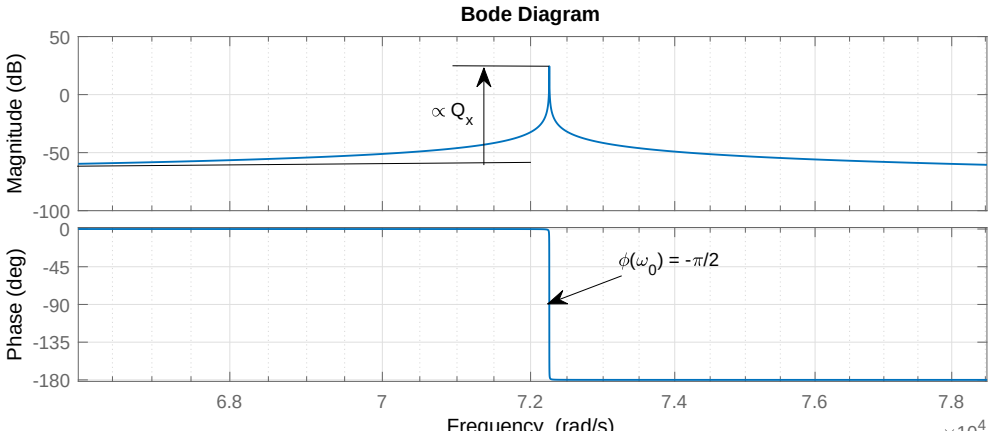

FIGURE 2.3: Bode diagram of the drive mode transfer function

$$\begin{aligned} F_{cy}(t) &= -2m_x\dot{x}(t)\Omega_z \\ F_{cx}(t) &= 2m_y\dot{y}(t)\Omega_z \end{aligned} \tag{2.4}$$

However, whether through purely mechanical solutions ($m_y << m_x$) or by using control strategies, the effect of F_{cx} is often minimized. Including equations (2.4) in (2.1), we obtain the complete equation of an ideal micro-gyroscope:

$$M\ddot{r}(t) + D\dot{r}(t) + Kr(t) = C\dot{r}(t) + F(t) \tag{2.5}$$

with the vector signals

$$r(t) = \begin{bmatrix} x(t) \\ y(t) \end{bmatrix}, \quad F(t) = \begin{bmatrix} F_x(t) \\ F_y(t) \end{bmatrix},$$

and the parameter matrices

$$M = \begin{bmatrix} m_x & 0 \\ 0 & m_y \end{bmatrix}, \quad D = \begin{bmatrix} d_{xx} & 0 \\ 0 & d_{yy} \end{bmatrix}, \quad K = \begin{bmatrix} k_{xx} & 0 \\ 0 & k_{yy} \end{bmatrix}, \quad C = \begin{bmatrix} 0 & 2m_y\Omega_z \\ -2m_x\Omega_z & 0 \end{bmatrix}.$$

Hence, in the presence of Coriolis effect, it is possible to indirectly obtain the angular rate Ω_z by measuring the Coriolis force F_{cy} in the sense mode. To this end, it is simultaneously necessary to induce the Coriolis effect and to estimate the Coriolis force. These two objectives are achieved by using feedback control strategies that are presented in the following.

2.1.2 Actuation and detection

Actuation

We have introduced the mechanical principle of a MEMS gyroscope. As we mentioned, the modes can be driven by applying external forces. To this end, an excitation mechanism must be provided, the question is how this is done at the microscale. The most common excitation method is the electrostatic (or capacitive) actuator [Sau08a, EKT+11].

In order to introduce the mechanism, we only consider the excitation of the drive mode, but the same principle is applied to the actuation of the sense mode. In a capacitive actuator, the force F_x applied to the drive mode is an attractive electrostatic force F_{esx}. The electrostatic force can be generated by applying an electric field between two separated electrodes, such as in classical parallel-plate capacitors. Then, the electrostatic force is given by the derivative of the electrostatic potential energy with respect to the displacement x.

$$F_x(t) = F_{esx} = -\frac{dE_{esx}}{dx}, \tag{2.6}$$

with the electric potential energy stored in a capacitor given by

$$E_{es} = \frac{1}{2}Cu_{exc}^2.$$

where C is the capacitance and u_{exc} the applied electric potential.

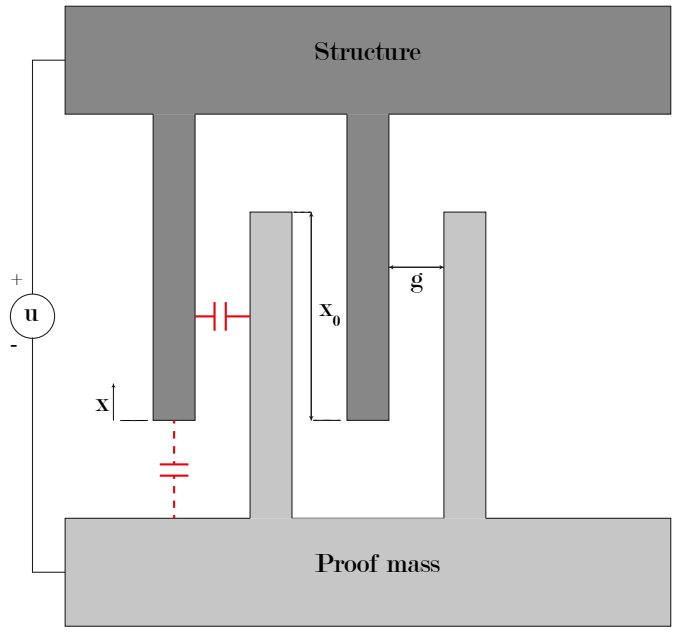

FIGURE 2.4: Schematic representation of a comb drive actuator

Now, the electrostatic actuator used on MEMS gyroscopes is of the type known as comb-drive actuator. The comb-drive actuator is composed of two structures having the form of a comb, which are disposed on an alternate configuration (Figure 2.4) such that the "fingers" can slide between each other. Then, two parallel-plate capacitors are formed. The capacitance of such a capacitor is given by the expression

$$C_x = \frac{\epsilon_{Tot} A_{Tot}}{g}$$

where ϵ_{Tot} is the product of the vacuum and dielectric isolation permittivities, A_{Tot} is the total overlap area of the two plates, and g is the separation (gap) between the two plates.

The fingers comb-drive structures are long and narrow, such that the overlap area between two parallel fingers A_{tot} is maximized, while the gap g between them is minimized. In the opposite, the overlap area at the tip of the fingers is minimized, and the separation is more important. With this configuration, the capacitance at the tip of the fingers can be neglected with respect to the capacitance along the fingers. Hence, the capacitance of the drive-mode actuator is given by

$$C_x = \frac{\epsilon_{Tot} n_g (x_0 - x) h}{g} \tag{2.7}$$

where n_g is the number of gaps between fingers, x_0 the initial overlap length and h is the thickens of the structures. Then replacing the expression of the capacitance in (2.6), we have that the applied force is given by

$$F_x(t) = k_c u_{exc}^2$$

where $k_c = (\epsilon_{Tot} N_{gap} h)/2g$.

Now, in order to induce an oscillatory displacement into the MEMS drive mode, it is necessary to apply a voltage of the form

$$u_{exc}(t) = V_{DC} + v_{ac}(t).$$

We can observe that the applied force is proportional to the square of the applied voltage, which represents a nonlinear effect.

There exists three main strategies to suppress or to mitigate the effect of the squared relationship.

1. **Digital compensation:** if the processor capacity allows it, it is possible to compute the square root of the necessary voltage to generate the desired force.
2. **Harmonic linearization:** if we apply a voltage

   $$u_{exc}(t) = V_{DC} + V_{AC}\sin(\omega_{exc}t),$$

   then, the applied force will be given by

   $$\begin{aligned} F_x(t) &\propto (V_{DC} + V_{AC}\sin(\omega_{exc}t))^2 \\ &= \underbrace{V_{DC}^2 + \frac{V_{AC}^2}{2}}_{DC} + \underbrace{2V_{DC}V_{AC}\sin(\omega_{exc}t)}_{\omega_{exc}} - \underbrace{\frac{V_{AC}^2}{2}\cos(2\omega_{exc}t)}_{2\omega_{exc}}. \end{aligned}$$

   The applied force will then have a constant component, an harmonic component at the frequency ω_{exc} and an harmonic component at $2\omega_{exc}$. Hence, we can choose an excitation frequency equals to the resonance frequency of the drive mode $\omega_{exc} = \omega_0$, or to the half of the resonance frequency $\omega_{exc} = \omega_0/2$. Then, given the high quality factor of the drive mode at ω_0, it will naturally amplify the chosen component and strongly attenuate the other ones, which allows to linearize the actuation.
3. **Double-sided actuation:** In this configuration, two comb-drive actuators will be placed at each side of the drive-mode, for instance, one at the left side and the other one of the right side, generating then electrostatic forces in opposite directions, the resulting force is then given by

   $$F_x = F_x^L - F_x^R.$$

   If we apply the same voltages to both comb actuators, then the resulting force will be zero. However, if we apply the same DC voltages and AC voltage of the same amplitude but with a phase shift of π, then we have that the applied force is

   $$\begin{aligned} F_x(t) &= k_c\left((V_{DC} + v_{ac}(t))^2 - (V_{DC} - v_{ac}(t))^2\right) \\ &= 4k_cV_{DC}v_{ac}(t). \end{aligned}$$

Detection

In order to measure the operation of the drive-mode vibrations, it is necessary to measure its displacements. This is done done by using the comb-drive actuator in a passive mode, that is, no voltage is applied to the structures. Then, according to the equation (2.7), the capacitance between fingers is proportional to the drive-mode position x.

Then, the displacement of x induces a change of the capacitance C_x, which can be converted into a voltage signal by using a charge amplifier [Sau08a].

2.1.3 Feedback control loop

Drive mode

As mentioned earlier, the first step to estimate the angular rate demands to induce the Coriolis effect in the two modes of the MEMS resonator. As we can observe on Equations (2.4), the Coriolis force F_{cy} of the sense mode is proportional to the linear velocity of the drive mode $\dot{x}(t)$. Then, F_{cy} can be generated by inducing an oscillatory displacement of the drive mode. To this end, it is necessary to apply a force F_x such that the drive mode maintains oscillations of constant amplitude at the steady-state, for instance,

$$x(t) = A_x \sin(\omega_{exc} t).$$

Furthermore, in order to obtain a good SNR while reducing the applied force, it is desirable to take advantage of the resonant effect by setting the excitation frequency very close to the resonance frequency of the drive mode ($\omega_{exc} \approx \omega_0$). Then, the Coriolis force F_{cy} affecting the sense mode is given by

$$F_{cy}(t) = -2m_x A_x \omega_{exc} \cos(\omega_{exc} t)\Omega_z.$$

Then, it is necessary to maintain constant amplitude oscillations A_x in order to obtain a stable Coriolis force that can be properly estimated.

Hence, the drive mode control objectives can be summarized as:

- the main objective is to maintain a constant amplitude A_x of the oscillations, at least for a given range of temperature, despite the Coriolis force F_{cx} disturbing the closed-loop;
- a secondary objective is to excite the drive mode at a frequency ω_{exc} that tends to be equal to the resonance frequency ω_0.

Several control strategies have been developed to achieve these objectives. Since the application demands the control of sinusoidal signals, we can classify them into two general approaches: the envelope-based approaches that consists in controlling the envelope of the sinusoidal signal, usually by controlling the amplitude and the phase [Sau08b, RCRW09, MVG01] or the phasor associated to the signal [SSK20]; and the direct control approaches, which consist in directly controlling the sinusoidal signals.

Among the envelope-based approaches, the most popular in the MEMS community are based on a combination of the refered to as Automatic Gain Control (AGC) and the Phase-Locked Loop (PLL) [Sau08b, RCRW09], which respectively control the amplitude and the phase of the oscillations, see Figure 2.5. The operation principle is the following: we want the drive mode position to oscillate as the sinusoidal function

$$x(t) = A_x \sin(\omega_{exc} + \phi_x).$$

Then, applying to x the device known as synchronous demodulation (see subsection 2.1.4), we can extract its amplitude A_x and its phase ϕ_x. Hence, the AGC loop is responsible of keeping the amplitude of the oscillations A_x to a level imposed by the reference amplitude A_r, while the PLL is aims to maintain the phase ϕ_x equals to a reference $\phi_r = -\pi/2$, given that, as shown on Figure 2.3, the resonance pic of the

drive mode is found at this phase shift. Finally, the computed amplitude and phase control signals are modulated and send to the drive mode. The advantage of this strategy is that we can implement simple controllers, such as proportional integral (PI) controllers. The inconvenient is mainly related to the use of modulation and demodulation in the closed-loop (we face a system with Harmonically Time-Varying parameters in the closed-loop). Moreover, the computation of the amplitude and the phase from the demodulated components introduces additional nonlinearities in the loop. These two aspect make difficult to offer formal guarantees of stability and performance.

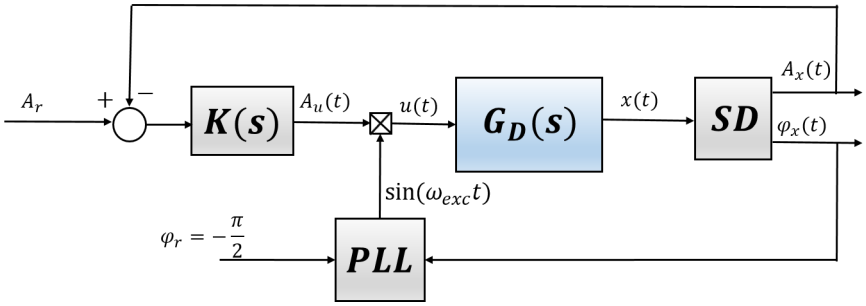

FIGURE 2.5: AGC + PLL drive mode control

The direct control approaches do not track the amplitude and the phase, but the sinusoidal reference itself, which has the form

$$x_r(t) = A_r \sin(\omega_{exc} t).$$

Hence, the controller directly computes and generates the sinusoidal control signals send to the drive mode ([SHS+99, DA09]). The advantage of such approaches is that neither modulators nor demodulators are required in the loop (only in open-loop at the output). Moreover the nonlinearities introduced by the transformation to amplitude and phase components disappear. This allows to obtain feedback control loop strategies that, from a control theory point of view, are closer to the classical ones (Figure 2.6). This potentially allows the implementation of a linear feedback loop for which formal guarantees of stability and performance can be provided. The main drawback comes from the fact that the control system must operate within a bandwidth around the resonance frequency of the drive mode (in the order of the kHz). Then, this strategy requires much higher sampling and processing frequencies with respect to those of the amplitude-phase control.

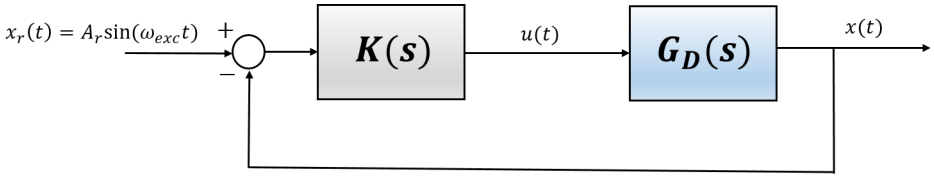

FIGURE 2.6: Direct control of drive mode

Sense mode

Next, with the induced Coriolis effect, then a Coriolis force F_{cy} disturbs the sense mode, the objective is now to obtain an accurate estimate of this Coriolis force, and

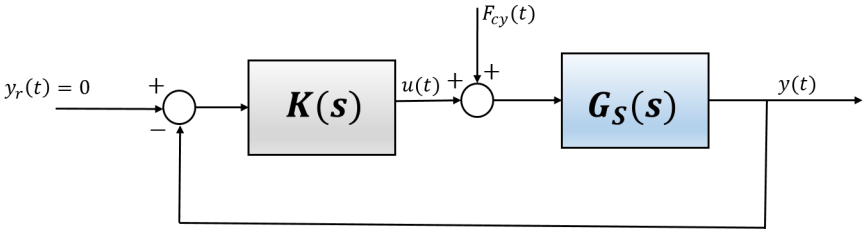

FIGURE 2.7: Force to rebalance sense mode control

by consequence, of the angular rate Ω_z. This estimation can be performed using different strategies.

The most straightforward approach is to obtain an estimation in open-loop, that is, setting $F_y = 0$ and letting only the Coriolis force F_{cy} to excite the sense mode resonator G_s. Then, we can measure y and estimate the Coriolis force through the relation:

$$Y(s) = G_s(s)F_{cy}(s).$$

This approach uses a rather simple and economic strategy. However, it has one of the main drawbacks of open-loop operations: it does not allow to correctly estimate the Coriolis force when unmodeled phenomena are present. Moreover, the dynamics of the estimator are normally desired to be fast, which is not easy to achieve when the estimator exclusively relies on the poorly damped dynamics of the sense mode resonator. Therefore, the limitations of the open-loop control strategy might lead to a reduced performance level.

Therefore, looking for more optimal performances, it is common to implement the Coriolis estimation in closed-loop. This approach consists in designing a control strategy that maintains the position of the sense mode $y(t)$ close to zero. Then, the force F_y applied by the controller will oppose the Coriolis force F_{cy} in order to keep the zero reference, that is

$$F_y \approx -F_{cy},$$

obtaining almost directly an estimate of the Coriolis force. In the following sections, we discuss how non-ideal phenomena cause the Coriolis force to not be equal to the applied force, requiring an additional estimation strategy.

This control approach is known in the MEMS community as *force to rebalance* control and, from a control point of view, comes to a disturbance rejection problem (Figure 2.7). The main advantages of this approach are that the dynamics of the estimator depends not only on the sense mode resonator but also on the designed controller, which can be optimized by design. Secondly, given that $y(t)$ is forced to remain very low, then the parasitic effect of the Coriolis force F_{cx} disturbing the drive mode is minimized to a level that allows to neglect it.

Within the force to rebalance control strategy, the proposed control solutions are similar to those of the drive mode, the envelope-based strategies are devoted to control the amplitude and the phase [Sau08b, LR02, MCZ+10], while the direct control ones direclty work with the sinusoidal signals [PH03].

Some control strategies of the NEXT4MEMS project

Within the scope of the NEXT4MEMS project, several control approaches were proposed. The objective of this project is to take the advantages of existing control solutions and to propose new approaches that allow to systematically design the

required controllers. The control strategies should achieve the stability and performance objectives, if possible by keeping a relatively simple architecture, and by providing formal guarantees of robust stability and robust performance.

The particular application demands performance criteria that can naturally be interpreted in the frequency domain. In this sense, advanced control design frequency-domain methods may be quite appropriate. The main employed design method in this project is the $\mathcal{H}_\infty$ control [ZD98, SP01], which is a linear control approach that makes it possible to translate the robustness and performance requirements into the form of frequency templates on the modulus of the closed-loop transfer functions, and to obtain the controller through an optimization problem.

Three main approaches, developed in this project, will be analyzed along this document. They are largely documented in the PhD manuscript of Fabricio Saggin [Sag21], and in our previous publications [ACSKS19, SACKS20, SSK20]. They are briefly listed below.

1. **MIMO direct control:** this approach can be grouped within the direct control solutions, both drive and sense modes are operated by directly controlling the sinusoidal signals involved, which allows to implement a classical linear feedback control architecture. Moreover, it is a Multi-Input Multi-Output (MIMO) approach that may allow to improve the performance and robustness of the system by taking into account the non-ideal couplings (section 2.4). This type of control will be considered for the analysis performed in chapter 4 and chapter 5.

2. **Phasor-based control:** this strategy may be seen as a bridge between the common amplitude-phase approach and the direct control one. Indeed, it can be considered among the envelope-based solutions since it employs modulation and demodulation in the loop but, in this case, instead of controlling the amplitude and phase of the sinusoidal signals, it controls the real and imaginary parts of the phasor associated to the sinusoidal signal. This allows to eliminate the nonlinearities related to the amplitude and phase estimation, allowing better stability and performance guarantees. This approach is analyzed in section 6.1.

3. **Parameter-dependent control:** This last approach can be seen as a linear adaptative control. During the project, some methods devoted to the tracking of the resonance frequency were developed [Mor21]. Disposing of a measure of the resonance frequency, it is possible to develop a rather simple linear parameter-dependent controller that, face to a derive of the MEMS resonance frequency, can easily adapts its dynamics by simple frequency normalizations. This last approach, as well as its implementation in discrete-time, is analyzed in section 6.2.

2.1.4 Synchronous demodulation

Independently of the adopted control strategy, at the output of the sense mode we retrieve an estimation of the Coriolis force, approximately given by

$$\tilde{f}_c(t) \approx 2m_x A_x \omega_{exc} \cos(\omega_{exc} t)\Omega_z,$$

that is,

$$\tilde{f}_c(t) = K_{c\Omega}\Omega_z \cos(\omega_{exc} t)$$

where $K_{c\Omega}$ is a constant gain that links the angular rate to the Coriolis force amplitude. Then, the closed-loop output is a harmonic oscillation whose amplitude gives an estimate of Ω_z.

Finally, in order to extract the desired magnitude from the modulated signal, it is necessary to apply the *synchronous demodulation*. Before describing how the angular rate is obtained, let us first introduce the operation principle of the ideal synchronous demodulation.

Ideal synchronous demodulation

When some signal $\tilde{z}$ has a spectrum that is highly concentrated around a particular frequency ω_0 (Figure 2.8), the signal can be considered as a modulated signal, defined as follows.

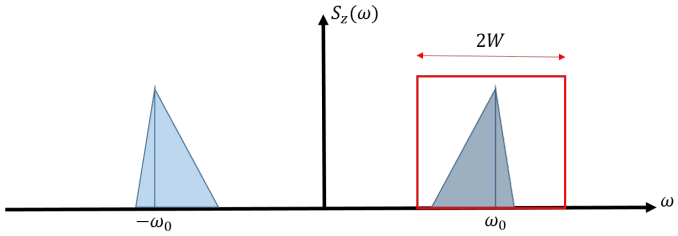

FIGURE 2.8: PSD of a modulated signal z

Definition 2.1 (Pure modulated signal.)**.** *A signal $\tilde{z}$ is said to be a pure modulated signal if its Power Spectral Density S_z has a limited bandwidth $2W$ around a frequency ω_0, with $W < \omega_0$, that is*

$$S_z(\omega) = 0 \quad \forall\, \omega \ \in]-\omega_0 + W, \omega_0 - W[\cup]\omega_0 + W, \infty[\cup]-\infty, -\omega_0 - W[, \tag{2.8}$$

Then, assuming that a signal z is a pure modulated signal in the sense of Definition 2.1, it can be accurately expressed as

$$\tilde{z}(t) = z_i(t)\cos(\omega_0 t) - z_q(t)\sin(\omega_0 t) \tag{2.9}$$

where $z(t)$ is the modulated signal, $z_i(t)$ its in-phase component and $z_q(t)$ its quadrature component. A consequence of assuming $\tilde{z}$ as a pure modulated signal is that the components z_i and z_q are low-frequency signals of limited bandwidth, that is, its Power Spectral Density (PSD) is zero for all $|\omega| > W$ [Lat70].

The assumption of signals being pure modulated, in the sense of Definition 2.1, is difficult to verify for two reasons: the presence of noise and the fact that real physical systems usually do not present output signals whose spectrum is exactly zero outside the operation bandwidth. Nevertheless, even if the PSD of real modulated signals outside the bandwidth $2W$ is not zero, it is usually negligible with respect to the PSD around the frequency ω_0, which allows to neglect its effect.

Next, the objective of synchronous demodulation is to extract these two components from the modulated signal. To do so, as shown in Figure 2.9, we first multiply the input modulated signal $z(t)$ by a cosine and a sine functions, obtaining

$$z_c(t) = 2\tilde{z}(t)\cos(\omega_0 t) = 2z_i(t)\cos^2(\omega_0 t) - 2z_q(t)\sin(\omega_0 t)\cos(\omega_0 t) \tag{2.10}$$

$$= z_i(t) + z_i(t)\cos(2\omega_0 t) - z_q(t)\sin(2\omega_0 t) \tag{2.11}$$

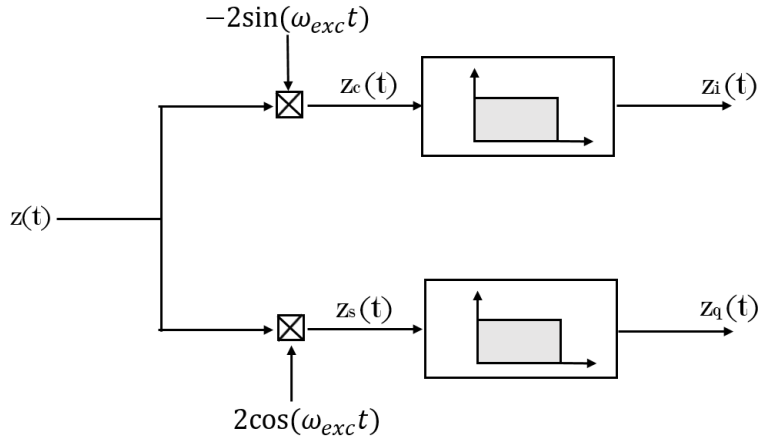

FIGURE 2.9: Schematic representation of the ideal synchronous demodulation

and

$$z_s(t) = -2\tilde{z}(t)\sin(\omega_0 t) = -2z_i(t)\cos(\omega_0 t)\sin(\omega_0 t) + 2z_q(t)\sin^2(\omega_0 t) \tag{2.12}$$
$$= -z_i(t)\sin(2\omega_0 t) + z_q(t) - z_q(t)\cos(2\omega_0 t) \tag{2.13}$$

Then, the signals z_c and z_i pass through low-pass filters. Let us introduce the following assumption related to an ideal low-pass filter (hence the name ideal synchronous demodulation) in the synchronous demodulator.

Assumption 2.1 (Ideal low-pass filter)**.** *A low-pass filter is ideal if, with a cut-off frequency W, is given by*

$$F_L(j\omega) = rect\left(\frac{\omega}{2W}\right), \tag{2.14}$$

where $rect(\cdot)$ is the rectangle function and $W < \omega_0$ is the bandwidth of the low-pass filter.

Hence, if we assume the ideal low-pass filter, the signals z_{cf} and zcs at the output of the demodulator will be given by

$$z_{cf}(t) = z_i(t) \tag{2.15}$$
$$z_{sf}(t) = z_q(t), \tag{2.16}$$

obtaining then the in-phase and quadrature components.

Extraction of Coriolis force

In the previous sections, we describe the operation of the closed-loop MEMS gyroscope, and we observed that, for a drive mode reference signal of the form $x_r(t) = A_r\sin(\omega_{exc}t)$, the modulated output, assuming a constant angular rate Ω_z, is approximately given by

$$\tilde{z}(t) \approx \tilde{f}_c\cos(\omega_{exc}t). \tag{2.17}$$

Then, $\tilde{z}$ is a particular pure modulated signal in the sense of Definition 2.1. Then, applying synchronous demodulation to $\tilde{z}$ in (2.17) we have, according to the equations (2.16), the quadrature component $z_q \approx 0$ and the gyroscope output z, given by

the in-phase component z_i, given by

$$z = z_i \approx \tilde{f}_c.$$

In MEMS gyroscopes control, synchronous demodulation is not only limited to the operation described just before. As mentioned in subsection 2.1.3, the envelope-based control approaches demand to integrate a synchronous demodulator inside the closed-loop. In the case of a phasor-based control, we directly use the in-phase and quadrature components, while in the case of AGC-PLL control we aim to extract the amplitude and phase of the modulated signal. This is done through the relations

$$A_z(t) = \sqrt{z_i(t)^2 + z_q(t)^2} \qquad \phi_z = \arctan\frac{z_q(t)}{z_i(t)}.$$

The impact of synchronous demodulation in the closed-loop for a phasor-based control strategy will be further discussed in chapter 6.

2.2 From gyroscope output to measured angular rate

Now, the last step consists in obtaining the angular rate Ω_z from the synchronous demodulator output, hereafter denoted z, which is ideally equivalent to the estimated Coriolis force. Nevertheless, given the signal conversions, the system imperfections and the measurement errors, the output signal is only an image of the estimated Coriolis force $\tilde{f}_c$, given in different units, for instance converting from degrees per second ($^\circ/s$) to number of least significant bits. Moreover, in some cases, it is not possible to accurately known some of the parameters that define the "gain" that links the angular rate to the Coriolis force.

However, at least we know that the gyroscope output is proportional to the angular rate. Hence, obtaining the angular rate from the value of the output z can be determined through a linear function between the Coriolis force and the angular rate that is, a priori, unknown.

To establish the relationship between the gyroscope output and the displayed angular rate, the most common approach is to perform a first experimental procedure. Several tests are performed over the whole range of input angular rates. Then, using linear regression approaches [TWY17], such as the least squares method (see Appendix B), a linear function z^{fit} is obtained and defined as

$$z^{fit}(\Omega_z) = SF^{fit}\Omega_z + B^{fit}. \tag{2.18}$$

Using the fitted function, it is possible to obtain the measured angular rate to be displayed through the following relation:

$$\tilde{\Omega}_z = \frac{z - B^{fit}}{SF^{fit}}. \tag{2.19}$$

We can note that the fitted function includes a bias term B^{fit} that indicates that, at zero input angular rate, the output can be different from zero, implying a non-ideal measure. Moreover, for a given input angular rate, it is common that the measured output z diverges from the value of the fitted function $z^{fit}(\Omega_z)$. These deviations from an ideal measure give an indication of the accuracy of the gyroscope. In the following section, we discuss the aspects of the sensor accuracy and we introduce the standard specifications to evaluate the performance of a MEMS gyroscope.

2.3 Gyroscope Performance Specifications

In the previous sections, we introduced the general operation of a vibratory MEMS gyroscope, as well as some of the control solutions that aim to improve the performance of the sensor. However, in order to define if a sensor has a good quality or not, it is necessary to establish which are the indicators that defines this quality. In this section, we will give a brief introduction about the standard performance specifications for MEMS gyroscopes, which are based on the Institute of Electrical and Electronics Engineers (IEEE) standards [IEE04, IEE06, IEE18]. Such performance specifications will be discussed in details in following chapters (chapter 4 and chapter 5).

Let us consider a MEMS gyroscope to which we apply an angular rate Ω_z at the input and from which we obtain a measure z at the output. In the ideal case, where the measurement errors are zero, and consequently the measure is perfect, the input-output relationship is given by the expression:

$$z^{ideal} = SF\,\Omega_z$$

where z^{ideal} is the ideal output and SF is the scale factor. The scale factor simply expresses the change of units in which the measure is given, for instance, to pass from degrees per second ($^\circ/s$) to number of least significant bits. This relation, ideally, is linear. However, the output is usually affected by different phenomena that modify the expected measure, as represented in Figure 2.10. This deviation can be characterized and quantified using two types of errors, defined in the following.

- **Bias:** the average over a specified time of the gyroscope output measured at specified conditions that has no correlation with input rotation.

This can be expressed as

$$B(T) = z \qquad \text{for } \Omega_z = 0, \qquad T = T_0$$

where B is the bias, T denotes the temperature and T_0 the nominal temperature.

Then, a scale factor error e_{sf} indicates a deviation from the ideal linear relationship between the input angular rate Ω_z and the corresponding output z. Having these two errors, the output is given by

$$z(\Omega_z) = (SF + e_{sf}(\Omega_z))\Omega_z + B(T).$$

In practice, when the bias is identified in nominal conditions, i.e. at nominal temperature and without vibrations, the sensor is calibrated to suppress this *nominal bias*. For this reason, in general, there is not a particular specification concerning the bias at nominal conditions. However, the bias is easily affected due to environmental changes, mainly caused by temperature changes and fatigue. There are then two performance indicators with respect to bias.

- **Bias thermal sensitivity:** ratio of a change in bias to a change in temperature.
- **Bias repeatability:** the closeness of agreement among repeated measurements of the bias under the same operating conditions when changes in operation conditions or nonoperating periods occur between measurements.

Concerning the scale factor error, the deviation can be more significant at certain angular rate intervals with respect to others, but it is desired that it remains within

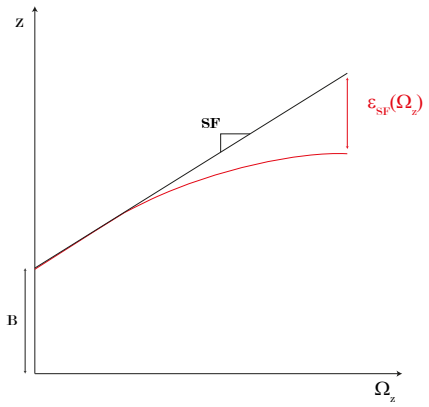

FIGURE 2.10: Input-output relationship of a MEMS gyroscope

specific limits. The first specification is a measure of the deviation from the ideal scale factor at nominal temperature.

- **Scale factor nonlinearity:** maximal deviation, at nominal conditions, from the straight line that defines the nominal input-output relationship over the whole range of operating angular rates.

The scale factor nonlinearity is usually computed as the maximum modulus of the output error ε_z, defined by

$$\varepsilon_z = z^{fit}(\Omega_z) - z(\Omega_z),$$

given in ppm ($\times 10^{-6}$), where $\Omega_z^{fit}(\Omega_z)$ is obtained by a linear regression of the measured points along the whole range of operative angular rates. Then, the SFNL is computed as

$$SFNL(T) = \sup_{\Omega_z \in [\underline{\Omega}_z, \overline{\Omega}_z]} \left(\frac{|\varepsilon_z|}{SF^{fit} \Omega^{fs}} \right) \text{ for } T = T_0,$$

which is equivalent to

$$SFNL(T) = \sup_{\Omega_z \in [\underline{\Omega}_z, \overline{\Omega}_z]} \left(\frac{|\Omega_z - \tilde{\Omega}_z|}{\Omega^{fs}} \right) \text{ for } T = T_0,$$

where T_0 is the nominal temperature and $\Omega^{fs} = (\overline{\Omega}_z - \underline{\Omega}_z)/2$ is the full-scale angular rate of operation.

Similar to the the bias, the scale factor error is also sensitive to variations of temperature and to mechanical fatigue, there are then two supplementary performance specifications that are identical to those of bias.

- **Scale factor thermal sensitivity:** ratio of a change in scale factor to a change in temperature.

- **Scale factor repeatability:** the closeness of agreement among repeated measurements of the scale factor under the same operating conditions when changes in operation conditions or nonoperating periods occur between measurements.

Finally, the last performance specifications concern the level of noise that is found at the output of the sensor, the first one is just the RMS noise defined as

- **RMS noise:** the square root of the output power noise, within a specified operation bandwidth.

The other noise specifications are evaluated by using a time-domain statistic method known as the Allan variance. This method and the respective specifications will be introduced in details in chapter 5 when output noise is analyzed. However, we give some general definitions that are independent of the evaluation method.

- **Angle random walk:** the angular error buildup with time that is due to white noise in angular rate. This error is typically expressed in degrees per square root of hour.

- **Bias instability:** nonstationary process characterized by a $1/\nu$ power spectral density. It is expressed as rad/s.

2.4 Nonidealities in MEMS gyroscopes: sources of uncertainty

2.4.1 Manufacturing dispersion

The increase of micromachining tools, mainly based on photolitography techniques, to fabricate very low scale mechanical and electrical systems, were fundamental for the fast development of MEMS inertial sensors technology [Apo06]. However, the current state of microfabrication processes remain limited to fulfill the technical specifications demanded by high-performance inertial measuring applications, such as automobile and aeronautics.

The limitations of the manufacturing techinques can affect the geometric, electrostatic and material properties of MEMS devices. This in turn derives on important deviations from nominal paramater values due to the high manufacturing tolerances. The result is then a limitation of the reachable performance and robustness properties [AS08].

2.4.2 Anisoelasticity

Probably, the most noticeable resulting errors during fabrication are related to geometric imperfections, which induces undesirable mechanical couplings between drive and sense modes. For instance, the axis of the beams linking the masses to the fixed structure must ideally run along the corresponding axis x or y of the corresponding mode Figure 2.11. In practice, we can find an imperfection that induces an angular mismatch between beam and mode axes [SSP+06]. This type of phenomena induces an elastic coupling between drive and sense modes; and it is known as anisoelasticity. These anisoelastic forces can be modeled by introducing non-diagonal elements in the stiffness matrix [AS08, PS02], as follows:

$$M\ddot{r}(t) + D\dot{r}(t) + Kr(t) = C\dot{r}(t) + F(t) \tag{2.20}$$

with

$$r(t) = \begin{bmatrix} x(t) \\ y(t) \end{bmatrix}, \qquad F(t) = \begin{bmatrix} F_x(t) \\ F_y(t) \end{bmatrix},$$

and

$$M = \begin{bmatrix} m_x & 0 \\ 0 & m_y \end{bmatrix}, \quad D = \begin{bmatrix} d_{xx} & 0 \\ 0 & d_{yy} \end{bmatrix}, \quad K = \begin{bmatrix} k_{xx} & k_{xy} \\ k_{yx} & k_{yy} \end{bmatrix}, \quad C = \begin{bmatrix} 0 & 2m_y\Omega_z \\ -2m_x\Omega_z & 0 \end{bmatrix}.$$

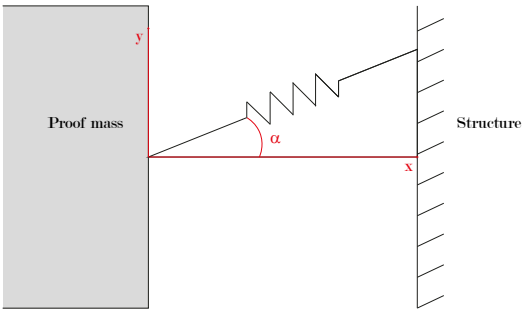

FIGURE 2.11: Schematic representation of anisoelasticity

2.4.3 Non-ideal Damping

The damping is associated to the energy dissipation of mechanical systems, usually comes whether from mechanical friction or due to the viscosity of the gas surrounding the mechanical structure. In MEMS vibratory gyroscopes, the effect of viscous damping is predominant over the structural friction.

We can find several damping mechanisms:

1. the side film damping that occurs between two plates that slide parallel to each other [AS08];
2. the squeeze film damping that occurs as a result of the compression of the gas between two parallel plates that move towards and away from each other, inducing a viscous resistance opposing to the gas flow that is expressed as an additional damping effect [You11];
3. the thermoelastic damping generated by heat flow, to its turn provoked by the compression and decompression inherent to an oscillating mouvement;
4. the hydrodynamic lift effect that, as its name indicates, due to displacement velocity in a viscous medium, lifts the plate into a orthogonal direction with respect to its displacement, directly inducing a couplig effect [WK06, KWB05, AS08].

Modeling separately this different phenomena is a difficult task, given that they can, in general, only be observed as global damping effects, some of them inducing cross-couplings between drive and sense modes. However, it is possible to regroup these different phenomena by adding non-diagonal damping terms in the MEMS mechanical model

$$M\ddot{r}(t) + D\dot{r}(t) + Kr(t) = C\dot{r}(t) + F(t) \tag{2.21}$$

with

$$r(t) = \begin{bmatrix} x(t) \\ y(t) \end{bmatrix}, \qquad F(t) = \begin{bmatrix} F_x(t) \\ F_y(t) \end{bmatrix},$$

and

$$M = \begin{bmatrix} m_x & 0 \\ 0 & m_y \end{bmatrix}, \quad D = \begin{bmatrix} d_{xx} & d_{xy} \\ d_{yx} & d_{yy} \end{bmatrix}, \quad K = \begin{bmatrix} k_{xx} & k_{xy} \\ k_{yx} & k_{yy} \end{bmatrix}, \quad C = \begin{bmatrix} 0 & 2m_y\Omega_z \\ -2m_x\Omega_z & 0 \end{bmatrix}.$$

Indeed, both anisoelasticity and non-ideal damping are commonly present in the vast majority of MEMS gyroscope. In Figure 2.12, we show the bode plot of a MEMS

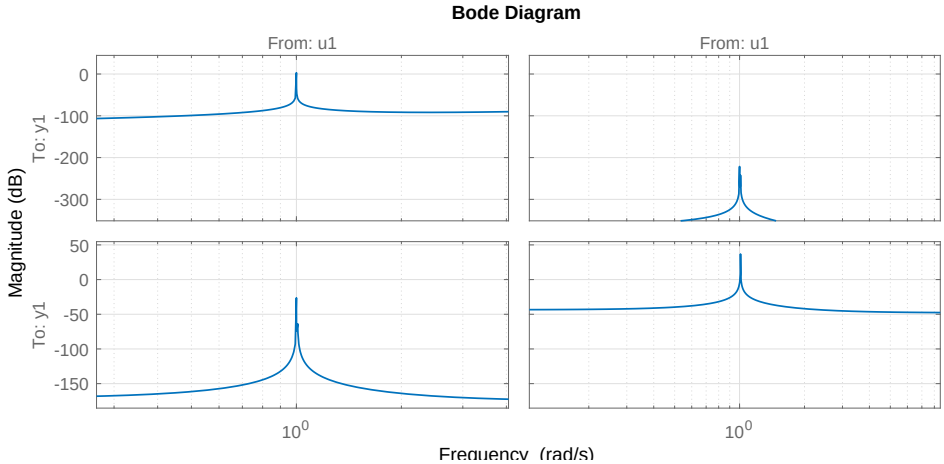

FIGURE 2.12: Identified model with cross-couplings

gyroscope model obtained by identification methods. We can observe that, in addition to the direct transfer functions (upper-left and lower-right Bode plots) expressing the dynamics of drive and sense modes, we also find cross-coupling dynamics between both modes (upper-right and lower-left Bode plots).

Please note that, in this case, if we apply a force to rebalance estimation strategy, which consists in the cancellation of the displacement y, and we directly consider the applied force F_y to estimate the Coriolis force, we obtain

$$F_y(t) = -F_{cy}(t) + d_{yx}\dot{x}(t) + k_{yx}x(t),$$

which can induce an estimation error. The term k_{yx} is usually canceled using the synchronous demodulation, given that the force induced by $k_{yx}x(t)$ is in quadrature with respect to the Coriolis force. Nevertheless, if there exists an error in the reference phase shift of the synchronous demodulation, a small contribution of this term might remain. In contrast, the coupling force provoked by the damping term d_{yx} is in phase with the Coriolis force and it cannot be canceled by synchronous demodulation. Then, it is important to take it into account in the control design process.

2.4.4 Environmental sensitivity

In addition to the inherent fabrication imperfections, variations in the environmental conditions have a disturbing effect on the dynamics of MEMS gyroscopes. Several research have been carried out to study the impact of the temperature on the quality factor Q and the resonance frequency ω_0 [XCWL09, CSL+12, SEGT00, FKP+05, GHL+15]. It was found that the resonance frequency linearly decreases as the temperature increases, while the quality factor decreases with a nonlinear function as the temperature increases.

The authors of [PTS13] described that the inversely linear dependency of the resonance frequency is well defined by elastic properties and its value is fixed for a given material, which is silicon in this case. Then, they found a relation $Q \propto 1/T^3$ (T for temperature) explaining that the main cause for this is the thermoelastic dissipation. In [KHC+08], the authors go further explaining the mechanisms affecting the quality factor. They found that there exists several phenomena that increases the

damping as temperature increases, decreasing then the quality factor. The dominating mechanisms are the air damping and the thermoelastic dissipation. Air damping becomes important at microscale, and it is proportional to the square root of the temperature, while thermoelastic dissipation is determined by the relation between mechanical properties and temperature. Depending on the temperature interval, one or other mechanism becomes dominant over the other ones.

In [You11], the authors described how the presence of humidity in the mechanical resonator can induce capillary forces in the microbeams, affecting the stiffness of the spring behavior.

2.4.5 Noise

Noise coming from different sources generally affects any obtained measure. However, given the scale of MEMS sensors, noise can considerably affect the reliability of the measure, potentially drawing the measure in the most extreme cases.

Mechanical thermal noise is the main reported source of stochastic behavior [Gab93, ALM99, Lel06, KM13]. It is due to the agitation of the molecules in the gas surrounding the MEMS gyroscope which, given the small inertia of the micro mechanical parts and low damping, can cause random motions of the solid parts. This type of noise behaves as a Gaussian white noise, whose power spectral density (PSD) is proportional to the temperature.

Other types of noise present in inertial sensors are presented in [IEE04]. In MEMS community practice, a remarkable importance has been given to $1/\nu$ noise, considered the main cause of the *bias instability*. However, to our knowledge, it has only been detected indirectly by application of the time-domain statistics tools [KJCT12] over very long measures, which can capture the presence of other deterministic phenomena, such as changes in the nominal bias due to temperature or fatigue.

2.4.6 Electronic phase-shift

In general, the amplitude and the phase of the system signals are mainly enforced by the MEMS resonators and the controllers. However, some devices, such as the displacement to voltage converters [SAH08], or the electronic filters associated to the system may induce a non-ideal phase-shift in the output signal. In such a case, the modulated output signal will have a phase error $-\phi$ with respect to the reference phase of the synchronous demodulator. Then, the obtained in-phase and quadrature signals will be given by

$$\begin{aligned} z_{cf}(t) &= z_i(t)\cos(\phi) + z_q(t)\sin(\phi) \\ z_{sf}(t) &= z_q(t)\cos(\phi) - z_i(t)\sin(\phi) \end{aligned}$$

Then, the phase-shift will combine the estimated angular rate and the quadrature error, inducing then a measurement error. In such cases, the demodulating signal employed to extract the angular rate must be adjusted to take into account the phase-shift induced by the electronic devices.

In chapter 3, we developed a set of tools that allow to analyze the effects of synchronous demodulation in the presence of phase-shifts.

2.4.7 Other non-idealities

Electrical coupling

The electronic circuits that excite and measure the displacement of the MEMS resonators might induce a parasitic electrical coupling effect that behaves as a capacitor connected in parallel to the main drive-resonator-sense chain [AS05, CSLB+19]. This may cause saturation of the sensing devices, as well as a radical deformation of the gyroscope transfer functions, in both cases deriving to a strong degradation of the performance or even to make impossible the operation of the system. However, this electric coupling can be minimized with relatively simple mechanism: either by adding capacitors in the circuit that compensates the coupling effect [LS09], or by adding a digital filter [CSLB+19]

Nonlinear effects

Depending on the precise mechanical design, the excitation devices and the associated electronics, each version of the MEMS gyroscope can present different types of nonlinearites. However, there exists two nonlinear phenomena that arise more frequently: spring softening and spring hardening.

In the spring softening, the resonance frequency decreases as the amplitude of the oscillations increases, while in the spring hardening the frequency increases as the amplitude increases. These phenomena are problematic in the case of resonating MEMS gyroscopes. In general, both effects can simultaneously appear, but one is always dominating over the other one.

In [EKT+11], exhaustive nonlinear models of the MEMS resonator excited by a capacitive comb actuator are developed. They conclude that large deformations inducing nonelastic behavior on the beams (springs on the model) cause the hardening effect, while the electrostatic force is responsible of the softening effect. Similar conclusions are presented in [ST17], where the authors argue that nonlinearities in MEMS come from two different sources: relatively large structural deformations and displacement-dependent excitation. More extensive information about nonlinear modeling of MEMS can be found on [You11]. Several studies also investigated the stability regions of MEMS containing spring hardening and softening behaviors [NYAR, AOPB09, MYKPT15].

2.5 Validation of the control design

The previous section presents the wide variety of non-ideal phenomena that can arise in a MEMS gyroscope. Therefore, the task of controlling a system that fulfills all the performance specifications under such conditions is not an easy task. First, the manufacturing imperfections and the undesirable cross-couplings limit the relevance of control strategies based on an uncoupled-modes assumption. Then, even if the controller ensures some performances at typical conditions, the behavior of the system might be modified by environmental changes.

The different control strategies that are proposed within the Next4MEMS project are based on models that are simplified versions of the actual system. These models adopt appropriate assumptions that allow to recast the original control design model into a simpler one (see chapter 4 and chapter 6). This allows to perform a more efficient controller synthesis. Hence, it is then necessary to carry out a performance validation step. The idea is to take into account all the phenomena that were

previously neglected. Then, to determine whether the proposed control solution, based on a model, correctly works or not when implemented on the real system. If the controlled system ensures stability and meets all the performance specifications during this step, then we can say that the design process has been successful.

It might seem obvious that performance validation must be done by experimental means, either on the real system or on a test bench. Indeed, experimental tests are essential to validate any application. However, in many cases, it can be a long, expensive and delicate process to be implemented. In other cases, the control designers do not have all the means of experimentation at their immediate disposal. Thus, when faced with the need of verifying an important number of control solutions, such an approach might not be the most efficient. Another approach, widely used, is to enrich the nominal model to make it more accurate and more faithful to the real system. Performance validation is then performed by running simulations on this new model. The disadvantage of such an approach is mainly related to the cost in terms of time and computational resources when the simulation model becomes too complex. In addition, despite the richness of this new model, in many cases there will always exist modeling errors and possible not considered scenarios.

Given that it is quite difficult to accurately describe a physical system by a single model, even in the case of complex models, it is probably more pertinent to introduce the notion of *sets of models*, considering that such a set can potentially contain an appropriate model of the real system, that is, a model which sufficiently describes the behavior of the system, allowing to ensure properties that are actually found in the real system. The notion of a system that can only be represented by a set of models is usually referred to as the *system uncertainty*.

Then, the objective of the validation process can be extended as the one of ensuring some stability and performance properties despite the system uncertainty. In the case of a model-based validation process, this can be referred to as assessing the system *robustness*. In general, robustness can be tested using probabilistic or worst-case approaches. The most common probabilistic approach for the evaluation of inertial sensors is the one known as the Monte Carlo method, in which the system is evaluated in a certain number of possible scenarios. The reliability of the result will therefore be a function of the number of tests, i.e., the more simulation tests are carried out, the better the guarantee of robustness will be. However, the reliability and efficiency of the Monte Carlo method decreases as the complexity of the system and the number of uncertainties become important.

The other approach is a worst-case one. It consists in systematically formulating mathematical conditions devoted to ensure a proper operation of the controlled system by integrating the system uncertainty. As discussed before, the assumption of a system model is rather an oversimplified one and thus insufficient, while the simulation models are more accurate but frequently time consuming and, in some cases, still insufficient to offer formal robustness guarantees. Therefore, a worst-case approach demands an analysis that it is found between nominal and simulation models. Such a model should be sufficiently general to include uncertainties of the real system and relatively simple in order to be able to efficiently perform robustness analysis without leading to an excessive conservatism. Hence, the choice of such an approach will be relevant insofar as it offers a good guarantee of robustness, uses more reasonable computation times than other approaches, and that do not lead to overly pessimistic results.

It is important to note that the performance and robustness validation methods here mentioned are not mutually exclusive. On the contrary, it is often advisable and even necessary to use some of these methods simultaneously during the design

process, so that in the end we will obtain results that are complementary, reinforcing the reliability of the solutions.

Concerning MEMS gyroscopes, when pre-experimental robust performance validation is mentioned, most of the literature is focused on Monte Carlo methods [ZTSL10, WHGS16]. To our best knowledge, the only tentative of using a worst-case approach is found on [DZG07]. Nevertheless, the analysis is based on classical stability margins using different parameters values, including minimal and maximal ones, which is not a formal guarantee of robustness.

There exists an evident gap to fulfill, which demands to propose alternative methods to test, within the control design process, the robustness of MEMS gyroscopes using more reliable and efficient methods.

2.6 MEMS gyroscope model and uncertainty

In the previous section, we explain that model-based methods are interesting candidates for an efficient validation of the control strategies implemented in MEMS gyroscopes. Let us briefly discuss some of the general elements of the models that are associated to the analysis problems to be solved. First, using the physical equations of the drive and the sense modes that integrate the non-ideal couplings (anisoelasticity and damping), as expressed in (2.21), we can write the state-space representation of the MEMS resonator model:

$$G_{\Omega_z}(s) = \begin{cases} \begin{bmatrix} \dot{x}(t) \\ \ddot{x}(t) \\ \dot{y}(t) \\ \ddot{y}(t) \end{bmatrix} &= A_{\Omega_z} \begin{bmatrix} x(t) \\ \dot{x}(t) \\ y(t) \\ \dot{y}(t) \end{bmatrix} + B \begin{bmatrix} u_x(t) \\ u_y(t) \end{bmatrix} \\ \begin{bmatrix} x(t) \\ y(t) \end{bmatrix} &= C \begin{bmatrix} x(t) \\ \dot{x}(t) \\ y(t) \\ \dot{y}(t) \end{bmatrix} + D \begin{bmatrix} u_x(t) \\ u_y(t) \end{bmatrix} \end{cases} \tag{2.22}$$

with

$$A_{\Omega_z} = \begin{bmatrix} 0 & 1 & 0 & 0 \\ -\frac{k_{xx}}{m_x} & -\frac{d_{xx}}{m_x} & -\frac{k_{xy}}{m_x} & -\frac{d_{xy}}{m_x} + \frac{2m_y}{m_x}\Omega_z \\ 0 & 0 & 0 & 1 \\ -\frac{k_{yx}}{m_y} & -\frac{d_{yx}}{m_y} - \frac{2m_x}{m_y}\Omega_z & -\frac{k_{yy}}{m_y} & -\frac{d_{yy}}{m_y} \end{bmatrix}$$

$$B = \begin{bmatrix} 0 & 0 \\ 1 & 0 \\ 0 & 0 \\ 0 & 1 \end{bmatrix}, \quad C = \begin{bmatrix} 1 & 0 & 0 & 0 \\ 0 & 0 & 1 & 0 \end{bmatrix}, \quad D = \begin{bmatrix} 0 & 0 \\ 0 & 0 \end{bmatrix}.$$

In this model, the input signals are the exciting forces ($u_x \approx F_x$ and $u_y \approx F_y$). The conversion from voltage to electrostatic force is then integrated as a part of the controller. We use the subscript Ω_z to indicate that the MEMS gyroscope model, at nominal conditions, can be seen as a linear model that linearly depends on the input angular rate Ω_z. This perspective of the model is useful to establish the accuracy performance criteria in chapter 4.

In section 2.4, we introduced several non-idealities that affect the ideal operation of the MEMS gyroscope. The consequence of some of these non-idealities, such as

manufacturing dispersion and changes in environmental conditions, is that the values of the model parameters are not exactly known. In other cases they can slowly evolve depending on the environmental conditions. These conditions make arise the notion of uncertainty.

The notion of uncertainty is appropriate to describe manufacturing dispersion or slow variations in environmental conditions. For instance, let us consider the example of a mechanical micro-resonator, where technological limitations force to build devices with springs (usually silicon beams) whose stiffness is given around a nominal value and with a certain manufacturing tolerance. As we observe on the Figure 2.13, introducing a model with parametric uncertainties allows to represent the variation of the resonance frequency and quality factor of the system due to the uncertainty of the springs stiffness and damping mechanisms.

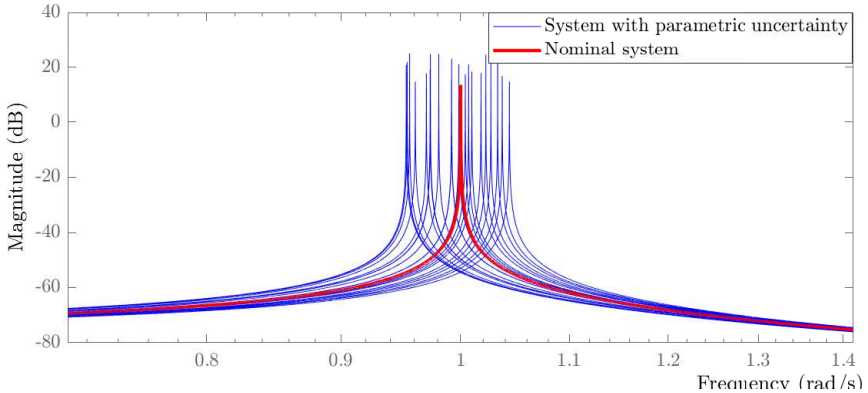

FIGURE 2.13: Effect of a parametric uncertainty on the drive mode resonator

In other cases, models are obtained through system identification (data-based) methods. In this project, the method that is mainly used is the prediction error method [Lju98, Col20]. These modeling methods provide parametric models whose parameter values are only approximately known because of the presence of noise in the experimental data. Then, the models that are obtained through prediction error methods can be naturally modeled as uncertain systems. This subject is further discussed in chapter 4.

Finally, a particular element of the system is the synchronous demodulation which, depending on the control strategy, can be found in the closed-loop or in open-loop at the system output. Synchronous demodulation implies the presence of harmonically time-varying parameters in the system. Hence, classical analysis tools for nominal LTI systems and uncertain systems are no longer sufficient to asses the stability and performance of the system. This question will be addressed from different perspectives all along this work: in chapter 3, a theoretical framework to analyze systems with harmonically time-varying elements is developed. Then, in chapter 4 and chapter 5, the performance analysis tools take into account the presence of synchronous demodulation and propose multiple solutions. Finally, in chapter 6, we address the analysis of the phasor-based control, which implies the implementation of synchronous demodulation inside the closed-loop.

2.7 Research problem formulation

Throughout this chapter, we have introduced the general operation of MEMS gyroscopes and we have shown that there are a variety of proposed control solutions to meet standard performance specifications. On the other hand, we have presented the different non-ideal phenomena that complicate the achievement of stability and performance objectives. Finally, we discuss the necessity of validating the designed control solution, if possible even before its implementation on the real application. Taken into account the different concepts and problems that have been introduced and discussed along this chapter, the main objective of this work can be stated as following.

Given a proposed control strategy for a MEMS gyroscope which meets the required performance specifications for a nominal model or a simplified model, how to efficiently assess whether the various performance specifications are met despite the presence of unmodeled phenomena.

In the context of the MEMS community, we can observe that the performance validation stage presents two main challenges that need to be faced and overcome: the consumption of resources (time, capital and computational capability) and the lack of formal robustness guarantees.

Performance validations of MEMS gyroscopes, given their uncertain and time-varying nature, naturally appears as a problem of testing some desired properties for a whole set of models. In this sense, the worst-case approaches arise as good candidates to achieve this objective.

Worst-case approaches from robust control and system analysis theory develop tools that allow us to analyze systems subject to "problematic" elements (uncertainties, nonlinearities) by stating the problem under the form of a mathematical criterion. Different analysis methods allow to test a variety of stability and performance properties.

In this context, the general performance validation objective, using a model-based worst-case approach, implies to solve three implicit problems of different nature.

1. How to determine an appropriate representation of the real system? In section 2.5, we discuss the interest of an analysis model that is sufficiently general to include system uncertainties, but simple enough to efficiently analyze the robustness of the system. The problem is to find a model that somehow captures the properties of the unmodeled system behavior. Ideally, all the important properties expressed by the model must be also found on the real system. Furthermore, the chosen representation must be compatible with the analysis methods.

2. How to interpret the standard performance specifications? In section E.3, we introduce some of the main performance specifications of MEMS gyroscopes. Such specifications evaluate different properties of the system and under different conditions. Moreover, the performance criteria are defined in terms of measures obtained under a given experimental protocol. The question is how these measures and test conditions can be translated into well defined mathematical criteria that can be tested using the system model.

3. How to test the robustness property of the model set? We have emphasized the necessity of offering formal robustness guarantees using an efficient method in terms of consumed resources. The problem is to propose a mathematical tool that allows to evaluate a defined property. The solution must take the form of a tractable algorithm, which should be accurate and computationally reasonable.

Chapter 3

Analysis of Uncertain and Harmonically Time-Varying Systems

In chapter 2 we introduce the description of the structure and operation of MEMS gyroscopes, the non-idealities that can be found in the system, as well as the performance specifications to be verified. Using a model-based approach, our first objective is to investigate an efficient form to analyze the stability of the controlled MEMS gyroscopes despite the aforementioned imperfections, followed by an assessment of the performance criteria under these uncertain conditions.

Since MEMS gyroscopes are systems that naturally tend to be uncertain, it is necessary to adopt an appropriate framework to cope with this class of analysis problem. The Robust Control framework offers several analysis tools that can be suitable candidates for our purposes. Hence, the first part of this chapter introduces the main theoretical concepts and methods that are exploited in this work, mainly focusing on the Integral Quadratic Constraints (IQC) approach.

In chapter 2, we also introduced the synchronous demodulation, an operation that allows to extract the components of a modulated signal. Synchronous demodulation is an element that is almost universally present in any control architecture, in some cases at the output of the system and in other ones inside the closed loop. Synchronous demodulation introduces in the model parameters that vary as sinusoidal functions of the time. We refer to this class of systems as Linear (Uncertain) Harmonically Time-Varying Systems (LHTV). Even if there exist tools in Robust Control that allow to take into account general time-varying systems, they are not completely adapted to their direct application on LHTV system. Therefore, the second part of this chapter introduces some of our main contributions, focused on extending the existing IQC analysis tools to the analysis of LHTV systems. This problem, despite its frequency in many applications, has not been widely addressed under this perspective, which conforms a promising perspective for the efficient analysis of heterogeneous systems, containing uncertainty, HTV parameters and nonlinearties.

3.1 Input-output stability and performance

Dynamical systems can be represented as input-output models. That is, the system is described as a mapping that associates, to each input, a corresponding output. Therefore, investigating specific constraints on the relationship between the input and the output of a system offers a characterization of its behavior. The first interesting property of a system to analyze is stability, which consists on assessing if the

operator representing the system is bounded. Stability can be investigated via input-output approaches [DV75]. More specifically, here we consider the notion of $\mathcal{L}_2$-gain stability which is defined as follows.

Definition 3.1 ($\mathcal{L}_2$-gain stability)**.** *Let be the system $G : \mathcal{L}_{2e}^{n_w} \to \mathcal{L}_{2e}^{n_z}$, with input w and output z. G is said to be $\mathcal{L}_2$-gain stable if there exists some $\gamma > 0$ such that*

$$\int_0^\infty |z(t)|^2 dt \leq \gamma^2 \int_0^\infty |w(t)|^2 dt \quad \forall\, w \in \mathcal{L}_2^{n_w} \tag{3.1}$$

That is, for any input $w(t)$ belonging to $\mathcal{L}_2^{n_w}$, the response of the system produces an output $z(t)$ defined in $\mathcal{L}_2^{n_z}$, and the ratio between the $\mathcal{L}_2$ norm of the output and the $\mathcal{L}_2$ norm of the input is bounded by γ^2, which can be interpreted as an upper bound of the maximal transmission of energy from the input to the output.

However, the information obtained from the assessment of stability is limited. In fact, evaluating performance of a system means that we need to quantify particular characteristics of its behavior, related to the performance requirements. Hence, it is necessary to derive calculable criteria. Performance can be as well characterized from the input-output relationship using a particular measure of the system output with respect to the system input. The input signal can be a reference signal, an external disturbance or a noise, while the output can be a signal containing information of interest, such as tracking errors, estimation errors, output noise, etc.

From Definition 3.1, we can observe that a quantity (γ) is obtained just by testing $\mathcal{L}_2$-gain stability. Therefore, it is also possible to evaluate performance using the $\mathcal{L}_2$-gain, which is actually a widely used performance measure in the input-output framework.

Definition 3.2 ($\mathcal{L}_2$-gain performance)**.** *Let be the $\mathcal{L}_2$-gain stable system $G : \mathcal{L}_{2e}^{n_w} \to \mathcal{L}_{2e}^{n_z}$. $\mathcal{L}_2$-gain performance of G is the smallest γ such that (3.1) is satisfied.*

The $\mathcal{L}_2$-gain of a given system G, denoted as $\|G\|_{\mathcal{L}_2}$, as a measure of an input-output energetic ratio, is also related to the notion of maximal system gain.

In this chapter we will work with the $\mathcal{L}_2$-gain to evaluate stability and performance. However, it is possible to employ other performance measures, for instance, in chapter 5 we use the $\mathcal{H}_2$ performance to investigate the noise level of output signals.

The introduced definitions for stability and performance are quite general, they can be used for a large class of systems, including time-varying systems. In this chapter we deal with uncertain and time-varying systems. Thus, we need to introduce the corresponding classes of systems, as well as the models that can be used to represent them, followed by the extensions of definitions 3.1 and 3.2 to the case of uncertain systems.

3.2 Representation of uncertain systems

In many cases, the assumption that a system is accurately represented by a unique model is not sufficient to obtain reliable measures of its properties. Indeed, this well-known model only describes the system at some particular (nominal) conditions, while, in reality, there are always some differences between models and systems. A system is said to be uncertain when this gap cannot be neglected. Then, it cannot be represented by a single model. When a system contains uncertainties, it is then more appropriate to represented it as a set of models describing all its possible behavior,

capturing the actual system in any potential scenario, see Figure 3.1 for a schematic representation of this concept. There exists several forms to include uncertainty in the system representation. Let us introduce some of the most common in the literature.

Some of the first models considered representations with the so-called unstructured uncertainties. That is, introducing a causal, bounded and unstructured block operator Δ tht is interconnected to the nominal part of the system. This allows to model unknown, possibly infinite dimensional, dynamics for which little information is available e.g. the size of the uncertainty in terms of $\mathcal{L}_2$-gain or weighted $\mathcal{L}_2$-gain [DS81]. However, since all the uncertainties are grouped in a single full-block operator, this type of representation may lead to an important conservatism when dealing with the case of systems comporting multiple uncertainties of different nature.

Another type of uncertain model, widely used today in the literature, is the polytopic representation, which describes uncertain systems containing parametric uncertainties that belong to a polytope [AGB95]. This type of representation is possible under the condition that a state-space representation of the system affinely depends on the parametric uncertainties.

In this memoir, we employ Linear Fractional Transformation (LFT) models, as they can model both parametric uncertainties and unmodeled dynamics [SP01, ZD98]. More importantly, they make possible to represent uncertain systems with a state-space representation that rationally depends on the uncertainties. This constitutes a larger class of uncertain systems than those that can be represented by polytopic models. Moreover, the LFT representation is also adapted to time-varying and nonlinear systems; which will become important in the following of this memoir.

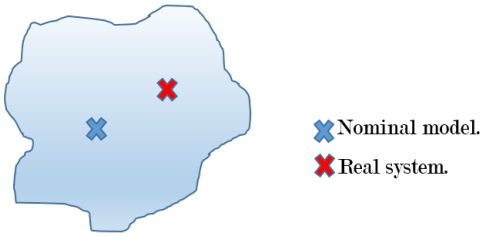

FIGURE 3.1: Representation of a set of models

3.2.1 Linear Fractional Transformation

The LFT representation describes the feedback interconnection of two operators. In robustness analysis, they typically are a well-known LTI system $G(s)$, called the "nominal system", and a block operator Δ containing all the "problematic elements" of the system, for instance, uncertainties, time-varying parameters and nonlinearities (Figure 3.2). We denote the LFT representation as $\Delta \star G$, which is defined by the equations:

$$\begin{aligned} \begin{bmatrix} q(s) \\ z(s) \end{bmatrix} &= \underbrace{\begin{bmatrix} G_{qp}(s) & G_{qw}(s) \\ G_{zp}(s) & G_{zw}(s) \end{bmatrix}}_{G(s)} \begin{bmatrix} p(s) \\ w(s) \end{bmatrix} \\ p(s) &= \Delta(q)(s) \end{aligned} \tag{3.2}$$

where $G \in \mathcal{RH}_\infty^{(n_p+n_w)\times(n_q+n_z)}$ is a stable LTI system, and $\Delta : \mathcal{L}_{2e}^{n_q} \to \mathcal{L}_{2e}^{n_p}$ can be any bounded and causal operator.

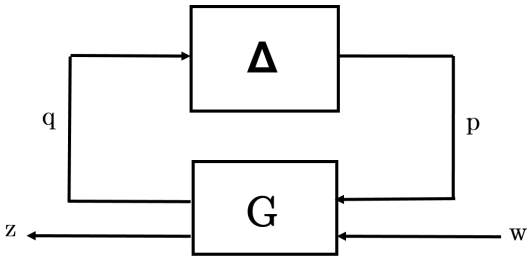

FIGURE 3.2: LFT representation $\Delta \star G$

Remark: Δ is an operator generally defined in the time-domain, $p(s)$ is then given by the Laplace transform of the signal $p(t)$, i.e. $p(s) = \mathcal{L}\{\Delta(q)(\cdot)\}(s)$. However, we employ the simplest notation of equation (3.2) to denote this operation.

Uncertainty is introduced when Δ belongs to some set $\mathbf{\Delta}$ that describes the nature and structure of the uncertain elements. The set $\mathbf{\Delta}$ generates a whole family of models $\mathbf{\Delta} \star G$ such that there exists an element Δ in the set $\mathbf{\Delta}$ describing the dynamics of the real system (Figure 3.1).

In the robust control framework, we usually consider sets of (diagonal) structured uncertainties. To give a clearer picture of the structure of uncertainties, let us introduce some of the most common sets of structured uncertainties. One is the set $\mathbf{\Delta_{TI}}$ of time-invariant uncertainties defined as:

$$\mathbf{\Delta_{TI}} = \left\{ \Delta_{TI} \in \mathcal{H}_\infty^{k\times k} \;\middle|\; \begin{array}{c} \exists\, \Delta_{TI,i} \in \mathcal{H}_\infty^{k_i\times k_i},\ \|\Delta_{TI,i}\|_\infty \le 1\ \forall\, i \in \{1,...,l\} \\ \exists\, \delta_{TI,j} \in \mathbb{R},\ |\delta_{TI,j}| \le 1\ \forall\, j \in \{1,...,m\} \\ \Delta_{TI} = \mathrm{diag}(\Delta_{TI,1},...,\Delta_{TI,l},\delta_{TI,1}I_{r_1},...,\delta_{TI,m}I_{r_m}) \\ \text{with } k = \sum_{i=1}^{l} k_i + \sum_{j=1}^{m} r_j \end{array} \right\} \tag{3.3}$$

and the set $\mathbf{\Delta_{TV}}$ of time-varying operators:

$$\mathbf{\Delta_{TV}} = \left\{ \Delta_{TV} : \mathcal{L}_{2e}^{k} \to \mathcal{L}_{2e}^{k} \;\middle|\; \begin{array}{c} \exists\, \Delta_{TV,i} : \mathcal{L}_{2e}^{k_i} \to \mathcal{L}_{2e}^{k_i},\ \|\Delta_{TV,i}\|_{\mathcal{L}2} \le 1\ \forall\, i \in \{1,...,l\} \\ \exists\, \delta_{TV,j} : [0,\infty[\to \mathbb{R},\ |\delta_{TV,j}(t)| \le 1\ \forall\, j \in \{1,...,m\} \\ \Delta_{TV} = \mathrm{diag}(\Delta_{TV,1},...,\Delta_{TV,l},\delta_{TV,1},...,\delta_{TV,m}) \\ \text{with } k = \sum_{i=1}^{l} k_i + \sum_{j=1}^{m} r_j \end{array} \right\} \tag{3.4}$$

It is also possible to combine the previous sets to define a more general uncertainty set $\mathbf{\Delta_{TIV}}$ that contains both time-invariant and time-varying uncertainties:

$$\mathbf{\Delta_{TIV}} = \left\{ \Delta : \mathcal{L}_{2e}^{n_q} \to \mathcal{L}_{2e}^{n_p} \;\middle|\; \begin{array}{c} \exists\, \Delta_{TI} \in \mathbf{\Delta_{TI}} \\ \exists\, \Delta_{TV} \in \mathbf{\Delta_{TV}} \\ \Delta_{TIV} = \mathrm{diag}(\Delta_{TI}, \Delta_{TV}) \end{array} \right\}, \tag{3.5}$$

with $\mathbf{\Delta_{TI}}$ given by (3.3) and $\mathbf{\Delta_{TV}}$ given by (3.4). These sets are introduced to illustrate the classical notion of uncertainties and time-varying elements in LFT models. There exists other possible extensions of these classes of sets, for instance, uncertainties in a polytope, rate-bounded time-varying parameters, sector bounded nonlinearities, etc [MR97, VSK16]. In this memoir, we investigate into details the class of Uncertain Harmonically Time-Varying Systems, which are introduced in section F.5 as the main contribution of this chapter.

After having presented the LFT representation and some examples of sets of uncertainties, let us now introduce the definition of an uncertain system under LFT representation.

Definition 3.3 (Uncertain system). *Let $G \in \mathcal{RH}_\infty^{(n_p+n_w)\times(n_q+n_z)}$ be a stable LTI system, and let $\mathbf{\Delta}$ be a set of bounded and causal operators. Then, an uncertain system $z = (\mathbf{\Delta} \star G)w$ is defined as:*

$$\exists\, \Delta \in \mathbf{\Delta} \begin{cases} \begin{bmatrix} q(s) \\ z(s) \end{bmatrix} = \underbrace{\begin{bmatrix} G_{qp}(s) & G_{qw}(s) \\ G_{zp}(s) & G_{zw}(s) \end{bmatrix}}_{G(s)} \begin{bmatrix} p(s) \\ w(s) \end{bmatrix} \\ p(s) = \Delta(q)(s). \end{cases} \tag{3.6}$$

Using this definition of uncertain systems, the notions of stability and performance, which were given for a general system, need to be adapted to the case of sets of models. To do so, we introduce the notion of *robustness* in the following section.

3.3 Robust stability and robust performance

Our objective is to investigate the stability and performance of uncertain and time-varying systems. In this case, we refer to uncertain systems under LFT representation given by (3.6). We then define the robustness as the property of retaining stability and performance for any model generated by each Δ in the set $\mathbf{\Delta}$. In this section, we introduce formal definitions of robust stability and robust performance.

3.3.1 Robust stability

Let us first consider the internal feedback interconnection (G_{qp}, Δ) represented in Figure 3.3 and defined by

$$\begin{aligned} q &= G_{qp}(s)p + q_{in} \\ p &= \Delta(q) + p_{in} \end{aligned} \tag{3.7}$$

with $G_{qp} \in \mathcal{RH}_\infty^{n_p \times n_q}$ a stable LTI system (the upper-left transfer function of G in the LFT representation (3.2)), and Δ any bounded and causal operator, $q \in \mathcal{L}_{2e}^{n_q}$ and $p \in \mathcal{L}_{2e}^{n_p}$ are the internal signals of the interconnection, and $q_{in} \in \mathcal{L}_{2e}^{n_q}$, $p_{in} \in \mathcal{L}_{2e}^{n_q}$ are external inputs disturbing the interconnection.

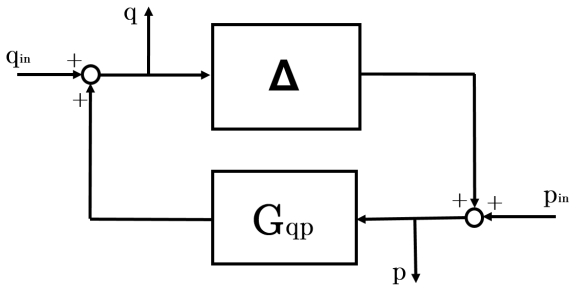

FIGURE 3.3: Feedback interconnection (G_{qp}, Δ)

Before defining stability, we need to ensure that the interconnection (G_{qp}, Δ) is a proper representation of a real physical system. To this end, the interconnection (G_{qp}, Δ) is required to have the *well-posedness* property, defined as follows [ZD98].

Definition 3.4 (Well-posedness)**.** *A feedback interconnection (G_{qp}, Δ), as the one of (3.7), is well-posed if, for every input $q_{in} \in \mathcal{L}_{2e}^{n_q}$ and $p_{in} \in \mathcal{L}_{2e}^{n_q}$, there exist unique solutions $q \in \mathcal{L}_{2e}^{n_q}$ and $p \in \mathcal{L}_{2e}^{n_p}$ that causally depend on q_{in} and p_{in}; that is, $(I - G_{qp}\Delta)$ has a causal inverse.*

In other words, well-posedness of interconnection (G_{qp}, Δ) implies that the internal signals q and p of the interconnection are well-defined functions of time that causally depend on the external disturbances q_{in} and p_{in}.

Following the notion of stability given by the $\mathcal{L}_2$-gain, we can now define the stability of the interconnection (G_{sp}, Δ), also known as internal stability.

Definition 3.5 (Internal stability)**.** *Let be the well-posed feedback interconnection (G_{qp}, Δ) defined by (3.7). The interconnection (G_{qp}, Δ) is said to be $\mathcal{L}_2$-gain stable with respect to Δ if it is well-posed and if there exists some α such that*

$$\|q\|_2^2 + \|p\|_2^2 \leq \alpha^2(\|q_{in}\|_2^2 + \|p_{in}\|_2^2) \quad \forall\, q_{in} \in \mathcal{L}_{2e}^{n_q},\ p_{in} \in \mathcal{L}_{2e}^{n_p} \tag{3.8}$$

In simple terms, the previous definition implies that, if for every pair of external bounded signals q_{in} and p_{in}, the energy of the internal signals p and q is upper bounded by α^2 times the energy of the disturbance, then the interconnection is internally stable.

Now, let us describe an uncertain interconnection $(G_{qp}, \mathbf{\Delta})$ as:

$$\exists\, \Delta \in \mathbf{\Delta} \begin{cases} q(s) & = G_{qp}(s)p + q_{in} \\ p & = \Delta(q) + p_{in}. \end{cases} \tag{3.9}$$

From Definition 3.5, and using the uncertain interconnection given by (3.9), we can introduce a formal definition of robust stability.

Definition 3.6 (Robust stability)**.** *Let G_{qp} be a stable LTI system, and let $\mathbf{\Delta}$ be a set of bounded and causal operators. Then, the uncertain system $(G_{qp}, \mathbf{\Delta})$, defined by (3.9), is said to be robustly stable if (G_{qp}, Δ) is well-posed and internally stable for all $\Delta \in \mathbf{\Delta}$.*

The uncertain interconnection $(G_{qp}, \mathbf{\Delta})$ is actually the internal feedback loop of the uncertain system $\mathbf{\Delta} \star G$, defined in (3.6). Hence, Definition 3.6 implies robust stability of $\mathbf{\Delta} \star G$, with $q_{in} = G_{qw}(s)w$ and $p_{in} = 0$ being signals in $\mathcal{L}_{2e}$. Then, since the nominal system G_{qp} (no Δ involved) is stable, robust stability means that no element in the set $\mathbf{\Delta}$ can destabilize G_{qp}, thus G.

3.3.2 Robust performance

Let us consider the uncertain system represented as the LFT system $\mathbf{\Delta} \star G$ defined by (3.6) and shown in Figure 3.2. Similar to the stability definition, the LFT $\Delta \star G$ is required to be well-posed in the sense of Definition 3.4, that is, if $(I - G_{qp}\Delta)$ has a causal inverse for all $\Delta \in \mathbf{\Delta}$, then $\Delta \star G$ is well-posed.

Performance of $\Delta \star G$ is usually characterized by the performance channel associating the external input w to the system output z. We can then introduce a definition for robust $\mathcal{L}_2$-gain performance.

Definition 3.7 (Robust $\mathcal{L}_2$-gain performance)**.** *Let G be a stable LTI system, and let $\mathbf{\Delta}$ be a set of bounded and causal operators. Then, $\mathbf{\Delta} \star G$, defined by (3.6), has a robust $\mathcal{L}_2$-gain of γ if it is robustly stable and if γ is the smallest scalar such that, for all $\Delta \in \mathbf{\Delta}$, $\Delta \star G$ satisfies condition (3.1).*

Having defined an uncertain system, as well as the notions of robust stability and robust performance, the question now is how can we evaluate if a given uncertain system is robustly stable, and how can we compute the corresponding robust performance indicator γ. This is introduced in the following sections.

3.4 Analysis of LFT systems

The origins of robustness analysis approaches date back to the sixties, even though the research objectives were quite different. In fact, the first results using LFT-like systems i.e. feedback interconnection of two operators, were devoted to the study of nonlinear systems, trying to establish stability conditions by separately studying the two operators.

The Russian literature focused on the Lur'e problem, which describes nonlinear systems as the feedback interconnection of an LTI system and a static nonlinearity, giving birth to the Absolute Stability Theory, which, in general, proposed analysis conditions for complete classes of nonlinearities. The first works led to the Circle and Popov criteria [Pop61], which became popular given their direct graphical interpretation using the Nyquist diagram. Further development of this theory was mainly carried out by the research group of Yakubovich [Yak65, Yak67, Yak71], who proposed frequency domain stability conditions for the nonlinear interconnection. Several crucial results were derived from these works:

1. It appeared for the first time the concept of Integral Quadratic Constraint (in time-domain).

2. The development of the Kalman-Yakubovich-Popov lemma, which establishes the link between a frequency domain condition and a Linear Matrix Inequality (LMI) constraint.

3. The use of an S-procedure argument to treat systems with multiple nonlinearities.

See [Lib06] for a survey on the Absolute Stability literature.

In the same time, the occidental literature relied on an energetic interpretation of the signals interacting with the operators, this by using the concepts of truncation and inner-products over extended signal spaces [San64, Zam66b]. The main approaches stemming from this vision are the Input-Output Stability framework [DV75] and the Dissipativity Theory [Wil72]. Within the input-output framework, the works devoted to the study of feedback interconnections of two nonlinear operators offered the celebrated Small-Gain and Passivity theorems [DV75, Zam66b]. These theorems, together with the Zames conic sectors [Zam66a], were extended and generalized by Safonov [Saf80] and his Separation of Graphs theorem. In addition, the use of loop transformations to improve stability conditions evolved to a more formal and stronger tool named Multiplier [Zam66a, O'S67, ZF68].

Later, in the eighties and from the nonlinear systems litterature, some researchs focused their attention on the analysis of linear uncertain systems, this by considering the interconnection of an LTI system and, initially, an unstructured uncertainty.

The strong interest of investigating such a problem comes from the fact that some results that offer only sufficient stability conditions for nonlinear systems, become sufficient and necessary conditions for some classes of linear uncertain systems. Then, in [Doy82], Doyle made a double contribution by proposing a systematic technique to exploit information about the structure of the uncertainty, transforming the problem into the analysis of an interconnection of an LTI system and a structured (block-diagonal) uncertainty; also, he introduced a new measure that provides necessary and sufficient stability conditions for this type of systems, known as the Structured Singular Value and noted as μ. The main inconvenient of this approach is that the exact computation of μ leads to a non-polynomial problem, restricting the method to systems with few or a single uncertainty. This problem is overcome by the introduction of the known as D-G scaling and the development of computation methods to obtain an upper-bound of μ, which allow to analyze systems with mixed uncertainties [PD93, FTD91, LTVD00, Fer99]. From there, the μ-analysis framework became one of the most popular tools of the robust control framework.

It would not be fair to skip the fact that these methods were expanded thanks to the development of efficient algorithms to solve convex optimization problems under LMI constraints [NN94], in which rely most of the robustness analysis tools and many other control theory problems.

The work of Megretski and Rantzer [MR97] introduces the Integral Quadratic Constraints (IQC) framework, which brings together multiple concepts of the Russian, occidental and robust control literature. The IQC framework offers an unified approach that allows to investigate the stability of LFT-like systems containing multiple uncertainties of different classes. Still more interesting is the fact that it is possible to analyze time-varying and nonlinear systems using the same concepts combined with other recent results [CS15, Sei14, Wai18, SV18]. Moreover, the stability results can be easily extended to the analysis of robust performance, with the possibility of considering a variety of performance measures. Finally, the stability and performance tests are generally obtained in the form of LMI optimization problems, offering tractable conditions. Given that MEMS gyroscopes are systems containing an important number of uncertain and time-varying elements, and given that we aim to validate different performance criteria, the flexibility and efficiency of the IQC framework make it suitable in the pursuit of our objectives, so it will be the main approach used in this memoir.

3.4.1 Integral Quadratic Constraints (IQC) approach

The IQC approach proposed by Megretski and Rantzer in [MR97] enables to investigate the stability and performance of a large class of uncertain, time-varying and nonlinear systems under an LFT representation. Here we consider systems described by the interconnection defined in (3.7), with G being an LTI system, and $\Delta \in \mathbf{\Delta}$ the block containing the uncertainties and time-varying elements. The stability analysis is performed by studying G and $\mathbf{\Delta}$ separately using Integral Quadratic Constraints (IQC).

The idea behind is to characterize the main properties of the uncertainty set $\mathbf{\Delta}$ as accurately as possible. To this end, we consider the mapping $p = \Delta(q)$ and we constraint input-output relations of Δ through an IQC. Let us state the definition of an IQC.

Definition 3.8 (Integral Quadratic Constraint)**.** *Let* $\Pi : j\mathbb{R} \to \mathbb{C}^{(n_q+n_p)\times(n_q+n_p)}$ *be a linear and bounded Hermitian-valued operator. Then,* Δ *is said to satisfy the IQC defined by*

Π ($\Delta \in IQC(\Pi)$) *if, for all* $q \in \mathcal{L}_2^{n_q}$,

$$\int_{-\infty}^{\infty} \begin{bmatrix} \widehat{q}(j\omega) \\ \widehat{p}(j\omega) \end{bmatrix}^* \underbrace{\begin{bmatrix} \Pi_{11}(j\omega) & \Pi_{12}(j\omega) \\ \Pi_{12}(j\omega)^* & \Pi_{22}(j\omega) \end{bmatrix}}_{\Pi(j\omega)} \begin{bmatrix} \widehat{q}(j\omega) \\ \widehat{p}(j\omega) \end{bmatrix} d\omega \geq 0. \tag{3.10}$$

with $\widehat{p}(j\omega)$ *and* $\widehat{q}(j\omega)$ *respectively being the Fourier transforms of* p *and* q*, and* $p = \Delta(q)$.

The operator Π defining the IQC is usually known as the multiplier. It allows to describe input-output relations of a given operator Δ. However, to evaluate robustness property, we need to construct a whole set of multipliers $\mathbf{\Pi}$, defined as follows.

Definition 3.9 (Set of multipliers)**.** *Let* $\mathbf{\Delta}$ *be a set of bounded and causal operators. Let consider the Integral Quadratic Constraint given by* (3.10)*. We define then a set of multipliers* $\mathbf{\Pi}$ *as*

$$\mathbf{\Pi} = \left\{ \; \Pi(j\omega) \;\middle|\; \Delta \in IQC(\Pi) \; \forall \, \Delta \in \mathbf{\Delta} \; \right\} \tag{3.11}$$

The conditions to construct a set of multipliers $\mathbf{\Pi}$ for a specific uncertain set $\mathbf{\Delta}$ are presented further in this section.

Robust stability

Let us now state an adapted version of the main IQC stability theorem introduced by Megretski and Rantzer in [MR97]. In fact, the original result is not defined in terms of robust stability i.e. for all $\Delta \in \mathbf{\Delta}$, but related to the stability of some feedback interconnection of an LTI system and an operator Δ replaced by a star-shaped set i.e. Δ replaced by $\tau\Delta$ with $\tau \in [0,1]$. However, the robust version presented here does not modify the essence of the original theorem, but will be more suitable for the following of our work.

Theorem 3.1. *Let* G_{qp} *be a stable LTI system, let* $\mathbf{\Delta}$ *be a set of bounded and causal operators, and let* $(G_{qp}, \mathbf{\Delta})$ *be defined by* (3.9)*. Let the set* $\mathbf{\Pi}$ *be defined by* (3.11)*.*

Assume that

1. *for all* $\tau \in [0,1]$*, for all* $\Delta \in \mathbf{\Delta}$*, the interconnection* $(G_{qp}, \tau\Delta)$ *is well-posed;*
2. *for all* $\tau \in [0,1]$*, for all* $\Delta \in \mathbf{\Delta}$ *and for all* $\Pi \in \mathbf{\Pi}$*,* $\tau\Delta \in IQC(\Pi)$*;*

Then, the interconnection $(G_{qp}, \mathbf{\Delta})$ *is robustly stable if there exists a* $\Pi \in \mathbf{\Pi}$ *and* $\epsilon > 0$ *satisfying the frequency domain inequality*

$$\begin{bmatrix} G_{qp}(j\omega) \\ I \end{bmatrix}^* \Pi(j\omega) \begin{bmatrix} G_{qp}(j\omega) \\ I \end{bmatrix} \preceq -\epsilon I \quad \forall \, \omega \in \overline{\mathbb{R}}. \tag{3.12}$$

The proof is available in the original work [MR97]. There, an homotopy argument is employed, from where the importance of introducing the star-shaped set $\tau\Delta$ with $\tau \in [0,1]$.

Remark: When the uncertainty block Δ is linear, well-posedness is implicitly satisfied by assumption 2 in Theorem 3.1 and condition (3.10). In such case, we can also prove it using a Nyquist argument such that (3.12) becomes a sufficient and necessary condition for the robust stability.

Remark: The introduced IQC approach employs two frequency domain conditions to test stability ((3.10) and (3.12)). Other results may consider IQCs in time domain [GS97, Sei14, CS15], since it may be considered to be less restrictive when we look

for stability conditions over finite time horizons, for instance in the case of periodic systems [OP19]. However, the IQCs in the time domain demand particular factorizations for the multiplier which, in turn, make the analysis restrictive. Moreover, since the construction of multipliers becomes much more straightforward in the frequency domain, where convolution products become simple multiplications, frequency IQCs are more adapted to the objectives and operators we will work with throughout this memoir.

To use the presented result, the procedure to test stability consists in looking for an appropiate set of multipliers $\mathbf{\Pi}$ corresponfing to the considered uncertainty set $\mathbf{\Delta}$, as defined in (3.10). For instance, [MR97, VSK16] present a large catalog of multipliers. Then, to evaluate the stability of the uncertain interconnection (3.9), we test if there exists some multiplier Π in the chosen set $\mathbf{\Pi}$ that satisfies condition (3.12).

The suitable choice of the set $\mathbf{\Pi}$ is a crucial point in robustness analysis. If for traditional uncertainties this question has been well studied, it is not always the case for nonlinear or time-varying operators. As it will be shown in section F.5, a suitable choice of multiplier set $\mathbf{\Pi}$ for the case of Harmonically Time-Varying Systems is proposed in this work.

Robust performance

To address the robust performance analysis, let us consider the uncertain LFT system $z = (\mathbf{\Delta} \star G)w$ defined in (3.6), with the nominal system G containing the performance channel that to z associates the input signal w.

As we mentioned before, there is not a single definition for robust performance but several performance criteria that can be employed depending on the pursued objectives. One may consider, for instance, the aforementioned $\mathcal{L}_2$-gain performance defined in (3.1), or passivity performance defined as $\int_{-\infty}^{\infty} z(t)^T w(t) dt \geq 0$. However, in any case, both performance criteria come to impose some particular constraint on the relationship between signals w and z. We can then characterize several performance measures through some Integral Quadratic Constraint of the form

$$\int_{-\infty}^{\infty} \begin{bmatrix} \widehat{z}(j\omega) \\ \widehat{w}(j\omega) \end{bmatrix}^* \Pi^{perf} \begin{bmatrix} \widehat{z}(j\omega) \\ \widehat{w}(j\omega) \end{bmatrix} d\omega \leq 0. \tag{3.13}$$

For instance, we can refer to the most known performance criteria:

1. the $\mathcal{L}_2$-gain of the system is lower than γ if (3.13) holds with

$$\Pi^{perf} = \begin{bmatrix} I & 0 \\ 0 & -\gamma^2 I \end{bmatrix}; \tag{3.14}$$

2. the system is strictly passive if (3.13) holds with

$$\Pi^{perf} = \begin{bmatrix} 0 & -I \\ -I & 0 \end{bmatrix}.$$

Remark: The upper-left element of Π^{perf} is demanded to be non-negative in order to simultaneously test robust stability and robust performance.

In order to clarify the performance characterization in the form of (3.13), let us develop the $\mathcal{L}_2$-gain performance, which is the main used performance measure in

this manuscript. If we consider

$$\Pi^{perf} = \begin{bmatrix} I & 0 \\ 0 & -\gamma^2 \end{bmatrix},$$

then, for some $\gamma > 0$, the IQC (3.13) leads to

$$\begin{aligned} & \int_{-\infty}^{\infty} \widehat{z}(j\omega)^* \widehat{z}(j\omega) d\omega \leq \gamma^2 \int_{-\infty}^{\infty} \widehat{w}(j\omega)^* \widehat{w}(j\omega) d\omega \\ \Leftrightarrow \quad & \int_0^{\infty} z(t)^T z(t) dt \leq \gamma^2 \int_0^{\infty} w(t)^T w(t) dt \\ \Leftrightarrow \quad & \|z\|_2^2 \leq \gamma^2 \|w\|_2^2 \\ \Leftrightarrow \quad & \|z\|_2 \leq \gamma \|w\|_2, \end{aligned}$$

yielding to the inequality introduced in (3.1).

Using this performance characterization, let us then introduce the following adapted version of the IQC performance theorem, here introduced for the case of $\mathcal{L}_2$-gain performance.

Theorem 3.2. *Let G be a stable LTI system, let $\mathbf{\Delta}$ be a set of bounded and causal operators, and let $\mathbf{\Delta} \star G$ be defined by (3.6). Let the set $\mathbf{\Pi}$ be defined by (3.11), and let*

$$\Pi^{perf} = \begin{bmatrix} I & 0 \\ 0 & -\gamma^2 \end{bmatrix}.$$

Assume that

1. *for all $\tau \in [0,1]$, for all $\Delta \in \mathbf{\Delta}$, $\Delta \star G$ is well-posed;*
2. *for all $\tau \in [0,1]$, for all $\Delta \in \mathbf{\Delta}$ and for all $\Pi \in \mathbf{\Pi}$, $\tau\Delta \in IQC(\Pi)$;*

Then, $\mathbf{\Delta} \star G$ is robustly stable and has robust $\mathcal{L}_2$-gain performance lower than γ if there exist $\Pi \in \mathbf{\Pi}$ and $\epsilon > 0$ satisfying the frequency domain inequality

$$\begin{bmatrix} G_{qp}(j\omega) & G_{qw}(j\omega) \\ I & 0 \\ G_{zp}(j\omega) & G_{zw}(j\omega) \\ 0 & I \end{bmatrix}^* \begin{bmatrix} \Pi(j\omega) & 0 \\ 0 & \Pi^{perf} \end{bmatrix} \begin{bmatrix} G_{qp}(j\omega) & G_{qw}(j\omega) \\ I & 0 \\ G_{zp}(j\omega) & G_{zw}(j\omega) \\ 0 & I \end{bmatrix} \preceq -\epsilon I \quad \forall\, \omega \in \overline{\mathbb{R}}. \tag{3.15}$$

The proof of this theorem can be found in [MR97, VSK16].

Other performance criteria may be less intuitive, for instance, in chapter 5 we present the IQC characterization of $\mathcal{H}_2$ performance, which considers a structural change in the involved inequalities. See [VSK16] for a larger class of IQC performance characterizations.

3.4.2 Multiple uncertainties

The IQC approach enables to confront the analysis of systems with several uncertainties that may be of different nature. Let us consider a system containing an uncertainty that belongs to a set $\mathbf{\Delta}$ composed of r structured uncertainties Δ_i of different

nature, each of them belonging to some specific set $\mathbf{\Delta_i}$, Δ is then written as

$$\Delta(q) = \text{diag}(\Delta_1(q_1), ..., \Delta_r(q_r)). \tag{3.16}$$

Let assume that for each uncertainty set $\mathbf{\Delta_i}$, there exists a set of multiplier $\mathbf{\Pi_i}$ that satisfies the IQC (3.10) for all $\Delta_i \in \mathbf{\Delta_i}$ and for all $\Pi_i \in \mathbf{\Pi_i}$. Let the multipliers in each set $\mathbf{\Pi_i}$ be partitioned as

$$\Pi_i = \begin{bmatrix} \Pi_{i,11} & \Pi_{i,12} \\ \Pi^*_{i,12} & \Pi_{i,22}. \end{bmatrix}$$

Then, the global uncertainty block Δ (3.16), belonging to $\mathbf{\Delta}$ satisfies the IQC (3.10), defined by the multiplier set

$$\mathbf{\Pi} = \left\{ \Pi \;\middle|\; \begin{array}{c} \exists\, \Pi_i \in \mathbf{\Pi_i}\ \forall\, i \in \{1, ..., r\}, \\ \Pi = \begin{bmatrix} \text{diag}(\Pi_{1,11}, ...\Pi_{r,12}) & \text{diag}(\Pi_{1,12}, ...\Pi_{r,11}) \\ \text{diag}(\Pi^*_{1,12}, ...\Pi^*_{r,11}) & \text{diag}(\Pi_{1,22}, ...\Pi_{r,22}) \end{bmatrix} \end{array} \right\}. \tag{3.17}$$

This rather simple notion makes the IQC approach an attractive tool for the analysis of a large class of systems since it offers flexibility when dealing with several types of uncertainties, time-varying elements and nonlinearities, as well as the assessment of different performance criteria.

We have at our disposal two theorems allowing us to analyze robust stability and robust performance. Now, in order to be able to exploit them, two important aspects remain to be addressed: defining the different classes or sets of multipliers; and establishing the conditions for the IQC theorems in the form of tractable optimization problems.

3.4.3 Classes of multipliers

The conditions of Theorem 3.1 and Theorem 3.2 allow to test robust stability and robust performance of uncertain systems by using the so-called multipliers. However, we did not give any additional information about how a set of multipliers can be defined for some specific uncertainty set $\mathbf{\Delta}$. The selection of a set of multipliers is far from being arbitrary, in fact, it is crucial in the precision and conservatism of the analysis results.

We present how an appropriate set of multipliers can be constructed for uncertainties with particular characteristics. We illustrate this concept through the example of a time-invariant parametric uncertainty $\delta \in \mathbb{R}$ repeated n_q times, i.e. $\Delta = \delta I_{n_q}$. The uncertainty δ is normalized such that $\delta \in [-1, 1]$. A first option may be to consider a set of constant diagonal multipliers allowing to capture the bounded nature of the uncertainty,

$$\mathbf{\Pi} = \left\{ \Pi \;\middle|\; \alpha > 0,\ \Pi = \begin{bmatrix} \alpha I_{n_q} & 0 \\ 0 & -\alpha I_{n_q} \end{bmatrix} \right\}. \tag{3.18}$$

Then, with $p = \Delta(q) = \delta q$, the IQC (3.10) gives

$$\begin{aligned}
&\int_{-\infty}^{\infty} \begin{bmatrix} \widehat{q}(j\omega) \\ \widehat{p}(j\omega) \end{bmatrix}^* \begin{bmatrix} \alpha I_{nq} & 0 \\ 0 & -\alpha I_{np} \end{bmatrix} \begin{bmatrix} \widehat{q}(j\omega) \\ \widehat{p}(j\omega) \end{bmatrix} d\omega \geq 0 \\
\Leftrightarrow &\int_{-\infty}^{\infty} \alpha(\widehat{q}(j\omega)^* \widehat{q}(j\omega) - \widehat{p}(j\omega)^* \widehat{p}(j\omega))\, d\omega \geq 0 \\
\Leftrightarrow &\int_{-\infty}^{\infty} \alpha(1-\delta^2)\widehat{q}(j\omega)^* \widehat{q}(j\omega) d\omega \geq 0 \\
\Leftrightarrow &|\delta| \leq 1.
\end{aligned}$$

Using this multiplier in Theorem 3.1, the inequality (3.12) gives

$$G_{qp}(j\omega)^* G_{qp}(j\omega) - I \prec 0 \quad \forall\, \omega \in \overline{\mathbb{R}},$$

that is $\|G_{qp}\|_\infty < 1$, which is actually a version of the small-gain theorem. Nevertheless, this choice may be too restrictive since the set $\mathbf{\Pi}$ (3.18) holds true for a set containing any Δ being an $n_q \times n_q$ LTI uncertainty whose $\mathcal{L}_2$-gain is less than one, which could be a very restrictive condition in some cases. Indeed, we need to look for the largest possible set of multipliers characterizing the corresponding set $\mathbf{\Delta}$ to get an accurate (non conservative) result. In order to introduce some "degrees of freedom", and thus enlarging the multiplier set $\mathbf{\Pi}$, it is more convenient to employ frequency dependent multipliers.

To do so, let us consider an invertible complex matrix function $T(j\omega) : \mathbb{C} \to \mathbb{C}^{n_q \times n_q}$. Since δ is scalar, it is possible to commute δ and T, that is $T\delta = \delta T$, hence $\delta = T^{-1}\delta T$ as it is shown in Figure 3.4. Note that, with Δ a $n_q \times n_q$ matrix, in general $T\Delta \neq \Delta T$. Then, having that $|\delta| \leq 1$, and by defining $\tilde{p} = Tp$ and $\tilde{q} = Tq$ we have that

$$\int_{-\infty}^{\infty} \widehat{p}(j\omega)^* T(j\omega)^* T(j\omega) \widehat{p}(j\omega) d\omega = \int_{-\infty}^{\infty} \widehat{\tilde{p}}(j\omega)^* \widehat{\tilde{p}}(j\omega) d\omega$$

$$\leq \int_{-\infty}^{\infty} \widehat{\tilde{q}}(j\omega)^* \widehat{\tilde{q}}(j\omega) d\omega = \int_{-\infty}^{\infty} \widehat{q}(j\omega)^* T(j\omega)^* T(j\omega) \widehat{q}(j\omega) d\omega$$

which is rewritten as

$$\int_{-\infty}^{\infty} \begin{bmatrix} \widehat{q}(j\omega) \\ \widehat{p}(j\omega) \end{bmatrix}^* \begin{bmatrix} T(j\omega)^* T(j\omega) & 0 \\ 0 & -T(j\omega)^* T(j\omega) \end{bmatrix} \begin{bmatrix} \widehat{q}(j\omega) \\ \widehat{p}(j\omega) \end{bmatrix} d\omega \geq 0$$

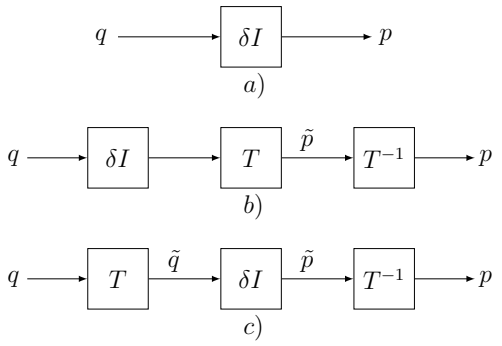

FIGURE 3.4: Equivalent representation of δI_{n_q}

For the set of invertible complex matrices $T(j\omega)$, the product $T(j\omega)^*T(j\omega)$ generates the set of hermitian and positive-definite matrices $X_D(j\omega)$, obtaining

$$\begin{bmatrix}\widehat{q}(j\omega)\\ \widehat{p}(j\omega)\end{bmatrix}^* \begin{bmatrix}X_D(j\omega) & 0\\ 0 & -X_D(j\omega)\end{bmatrix} \begin{bmatrix}\widehat{q}(j\omega)\\ \widehat{p}(j\omega)\end{bmatrix} d\omega \geq 0 \tag{3.19}$$

which satisfies IQC (3.10) for the considered set of parametric uncertainties. We can observe that αI_{n_q} is a particular case of $X_D(j\omega)$, thus Π of (3.19) allows to construct a more general set.

It is important to note that the set of multipliers used in (3.19) holds true when $\delta \in \mathbb{C}$. It may then be interesting to use the fact that δ is real to enhance the class of multipliers. Considering the complex conjugate $\overline{\delta}$ of δ, we have for a real δ that $\overline{\delta} = \delta$, which implies

$$\widehat{p}(j\omega)^*\widehat{q}(j\omega) = \widehat{q}(j\omega)^*\overline{\delta}\widehat{q}(j\omega) = \widehat{q}(j\omega)^*\delta\widehat{q}(j\omega) = \widehat{q}(j\omega)^*\widehat{p}(j\omega) \tag{3.20}$$

and, therefore,

$$\begin{bmatrix}\widehat{q}(j\omega)\\ \widehat{p}(j\omega)\end{bmatrix}^* \begin{bmatrix}0 & I_{nq}\\ -I_{nq} & 0\end{bmatrix} \begin{bmatrix}\widehat{q}(j\omega)\\ \widehat{p}(j\omega)\end{bmatrix} = 0$$

We can also introduce frequency domain operators by replacing I_{nq} and $-I_{nq}$ by a skew-hermitian matrix operator $X_G(j\omega) = -X_G^*(j\omega)$ and its hermitian conjugate respectively, obtaining

$$\begin{aligned}
&\begin{bmatrix}\widehat{q}(j\omega)\\ \widehat{p}(j\omega)\end{bmatrix}^* \begin{bmatrix}0 & X_G(j\omega)\\ X_G(j\omega)^* & 0\end{bmatrix} \begin{bmatrix}\widehat{q}(j\omega)\\ \widehat{p}(j\omega)\end{bmatrix}\\
&= \widehat{p}(j\omega)^*X_G(j\omega)^*\widehat{q}(j\omega) + \widehat{q}(j\omega)^*X_G(j\omega)\widehat{p}(j\omega)\\
&= \widehat{q}(j\omega)^*\overline{\delta}X_G(j\omega)^*\widehat{q}(j\omega) + \widehat{q}(j\omega)^*X_G(j\omega)\delta\widehat{q}(j\omega)\\
&= \delta\widehat{q}(j\omega)^*(X_G(j\omega)^* + X_G(j\omega))\widehat{q}(j\omega)\\
&= 0,
\end{aligned} \tag{3.21}$$

since $X_G(j\omega) = -X_G(j\omega)^*$. Finally, adding (3.19) and (3.21), we obtain the inequality

$$\int_{\infty}^{\infty} \begin{bmatrix}\widehat{q}(j\omega)\\ \widehat{p}(j\omega)\end{bmatrix}^* \begin{bmatrix}X_D(j\omega) & X_G(j\omega)\\ X_G(j\omega)^* & -X_D(j\omega)\end{bmatrix} \begin{bmatrix}\widehat{q}(j\omega)\\ \widehat{p}(j\omega)\end{bmatrix} d\omega \geq 0$$

which defines the following set of multipliers:

$$\boldsymbol{\Pi_\theta} = \left\{ \Pi \;\middle|\; \begin{array}{l} \exists\, X_D(j\omega) \;/\; X_D(j\omega) = X_D(j\omega)^* \succ 0,\\ \exists\, X_G(j\omega) \;/\; X_G(j\omega) = -X_G(j\omega)^*,\\ \Pi(j\omega) = \begin{bmatrix}X_D(j\omega) & X_G(j\omega)\\ X_G(j\omega)^* & -X_D(j\omega)\end{bmatrix} \end{array} \right\}. \tag{3.22}$$

This is a valid set of multipliers for any set $\boldsymbol{\Delta}$ containing a repeated real parametric uncertainty bounded by one in norm. Actually, this set of multipliers is not conservative for one repeated parametric uncertainty [MIF00]. The introduction of the previous example allows us to observe how it is possible to derive multipliers through analysis in the frequency domain, by exploiting the main features of the uncertainty. In Table 3.1, we present different sets of multipliers used for the uncertainties of the sets (3.3) and (3.4).

Remark: In the case of nonlinearities, it is often possible to construct multipliers that capture their main properties. However, it is less intuitive to define generic

Uncertainty Δ	Multiplier $\Pi(j\omega)$
TI parametric $\Delta = \delta I_{n_q},\ \delta \in \mathbb{R},\ \lvert\delta\rvert \leq 1$	$\begin{bmatrix} X_D(j\omega) & X_G(j\omega) \\ X_G(j\omega)^* & -X_D(j\omega) \end{bmatrix}$, with $\begin{cases} X_D(j\omega) = X_D(j\omega)^* \succ 0 \\ X_G(j\omega) = -X_G(j\omega)^* \end{cases}$
TI dynamic $\Delta = \Delta_{TI},\ \lVert\Delta\rVert_\infty \leq 1$	$\begin{bmatrix} x_D(j\omega) I_{n_q} & 0 \\ 0 & -x_D(j\omega) I_{n_p} \end{bmatrix}$, with $x_D(j\omega) \succ 0$
TV parametric $\Delta = \delta(t) I_{n_q},\ \lvert\delta(t)\rvert \leq 1$	$\begin{bmatrix} X_D & X_G \\ X_G^T & -X_D \end{bmatrix}$, with $\begin{cases} X_D = X_D^T \succ 0 \\ X_G = -X_G^T \end{cases}$
Unstructured $\Delta = \Delta_{TV},\ \lVert\Delta\rVert_{\mathcal{L}_2} \leq 1$	$\begin{bmatrix} x_D I_{n_q} & 0 \\ 0 & -x_D I_{n_p} \end{bmatrix}$, with $x_D > 0$

TABLE 3.1: Classes of multipliers

sets of multipliers $\mathbf{\Pi}$ since each type of nonlinearity demands a quite specific set. For some of them, as well as for some particular time-invariant and time-varying uncertainties, there exist available catalogs, for instance, in [MR97, VSK16].

The reader familiarized with the μ-analysis framework, may find similitude with respect to the construction of multipliers and the computation of upper bounds on the structured singular value μ. In fact, the described approach employs the same arguments to derive the operators X_D and X_G as the ones used to determine the D and G scalings, respectively [FTD91].

3.4.4 Finite dimensional conditions

Despite the importance of Theorem 3.1 and Theorem 3.2 to test robust stability and robust performance, as they were presented, testing conditions (3.12) and (3.13) is an infinite dimensional optimization problem. In fact, the set of multipliers $\mathbf{\Pi}$ that satisfies IQC (3.10) belongs to a functional space of infinite dimension. In addition, conditions (3.12) and (3.13) must be satisfied for all $\omega \in \mathbb{R}$, that is, we need to satisfy an infinite number of constraints. To face this problem, two possible approaches can be exploited to establish finite dimensional conditions in the form of convex optimization problems under LMI constraints.

State-space solution. The state-space resolution is the approach proposed by Megretski and Rantzer in [MR97]. To solve the problem, we need first to constraint the chosen set of multipliers $\mathbf{\Pi}$ to a finite set of complex and proper rational functions, i.e. $\mathbf{\Pi} \in \mathcal{RL}_\infty$. In this memoir, we consider sets of multipliers that can be parameterized as $\mathbf{\Pi} = \{\Pi | \exists M \in \boldsymbol{M}, \Pi = \Psi M \Psi\}$, with $\boldsymbol{M} \in \mathbb{S}^\bullet$ being a set of real symmetric matrices and $\Psi \in \mathcal{RH}_\infty^{\bullet \times n_p}$ some fixed tall transfer function matrix, usually called basis.

To get a finite dimensional set, we consider the basis Ψ proposed in [SF06] that constraints Ψ to a set of proper transfer functions of order v. To construct such a basis, first, we set the denominator of Ψ as the scalar function $d(s) = s^v + d_{v-1}s^{v-1} + ... + d_0$ with roots in the open left-half complex plane $\mathbb{C}^-$. Then $\Psi(j\omega)$ is represented by

$$\Psi(j\omega) = \frac{N(j\omega)}{d(j\omega)}$$

Let us then fix a basis for N defined by the vector function $B : \mathbb{C} \to \mathbb{C}^{v+1}$ written as

$$B(s) = \begin{bmatrix} 1 \\ s \\ \vdots \\ s^v \end{bmatrix}$$

Finally, we obtain the basis $\Psi(j\omega)$ defined as

$$\Psi(j\omega) = \frac{B(j\omega)}{d(j\omega)} \otimes I_{n_q} \tag{3.23}$$

where $\otimes$ defines the Kronecker product.

Using the introduced parameterization, and considering $H = \Psi \begin{bmatrix} G \\ I \end{bmatrix}$, we can exploit the Kalman-Yakubovich-Popov (KYP) Lemma to transform the frequency domain inequalities (3.12) and (3.15) into a single LMI condition involving state-space matrices that satisfy (3.12) and (3.15) for all $\omega \in \overline{\mathbb{R}}$, here we present a version adapted from [Ran96].

Lemma 3.1 (Kalman-Yakubovich-Popov). *Let be $H \in \mathcal{RL}_\infty^{\bullet\times\bullet}$ having the minimal state-space realization (A,B,C,D) with $A \in \mathbb{R}^{n_h \times n_h}$, and let $M \in \mathbb{S}^\bullet$. Then, the following two statements are equivalent*

1. $H(j\omega)^* M H(j\omega) \prec 0 \; \forall \omega \in \overline{\mathbb{R}}$.
2. *There exists a matrix $P \in \mathbb{S}^{n_h \times n_h}$ such that*

$$\begin{bmatrix} I & 0 \\ A & B \\ C & D \end{bmatrix}^T \begin{bmatrix} 0 & P & 0 \\ P & 0 & 0 \\ 0 & 0 & M \end{bmatrix} \begin{bmatrix} I & 0 \\ A & B \\ C & D \end{bmatrix} \prec 0. \tag{3.24}$$

Therefore, to apply KYP lemma, it is not enough to find a set of multipliers that satisfies IQC (3.10), but it is necessary to look for multipliers that admits a suitable parameterization of Π, which is not always trivial. Considering the previous results, let us then state the following corollary concerning stability analysis.

Corollary 3.1. *Let G_{qp} be a stable LTI system, let $\mathbf{\Delta}$ be a set of bounded and causal operators, let $(G_{qp}, \mathbf{\Delta})$ be defined by (3.9). Let $\boldsymbol{M} \subset \mathbb{S}^\bullet$ and let $\mathbf{\Pi} = \{\Pi | \forall \Delta \in \mathbf{\Delta} \; \Delta \in IQC(\Pi) \exists M \in \boldsymbol{M}, \Pi = \Psi M \Psi\}$ with $\Psi \in \mathcal{RH}_\infty$, and let $\Psi \begin{bmatrix} G_{qp} \\ I \end{bmatrix}$ have the minimal state-space realization* $\begin{bmatrix} A & B \\ C & D \end{bmatrix}$
Assume that

1. *for all $\tau \in [0,1]$, for all $\Delta \in \mathbf{\Delta}$, the interconnection $(G_{qp}, \tau\Delta)$ is well-posed;*
2. *for all $\tau \in [0,1]$, for all $\Delta \in \mathbf{\Delta}$ and for all $\Pi \in \mathbf{\Pi}$, $\tau\Delta \in IQC(\Pi)$;*

Then, the interconnection $(G_{qp}, \mathbf{\Delta})$ is robustly stable if there exists $M \in \boldsymbol{M}$, $P \in \mathbb{S}^\bullet$ and $\epsilon > 0$ satisfying

$$\begin{bmatrix} I & 0 \\ A & B \\ C & D \end{bmatrix}^T \begin{bmatrix} 0 & P & 0 \\ P & 0 & 0 \\ 0 & 0 & M \end{bmatrix} \begin{bmatrix} I & 0 \\ A & B \\ C & D \end{bmatrix} \preceq -\epsilon I \tag{3.25}$$

Next, let us state the following corollary for a state-space solution of the IQC robust performance theorem, here introduced for the case of robust $\mathcal{L}_2$-gain performance.

Corollary 3.2. *Let G be a stable LTI system, let $\mathbf{\Delta}$ be a set of bounded and causal operators, and let $\mathbf{\Delta} \star G$ be defined by (3.6), let $\mathbf{\Pi} = \{\Pi | \forall \Delta \in \mathbf{\Delta}\ \Delta \in IQC(\Pi) \exists M \in \mathbf{M}, \Pi = \Psi M \Psi\}$ with $\Psi \in \mathcal{RH}_\infty$, let*

$$M^{perf} = \begin{bmatrix} I & 0 \\ 0 & -\gamma^2 I \end{bmatrix},$$

and let

$$\begin{bmatrix} \Psi & 0 \\ 0 & I \end{bmatrix} \left[\begin{array}{cc} G_{qp} & G_{qw} \\ I & 0 \\ \hline G_{zp} & G_{zw} \\ 0 & I \end{array}\right] \sim \left[\begin{array}{c|cc} A & B_1 & B_2 \\ \hline C_1 & D_{11} & D_{12} \\ C_2 & D_{21} & D_{22} \end{array}\right].$$

Assume that

1. *for all $\tau \in [0,1]$, for all $\Delta \in \mathbf{\Delta}$, $\Delta \star G$ is well-posed;*
2. *for all $\tau \in [0,1]$, for all $\Delta \in \mathbf{\Delta}$ and for all $\Pi \in \mathbf{\Pi}$, $\tau\Delta \in IQC(\Pi)$;*

Then, $\mathbf{\Delta} \star G$ is robustly stable and guarantees robust performance defined by

$$\Psi^{perf} * M^{perf} \Psi^{perf}$$

if there exist $M \in \mathbf{M}$, $P \in \mathbb{S}^\bullet$ and $\epsilon > 0$ satisfying

$$\begin{bmatrix} I & 0 & 0 \\ A & B_1 & B_2 \\ C_1 & D_{11} & D_{12} \\ C_2 & D_{21} & D_{22} \end{bmatrix}^T \begin{bmatrix} 0 & P & 0 & 0 \\ P & 0 & 0 & 0 \\ 0 & 0 & M & 0 \\ 0 & 0 & 0 & M^{perf} \end{bmatrix} \begin{bmatrix} I & 0 & 0 \\ A & B_1 & B_2 \\ C_1 & D_{11} & D_{12} \\ C_2 & D_{21} & D_{22} \end{bmatrix} \preceq -\epsilon I \tag{3.26}$$

Corollary 3.1 and Corollary 3.2 respectively establish robust stability and robust performance tests in the form of convex optimization problems under LMI constraints, which is a class of optimization problems for which efficient solvers are available.

It is important to note that the parameterization implies to consider a subset of the original set of multipliers $\mathbf{\Pi}$. Then, the parameterized set of multipliers may possibly introduce some conservatism to the analysis results. To cope with this issue, we can increase the order v of the fixed basis Ψ to expand the set of multipliers, which can reduce the conservatism, with an additional computational cost.

Frequency domain solution One can also consider, with some caution, a direct resolution in the frequency domain. This approach is inspired from the classical results of the μ-analysis framework [FTD91], where the indicator μ was computed in the frequency domain by considering frequency gridding. First, it is necessary to define a finite set of frequencies to be tested $\mathbf{\Omega} = \{\omega_1, ..., \omega_i, ..., \omega_n\}$.

Once defined $\mathbf{\Omega}$, we test Condition (3.12) or Condition (3.13) for the finite number of frequencies contained in the set $\mathbf{\Omega}$. Indeed, for a given frequency $\omega \in \Omega$, conditions (3.12) and (3.13) become complex LMI constraints that can be decomposed into real LMI conditions and solved efficiently.

We can note that this approach implies a potential risk of missing some critical frequency. However, there exist methods focused on mitigating that risk. The objective of this work is not to develop advanced methods to refine the choice of proper frequency sets. The reader interested in such a topic can see [LTVD00, FB98, FB01].

The advantage with respect to the state-space resolution is that it is not necessary to restrict the multipliers to be proper rational functions. Then, since the space of considered multipliers is larger, the frequency domain resolution can potentially leads to less conservative results. However, such a direct frequency domain gridding solution is limited, in general, to the case of time-invariant uncertainties, restricting the classes of systems that can be analyzed.

3.5 Uncertain Harmonically Time-Varying Systems

In chapter 2, we introduced the general operation of MEMS gyroscopes. We discussed that the link between the internal modulated signals interacting with the resonator and the low-frequency sensor output is the synchronous demodulation process. If we take it into account, this makes appear time-varying sine and cosine parameters in the model. A particularly critical case in MEMS gyroscopes is the implementation of control strategies that introduce synchronous demodulation in the feedback loop, which compromises the system stability, see, for instance, the stability analysis of the the phasor-based control in chapter 6. This type of systems can be modeled as the feedback interconnection of a Linear Time-Invariant system and some harmonic time-varying oscillations, referred to as Linear Harmonically Time-Varying Systems (LHTV). In addition, we mentioned that MEMS sensors are systems that naturally tend to be uncertain. Then, we need a framework that is compatible with both harmonic oscillations and uncertainties. A first possibility may be to model the harmonic oscillations as belonging to the set of arbitrarily fast time-varying parameters $\boldsymbol{\Delta_{TV}}$ introduced in (3.4). However, as it will be further discussed in this chapter, this might lead to very pessimistic analysis results. We then must look for analysis tools that are more adapted to Uncertain Harmonically Time-Varying Systems.

LHTV systems have been historically investigated as part of the larger class of systems called Linear Periodically Time-Varying Systems (LPTV) [BC09, Far94, LR03, BLA12, FF17, HO10]. The most common tool for the stability analysis of LPTV systems uses a combination of the Floquet theory and the Lyapunov stability, which allows to transform the problem into a time-invariant form, thus to derive a time-invariant stability condition [Far94, BC88, ZHA02]. However, Floquet theory is limited for the robustness analysis of uncertain LPTV systems. Actually, it does not allow to perform the transformation to time-invariant form of the LPTV system and to take into account the effect of the uncertainties after the transformation.

Different approaches addressed the case of uncertain LPTV systems. Some methods employ the ν-gap metric [CG98, CG00], which considers only a particular unstructured uncertainty. Then, it can be a restrictive representation of uncertain LPTV systems. Other approaches consist in first sampling the LPTV system to transform it into a discrete-time system, then applying the Lifting Technique [BP92] to obtain an equivalent uncertain LTI system under an LFT representation. Using this representation, we can then apply classical robustness analysis tools for uncertain LTI systems, such as the μ-analysis [KBP06]. The main drawback of lifting-based approach is that the size of the obtained uncertain block increases with the number of

samples per period employed to discretize the LPTV system, which can lead to solve considerably high-dimensional problems.

The Integral Quadratic Constraints (IQC) approach offers very attractive tools for efficient robustness analysis of a large class of uncertain, time-varying and nonlinear systems. This approach has been already applied to the analysis of uncertain LPTV systems. In [JKM99], the authors propose two IQC-based approaches for the analysis of uncertain LPTV systems. The first technique employs a Fourier series expansion of the periodic time-varying state-space matrices, the system is then represented as the feedback interconnection of an LTI system and a block containing the uncertainties and the harmonics of the Fourier decomposition. However, as the authors concluded, the lack of good IQC characterizations of harmonic oscillations implies conservative results. The second proposed method represents the system as the interconnection of the original LPTV system and the purely uncertain block. The system is then analyzed deriving periodic IQC conditions to test robust stability, relying on the fact that the homotopy argument used to proof stability of an LTI nominal system, holds also for a nominal LPTV system. However, the solution for the obtained stability condition is an infinite-dimensional problem. Then, in [KMJ01], the authors proposed a cutting-plane algorithm to obtain a finite-dimensional problem.

A different IQC approach for uncertain LPTV systems is proposed in the recent work of [OP19]. The proposed method relies in the dissipative interpretation of the IQC framework [Sei14]. More specifically, it considers the interconnection of an LPTV system and an uncertain block. Then, it combines a periodic version of the Bounded Real Lemma with an IQC characterization of the system uncertainties to finally derive a time-domain condition to test the worst-case $\mathcal{L}_2$ performance of the uncertain LPTV system.

LHTV systems, as a particular case of the LPTV systems, present some particular characteristics that can be exploited to decrease the conservatism of the analysis results. From signal processing framework, we know that harmonic functions have a straightforward interpretation in the frequency domain. This has been already observed by Megretski and Rantzer, who proposed in [MR97] a frequency domain multiplier that allows to analyze the stability of the feedback interconnection of an LTI system with a repeated cosine gain. However, to our knowledge, the formal proof of the construction of this IQC multiplier is not available in the literature, which potentially can limit the motivation to employ it in analysis methods.

Furthermore, neither frequency-domain nor state-space solutions have been proposed for this harmonic multiplier, remaining unexploited for tractable robustness analysis tests. In this section, several contributions are made to extend the current available tools for the robustness analysis of LHTV systems.

- In subsection 3.4.3, we present the arguments that allow to systematically construct the multiplier for a single repeated cosine gain, introduced in [MR97]. Then, the sets of harmonic multipliers for a single repeated cosine-gain are enlarged by introducing off-diagonal functions (G-scalings) in the multiplier.

- In subsection 3.5.3 and subsection 3.5.4, we respectively propose new sets of general harmonic multipliers: multipliers for coupled harmonic parameters (including synchronous demodulation) and multipliers for full-block harmonic operators (including time-varying rotation matrices).

- We propose state-space analysis conditions, this by introducing a set of factorizable harmonic multipliers.

- We propose a frequency-domain analysis condition using the concept of frequency-gridding, which is rare in the case of time-varying systems.

3.5.1 System description

Let us consider Uncertain Harmonically Time-Varying Systems that can be described as uncertain feedback interconnections. For the sake of clarity, along this section we exclusively focus on Harmonically Time-varying systems with uncertain phase. Given that the introduced approaches are based on the IQC framework, the inclusion of other uncertainties can be easily done, as shown in subsection 3.4.2.

Let us first define the set $\boldsymbol{\Delta_H^{\omega_0}}$ of harmonically time-varying operators.

Given $\omega_0 > 0$,

$$\boldsymbol{\Delta_H^{\omega_0}} = \left\{ \Delta_H^{\omega_0} : \mathcal{L}_{2e}^{k_\theta} \to \mathcal{L}_{2e}^{k_\theta} \;\middle|\; \exists\, \phi \in [0, 2\pi[, \quad \forall t, \quad \Delta_H^{\omega_0}(q)(t) = \theta^{\omega_0}(t) q(t) \right\} \tag{3.27}$$

where θ^{ω_0} represents the harmonic operator to be investigated. Here, we analyze three cases of harmonic operators.

1. Single repeated harmonic parameter

$$\theta^{\omega_0}(t) = \cos(\omega_0 t + \phi) I_{n_q} \tag{3.28}$$

   where ϕ is an uncertain phase.

2. Coupled harmonic parameters

$$\theta^{\omega_0}(t) = \begin{bmatrix} \cos(\omega_0 t + \phi) I_{n_q} & 0 \\ 0 & \cos(\omega_0 t + \phi + \psi) I_{n_q} \end{bmatrix} \tag{3.29}$$

   where ψ is a known phase-shift between two harmonic functions, while ϕ is an uncertain phase.

3. Full-block harmonic operator

$$\theta^{\omega_0}(t) = \begin{bmatrix} \cos(\omega_0 t + \phi) I_{n_q} & \cos(\omega_0 t + \phi + \psi_1) I_{n_q} \\ \cos(\omega_0 t + \phi + \psi_2) I_{n_q} & \cos(\omega_0 t + \phi + \psi_3) I_{n_q} \end{bmatrix} \tag{3.30}$$

   where ψ_1, ψ_2 and ψ_3 are known phase-shifts between harmonic functions, and ϕ an uncertain phase.

These three cases are addressed since they are representative of commonly found closed-loop control systems. Case 1 represents systems containing repeated scalar harmonic functions that are found, for instance, in the fields of electrical engineering, electronics and mechanical vibrations, see the example in section 3.5.2. Case 2 is found in systems employing synchronous demodulation, such as synchronous generators control or in microelectronics [ACSKS19]. Case 3 represents systems whose equations contain rotation matrices, used in electronics, flight dynamics, mobile robotics, etc. (see the phasor-based analysis in chapter 6).

Using the previously defined sets, we can give a formal definition of an Uncertain Harmonically Time-Varying System.

Definition 3.10 (Uncertain Harmonically Time-Varying System). *Let $G_{qp} \in \mathcal{RH}_\infty^{(n_p)\times(n_q)}$ be a stable LTI system, and let $\boldsymbol{\Delta_H^{\omega_0}}$ be the set defined by (3.27). Then, an Uncertain Harmonically Time-Varying System is defined as:*

$$\exists\, \Delta_H^{\omega_0} \in \boldsymbol{\Delta_H^{\omega_0}},\ \ (G_{qp}, \boldsymbol{\Delta_H^{\omega_0}}) = \left\{ \begin{array}{ll} q & = G_{qp}(s)p + q_{in} \\ p & = \Delta_H^{\omega_0}(q) + p_{in}. \end{array} \right. \tag{3.31}$$

In following subsections, we introduce IQC frequency domain multipliers, as well as resolution methods, for the aforementioned cases of Uncertain Harmonically Time-varying systems.

3.5.2 IQC multiplier for one repeated harmonic parameter

Let us begin from the simplest harmonically time-varying system, containing a single repeated harmonic parameter, given by the set (3.27) with $\theta^{\omega_0}(t)$ defined by (3.28).

Before looking for a suitable set of multipliers satisfying an IQC for harmonic parameters, let us first observe uncertain sets for which multipliers have been already obtained. We can consider the set of repeated uncertain parameters defined as $\boldsymbol{\Delta_{TI}} = \{\delta I_{n_q} | \delta \in \mathbb{R},\ |\delta| \leq 1\}$, and the set of arbitrarily fast time-varying parameters $\boldsymbol{\Delta_{TV}} = \{\delta I_{n_q} | \delta : \mathbb{R} \to \mathbb{R}, |\delta(t)| \leq 1\}$.

A first obvious observation is that $\boldsymbol{\Delta_\theta^{\omega_0}} \subset \boldsymbol{\Delta_{TV}}$ since a harmonic parameter is a particular function of time that is bounded by 1. In addition, note that if we set the oscillation frequency ω_0 to zero, then $\theta^{\omega_0}(t) = \theta^0(t) = \cos(\phi)$ with $\phi \in [0, 2\pi[$, that is an uncertain parameter bounded by one. Hence, $\boldsymbol{\Delta_{TI}} = \boldsymbol{\Delta_\theta^0} \subset \boldsymbol{\Delta_{TV}}$, see the left part of Figure 3.5.

Therefore, the set of multipliers $\boldsymbol{\Pi_{TV}}$, defined as

$$\boldsymbol{\Pi_{TV}} = \left\{ \Pi_{TV} \;\middle|\; \begin{array}{l} \exists\, X_D \ /\ X_D = X_D^T \succ 0, \\ \exists\, X_G \ /\ X_G = -X_G^T, \\ \Pi_{TV} = \left[\begin{array}{cc} X_D & X_G \\ X_G^T & -X_D \end{array} \right] \end{array} \right\} \tag{3.32}$$

satisfies $\delta \in IQC(\boldsymbol{\Pi_{TV}})\ \ \forall \delta \in \boldsymbol{\Delta_{TV}},\ \ \forall \Pi_{TV} \in \boldsymbol{\Pi_{TV}}$.

This set also satisfies $\theta^{\omega_0} \in IQC(\Pi_{TV})\ \ \forall \theta^{\omega_0} \in \boldsymbol{\Delta_H^{\omega_0}},\ \ \forall \Pi_{TV} \in \boldsymbol{\Pi_{TV}}$ with θ^{ω_0} given by (3.28). This set of constant (frequency independent) multipliers can then be used to test robust stability of LHTV systems with a repeated harmonic parameter. However, as mentioned earlier, this choice may be too restrictive since harmonic parameters are not arbitrarily fast but well-defined functions of time.

Now, there exists the set $\boldsymbol{\Pi_{TI}}$:

$$\boldsymbol{\Pi_{TI}} = \left\{ \Pi_{TI}(j\omega) \;\middle|\; \begin{array}{l} \exists\, X_D(j\omega) \ /\ X_D(j\omega) = X_D(j\omega)^* \succ 0, \\ \exists\, X_G(j\omega) \ /\ X_G(j\omega) = -X_G(j\omega)^*, \\ \Pi_{TI}(j\omega) = \left[\begin{array}{cc} X_D(j\omega) & X_G(j\omega) \\ X_G(j\omega)^* & -X_D(j\omega) \end{array} \right] \end{array} \right\}. \tag{3.33}$$

From the μ-analysis literature, we know that such a multiplier (in terms of $D-G$ scaling) is non conservative for the case of one repeated parametric uncertainty [MIF00].

In contrast to the set $\mathbf{\Pi_{TV}}$, $\mathbf{\Pi_{TI}}$ is a frequency dependent set, then a larger set including $\mathbf{\Pi_{TV}}$, i.e. $\mathbf{\Pi_{TV}} \in \mathbf{\Pi_{TI}}$. In the case of harmonic parameters, however, the set $\mathbf{\Pi_{TI}}$ can be only used for the particular case $\omega_0 = 0$. In this memoir, we propose another generalization of the sets $\mathbf{\Pi_{TV}}$ and $\mathbf{\Pi_{TI}}$: the set of frequency dependent multipliers $\mathbf{\Pi_{\theta}^{\omega_0}}$ which satisfies IQC involving harmonic parameters for any ω_0. Moreover, since this set is frequency dependent, as in the case of $\mathbf{\Pi_{TI}}$, the proposed multiplier set allows a significant conservatism reduction of the stability analysis when applying Theorem 3.1.

We can make a similar observation as the one of the inclusion of sets of uncertainties. Note that the set of multipliers for time-varying parameters $\mathbf{\Pi_{TV}}$ is included in the set for parametric uncertainties $\mathbf{\Pi_{TI}}(j\omega)$, as represented in the right side of Figure 3.5. Hence, considering this "inverse hierarchy" of the inclusion of multiplier sets with respect to the inclusion of uncertainties, the question becomes: is it possible to find a set of frequency dependent multipliers that satisfy an IQC for a repeated harmonically time-varying parameter and which is included in $\mathbf{\Pi_{TI}}$ but larger than $\mathbf{\Pi_{TV}}$? If it is the case, this set would be then a suitable candidate to derive accurate analysis conditions.

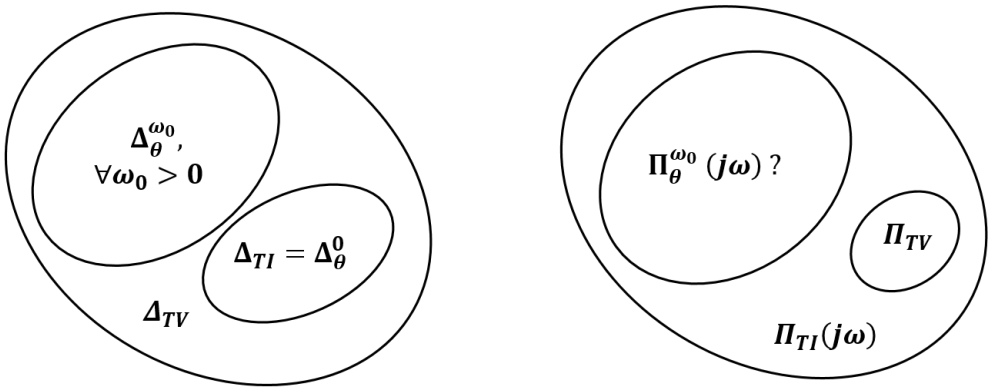

FIGURE 3.5: Schematic representation of sets of uncertainties and multipliers

As we observed in subsection 3.4.3, the construction of a non conservative set of multipliers is possible by exploiting as much information as possible about the structure and the nature of the uncertainty under consideration. For instance, the set $\mathbf{\Pi_{TI}}$ is obtained by using the fact that δ_{TI} is scalar, bounded and real (then constant in both time and frequency domain), which allows to employ commutation properties.

Concerning a single harmonic parameter, we know that it is bounded and scalar, but it is a function of the time. We will see that this last characteristic does not allow to use a simple commutation property. However, there exists another property that, combined with commutation, allows the construction of frequency dependent multipliers.

Taking the complex exponential form $\cos(\omega_0 t) = \frac{1}{2}(e^{j\omega_0 t} + e^{-j\omega_0 t})$, we will find $e^{j\omega_0 t} I$ instead of δI. This leads us to the modulation property, which is given by the product of a signal, in time domain, with the modulation operator $e^{j\omega_0 t}$. Let us then state the following Lemma regarding modulation of signals and systems.

Lemma 3.2 (Modulation). *Let $T(s)$ be a stable LTI system, with input signal $q \in \mathcal{L}_2^{\bullet}$ and output signal given, in the frequency domain, by $\widehat{p}(j\omega) = T(j\omega)\widehat{q}(j\omega)$. Then, application*

of the modulation operator $e^{j\omega_0 t}$ at the output, gives the signal $\tilde{p}(t) = e^{j\omega_0 t}T(q(\cdot))(t)$ in time-domain, and produces the modulated frequency response

$$\widehat{\tilde{p}}(j\omega) = T(j(\omega-\omega_0))\widehat{q}(j(\omega-\omega_0)). \tag{3.34}$$

Proof. The frequency domain output signal $\widehat{p}(j\omega)$ is obtained by applying the Fourier transform to $T(q(\cdot))(t)$, i.e. $\widehat{p}(j\omega) = \mathcal{F}\{T(q)(\cdot)\}(j\omega)$, which gives $T(j\omega)\widehat{q}(j\omega)$. Then, for any function $f(t)$, the modulation property of the Fourier transform states that $\mathcal{F}\{e^{j\omega_0\cdot}f(\cdot)\}(j\omega) = \mathcal{F}\{f(\cdot)\}(j(\omega-\omega_0))$, that is, the Fourier transform of the function f evaluated in $\omega-\omega_0$. Applying this property to $\tilde{p}(t)$, we obtain the result of (3.34) □

Exploiting this Lemma, we can now state the following Theorem that introduces a new class of multipliers that satisfies the IQC (3.10) for the case of a repeated harmonic time-varying parameter.

Theorem 3.3. *Let be the set $\boldsymbol{\Delta_H^{\omega_0}}$, defined in (3.27) with $\theta^{\omega_0}(t)$ given by (3.28). Then, the IQC (3.10) holds with Π belonging to the set of multipliers*

$$\boldsymbol{\Pi_\theta^{\omega_0}} = \left\{ \Pi \;\middle|\; \begin{array}{c} \exists\, X_D(j\omega) \;/\; X_D(j\omega) = X_D(j\omega)^* \succ 0, \\ \exists\, X_G(j\omega) \;/\; X_G(j\omega) = -X_G(j\omega+j\omega_0)^*, \\ \Pi = \begin{bmatrix} X_{D+}(j\omega)+X_{D-}(j\omega) & X_G(j\omega) \\ X_G(j\omega)^* & -2X_D(j\omega) \end{bmatrix} \\ X_{D+} = X_D(j(\omega+\omega_0)) \\ X_{D-} = X_D(j(\omega-\omega_0)) \end{array} \right\} \tag{3.35}$$

Proof. **First part: $\boldsymbol{X_D(j\omega)}$.** In the time domain, we have θ^{ω_0}, given by (3.28) $p(t) = \frac{1}{2}(e^{j(\omega_0 t+\phi)} + e^{-j(\omega_0 t+\phi)})q(t)$. The equivalent scheme of this is shown on Figure 3.6 and the corresponding equations in time and frequency domains are

$$\begin{array}{rclcrcl} p(t) & = & \frac{1}{2}\left(p_{up}(t)+p_{low}(t)\right) & & \widehat{p}(j\omega) & = & \frac{1}{2}\left(\widehat{p}_{up}(j\omega)+\widehat{p}_{low}(j\omega)\right) \\ \begin{bmatrix} p_{up}(t) \\ p_{low}(t) \end{bmatrix} & = & \begin{bmatrix} e^{j(\omega_0 t+\phi)}q_{up}(t) \\ e^{-j(\omega_0 t+\phi)}q_{low}(t) \end{bmatrix} & & \begin{bmatrix} \widehat{p}_{up}(j\omega) \\ \widehat{p}_{low}(j\omega) \end{bmatrix} & = & \begin{bmatrix} \widehat{q}_{up}(j(\omega-\omega_0))e^{j\phi} \\ \widehat{q}_{low}(j(\omega+\omega_0))e^{-j\phi} \end{bmatrix} \\ \begin{bmatrix} q_{up}(t) \\ q_{low}(t) \end{bmatrix} & = & \begin{bmatrix} q(t) \\ q(t) \end{bmatrix} & & \begin{bmatrix} \widehat{q}_{up}(j\omega) \\ \widehat{q}_{low}(j\omega) \end{bmatrix} & = & \begin{bmatrix} \widehat{q}(j\omega) \\ \widehat{q}(j\omega) \end{bmatrix} \end{array} \tag{3.36}$$

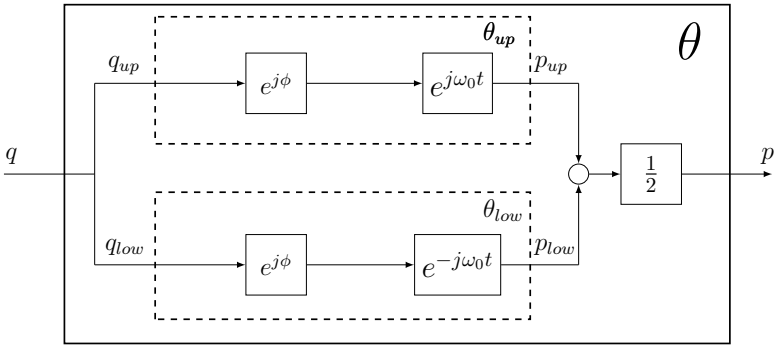

FIGURE 3.6: Representation of the exponential form of $\cos(\omega_0 t+\phi)$

Since the IQCs and the multipliers considered here are defined in the frequency domain, the proof is then developed in this domain. To derive the multiplier, we use a hierarchical approach. We first study the upper branch of the diagram in Figure 3.6, containing the operator θ_{up}, its input signal q_{up} and its output signal p_{up}, as shown in Figure 3.7 a).

We can observe in Figure 3.7 b) that the operator θ_{up} has the same input-output relation than $T^{-1}T\theta_{up}$, with $T(j\omega)$ being any invertible complex matrix function. We define then the signal $\tilde{p}_{up}$ whose frequency response is given by

$$\widehat{\tilde{p}}_{up}(j\omega) = T(j\omega)\widehat{q}_{up}(j(\omega-\omega_0))e^{j\phi}.$$

Note that in this case, because of the modulation operator θ_{up}, a simple commutation between θ_{up} and T does not keep the input-output relations. Hence, in order to perform this commutation, the following must be satisfied

$$\widehat{\tilde{p}}_{up}(j\omega) = \underbrace{\tilde{T}(j\omega)\widehat{q}_{up}(j(\omega-\omega_0))}_{\widehat{\tilde{q}}_{up}(j(\omega-\omega_0))} e^{j\phi}.$$

Then, using modulation/commutation property, we have that $\tilde{T}$ must be

$$\tilde{T}(j\omega) = T(j(\omega+\omega_0)).$$

compensating then the effect of the modulation.

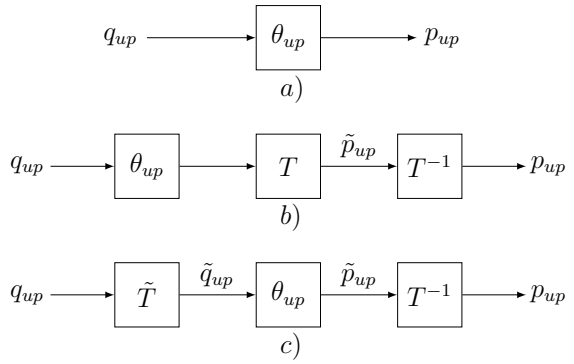

FIGURE 3.7: Equivalent representation of θ_{up}

Now, we have that the operator $\theta_{up}(t)$ is bounded by one, that is $|\theta_{up}(t)| \leq 1$. Using the Parseval's equality, this bound can be expressed in the frequency domain constraint as

$$\int_{-\infty}^{\infty} \widehat{\tilde{p}}_{up}(j\omega)^* \widehat{\tilde{p}}_{up}(j\omega)d\omega \leq \int_{-\infty}^{\infty} \widehat{\tilde{q}}_{up}(j\omega)^* \widehat{\tilde{q}}_{up}(j\omega)d\omega \tag{3.37}$$

Then, using the relations $\widehat{\tilde{q}}_{up} = \tilde{T}\tilde{q}_{up}$ and $\widehat{\tilde{p}}_{up} = T\tilde{p}_{up}$, we obtain

$$\int_{-\infty}^{\infty} \widehat{p}_{up}(j\omega)^* T(j\omega)^* T(j\omega)\widehat{p}_{up}(j\omega)d\omega \leq \int_{-\infty}^{\infty} \widehat{q}_{up}(j\omega)^* T(j(\omega+\omega_0))^* T(j(\omega+\omega_0))\widehat{q}_{up}(j\omega)d\omega \tag{3.38}$$

The product of the two invertible matrices $T(j\omega)^*T(j\omega)$ generates the space of Hermitian and positive definite matrices $T(j\omega)^*T(j\omega) = X_D(j\omega) = X_D(j\omega)^* \succ 0$, leading to

$$\int_{-\infty}^{\infty} \widehat{p}_{up}(j\omega)^* X_D(j\omega)\widehat{p}_{up}(j\omega)d\omega \leq \int_{-\infty}^{\infty} \widehat{q}_{up}(j\omega)^* X_D(j(\omega+\omega_0))\widehat{q}_{up}(j\omega)d\omega \quad (3.39)$$

The same procedure is employed for the lower branch, leading to the inequality

$$\int_{-\infty}^{\infty} \widehat{p}_{low}(j\omega)^* X_D(j\omega)\widehat{p}_{low}(j\omega)d\omega \leq \int_{-\infty}^{\infty} \widehat{q}_{low}(j\omega)^* X_D(j(\omega-\omega_0))\widehat{q}_{low}(j\omega)d\omega \quad (3.40)$$

If we add the inequalities (3.39) and (3.40), we obtain

$$\begin{aligned}&\int_{-\infty}^{\infty} \widehat{p}_{up}(j\omega)^* X_D(j\omega)\widehat{p}_{up}(j\omega) + \widehat{p}_{low}(j\omega)^* X_D(j\omega)\widehat{p}_{low}(j\omega)d\omega \\ &\leq \int_{-\infty}^{\infty} \widehat{q}_{up}(j\omega)^* X_D(j(\omega+\omega_0))\widehat{q}_{up}(j\omega) + \widehat{q}_{low}(j\omega)^* X_D(j(\omega-\omega_0))\widehat{q}_{low}(j\omega)d\omega\end{aligned}$$

Now, by studying the right and left sides of the inequality separately, we can exploit the following arguments:

- $q_{up} = q_{low} = q$.
- Since the function $p^* X_D p$ is convex, we have that $\frac{1}{2}(p_{up} + p_{low})^* X_D(p_{up} + p_{low}) \leq p_{up}^* X_D p_{up} + p_{low}^* X_D p_{low}$.
- $2p = p_{up} + p_{low}$.

Obtaining the inequality

$$2\int_{-\infty}^{\infty} \widehat{p}(j\omega)^* X_D(j\omega)\widehat{p}(j\omega)d\omega \leq \int_{-\infty}^{\infty} \widehat{q}(j\omega)^*[X_D(j(\omega+\omega_0)) + X_D(j(\omega-\omega_0))]\widehat{q}(j\omega)d\omega$$

leading to the frequency domain IQC

$$\int_{-\infty}^{\infty} \begin{bmatrix}\widehat{q}(j\omega)\\ \widehat{p}(j\omega)\end{bmatrix}^* \begin{bmatrix}X_D(j(\omega+\omega_0)) + X_D(j(\omega-\omega_0)) & 0\\ 0 & -2X_D(j\omega)\end{bmatrix} \begin{bmatrix}\widehat{q}(j\omega)\\ \widehat{p}(j\omega)\end{bmatrix} d\omega \geq 0$$

which defines the function $X_D(j\omega)$ of multiplier (3.35).

Second part: $X_G(j\omega)$. We consider the following frequency equality constraint

$$\int_{-\infty}^{\infty} \begin{bmatrix}\widehat{q}(j\omega)\\ \widehat{p}(j\omega)\end{bmatrix}^* \begin{bmatrix}0 & X_G(j\omega)\\ X_G(j\omega)^* & 0\end{bmatrix} \begin{bmatrix}\widehat{q}(j\omega)\\ \widehat{p}(j\omega)\end{bmatrix} d\omega = 0$$

with $X_G(j\omega)$ being a complex-valued matrix function. We aim then to find out the necessary properties of $X_G(j\omega)$ such that equality constraint is satisfied for $\widehat{p}(j\omega) = \frac{1}{2}\left(\widehat{q}(j\omega + j\omega_0)e^{-j\phi} + \widehat{q}(j\omega - j\omega_0)e^{j\phi}\right)$.

Then replacing $\widehat{p}(j\omega)$ by its modulated form, the equality becomes:

$$\begin{aligned}&\int_{-\infty}^{\infty} \widehat{q}(j\omega)^* X_G(j\omega)\widehat{q}((j\omega+\omega_0))e^{-j\phi}d\omega + \int_{-\infty}^{\infty} \widehat{q}(j\omega)^* X_G(j\omega)\widehat{q}(j(\omega-\omega_0))e^{j\phi}d\omega \\ &+ \int_{-\infty}^{\infty} \widehat{q}(j(\omega+\omega_0))^* X_G(j\omega)^*\widehat{q}(j\omega)e^{j\phi}d\omega + \int_{-\infty}^{\infty} \widehat{q}(j(\omega-\omega_0))^* X_G(j\omega)^*\widehat{q}(j\omega)e^{-j\phi}d\omega \\ &= 0\end{aligned}$$

Since the integrals are evaluated from $-\infty$ to ∞, a frequency-shifting does not modify the integrals. We can then perform a change of variable in two of the four integrals, getting

$$\begin{aligned}
&\int_{-\infty}^{\infty} \widehat{q}(j\omega)^* X_G(j\omega)\widehat{q}((j\omega+\omega_0))e^{-j\phi}d\omega \\
&+\int_{-\infty}^{\infty} \widehat{q}(j(\omega+\omega_0))^* X_G(j(\omega+\omega_0))\widehat{q}(j\omega)e^{j\phi}d\omega \\
&+\int_{-\infty}^{\infty} \widehat{q}(j(\omega+\omega_0))^* X_G(j\omega)^*\widehat{q}(j\omega)e^{j\phi}d\omega \\
&+\int_{-\infty}^{\infty} \widehat{q}(j\omega)^* X_G(j(\omega+\omega_0))^*\widehat{q}(j(\omega+\omega_0))e^{-j\phi}d\omega \\
&=0
\end{aligned}$$

Regrouping the obtained terms, we obtain:

$$\int_{-\infty}^{\infty} \begin{bmatrix} \widehat{q}(j\omega) \\ \widehat{q}(j(\omega+\omega_0)) \end{bmatrix}^* \tilde{X}_G(j\omega) \begin{bmatrix} \widehat{q}(j\omega)e^{j\phi} \\ \widehat{q}(j(\omega+\omega_0))e^{-j\phi} \end{bmatrix} d\omega$$

with

$$\tilde{X}_G(j\omega) = \begin{bmatrix} 0 & X_G(j\omega)+X_G(j\omega+j\omega_0)^* \\ X_G(j\omega)^*+X_G(j\omega+j\omega_0) & 0 \end{bmatrix}$$

which is equals to zero, for all $q \in \mathcal{L}_2^{n_q}$, if

$$\forall \omega \in \overline{\mathbb{R}}, \qquad X_G(j\omega) = -X_G(j(\omega+\omega_0))^*$$

□

Please note that $\mathbf{\Pi}_{\boldsymbol{\theta}}^{\boldsymbol{\omega_0}}$ (3.35) can be seen as a generalization of $\mathbf{\Pi}_{\boldsymbol{TI}}$ (3.33) and $\mathbf{\Pi}_{\boldsymbol{TV}}$ (3.33). First, if we set to zero the harmonic frequency ω_0 of a multiplier in the set $\mathbf{\Pi}_{\boldsymbol{\theta}}^{\boldsymbol{\omega_0}}$, we have $X_D(j(\omega+\omega_0)) = X_D(j(\omega-\omega_0)) = X_D(j\omega)$, and condition for $X_G(j\omega)$ becomes $X_G(j\omega) = -X_G(j\omega)^*$, obtaining the multipliers belonging to the set $\mathbf{\Pi}_{\boldsymbol{TI}}$. Similarly, if we consider the case where $X_D(j\omega)$ and $X_G(j\omega)$ are constant matrices for all ω (frequency independent functions) we obtain the multipliers in the set $\mathbf{\Pi}_{\boldsymbol{TV}}$.

The set of multipliers $\mathbf{\Pi}_{\boldsymbol{\theta}}^{\boldsymbol{\omega_0}}$ (3.35) is also a generalization of the harmonic frequency-domain multiplier proposed in [MR97], this by introducing the off-diagonal functions $X_G(j\omega)$.

Having the set of multipliers given by (3.35), we can state an IQC stability conditions for Harmonically Time-Varying Systems.

Theorem 3.4. *Let G_{qp} be a stable LTI system, let $\mathbf{\Delta}_{\boldsymbol{H}}^{\boldsymbol{\omega_0}}$ be the set defined by (3.27), with θ^{ω_0} given by (3.28). Let be the set of multipliers $\mathbf{\Pi}_{\boldsymbol{\theta}}^{\boldsymbol{\omega_0}}$ given by (3.35). Then, the interconnection $(G_{qp}, \mathbf{\Delta}_{\boldsymbol{H}}^{\boldsymbol{\omega_0}})$ is robustly stable if there exists $\Pi \in \mathbf{\Pi}_{\boldsymbol{\theta}}^{\boldsymbol{\omega_0}}$ and $\epsilon > 0$ satisfying, $\forall\ \omega\ \in\ \overline{\mathbb{R}}$,*

$$\begin{bmatrix} G_{qp}(j\omega) \\ I \end{bmatrix}^* \begin{bmatrix} X_D(j(\omega-\omega_0))+X_D(j(\omega+\omega_0)) & X_G(j\omega) \\ X_G(j\omega)^* & -2X_D(j\omega) \end{bmatrix} \begin{bmatrix} G_{qp}(j\omega) \\ I \end{bmatrix} \preceq -\epsilon I \tag{3.41}$$

Proof. Based on Theorem 3.1, well-posedness property is assumed, satisfying the first condition. By construction of multipliers (3.35) in Theorem 3.3, we know that the second condition holds. Then, condition (F.21) is equivalent to condition (3.12) using multipliers (3.35). □

Similar to the theorems of subsection 3.4.1, testing the stability condition of Theorem 3.4 demands to test the feasibility of problem under an infinite number of LMI constraints, which can be transformed into a tractable test using either a state-space or a frequency domain resolution.

First, the introduced state-space resolution demands to find an appropriate parameterization of the form $\Pi = \Psi^* M \Psi$ with $\Psi \in \mathcal{RH}_\infty^{\bullet\times\bullet}$. Such a parameterization comes to restrict the set of multipliers $\mathbf{\Pi}_\theta$ to belong to a set of fixed order rational functions of ω. As we will observe further in this section, the elements $X_D(j\omega)$ of the multiplier (3.35) can be parameterized as rational functions. Nevertheless, please note that $X_G(j\omega)$ is a periodic function of the frequency ($X_G(j\omega) = X_G(j(\omega + 2\omega_0))$), making difficult to find a suitable parameterization of $X_G(j\omega)$ that can be restricted to a set of rational functions. For this reason, we will introduce a state-space resolution for a partial version of the set of Multipliers $\mathbf{\Pi_\theta}$ given by (3.35), which contains only the on-diagonal functions $X_D(j\omega)$.

We can still cope with the infinite dimensional problem that implies testing Condition (F.21) with the complete version of the multipliers belonging to $\mathbf{\Pi_\theta}$ of (3.35). To do so, we can employ the alternative approach commonly used in the μ-analaysis framework [FTD91] and known as frequency gridding. This method is usually applied to the analysis of uncertain systems containing parametric and dynamic LTI uncertainties. However, the analysis of harmonic time-varying systems makes the gridding procedure more complex than usual.

In the following subsections, we first introduce a proposition that allows to exploit a frequency domain resolution for the case of harmonic operators. Then, we present a multiplier parametrization for harmonic multipliers, as well as the corresponding stability conditions allowing a state-space resolution.

Frequency domain solution

The frequency domain solution is based on a frequency gridding, which is a commonly used technique in the μ-analysis framework. It basically consists in sampling the frequency axis and testing condition (3.12) of Theorem 1 for the selected grid frequency points. Our procedure is also based on this idea, however, it should be extended to the case of LHTV systems. Indeed, in common μ-analysis routine, the multipliers are independent across the frequency ω since it is applied to the interconnection of LTI systems. There is thus no difficulty to test the obtained conditions for different frequencies in the grid. However, due to the modulation property used in the case of harmonic parameters, the scaling matrices $X_D(j\omega)$ and $X_G(j\omega)$, for a fixed frequency ω, are strongly linked to the scaling matrices at the shifted frequencies $\omega + \omega_0$ and $\omega - \omega_0$. Additionally, we must sample both positive and negative frequencies given the lack of properties when ω is replaced by $-\omega$. Both aspects are crucial to properly construct the frequency gridding and the analysis test and they are addressed hereafter.

A first difficulty in frequency gridding is to chose maximal frequency ω_{max} to be sampled since condition (3.12) implies to test also frequencies that tend to the infinity. This is not actually a real issue since the nominal system G is assumed to be LTI and stable, hence its transfer function is a proper or strictly proper function of s replaced by $j\omega$, leading to two possible scenarios.

1. $\overline{\sigma}(G(j\omega)) \to 0$ when $\omega \to \infty$. Then, condition (3.12) converges to the condition

$$\Pi_{22}(j\omega) \prec 0,$$

which is always satisfied for multipliers characterizing bounded operators.

2. $G(j\omega) \to G_\infty$ when $\omega \to \infty$, with G_∞ being a constant matrix. Then, there exists a frequency ω_{max} such that for any frequency $\omega \geq \omega_{max}$ the nominal system tends to the same constant matrix, implying to test the same conditions for all $\omega \geq \omega_{max}$.

The second difficulty, again as in the μ-analysis gridding procedure, is that the scaling matrices are continuous functions of ω, that is, an infinitesimally divisible set of frequencies, which is solved using the gridding and performing the analysis over a finite set of frequencies. In this aspect, frequency gridding does not offer hard guarantees for analysis. Nevertheless, investigating the nominal system and the nature of the element in the set $\mathbf{\Delta}$, and using an adequate judgment of the number and localization of the grid points, it is possible to obtain accurate results.

In the case of harmonic multipliers, we have a dependency on the harmonic frequency ω_0. Then, we define the minimal step of the gridding ω_u as a fraction of ω_0:

$$\omega_u = \frac{\omega_0}{N_u},$$

where N_u is the number of grid points. We define the maximal frequency to be tested ω_{max} as a linear proportion of ω_0:

$$\omega_{max} = N_{max}\omega_0,$$

with N_{max} being a positive integer.

A third difficulty comes from the fact that, in contrast to the classical frequency gridding of μ-analysis, where the uncertain elements of $\mathbf{\Delta}$ are LTI, in the case of harmonic multipliers, we must sample both positive and negative frequencies given the lack of symmetry in the constraints generated by the harmonic multipliers. Hence, the obtained frequency grid constitutes the finite set (described on Fig. 3.8)

$$\mathbf{\Omega_s} = \{-N_{max}\omega_0, ..., -\omega_u, 0, \omega_u, ..., N_{max}\omega_0\}. \tag{3.42}$$

Then, testing condition (3.12) for each frequency in the set $\mathbf{\Omega_s}$ will generate a complex LMI constraint to be tested.

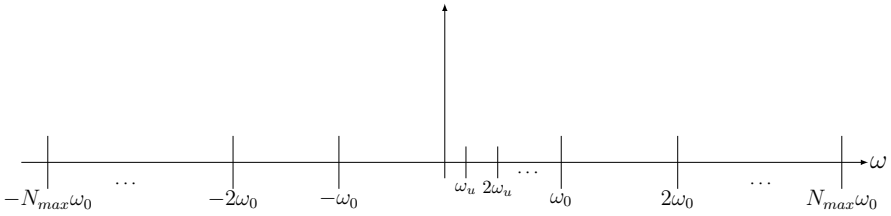

FIGURE 3.8: Frequency gridding

Another difference with respect to the classical gridding, is that, in the μ-analysis, the obtained scaling matrices for one specific frequency are independent from the same matrices at another frequency. While in the case of harmonic multipliers inducing the modulation property, the functions $X_D(j\omega)$ and $X_G(j\omega)$ impose inter-frequency conditions. For instance, as we show on Fig. 3.9 for $X_D(j\omega)$, if we aim to test condition (3.12) for a particular frequency $\omega_i \in \mathbf{\Omega_s}$ using a harmonic multiplier, we need to consider $G(j\omega_i)$ and to construct the complex function $X_D(j\omega_i) = X_{D_i}$,

but also $X_D(j(\omega_i + \omega_0)) = X_{D_{i+N_u}}$ and $X_D(j(\omega_i - \omega_0))X_{D_{i-N_u}}$. The latter functions will be then used in the same condition (3.12) but at the frequencies $\omega_{i+/-N_u}$.

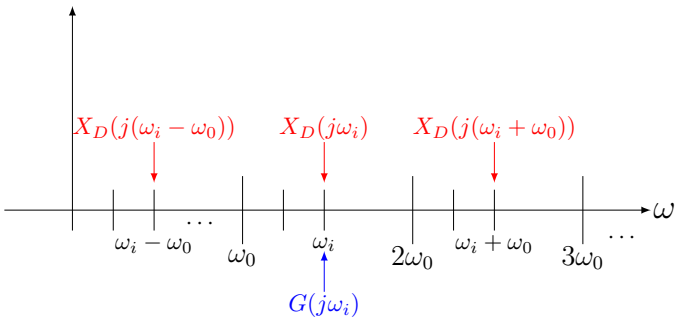

FIGURE 3.9: Construction of $X_D(j\omega)$

The functions $X_G(j\omega)$ are particular cases of periodic functions, whose periodicity depends on the set of multipliers. To illustrate their construction, let us consider the harmonic multipliers for a single repeated harmonic parameter. We need to define the function $X_G(j\omega_k) = X_{Gk}$ only for one interval $[0, \omega_0[$ since $X_G(j\omega) = -X_G(j(\omega + \omega_0))^* = X_G(j(\omega + 2\omega_0))$, see Fig. 3.10.

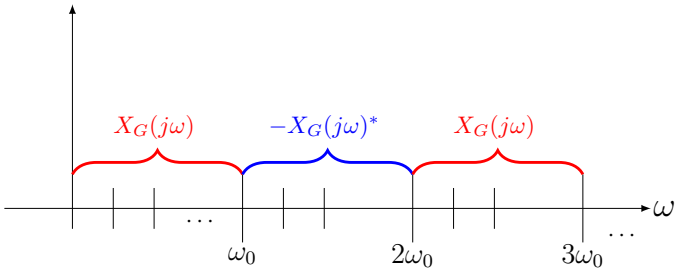

FIGURE 3.10: Construction of $X_G(j\omega)$

To completely clarify the concept, let us present a simple numerical example. Consider a harmonic frequency $\omega_0 = 2$ rad/s that we divide in two parts, this is $N_u = 2$ and $\omega_u = 1$ rad/s. Additionally, let $N_{max} = 3$, making $\omega_{max} = 6$ rad/s. Then, one of the constraints to be tested, at the frequency $\omega_u = 1$ rad/s, is

$$\begin{bmatrix} G_{qp}(j) \\ I \end{bmatrix}^* \begin{bmatrix} X_D(-j) + X_D(j3) & X_G(j) \\ X_G(j)^* & -2X_D(j) \end{bmatrix} \begin{bmatrix} G_{qp}(j) \\ I \end{bmatrix} \preceq -\epsilon I$$

then, other constraint at the frequency $\omega_0 + \omega_u = 3$ rad/s, is

$$\begin{bmatrix} G_{qp}(j3) \\ I \end{bmatrix}^* \begin{bmatrix} X_D(j) + X_D(j5) & -X_G(j)^* \\ -X_G(j) & -2X_D(j3) \end{bmatrix} \begin{bmatrix} G_{qp}(j3) \\ I \end{bmatrix} \preceq -\epsilon I$$

In this example, we can observe that the variables $X_D(j)$ and $X_G(j)$ appear in both inequalities, the different LMI conditions are then constrained between them through the variables X_D and X_G.

Finally, the global analysis problem can be then summarized as: test if there exists a combination of all the variables X_{Di} and X_{Gk} satisfying simultaneously all the LMI constraints generated at each frequency in $\mathbf{\Omega_s}$. If all the constraints are satisfied, then the system is robustly stable with respect to the set of harmonic functions.

State-space solution

The following lemma proposes a parameterization for a partial version of the multipliers in the set (3.35), that is, considering $X_G(j\omega) = 0_{n_q \times n_q}$. We then define the subset $\underline{\boldsymbol{\Pi}}_{\boldsymbol{\theta}} \subset \boldsymbol{\Pi}_{\boldsymbol{\theta}}$.

Lemma 3.3. *Let be the set $\boldsymbol{\Delta}_{\boldsymbol{H}}^{\boldsymbol{\omega_0}}$, defined in (3.27) with $\theta^{\omega_0}(t)$ given by (3.28). Let $\boldsymbol{M_D} = \{M_D | M_D \in \mathbb{S}^\bullet, \Psi(j\omega)^* M_D \Psi(j\omega) \succ 0 \; \forall \; \omega\}$, and let be the basis function Ψ belongs to $\mathcal{RH}_\infty^{(v+1)n_q \times n_q}$ Then, the IQC (3.10) holds with Π belonging to the subset $\underline{\boldsymbol{\Pi}}_{\boldsymbol{\theta}}$ defined as*

$$\underline{\boldsymbol{\Pi}}_{\boldsymbol{\theta}} = \left\{ \Pi \;\middle|\; \begin{array}{c} \exists\, M_D \in \boldsymbol{M_D}, \\ \Pi(j\omega) = \left[\begin{array}{c} \star \\ \star \\ \star \end{array}\right]^* \left[\begin{array}{cc|c} \frac{1}{2}M_D & 0 & 0 \\ 0 & \frac{1}{2}M_D & 0 \\ \hline 0 & 0 & -2M_D \end{array}\right] \left[\begin{array}{c|c} \Psi_+ + \Psi_- & 0 \\ -j(\Psi_+ - \Psi_-) & 0 \\ \hline 0 & \Psi \end{array}\right], \\ \text{with } \Psi_+(j\omega) := \Psi(j(\omega+\omega_0)),\; \Psi_-(j\omega) := \Psi(j(\omega-\omega_0)), \end{array} \right\}. \tag{3.43}$$

Proof. Considering the parameterization $X_D(j\omega) = \Psi(j\omega)^* M_D \Psi(j\omega)$, with $M_D \in \mathbb{S}^\bullet$ and $\Psi \in \mathcal{RH}_\infty^{\bullet \times n_q}$, we obtain

$$\begin{aligned} X_D(j(\omega+\omega_0)) &= \Psi(j(\omega+\omega_0))^* M_D \underbrace{\Psi(j(\omega+\omega_0))}_{\Psi_+} \\ X_D(j(\omega-\omega_0)) &= \Psi(j(\omega-\omega_0))^* M_D \underbrace{\Psi(j(\omega-\omega_0))}_{\Psi_-}. \end{aligned}$$

Hence, the upper-left block of the multiplier Π in the set (3.35) is expressed as follows

$$X_{D+} + X_{D-} = \Psi_+^* M_D \Psi_+ + \Psi_-^* M_D \Psi_-,$$

which can be rewritten as

$$\begin{aligned} X_{D+} + X_{D-} = &\frac{1}{2} \left[\Psi_+ + \Psi_-\right]^* M_D \left[\Psi_+ + \Psi_-\right] \\ &+ \frac{1}{2} \left[-j(\Psi_+ - \Psi_-)\right]^* M_D \left[-j(\Psi_+ - \Psi_-)\right]. \end{aligned}$$

Then, combining this factorization with the one of X_D, we can easily obtain the final factorization of Π belonging to the set $\underline{\boldsymbol{\Pi}}_{\boldsymbol{\theta}}$ given by (3.43). □

In order to obtain an efficient finite-dimensional stability tests through Lemma 3.1, it is necessary to find a suitable state-space realization for the elements of (3.43). Let us then introduce the following auxiliary lemma.

Lemma 3.4. *Let be $\Psi \in \mathcal{RH}_\infty^{n_y \times n_u}$ with the minimal realization*

$$\left[\begin{array}{c|c} A_\Psi & B_\Psi \\ \hline C_\Psi & D_\Psi \end{array}\right]$$

where $A_\Psi \in \mathbb{R}^{n \times n}$, $B_\Psi \in \mathbb{R}^{n \times n_u}$, $C_\Psi \in \mathbb{R}^{n_y \times n}$, $D_\Psi \in \mathbb{R}^{n_y \times n_u}$. Then

$$\left[\begin{array}{c} \Psi(s+j\omega_0) + \Psi(s-j\omega_0) \\ -j(\Psi(s+j\omega_0) - \Psi(s-j\omega_0)) \end{array}\right] \tag{3.44}$$

has the state-space realization

$$\left[\begin{array}{cc|c} A_\Psi & \omega_0 I & B_\Psi \\ -\omega_0 I & A_\Psi & 0 \\ \hline 2C_\Psi & 0 & 2D_\Psi \\ 0 & 2C_\Psi & 0 \end{array}\right]. \tag{3.45}$$

Proof. With $\Psi(s) = C_\Psi(sI_n - A_\Psi)^{-1}B_\Psi + D_\Psi$, a shift $+\omega_0$ of the transfer function gives $\Psi(s+j\omega_0) = C_\Psi(sI_n + j\omega_0 I_n - A_\Psi)^{-1}B_\Psi + D_\Psi$ and, similarly, $\Psi(s-j\omega_0) = C_\Psi(sI_n - j\omega_0 I_n - A_\Psi)^{-1}B_\Psi + D_\Psi$. Let us then introduce the state-space equations of $\Psi(s+j\omega_0)$:

$$\left\{\begin{array}{ll} \dot{x}_+ & = (A_\Psi - j\omega_0 I)x_+ + B_\Psi u \\ y_+ & = C_\Psi x_+ + D_\Psi u \end{array}\right. \tag{3.46}$$

and of $\Psi(s-j\omega_0)$:

$$\left\{\begin{array}{ll} \dot{x}_- & = (A_\Psi + j\omega_0 I)x_- + B_\Psi u \\ y_- & = C_\Psi x_- + D_\Psi u \end{array}\right. . \tag{3.47}$$

We observe that the state equation of (3.46) is the complex conjugate of the state equation of (3.47). With $x_+(0) = 0$ and $x_-(0) = 0$, we have that $x_+ = \bar{x}_-$. We then note $x_+ = x_{Re} + jx_{Im}$ and $x_- = x_{Re} - jx_{Im}$, and we introduce the state-space vector $x = [x_{Re}^T\ x_{Im}^T]^T$. In this form, the output $(y_+ + y_-)$ is given by $2C_\Psi x_{Re} + 2D_\Psi u$ and the output $-j(y_+ + y_-)$ by $2C_\Psi x_{Im}$. Thus, the system (3.44) has the state-space representation (3.45). □

Given the previous parameterization, we can state the following LMI stability condition.

Theorem 3.5. *Let G_{qp} be a stable LTI system admitting the state-space realization (A, B, C, D), let $\mathbf{\Delta_H^{\omega_0}}$ be the set defined by (3.27), with θ^{ω_0} given by (3.28). Let be the set of multipliers $\underline{\mathbf{\Pi_\theta}}$ given by (3.43) with Ψ admitting minimal state-space realization $(A_\Psi, B_\Psi, C_\Psi, D_\Psi)$.*

Then, the interconnection $(G_{qp}, \mathbf{\Delta_H^{\omega_0}})$ is robustly stable if there exists $M_D \in \mathbf{M_D}$, $P \in \mathbb{S}^\bullet$ and $\epsilon > 0$ such that

$$\left[\begin{array}{cc} I & 0 \\ \tilde{A} & \tilde{B} \\ \tilde{C} & \tilde{D} \end{array}\right]^T \left[\begin{array}{ccc} 0 & P & 0 \\ P & 0 & 0 \\ 0 & 0 & \tilde{M}_D \end{array}\right] \left[\begin{array}{cc} I & 0 \\ \tilde{A} & \tilde{B} \\ \tilde{C} & \tilde{D} \end{array}\right] \preceq -\epsilon I \tag{3.48}$$

with $\tilde{M}_D = diag(\frac{1}{2}M_D, \frac{1}{2}M_D, -2M_D)$, and

$$\tilde{A} = \left[\begin{array}{cccc} A_\Psi & \omega_0 I & 0 & B_\Psi C \\ -\omega_0 I & A_\Psi & 0 & 0 \\ 0 & 0 & A_\Psi & 0 \\ 0 & 0 & 0 & A \end{array}\right], \tilde{B} = \left[\begin{array}{c} B_\Psi D \\ 0 \\ B_\Psi \\ B \end{array}\right],$$
$$\tilde{C} = \left[\begin{array}{cccc} 2C_\Psi & 0 & 0 & 2D_\Psi C \\ 0 & 2C_\Psi & 0 & 0 \\ 0 & 0 & C_\Psi & 0 \end{array}\right], \tilde{D} = \left[\begin{array}{c} 2D_\Psi D \\ 0 \\ D_\Psi \end{array}\right].$$

Proof. Stability is tested applying Theorem 3.1. First, observe that if (3.48) is satisfied, then $\tilde{D}^T\tilde{M}_D\tilde{D} \prec -\varepsilon I$. Developing the expression we have

$$\left[\begin{array}{c} 2D_\Psi D \\ 0 \\ D_\Psi \end{array}\right]^T \left[\begin{array}{ccc} \frac{1}{2}M_D & 0 & 0 \\ 0 & \frac{1}{2}M_D & 0 \\ 0 & 0 & -2M_D \end{array}\right] \left[\begin{array}{c} 2D_\Psi D \\ 0 \\ D_\Psi \end{array}\right] \preceq -\epsilon I, \tag{3.49}$$

with the matrix D_Ψ having the following structure

$$D_\Psi = \begin{bmatrix} 0_{vn_q \times n_q} \\ I_{n_q \times n_q} \end{bmatrix}.$$

Then, if we partition the matrix M_D as $M_D = \begin{bmatrix} M_{D11} & M_{D12} \\ M_{D12}^T & M_{D22} \end{bmatrix}$ with submatrices of proper dimensions, inequality (3.49) gives

$$D^T M_{D22} D \prec M_{D22},$$

with $M_{D22} \in \mathbb{S}^{n_q}$. Such a condition ensures that $(I - D\Delta)$ is invertible and, since Δ is defined by a continuous varying gain $\theta(\omega_0, t) I_{n_q}$, then $(I - G\Delta)$ has a causal inverse. As a consequence, the interconnection (G, Δ) is well-posed for any $\Delta \in \boldsymbol{\Delta}_{\boldsymbol{H}}^{\boldsymbol{\omega_0}}$ defined by (3.27) with $m = 1$.

From Lemma 3.3, we know that $\boldsymbol{\Delta_\theta} \in IQC(\Pi)$ with $\Pi \in \underline{\boldsymbol{\Pi}}_{\boldsymbol{\theta}}$ defined by (3.43). By applying Theorem 3.1 with the set $\underline{\boldsymbol{\Pi}}_{\boldsymbol{\theta}}$ defined by (3.43) in Lemma 3.3, based on the state-space realization (3.45) of Lemma 3.4, the stability is ensured if

$$H(j\omega)^* \tilde{M}_D H(j\omega) \preceq -\epsilon I \quad \forall\, \omega \in \mathbb{R} \tag{3.50}$$

with

$$H = \left[\begin{array}{c|c} \Psi_+ + \Psi_- & 0 \\ -j(\Psi_+ - \Psi_-) & 0 \\ \hline 0 & \Psi \end{array}\right] \left[\begin{array}{c} G \\ \hline I \end{array}\right] \sim \left[\begin{array}{c|c} \tilde{A} & \tilde{B} \\ \hline \tilde{C} & \tilde{D} \end{array}\right]. \tag{3.51}$$

Condition (3.50) is equivalent to condition (3.48) by Lemma 3.1.

□

In order to illustrate the interest of the proposed set of multipliers, as well as the different resolution approaches for the stability tests, we present the following example.

Example

We address a classical problem of mechanical vibrations known as the Mathiew-Hill equation. This particular problem is chosen since it has been largely documented and exact solutions of the stability domain are available in the literature, for instance, the stability domain diagrams obtained by Pedersen in [Ped80] using the Gubnov-Galerkin procedure.

Mathieu-Hill equations The Mathieu-Hill equation is a differential equation of the form

$$\ddot{y} + 2c\dot{y} + (k + 2\beta\varphi(t))y = 0$$

with φ the periodic function $\varphi(t) = \cos(\omega_0 t) + b\cos(2\omega_0 t)$. The Mathieu-Hill equation is found, for example, when one tries to study the damping of any wave in a free system. This equation can be expressed in the state-space form of a non-forced system $\dot{x}(t) = A(t)x(t)$, with the state matrix given by:

$$A(t) = \begin{bmatrix} 0 & 1 \\ -k - 2\beta\varphi(t) & -2c \end{bmatrix}$$

The stability domain is plotted in the (k, β) plane, for a given b and a given c, within the value intervals $0 \leq k \leq 6$ and $0 \leq \beta \leq 2$. Two studies were conducted with $c = 0.1$.

Here, we investigate two different cases, the first one with $b = 0$ which comes to a Harmonic time varying system with a single cosine function. Then a second case with $b = 0.75$, which involves two cosine functions.

Case b=0. In this case, the dynamic matrix $A(t)$ of the Mathieu-Hill equation becomes

$$A(t) = \begin{bmatrix} 0 & 1 \\ -k - 2\beta\cos(\omega_0 t) & -2c \end{bmatrix}$$

Now, it is necessary to write the system as a feedback interconnection form given by (3.7), with $\theta^{\omega_0}(t) = \cos(\omega_0 t)$ interconnected to the nominal system $G(s)$. This can be easily obtained by defining the signals $p(t) = \cos(\omega_0 t)q(t)$, then we can pick $q(t) = x_1(t)$, to finally define the second state equation as $\dot{x}_2(t) = -kx_1(t) - 2cx_2(t) - 2\beta p(t)$. So, the feedback interconnection is defined by the nominal system

$$G_{qp} : \begin{cases} \begin{bmatrix} \dot{x}_1(t) \\ \dot{x}_2(t) \end{bmatrix} &= \begin{bmatrix} 0 & 1 \\ -k & -2c \end{bmatrix} \begin{bmatrix} x_1(t) \\ x_2(t) \end{bmatrix} + \begin{bmatrix} 0 \\ -2\beta \end{bmatrix} p(t) \\ q(t) &= \begin{bmatrix} 1 & 0 \end{bmatrix} \begin{bmatrix} x_1(t) \\ x_2(t) \end{bmatrix} \end{cases} \tag{3.52}$$

and

$$p(t) = \cos(\omega_0 t)q(t)$$

case b=0.75 Now the dynamic matrix $A(t)$ of the time-varying system is

$$A(t) = \begin{bmatrix} 0 & 1 \\ -k - 2\beta(\cos(\omega_0 t) + b\cos(2\omega_0 t)) & -2c \end{bmatrix}$$

At first glance, we have a system with two harmonic parameters of different frequencies. However, we have the trigonometric identity

$$\cos(2\omega_0 t) = 2\cos(\omega_0 t)^2 - 1$$

that allows to transform the combination of two cosine functions at frequencies ω_0 and $2\omega_0$ into a repeated harmonic parameter of frequency ω_0. Then, $\varphi(t)$ can be rewritten as

$$\varphi(t) = \cos(\omega_0 t)(1 + 2b\cos(\omega_0 t)) - b$$

Then, defining the signals $p_1(t) = \cos(\omega_0 t)q_1(t)$ and $p_2(t) = \cos(\omega_0 t)q_2(t)$, $q_2(t) = p_1(t) + x_1(t)$ and $q_1(t) = 2bx_1(t)$, we can derive the LFT system with nominal system G_{qp} defined by state-space equations:

$$G_{qp} : \begin{cases} \begin{bmatrix} \dot{x}_1(t) \\ \dot{x}_2(t) \end{bmatrix} &= \begin{bmatrix} 0 & 1 \\ (-k + 2\beta b) & -2c \end{bmatrix} \begin{bmatrix} x_1(t) \\ x_2(t) \end{bmatrix} + \begin{bmatrix} 0 & 0 \\ 0 & -2\beta \end{bmatrix} \begin{bmatrix} p_1(t) \\ p_2(t) \end{bmatrix} \\ \begin{bmatrix} q_1(t) \\ q_2(t) \end{bmatrix} &= \begin{bmatrix} 2b & 0 \\ 1 & 0 \end{bmatrix} \begin{bmatrix} x_1(t) \\ x_2(t) \end{bmatrix} + \begin{bmatrix} 0 & 0 \\ 1 & 0 \end{bmatrix} \begin{bmatrix} p_1(t) \\ p_2(t) \end{bmatrix} \end{cases} \tag{3.53}$$

and

$$\begin{bmatrix} p_1(t) \\ p_2(t) \end{bmatrix} = \begin{bmatrix} \cos(\omega_0 t) & 0 \\ 0 & \cos(\omega_0 t) \end{bmatrix} \begin{bmatrix} q_1(t) \\ q_2(t) \end{bmatrix}$$

Results

Case b = 0 We perform multiple analyses, one considering two subsets of multipliers belonging to the set $\mathbf{\Pi_\theta}$ defined by (3.35): a partial version containing only $X_D(j\omega)$, and the second one introducing $X_G(j\omega)$ in the multiplier, in both cases using the frequency domain resolution introduced in section 3.5.2 - frequency domain resolution. We performed a third analysis by exploiting the parameterization of the multiplier defining the set of multipliers $\underline{\mathbf{\Pi}}_{\boldsymbol{\theta}}$ given by (3.43), then solving through Theorem 3.5. The results are compared with the quasi-exact solutions presented by Pedersen [Ped80] using the Bubnov-Galerkin method.

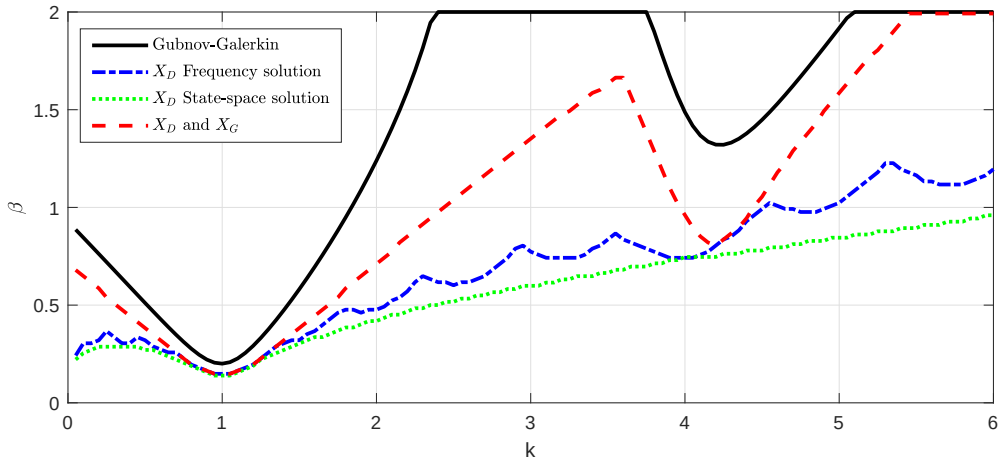

FIGURE 3.11: Stability domain of Mathieu-Hill equation with $b = 0$

As expected, the proposed approach is a sufficient condition and leads to a lower boundary of the stability region than the Bubnov-Galerkin method, which is an almost analytic solution.

Then, comparing the results involving multipliers with only $X_D(j\omega)$, we observe that the approach parameterizing the multiplier is slightly more conservative than the one using frequency gridding. This is natural since the parameterized multiplier is constrained to belong to a smaller set than the original one.

Finally, a significant increase in the stability region boundaries is observed when we test the multiplier containing X_G. The difference is more noticeable in the second case with $b = 0.75$, since X_G passes of being scalar to matrix-valued, then the periodic skew-hermitian structure is better exploited.

Case b = 0.75 We performed the same four analyses for the case of $b = 0.75$, i.e. for the case with the system containing a twice repeated cosine gain.

The obtained results for each approach are similar in the analysis of both cases $b = 0$ and $b = 0.75$. The main difference in this second case is that the introduction of a second cosine function made more noticeable that $X_G(j\omega)$ plays a significant role in the reduction of conservatism.

The comparison with the Gubnov-Galerkin method employed by Pedersen allowed us to test the different sets of multipliers proposed until now. However, we need to notice that the Gubnov-Galerkin method is derived from the pursuit of exact solutions for a quite particular problem, while our objective is to propose efficient methods that, offering sufficient conditions, allows to test a wide variety of uncertain and harmonically time-varying systems.

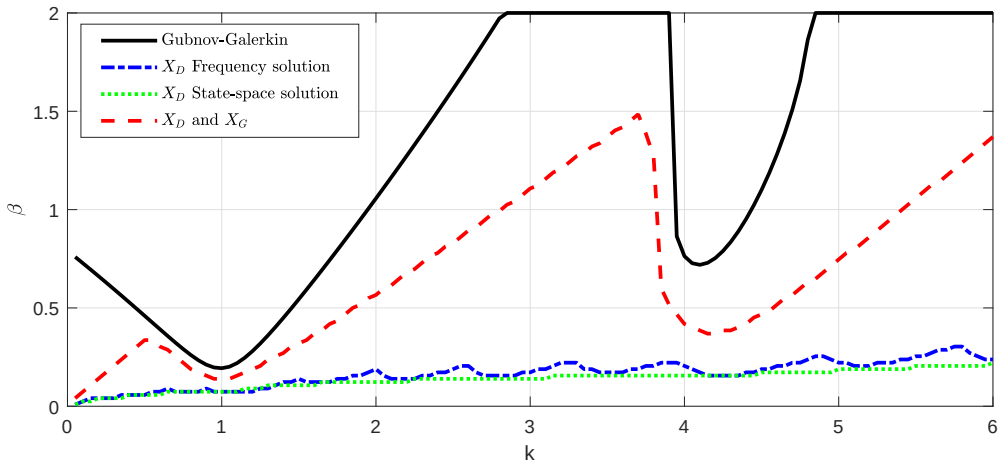

FIGURE 3.12: Stability domain of Mathieu-Hill equation with $b = 0.75$

3.5.3 Multiplier for coupled harmonic parameters

Coupled harmonic parameters are defined by two repeated HTVs parameters of same frequency ω_0 but with a particular phase-shift ψ between them, which includes the case of systems containing synchronous demodulation modules. This operator belongs to the set $\mathbf{\Delta}_{\boldsymbol{H}}^{\boldsymbol{\omega_0}}$, given by (3.27), with $\theta^{\omega_0}(t)$ defined by (3.29).

We dispose of several multipliers that can be used to analyze such a system. Following the discussion of subsection 3.5.2, one possible option is to model the synchronous demodulation operator as two uncoupled harmonic parameters. Then we can employ the set of multipliers (3.35) for each repeated harmonic parameter, obtaining a multiplier with the form

$$\Pi(j\omega) = \begin{bmatrix} X_{D+}(j\omega) + X_{D-}(j\omega) & X_G(j\omega) \\ X_G(j\omega)^* & -2X_D(j\omega) \end{bmatrix}, \tag{3.54}$$

where

$$X_{D+} = \text{diag}(X_{D1}(j(\omega+\omega_0)), X_{D2}(j(\omega+\omega_0))),$$
$$X_{D-} = \text{diag}(X_{D1}(j(\omega-\omega_0)), X_{D2}(j(\omega-\omega_0))),$$
$$X_D = \text{diag}(X_{D1}(j\omega), X_{D2}(j\omega))$$

and

$$X_G(j\omega = \text{diag}(X_{G1}(j\omega), X_{G2}(j\omega)).$$

Multiplier (3.54) considers that $\theta(t,\omega_0)$ is bounded, as well as its harmonic nature. The question now is if this result can be extended to the case of two harmonic parameters that are somehow coupled, as is the case of cosine and sine functions with respect to the constant phase-shift between them. The next theorem proposes a new class of multipliers that are specially derived for harmonic time-varying operators containing cosine and sine functions simultaneously.

Theorem 3.6. *Let be the set* $\boldsymbol{\Delta_H^{\omega_0}}$, *defined in* (3.27) *with* $\theta^{\omega_0}(t)$ *given by* (3.29). *Then, the IQC* (3.10) *holds with* Π *belonging to the set of multipliers*

$$\boldsymbol{\Pi_{\theta SD}^{\omega_0}} = \left\{ \Pi \;\middle|\; \begin{array}{c} \exists\, X_D(j\omega) \;/\; X_D(j\omega) = X_D(j\omega)^* \succ 0, \\ \\ \exists\, X_G(j\omega) \;/ \\ X_G(j(\omega+\omega_0)) = -\begin{bmatrix} I & 0 \\ 0 & e^{j\psi}I \end{bmatrix} X_G(j\omega)^* \begin{bmatrix} I & 0 \\ 0 & e^{-j\psi}I \end{bmatrix} \\ \\ \Pi(j\omega) = \begin{bmatrix} \tilde{X}_{D+}(j\omega) + \tilde{X}_{D-}(j\omega) & X_G(j\omega) \\ X_G(j\omega)^* & -2X_D(j\omega) \end{bmatrix}, \\ \textit{with} \\ \tilde{X}_{D+}(j\omega) = \begin{bmatrix} I & 0 \\ 0 & e^{-j\psi}I \end{bmatrix} X_D(j(\omega+\omega_0)) \begin{bmatrix} I & 0 \\ 0 & e^{j\psi}I \end{bmatrix}, \\ \\ \tilde{X}_{D-}(j\omega) = \begin{bmatrix} I & 0 \\ 0 & e^{j\psi}I \end{bmatrix} X_D(j(\omega-\omega_0)) \begin{bmatrix} I & 0 \\ 0 & e^{-j\psi}I \end{bmatrix}, \end{array} \right\}. \quad (3.55)$$

The proof follows a similar procedure of that of Theorem 3.3, and it is detailed in Appendix A.

Remark: Similar to the multipliers for a single harmonic parameter (3.35), the function $X_G(j\omega)$ is periodic, with the difference that the period of the multiplier for coupled harmonic parameters (3.55) is $4\omega_0$, i.e. $X_G(j\omega) = X_G(j(\omega + 4\omega_0))$.

Similar to the set of multipliers for a single repeated harmonic parameter, this multipliers takes into account information about the oscillation frequency ω_0. Additionally, it includes phase matrices $\text{diag}(I, e^{+/-j\psi})$ allowing to verify how the phase-shift can affect the closed loop system stability. In chapter 6, we present an application to the MEMS gyroscopes control, showing how important is to consider this information.

The procedure for the frequency domain solution is almost the same that the one presented in subsection 3.5.2, with the difference of the inclusion of phase matrices. Since both procedures are similar, the frequency-domain solution is not presented for this set of multipliers.

State-space resolution

Similar to the case of the set of multipliers $\boldsymbol{\Pi_\theta}$ (3.35), we propose a particular parameterization for the set $\boldsymbol{\Pi_{\theta SD}}$ (3.55), with the restriction of the operator X_G being a zero matrix. We define then the subset $\underline{\boldsymbol{\Pi}}_{\boldsymbol{\theta SD}} \subset \boldsymbol{\Pi_{\theta SD}}$.

Lemma 3.5. *Let be the set* $\boldsymbol{\Delta_H^{\omega_0}}$, *defined in* (3.27) *with* $\theta^{\omega_0}(t)$ *given by* (3.29). *Let* $\boldsymbol{M_D} = \{M_D | M_D \in \mathbb{S}^\bullet, \Psi(j\omega)^* M_D \Psi(j\omega) \succ 0 \;\forall\; \omega\}$, *and let be the basis function* $\Psi \in \mathcal{RH}_\infty^{(v+1)n_q \times n_q}$.

Then, the IQC (3.10) holds with Π belonging to the subset $\underline{\boldsymbol{\Pi}}_{\boldsymbol{\theta SD}}$ of (3.55), defined by

$$\underline{\boldsymbol{\Pi}}_{\boldsymbol{\theta SD}} = \left\{ \Pi \;\middle|\; \begin{array}{c} \exists\, M_D \in \boldsymbol{M_D}, \\ \Pi(j\omega) = \begin{bmatrix} \star \\ \star \\ \star \end{bmatrix}^{*} \tilde{M}_D \left[\begin{array}{c|c} \tilde{\Psi}_+ + \tilde{\Psi}_- & 0 \\ -j(\tilde{\Psi}_+ - \tilde{\Psi}_-) & 0 \\ \hline 0 & \Psi \end{array}\right], \\ \textit{with} \\ \tilde{\Psi}_+(j\omega) = \Psi(j(\omega+\omega_0)) \begin{bmatrix} I & 0 \\ 0 & e^{j\psi} I \end{bmatrix}, \\ \tilde{\Psi}_-(j\omega) = \Psi(j(\omega-\omega_0)) \begin{bmatrix} I & 0 \\ 0 & e^{-j\psi} II \end{bmatrix}. \end{array} \right\}, \tag{3.56}$$

Proof is given in Appendix A.

Then, considering the basis defined by (3.23), we state the following Lemma to obtain the state-space realization for the elements of (3.56),

Lemma 3.6. *Let be $\Psi \in \mathcal{RH}_\infty^{n_y \times n_u}$ admitting the minimal realization $(A_\Psi, B_\Psi, C_\Psi, D_\Psi)$ with $A_\Psi \in \mathbb{R}^{n\times n}$, $B_\Psi \in \mathbb{R}^{n\times n_u}$, $C_\Psi^{n_y\times n}$, $D_\Psi^{n_y\times n_u}$, then, with $B_\Psi = [B_{\Psi,1}\ B_{\Psi,2}]$ and $D_\Psi = [D_{\Psi,1}\ D_{\Psi,2}]$,*

$$\begin{bmatrix} \tilde{\Psi}_+ + \tilde{\Psi}_- \\ -j(\tilde{\Psi}_+ - \tilde{\Psi}_-) \end{bmatrix} \tag{3.57}$$

has the state-space realization

$$\left[\begin{array}{cc|cc} A_\Psi & \omega_0 I & B_{\Psi,1} & B_{\Psi,2}\mathcal{R}\{e^{j\psi}\} \\ -\omega_0 I & A_\Psi & 0 & B_{\Psi,2}\mathcal{I}\{e^{j\psi}\} \\ \hline 2C_\Psi & 0 & 2D_{\Psi,1} & 2D_{\Psi,2}\mathcal{R}\{e^{j\psi}\} \\ 0 & 2C_\Psi & 0 & 2D_{\Psi,2}\mathcal{I}\{e^{j\psi}\} \end{array}\right]. \tag{3.58}$$

Proof. With $\Psi(s) = C_\Psi(sI_n - A_\Psi)^{-1}B_\Psi + D_\Psi$, a shift $+\omega_0$ of the transfer function gives $\Psi(s+j\omega_0) = C_\Psi(sI_n + j\omega_0 I_n - A_\Psi)^{-1}B_\Psi + D_\Psi$ and, similarly, $\Psi(s-j\omega_0) = C_\Psi(sI_n - j\omega_0 I_n - A_\Psi)^{-1}B_\Psi + D_\Psi$. Let us then introduce the state-space equations of $\tilde{\Psi}_+$:

$$\left\{ \begin{array}{ll} \dot{x}_+ & = (A_\Psi - j\omega_0 I)x_+ + B_\Psi \underbrace{\begin{bmatrix} I & 0 \\ 0 & e^{j\psi} I \end{bmatrix} u}_{\tilde{u}_+} \\ y_+ & = C_\Psi x_+ + D_\Psi \tilde{u}_+ \end{array} \right. \tag{3.59}$$

and $\tilde{\Psi}_-$:

$$\left\{ \begin{array}{ll} \dot{x}_- & = (A_\Psi + j\omega_0 I)x_- + B_\Psi \underbrace{\begin{bmatrix} I & 0 \\ 0 & e^{-j\psi} I \end{bmatrix} u}_{\tilde{u}_-} \\ y_- & = C_\Psi x_- + D_\Psi \tilde{u}_-. \end{array} \right. \tag{3.60}$$

We observe that the state equation of (3.59) is the complex conjugate of the state equation of (3.60). With $x_+(0) = 0$ and $x_-(0) = 0$, we have that $x_+ = \bar{x}_-$. We note $x_+ = x_{Re} + jx_{Im}$ and $x_- = x_{Re} - jx_{Im}$, and we introduce the state-space vector $x = [x_{Re}^T\ x_{Im}^T]^T$.

In this form, with $B_\Psi = [B_{\Psi,1}\ B_{\Psi,2}]$ and $D_\Psi = [D_{\Psi,1}\ D_{\Psi,2}]$, the output $y_+ + y_-$ is given by $2C_\Psi x_{Re} + [2D_{\Psi,1}\ 2D_{\Psi,2}\mathcal{R}\{e^{j\psi}\}]u$ and the output $-j(y_+ + y_-)$ by $2C_\Psi x_{Im} + [0\ 2D_{\Psi,2}2D_{\Psi,2}\mathcal{I}\{e^{j\psi}\}]u$. Thus, the complete system (3.57) has the state-space representation (3.58). □

Finally, the stability condition is given by the following theorem.

Theorem 3.7. *Let G_{qp} be a stable LTI system with the state-space realization $(A, B, C = [C_1^T \; C_2^T]^T, D = [D_1^T \; D_2^T]^T)$. Let be the set $\boldsymbol{\Delta_H^{\omega_0}}$, defined in (3.27) with $\theta^{\omega_0}(t)$ given by (3.29). Let be the set of multipliers $\boldsymbol{\underline{\Pi}_{\theta SD}}$ given by (3.56) where Ψ has the minimal state-space realization $(A_\Psi, B_\Psi = [B_{\Psi,1} \; B_{\Psi,2}], C_\Psi, D_\Psi = [D_{\Psi,1} \; D_{\Psi,2}])$.*

Then, the interconnection $(G_{qp}, \boldsymbol{\Delta_{\theta SD}^{\omega_0}})$ is stable if there exists $M_D \in \boldsymbol{M_D}$, $P \in \mathbb{S}^\bullet$ and $\epsilon > 0$ such that

$$\begin{bmatrix} \star \\ \star \\ \star \end{bmatrix}^T \begin{bmatrix} 0 & P & 0 \\ P & 0 & 0 \\ 0 & 0 & \tilde{M}_D \end{bmatrix} \begin{bmatrix} I & 0 \\ \tilde{A} & \tilde{B} \\ \tilde{C} & \tilde{D} \end{bmatrix} \preceq -\epsilon I \tag{3.61}$$

with $\tilde{M}_D = diag(\frac{1}{2}M_D, \frac{1}{2}M_D, -2M_D)$, and

$$\tilde{A} = \begin{bmatrix} A_\Psi & \omega_0 I & 0 & B_{\Psi,1}C_1 + B_{\Psi,2}\mathcal{R}\{e^{j\psi}\}C_2 \\ -\omega_0 I & A_\Psi & 0 & B_{\Psi,2}B_{\Psi,2}\mathcal{I}\{e^{j\psi}\}C_2 \\ 0 & 0 & A_\Psi & 0 \\ 0 & 0 & 0 & A \end{bmatrix}, \tilde{B} = \begin{bmatrix} B_{\Psi,1}D_1 + B_{\Psi,2}\mathcal{R}\{e^{j\psi}\}D_2 \\ B_{\Psi,2}B_{\Psi,2}\mathcal{I}\{e^{j\psi}\}D_2 \\ B_\Psi \\ B \end{bmatrix},$$

$$\tilde{C} = \begin{bmatrix} 2C_\Psi & 0 & 0 & 2D_{\Psi,1}C_1 + D_{\Psi,2}\mathcal{R}\{e^{j\psi}\}C_2 \\ 0 & 2C_\Psi & 0 & 2D_{\Psi,2}B_{\Psi,2}\mathcal{I}\{e^{j\psi}\}C_2 \\ 0 & 0 & C_\Psi & 0 \end{bmatrix},$$

$$\tilde{D} = \begin{bmatrix} 2D_{\Psi,1}D_1 + D_{\Psi,2}\mathcal{R}\{e^{j\psi}\}D_2 \\ 2D_{\Psi,2}\mathcal{I}\{e^{j\psi}\}D_2 \\ D_\Psi \end{bmatrix}.$$

The proof of Theorem 3.7 is the same as the one of Theorem 3.5, with the only difference that H is given by

$$H = \left[\begin{array}{c|c} \tilde{\Psi}_+ + \tilde{\Psi}_- & 0 \\ -j(\tilde{\Psi}_+ - \tilde{\Psi}_-) & 0 \\ \hline 0 & \Psi \end{array}\right] \left[\begin{array}{c} G \\ \hline I \end{array}\right] \sim \left[\begin{array}{c|c} \tilde{A} & \tilde{B} \\ \hline \tilde{C} & \tilde{D} \end{array}\right]. \tag{3.62}$$

The set of multipliers $\boldsymbol{\Pi_{\theta SD}}$ and the state-space resolution, introduced in this section, are applied in chapter 6 for the analysis of a phasor-based control for MEMS gyroscopes.

3.5.4 Extension to full-block harmonic operators

The previous results allow us to address the analysis of uncertain systems containing synchronous demodulation modules. Now, it is convenient to extend the introduced concepts to the case of full-block harmonic operators (operators containing off-diagonal harmonic functions), considering rotational operators as one particularly important case.

The last case investigated in this work focused on full-block harmonic operators, which are full-block matrices of harmonic parameters at the frequency ω_0 and phase-shifts ψ_1, ψ_2 and ψ_3, as defined by (3.30). In order to clarify these phase-shift restrictions, let us rewrite (3.30) under its complex exponential form, with $p =$

$\frac{1}{2}\left(p_{up}+p_{low}\right)$ and

$$\begin{aligned} p_{up}(t) &= \underbrace{\begin{bmatrix} I & e^{j\psi_1}I \\ e^{j\psi_2}I & e^{j\psi_3}I \end{bmatrix}}_{\Phi_{up}} e^{j(\omega_0 t+\phi)}q(t) \\ p_{low}(t) &= \underbrace{\begin{bmatrix} I & e^{-j\psi_1}I \\ e^{-j\psi_2}I & e^{-j\psi_3}I \end{bmatrix}}_{\Phi_{low}} e^{-j(\omega_0 t+\phi)}q(t). \end{aligned} \tag{3.63}$$

However, in order to preserve modulation-commutation properties to derive the corresponding multipliers, the phase-shifts will be constrained. Two different cases of phase-shift constraints can appear:

- Case a). $\psi_3 = \psi_1 + \psi_2 + \pi$, giving

$$\theta^{\omega_0}(t) = \begin{bmatrix} \cos(\omega_0 t+\phi)I_{n_q} & \cos(\omega_0 t+\phi+\psi_1)I_{n_q} \\ \cos(\omega_0 t+\phi+\psi_2)I_{n_q} & -\cos(\omega_0 t+\phi+\psi_1+\psi_2)I_{n_q} \end{bmatrix} \tag{3.64}$$

- Case b). $\psi_2 = \psi_1 + \pi$ and $\psi_3 = 2\psi_1 + \pi$, giving

$$\theta^{\omega_0}(t) = \begin{bmatrix} \cos(\omega_0 t+\phi)I_{n_q} & \cos(\omega_0 t+\phi+\psi_1)I_{n_q} \\ -\cos(\omega_0 t+\phi+\psi_1)I_{n_q} & -\cos(\omega_0 t+\phi+2\psi_1)I_{n_q} \end{bmatrix} \tag{3.65}$$

The case a) allows two degrees of freedom for the relative phase-shifts while ensuring the non-singularity of the phase matrices Φ_{up} and Φ_{low}. The case b) has only one degree of freedom for the phase-shifts, and corresponds to the case of singular phase matrices, i.e. $\det(\Phi_{up}) = \det(\Phi_{low}) = 0$. In the latter case, since the phase matrices of (3.65) have a degenerated rank, the modulation-commutation is possible by decomposing them as

$$\begin{aligned} p_{up}(t) &= \underbrace{\begin{bmatrix} I \\ -e^{j\psi_1}I \end{bmatrix}\begin{bmatrix} I & e^{j\psi_1}I \end{bmatrix}}_{\Phi_{up}} e^{j(\omega_0 t+\phi)}q(t) \\ p_{low}(t) &= \underbrace{\begin{bmatrix} I \\ -e^{-j\psi_1}I \end{bmatrix}\begin{bmatrix} I & e^{-j\psi_1}I \end{bmatrix}}_{\Phi_{low}} e^{-j(\omega_0 t+\phi)}q(t). \end{aligned}$$

This last case is a generalization of the rotation matrix set. Indeed, with $\psi_1 = \pi/2$, the following matrix is obtained

$$\begin{bmatrix} \cos(\omega_0 t+\phi) & \sin(\omega_0 t+\phi) \\ -\sin(\omega_0 t+\phi) & \cos(\omega_0 t+\phi) \end{bmatrix}$$

representing the rotation of $\omega_0 t + \phi$.

Let us first state the theorem by introducing the set of multipliers for full-block harmonic operators with non-singular phase matrices.

Theorem 3.8. *Let be the set* $\boldsymbol{\Delta_H^{\omega_0}}$*, defined in* (3.27) *with* $\theta^{\omega_0}(t)$ *given by* (3.64)*. Then, the IQC* (3.10) *holds with* Π *belonging to the set of multipliers*

$$\boldsymbol{\Pi_{\theta RnS}} = \left\{ \Pi \;\middle|\; \begin{array}{c} \exists\, X_D(j\omega) \;/\; X_D(j\omega) = X_D(j\omega)^* \succ 0, \\ \\ \exists\, X_G(j\omega) \;/ \\ X_G(j(\omega+\omega_0)) = \\ \left[\begin{array}{cc} I & e^{j\psi_2} I \\ e^{j\psi_1} I & -e^{j(\psi_1+\psi_2)} I \end{array}\right] \frac{X_G(j\omega)^*}{2e^{j(\psi_1+\psi_2)}} \left[\begin{array}{cc} -e^{j(\psi_1+\psi_2)} I & -e^{j\psi_1} I \\ -e^{j\psi_2} I & I \end{array}\right] \\ \\ \Pi(j\omega) = \left[\begin{array}{cc} \tilde{X}_{D+}(j\omega) + \tilde{X}_{D-}(j\omega) & X_G(j\omega) \\ X_G(j\omega)^* & -2X_D(j\omega) \end{array}\right], \\ \\ \textit{with} \\ \tilde{X}_{D+}(j\omega) = \\ \left[\begin{array}{cc} I & e^{-j\psi_2} I \\ e^{-j\psi_1} I & -e^{-j(\psi_1+\psi_2)} I \end{array}\right] X_{D+}(j\omega) \left[\begin{array}{cc} I & e^{j\psi_1} I \\ e^{j\psi_2} I & -e^{j(\psi_1+\psi_2)} I \end{array}\right], \\ \\ \tilde{X}_{D-}(j\omega) = \\ \left[\begin{array}{cc} I & e^{j\psi_2} I \\ e^{j\psi_1} I & -e^{j(\psi_1+\psi_2)} I \end{array}\right] X_{D-}(j\omega) \left[\begin{array}{cc} I & e^{-j\psi_1} I \\ e^{-j\psi_2} I & -e^{-j(\psi_1+\psi_2)} I \end{array}\right] \end{array} \right\}. \tag{3.66}$$

The proof is given in Appendix A

Similar to the previous multiplier sets, this set includes the information about the oscillation frequency ω_0 as well as fixed phase-shifts ψ_1 and ψ_2 between the elements of the matrix θ^{ω_0}.

The obtained multiplier (3.66) is actually a subset of the multiplier (3.35), then both frequency domain and parameterization for the state-space resolution are possible.

Now, let us introduce the set of multipliers for the case of full-block harmonic operators with singular phase matrices.

Theorem 3.9. *Let be the set* $\boldsymbol{\Delta_H^{\omega_0}}$*, defined in* (3.27) *with* $\theta^{\omega_0}(t)$ *given by* (3.65)*. Then, the IQC* (3.10) *holds with* Π *belonging to the set of multipliers*

$$\boldsymbol{\Pi_{\theta Rs}^{\omega_0}} = \left\{ \Pi \;\middle|\; \begin{array}{c} \exists\, x_D(j\omega) \;/\; x_D(j\omega) = x_D(j\omega)^* \succ 0, \\ \\ \exists\, x_G(j\omega) \;/\; x_G(j\omega) = -x_G(j(\omega+\omega_0))^* \\ \\ \Pi(j\omega) = \left[\begin{array}{cc} 2\tilde{X}_{D+}(j\omega) + 2\tilde{X}_{D-}(j\omega) & X_G(j\omega) \\ X_G(j\omega)^* & -X_D(j\omega) \end{array}\right], \\ \\ \textit{with} \\ \tilde{X}_{D+}(j\omega) = \left[\begin{array}{cc} x_D(j(\omega+\omega_0)) & 0 \\ 0 & x_D(j(\omega+\omega_0)) \end{array}\right], \\ \\ \tilde{X}_{D-}(j\omega) = \left[\begin{array}{cc} x_D(j(\omega-\omega_0)) & 0 \\ 0 & x_D(j(\omega-\omega_0)) \end{array}\right], \\ X_G(j\omega) = \left[\begin{array}{cc} x_G(j\omega) & 0 \\ 0 & x_G(j(\omega+\omega_0))^* \end{array}\right] \end{array} \right\}. \tag{3.67}$$

The proof is given in Appendix A.

3.6 Chapter conclusion

In this chapter we introduce the necessary concepts for the study of the stability and the performance validation of MEMS gyroscopes. We presented the definitions of $\mathcal{L}_2$-gain stability and performance that are used in this memoir. We also present the LFT representation that is used for the modeling of uncertain and time-varying systems considered in this work, followed by the introduction of the notions of robust stability and robust performance.

Our work focuses on the use of the IQC framework, since it allows us to treat the case of systems containing uncertain and time-varying elements simultaneously. Emphasis was placed on the construction of multipliers for the most common uncertainties, this in order to understand the general procedure to construct them. We discussed that there exist two possible approaches to obtain tractable stability and performance conditions: frequency domain resolution and state-space resolution. Frequency domain resolution is possible by using frequency gridding, and state-space resolution is only possible under the condition that the multiplier admits a suitable parameterization.

In the last part, we introduce the analysis of uncertain Harmonically Time-Varying Systems within the IQC framework. There, we present our main contributions devoted to develop a catalog of frequency dependent multipliers for multiple types of harmonic operators. The derived multipliers exploit more information of the harmonic parameters with respect to any other existing multiplier in the literature. To complement these results, we offered approaches for both frequency domain and state-space resolutions of the stability and performance assessment tests.

The concepts introduced in this chapter are the basis for the development of the analysis methods that allow us to deal with the different problems related to the validation of performance specifications, introduced in the following chapters. Nevertheless, each performance criterion have particular features that will be investigated into details, leading to other interesting innovations in the robust performance analysis framework.

Chapter 4

Analysis of Bias and Scale Factor Nonlinearity

In chapter 2, we briefly introduce the standard specifications to evaluate the quality of a MEMS gyroscope. In this chapter, we further investigate the specifications that are related to the accuracy and the sensitivity of MEMS gyroscopes, except those that are related to noise (adressed in chapter 5).

General guidelines about the definition of performance specifications, as well as the test conditions under which they must be measured, are presented in the IEEE standards [IEE04, IEE06, IEE18]. Other specific details about how the specifications are interpreted in the industry, and how the tests are performed, were acquired through literature review [TWY17], manufacturers documentation and exchanges with industrial partners [SKP+20].

In the first section, we introduce the definitions of the standard specifications to evaluate MEMS gyroscopes accuracy and sensitivity. Then, the main objective of this chapter is to propose a set of tools that allow to evaluate the different performance specifications within the control design process, that is, before the experimental validation.

Such methods must rely on model-based approaches. This requires recasting the performance specifications as mathematical criteria that are related to the system model and that can be formally analyzed. As it will be observed during the chapter, the different specifications and types of models make appear performance analysis problems that depend on one or more parameters that belong to some particular set. Then, several notions derived from the robust analysis framework, such as the LFT interconnections, worst-case performance and solutions in the form of finite dimensional LMI optimization problems (some of them discussed in chapter 3), are exploited to address the validation of the corresponding performance specifications.

4.1 MEMS standard specifications and tests

4.1.1 Accuracy specifications

The first two specifications allow to characterize the accuracy of the gyroscope at environmental conditions that are said to be nominal, which are mainly related to perform the tests at some specific temperatures. Let us remind that, from the perspective of the performance specifications, the gyroscope input is the angular rate Ω_z and the output is the obtained measure z. Let us then state the definition of nominal bias.

Definition 4.1 (Nominal bias)**.** *The bias is the measured value at the gyroscope output z, at the steady-state, without rotation, that is, for $\Omega_z = 0$. The measure must be obtained at*

nominal conditions, particularly with respect to temperature.

$$B(T) = z \qquad for\ \ \Omega_z = 0, \qquad T = T_0$$

where T denotes temperature, and T_0 indicates the nominal temperature.

In practice, the nominal bias is not very problematic. The common procedure consists in measuring the nominal bias, then applying calibration to suppress its effect on the output measure, see (2.19). However, deriving a mathematical performance criterion associated to the bias will allow to obtain other analysis tools to investigate how bias is affected by changes in operation conditions.

Next, following with the performance specifications at nominal conditions, let us introduce the scale factor nonlinearity (SFNL). As discussed in chapter 2, the scale factor refers to the relationship between the input angular rate and the measured angular rate at the output. We mentioned that, ideally, and without considering a change of units, the scale factor should be a linear function of unitary slope.

Then, according to the standard definition section E.3, the scale factor nonlinearity is defined as the *maximal deviation from the straight line that defines the nominal input-output relationship over the whole range of operating angular rates*.

As discussed in section 2.2, the most common practice is to determine the input-output relationship through a linear regression process by using the experimental data points of a finite number of performed measures[1], obtaining the fitted function

$$z^{fit}(\Omega_z) = SF^{fit}\Omega_z + B^{fit}. \tag{4.1}$$

Using the fitted function $z^{fit}(\Omega_z)$, the measured angular rate is computed by using the expression of (2.19).

Let us then introduce a formal definition of the scale factor nonlinearity (SFNL).

Definition 4.2 (Scale factor nonlinearity)**.** *Let z be the measured output, at the steady-state, for a given input angular rate Ω_z. Let $z^{fit}(\Omega_z)$ be the fitted output given by (4.1).*

Then, the scale factor nonlinearity is defined as the normalized maximal error, over the whole interval $[\underline{\Omega}_z, \overline{\Omega}_z]$, between the measured output z and the fitted output $z^{fit}(\Omega_z)$, that is

$$SFNL(T) = \sup_{\Omega_z \in [\underline{\Omega}_z, \overline{\Omega}_z]} \left(\frac{|z^{fit}(\Omega_z) - z(\Omega_z)|}{SF^{fit}\Omega^{fs}} \right) \ \ for\ \ T = T_0, \tag{4.2}$$

where $\Omega^{fs} = (\overline{\Omega}_z - \underline{\Omega}_z)/2$, T denotes the temperature, and T_0 indicates the nominal temperature.

Note that the definition of SFNL given by (G.1) is equivalent to the maximum modulus of the relative error between the real angular rate and the measured one. In fact, $\tilde{\Omega}_z$ is obtained by the relation (**??**). Then, if we apply the same expression to z^{fit}, we have that

$$\Omega_z^{fit}(\Omega_z) = \frac{z^{fit}(\Omega_z) - B^{fit}}{SF^{fit}} = \frac{SF^{fit}\Omega_z + B^{fit} - B^{fit}}{SF^{fit}} = \Omega_z,$$

and the SFNL can be rewritten as

$$SFNL(T) = \sup_{\Omega_z \in [\underline{\Omega}_z, \overline{\Omega}_z]} \left(\frac{|\Omega_z - \tilde{\Omega}_z|}{\Omega^{fs}} \right) \ \ \text{for}\ \ T = T_0. \tag{4.3}$$

[1] In some cases, even higher degrees polynomials are used to define the input-output relation [TWY17]

The SFNL is then computed as the worst-case of the absolute value of the output error

$$\varepsilon_z = z^{fit}(\Omega_z) - z(\Omega_z),$$

for all the possible input angular rates Ω_z in the range $[\underline{\Omega}_z, \overline{\Omega}_z]$.

At this point, we have introduced performance specifications that have to meet at some particular environmental conditions, especially at a fixed nominal temperature. However, the accuracy and reliability of a MEMS gyroscope is affected by changes in the environmental conditions. These properties are also considered in the performance validation of MEMS gyroscopes and they are known as sensitivity specifications.

Sensitivity specifications

The following requirements concern the thermal sensitivity of the gyroscope, which is a measure of the degradation of the performance specifications as the temperature changes from the nominal value.

Definition 4.3 (Bias thermal sensitivity)**.** *The bias thermal sensitivity is the maximal bias over the specified range of temperature, that is*

$$B_{ts} = \max_{T \in [\underline{T}, \overline{T}]} |B(T)|$$

with

$$B(T) = z(T) \qquad for\ \ \Omega_z = 0,$$

where T denotes temperature, while $\underline{T}$ and $\overline{T}$ indicate the minimal and maximal temperatures.

Definition 4.4 (Scale factor thermal sensitivity)**.** *The scale factor thermal sensitivity is the maximal scale factor nonlinearity over the specified range of temperature, that is*

$$SFNL_{ts} = \max_{T \in [\underline{T}, \overline{T}]} SFNL(T)$$

with

$$SFNL(T) = \sup_{\Omega_z \in [\underline{\Omega}_z, \overline{\Omega}_z]} \left(\frac{|z^{fit}(\Omega_z) - z(\Omega_z)|}{SF^{fit} \Omega^{fs}} \right),$$

and $T \in [\underline{T}, \overline{T}]$ denoting the temperature.

Finally the last specifications are related to the repeatability, which is an indicator of the gyroscope reliability. In fact, the presence of noise, as well as the inherent uncertainty in the system induces variations in the measure, even for tests at the same conditions.

To summarize, three levels of specifications can be stated:

- **the performance measure:** strictly speaking, all the performance specifications are related to one performance measure, that is, the measurement error with respect to what is ideally expected at the steady-state;
- **the operation conditions:** the sensitivity is an indicator of the degradation of the sensor accuracy when environmental conditions deviate from nominal ones. In some sense, we can say that we are collecting the same measure for a slightly different system.

- **the reliability of the measures:** the objective of the repetability is to offer a certificate of the level of confidence with respect to some measure. Somehow, we can say that even at nominal conditions, a small amount of uncertainty, from the sensor itself or from external factors, will always arise.

The common procedure to validate the performance specifications of a gyroscope is performed through experimental tests. Our objective here is to provide pre-experimental tools that predicts the performance and robustness of a controlled MEMS gyroscope, allowing to compare the relevance of different solutions within the control design process. To this purpose, it is necessary to consider a model-based approach, that is, bringing the evaluation of the output signals associated to the performance specifications into mathematical criteria that are based on the model of the system that generates the signal.

In order to formally ensure some performance and robustness properties from a system model, taking into account the system uncertainty and the environmental changes, we apply a robustness analysis approach, which allows to evaluate the (robust) performance while offering better guarantees and efficiency (in time and computational resources) with respect to Monte Carlo or simulation-based methods. We can then state the general objective of this chapter.
Given the measures of performance and the test conditions under which they are obtained, how to guarantee a certain level of performance in such conditions by using the system model and some information about the system uncertainty.

In order to give an answer to this objective, different problems will be addressed along this chapter.

1. In section 4.2, we introduce how the estimated Coriolis force $\tilde{f}_c$, depending on the angular rate Ω_z, is obtained from an LFT model. Then, we investigate the effect of the synchronous demodulation on the gyroscope output z. Finally, we discuss how the output error ε_z, related to the SFNL and thermal sensitivity, can be expressed as a model-based performance criterion.

2. In section 4.3, we introduce a result, based on an LMI optimization problem, that provides a necessary and sufficient condition to compute the SFNL from a known system model,

3. In section 4.4, we propose a second analysis tool that provides a sufficient condition to determine the thermal sensitivity from a system-model.

4. In section 4.5, we introduce a supplementary analysis method that allows to compute the worst-case SFNL for system models that are obtained through system identification (data-based) methods, as in the case of the Next4MEMS project.

Finally, in section 4.6 and section 4.7 we respectively test the proposed analysis tools on an illustrative example and on an experimental case.

4.2 From standard specifications to analysis criteria

The purpose of this section is to propose a model-based method to efficiently compute the SFNL. According to the protocols and the test conditions to evaluate the SFNL, the gyroscope output z is measured for a fixed angular rate Ω_z and when the the steady-state is reached. In such case, as we can observe in the MEMS gyroscope

model of (2.22), the angular rate is not an exogenous disturbance but a model parameter. Therefore, hereafter we assume that Ω_z is a constant parameter which can take any value in the range $[\underline{\Omega}_z, \overline{\Omega}_z]$.

Since the SFNL is proportional to the maximal output error $\varepsilon_z = z^{fit} - z$, related to the notion of worst-case performance in the Robust Control framework, we proceed by deriving adapted model-based mathematical criteria for z, z^{fit} and finally ε_z that can be computed based on a Robust Control approach.

Without loss of generality, in this chapter, we consider an LTI Multi-Input Multi-output (MIMO) controller using a direct control strategy for both drive and sense modes (see Figure 4.1), that is, tracking and rejecting sinusoidal signals whose frequency is close to the resonance frequency of the MEMS resonators (subsection 2.1.3). The reference of the drive mode is then a sinusoidal signal at the excitation frequency ω_{exc}, that is, $x_r(t) = A\sin(\omega_{exc}t)$.

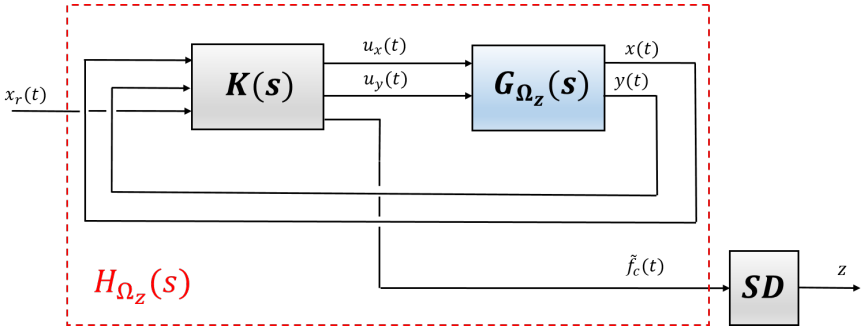

FIGURE 4.1: Closed-loop MIMO direct control

The MEMS resonator model $G_{\Omega_z}(s)$ is represented by an LTI system (see (2.22)). According to the test protocols of Definition G.2, the model depends on a constant angular rate Ω_z $[\underline{\Omega}_z, \overline{\Omega}_z]$. Then, the closed-loop system H_{Ω_z} is given by an LTI system with a harmonic input and whose output depends on the parameter Ω_z.

The SFNL specifications directly depends on the output error $\varepsilon_z = z^{fit} - z$. Then, we first determine how the gyroscope output z can be computed from the system model when it is obtained by ideal synchronous demodulation, which is a time-varying operation. Since the reference signal is a harmonic signal $x_r(t) = \sin(\omega_{exc}t)$, the estimation of the Coriolis force is given by the harmonic response of the closed-loop system H_{Ω_z}

$$\tilde{f}_c(t) = |H_{\Omega_z}(j\omega_{exc})|\sin(\omega_{exc}t + \arg(H_{\Omega_z}(j\omega_{exc}))),$$

which is a modulated signal that can be decomposed as

$$\tilde{f}_c(t) = z_i(t)\cos(\omega_{exc}t) - z_q(t)\sin(\omega_{exc}t)$$

where $z_i(t)$ and $z_q(t)$ respectively are the in-phase and the quadrature components, given by

$$\begin{cases} z_i(t) &= |H_{\Omega_z}(j\omega_{exc})|\sin(\arg(H_{\Omega_z}(j\omega_{exc})), \\ z_q(t) &= |H_{\Omega_z}(j\omega_{exc})|\cos(\arg(H_{\Omega_z}(j\omega_{exc})) \end{cases}.$$

Next, according to subsection 2.1.4, the application of an ideal synchronous demodulation (the filter F_L is an ideal low-pass filter), as illustrated in Figure 4.2, allows to extract the in-phase component containing the amplitude of the Coriolis force. Hence, the gyroscope output after applying the synchronous demodulation,

is given by

$$\begin{aligned} z = z_i &= |H_{\Omega_z}(j\omega_{exc})| \sin(\arg(H_{\Omega_z}(j\omega_{exc}))) \\ &= \Im\{H_{\Omega_z}(j\omega_{exc})\} \end{aligned}$$

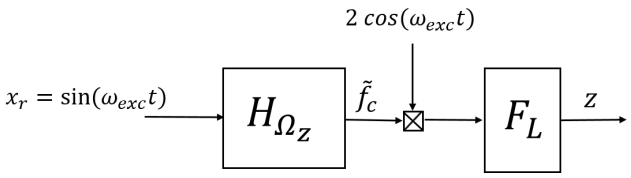

FIGURE 4.2: Extraction of the in-phase component

Therefore, the MEMS gyroscope output z is given by the imaginary part of the closed-loop harmonic response at the excitation frequency ω_{exc} of the input reference signal x_r.

The following step is to derive a mathematical criterion that explicitly expresses the output z as a function of Ω_z. Since the closed-loop system H_{Ω_z} linearly depends on the angular rate Ω_z, the system can be then reconfigured to obtain the LFT model:

$$H_{\Omega_z} = \Omega_z I_2 \star M_H.$$

Then, we have $z = \Im\{\Omega_z I_2 \star M_H(j\omega_{exc})\}$. The extraction of the imaginary part of an LFT interconnection leads to another LFT interconnection that doubles the size of the parameter repetitions:

$$z = \Omega_z I_4 \star \underbrace{\begin{bmatrix} \tilde{M}_H^{11} & \tilde{M}_H^{12} \\ \tilde{M}_H^{21} & \tilde{M}_H^{22} \end{bmatrix}}_{\tilde{M}_H}.$$

For the sake of readability, the detailed derivation of the LFT interconnection and the expression of $\tilde{M}_H$ is given in subsection B.1.1.

Now, the expression of the fitted output z^{fit} is given by

$$z^{fit}(\Omega_z) = SF^{fit}\Omega_z + B^{fit},$$

which can be straightforwardly computed from the LFT:

$$z^{fit} = (\Omega_z \star M^{fit}),$$

with

$$M^{fit} = \begin{bmatrix} 0 & 1 \\ SF^{fit} & B^{fit} \end{bmatrix}.$$

Hence, given that both z and z^{fit} can be obtained from LFT interconnections of Ω_z, the output error $\varepsilon_z(\Omega_z) = z^{fit}(\Omega_z) - z(\Omega_z)$ can be also obtained from an LFT, represented in Figure 4.3, given by

$$\varepsilon_z = (\Omega_z I_5 \star M_\varepsilon) \cdot 1 : \begin{cases} \begin{bmatrix} p \\ p^{fit} \end{bmatrix} &= \Omega_z \, I_5 \begin{bmatrix} q \\ q^{fit} \end{bmatrix} \\ \begin{bmatrix} q \\ q^{fit} \\ \varepsilon_z \end{bmatrix} &= M_\varepsilon \begin{bmatrix} p \\ p^{fit} \\ 1 \end{bmatrix} \end{cases}$$

with M_ε given by

$$M_\varepsilon = \left[\begin{array}{cc|c} \tilde{M}_H^{11} & 0 & \tilde{M}_H^{12} \\ 0 & 0 & 1 \\ \hline -\tilde{M}_H^{21} & SF^{fit} & B^{fit} - \tilde{M}_H^{22} \end{array}\right]$$

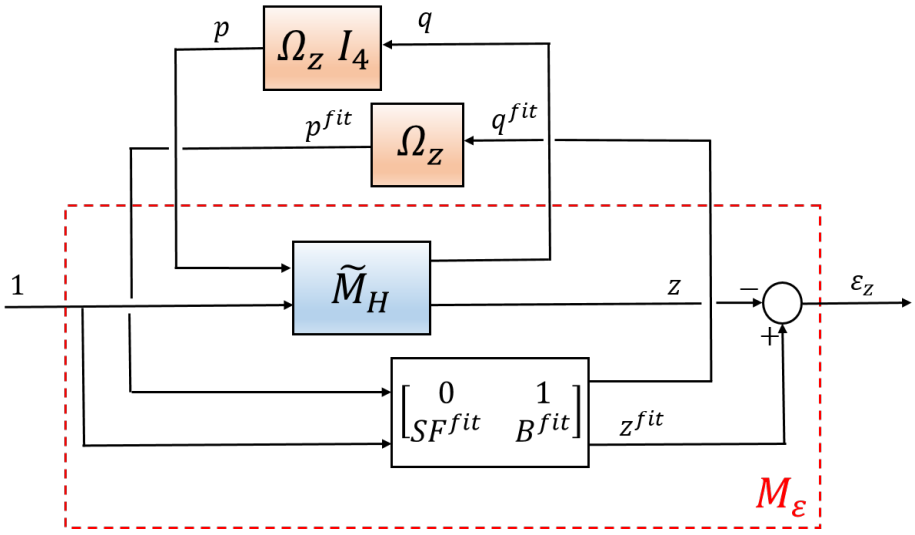

FIGURE 4.3: LFT for the computation of the output error ε_z

Finally, the model-based SFNL is given by the greatest absolute value of the output error ε_z over the interval $[\underline{\Omega}_z, \overline{\Omega}_z]$ divided by $(SF^{fit}\ \Omega^{fs})$, that is,

$$SFNL = \sup_{\Omega_z \in [\underline{\Omega}_z, \overline{\Omega}_z]} \left(\frac{|\Omega_z\ I_5 \star M_\varepsilon|}{SF^{fit}\ \Omega^{fs}} \right). \tag{4.4}$$

Such a case can be naturally addressed as a worst-case analysis with performance objective ε_z and depending on the parameter Ω_z. In the following section, we propose a model-based analysis method that allows to exactly compute the SFNL through an LMI optimization problem.

4.3 Scale factor nonlinearity LMI condition

In the previous sections, we introduce the LFT models of the MEMS resonator G_{Ω_z} and the closed-loop system H_{Ω_z}. We discussed how the gyroscope output z and the fitted output z^{fit} can be obtained from LFT interconnections. Then, we present how the output error ε_z, associated to the SFNL, can be computed from an LFT written as

$$\varepsilon_z = \Omega_z\ I_5 \star \tilde{M}_H = D_\varepsilon + C_\varepsilon \Omega_z (I - A_\varepsilon \Omega_z)^{-1} B_\varepsilon, \tag{4.5}$$

as illustrated in Figure 4.4.

As previously discussed, the SFNL is given by the greatest absolute value of the the worst-case output error ε_z. Its computation can be expressed as

$$SFNL = \frac{\sqrt{\eta_{SF}}}{SF^{fit}\Omega^{fs}}$$

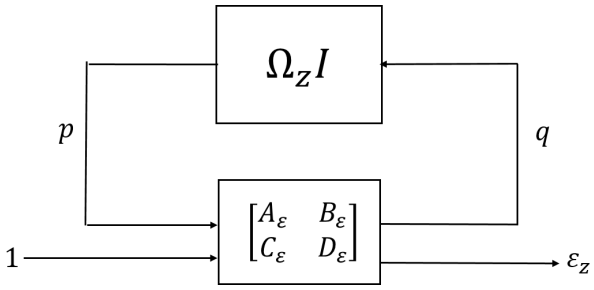

FIGURE 4.4: Interconnection associated to the output error

where η_{SF} is the solution of the optimization problem

$$\min_{\eta} \quad \eta$$

such that

$$\forall \Omega_z \in [\underline{\Omega}_z, \overline{\Omega}_z], \quad \left[\begin{array}{c} \Omega_z I \star \left[\begin{array}{cc} A_\varepsilon & B_\varepsilon \\ C_\varepsilon & D_\varepsilon \end{array} \right] \\ 1 \end{array} \right]^T \left[\begin{array}{cc} I & 0 \\ 0 & -\eta \end{array} \right] \left[\begin{array}{c} \Omega_z I \star \left[\begin{array}{cc} A_\varepsilon & B_\varepsilon \\ C_\varepsilon & D_\varepsilon \end{array} \right] \\ 1 \end{array} \right] \prec 0 \ . \tag{4.6}$$

This is a convex optimization problem under LMI constraints. Unfortunately, the number of LMI constraints is infinite, which precludes the problem solution. The following theorem allows to shows that we can replace the infinite-dimensional LMI condition (depending of a parameter in a continuous set) (4.6) by an equivalent LMI condition with a finite number of decision variables.

Theorem 4.1. *Let $\Omega_z \in [\underline{\Omega}_z, \overline{\Omega}_z]$ and let be the LFT interconnection*

$$\Omega_z I_n \star \left[\begin{array}{cc} A_\varepsilon & B_\varepsilon \\ C_\varepsilon & D_\varepsilon \end{array} \right].$$

Let $\boldsymbol{W}$ *be the set*

$$\boldsymbol{W} = \left\{ W = W^T \;\middle|\; \begin{array}{c} \exists \ X_D \in \mathbb{R}^{n\times n}, \ X_D \succ 0, \ \exists X_G = -X_G^T \in \mathbb{R}^{n\times n}, \\ W = \left[\begin{array}{cc} -2(\underline{\Omega}_z \overline{\Omega}_z) X_D & (\underline{\Omega}_z + \overline{\Omega}_z) X_D + X_G \\ (\underline{\Omega}_z + \overline{\Omega}_z) X_D + X_G^T & -2X_D \end{array} \right] \end{array} \right\}. \tag{4.7}$$

Then, the following two statements are equivalent:

1. *the quadratic constraint*

$$\left[\begin{array}{c} \Omega_z I \star \left[\begin{array}{cc} A_\varepsilon & B_\varepsilon \\ C_\varepsilon & D_\varepsilon \end{array} \right] \\ 1 \end{array} \right]^T \left[\begin{array}{cc} I & 0 \\ 0 & -\eta \end{array} \right] \left[\begin{array}{c} \Omega_z I \star \left[\begin{array}{cc} A_\varepsilon & B_\varepsilon \\ C_\varepsilon & D_\varepsilon \end{array} \right] \\ 1 \end{array} \right] \prec 0 \tag{4.8}$$

   is satisfied for all $\Omega_z \in [\underline{\Omega}_z, \overline{\Omega}_z]$;

2. *there exists $W \in \boldsymbol{W}$ such that*

$$\left[\begin{array}{cc} C_\varepsilon & D_\varepsilon \\ 0 & 1 \end{array} \right]^T \left[\begin{array}{cc} I & 0 \\ 0 & -\eta \end{array} \right] \left[\begin{array}{cc} C_\varepsilon & D_\varepsilon \\ 0 & 1 \end{array} \right] + \left[\begin{array}{cc} A_\varepsilon & B_\varepsilon \\ I_n & 0 \end{array} \right]^T W \left[\begin{array}{cc} A_\varepsilon & B_\varepsilon \\ I_n & 0 \end{array} \right] \prec 0 \tag{4.9}$$

The proof is a straightforward application of Theorem 1.1 in page 28 and Lemma 1.6 in page 41 of [Din05], with slight adaptations to our particular case.

Therefore, the computation of the SFNL is recast as

$$SFNL = \frac{\sqrt{\eta_{SF}}}{SF^{fit}\Omega^{fs}}$$

with η_{SF} the solution of

$$\begin{array}{c} \min\limits_{\eta} \quad \eta \\ \text{such that} \\ \exists\, W \in \boldsymbol{W}, \\ \left\{ \begin{bmatrix} C_\varepsilon & D_\varepsilon \\ 0 & 1 \end{bmatrix}^T \begin{bmatrix} I & 0 \\ 0 & -\eta \end{bmatrix} \begin{bmatrix} C_\varepsilon & D_\varepsilon \\ 0 & 1 \end{bmatrix} + \begin{bmatrix} A_\varepsilon & B_\varepsilon \\ I_n & 0 \end{bmatrix}^T W \begin{bmatrix} A_\varepsilon & B_\varepsilon \\ I_n & 0 \end{bmatrix} \prec 0 \right. , \end{array} \tag{4.10}$$

with $\boldsymbol{W}$ given by (4.7).

Please note that the bias can be easily determined as the particular case of computing the output z for $\Omega_z = 0$ in (4.5), having directly the equality $B = D_\varepsilon - B^{fit}$.

A final and interesting practical remark is that the output error can be influenced by the excitation frequency ω_{exc} of the applied drive mode reference signal. Indeed, given that $z = \Im\{H_{\Omega_z}(j\omega_{exc})\}$, an important mismatch between resonance frequency of the drive mode and the excitation frequency of the reference might lead to a deterioration of the gyroscope performance. This issue will be address in chapter 6, where an adaptative control strategy to compensate such mismatches is analyzed.

4.4 Thermal sensitivity LMI condition

The thermal sensitivity refers to the worst-case bias and the SFNL obtained in tests performed over an interval of temperature. As discussed in chapter 2, the temperature affects the damping mechanisms, the stiffness of the mechanical structures, among other effects. From a modeling point of view, the temperature does not modify the essential structure of the system (order and number of parameters), but the values of the system parameters. Hence, since the system model rationally depends on the parameters that are affected by the temperature T, the thermal sensitivity can be, as the model-based SFNL, evaluated by computing the maximum modulus of the output of an LFT interconnection between the parameters $\Omega_z \in [\underline{\Omega}_z, \overline{\Omega}_z]$, $T \in [\underline{T}, \overline{T}]$ and a constant matrix, as illustrated in Figure 4.5. This interconnection is given by

$$\exists \Delta(\Omega_z, T) \in \boldsymbol{\Delta_{ts}}, \Delta(\Omega_z, T) \star M_{H\varepsilon} = \left\{ \begin{array}{ll} p & = \Delta(\Omega_z, T) q \\ \begin{bmatrix} q \\ \varepsilon_z \end{bmatrix} & = \begin{bmatrix} A_\varepsilon & B_\varepsilon \\ C_\varepsilon & D_\varepsilon \end{bmatrix} \begin{bmatrix} p \\ 1 \end{bmatrix}, \end{array} \right. , \tag{4.11}$$

where the set $\boldsymbol{\Delta_{ts}}$ is defined as

$$\boldsymbol{\Delta_{ts}} = \left\{ \Delta(\Omega_z, T) \;\middle|\; \begin{array}{c} \exists\, \Omega_z \in [\underline{\Omega}_z, \overline{\Omega}_z], \\ \exists\, T \in [\underline{T}, \overline{T}], \\ \Delta = \mathrm{diag}(\Omega_z I_5, T I_n) \end{array} \right\}. \tag{4.12}$$

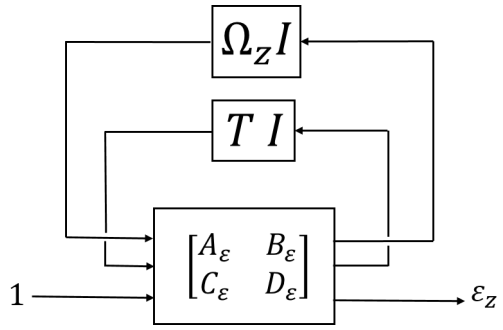

FIGURE 4.5: LFT model for thermal sensitivity

Similar to the model-based SFNL, the model-based thermal sensitivity can be computed as:

$$SFNL_{ts} = \frac{\sqrt{\eta_{ts}}}{SF^{fit}\Omega^{fs}}$$

where η_{ts} is the solution of the optimization problem

$$\min_{\eta} \quad \eta$$

such that

$$\forall \Delta \in \boldsymbol{\Delta_{ts}}, \quad \left[\Delta \star \begin{bmatrix} A_\varepsilon & B_\varepsilon \\ C_\varepsilon & D_\varepsilon \\ & 1 \end{bmatrix} \right]^T \begin{bmatrix} I & 0 \\ 0 & -\eta_{ts} \end{bmatrix} \left[\Delta \star \begin{bmatrix} A_\varepsilon & B_\varepsilon \\ C_\varepsilon & D_\varepsilon \\ & 1 \end{bmatrix} \right] \prec 0. \quad , \tag{4.13}$$

Let us then state the following theorem that introduces a sufficient condition that allows to obtain an upper bound on η_{ts} by solving a finite dimensional optimization problem.

Theorem 4.2. *Let be the bounded set* $\boldsymbol{\Delta_{ts}}$ *defined by* (4.12)*. Let be the LFT interconnection*

$$\Delta(\Omega_z, T) \star \begin{bmatrix} A_\varepsilon & B_\varepsilon \\ C_\varepsilon & D_\varepsilon \end{bmatrix}.$$

Let $\boldsymbol{W_{ts}}$ *be the set*

$$\boldsymbol{W_{ts}} = \left\{ \begin{bmatrix} W_{11} & W_{12} \\ W_{12}^T & W_{22} \end{bmatrix} \;\middle|\; \begin{array}{c} \exists\, X_{D\Omega_z} = X_{D\Omega_z}^T \in \mathbb{R}^{k_{\Omega_z} \times k_{\Omega_z}},\ X_{D\Omega_z} \succ 0, \\ \exists\, X_{G\Omega_z} = -X_{G\Omega_z}^T \in \mathbb{R}^{k_{\Omega_z} \times k_{\Omega_z}}, \\ \exists\, X_{DT} = X_{DT}^T \in \mathbb{R}^{k_T \times k_T},\ X_{DT} \succ 0, \\ \exists\, X_{GT} = -X_{GT}^T \in \mathbb{R}^{k_T \times k_T}, \\ \\ W_{11} = diag(-2\underline{\Omega_z}\overline{\Omega}_z X_{D\Omega_z}, -2\underline{T}\overline{T} X_{DT}) \\ \\ W_{12} = diag((\underline{\Omega_z} + \overline{\Omega}_z) X_{D\Omega_z} + X_{G\Omega_z}, \\ \qquad (\underline{T} + \overline{T}) X_{DT} + X_{GT}), \\ \\ W_{22} = diag(-2X_{D\Omega_z}, -2X_{DT}) \end{array} \right\} \tag{4.14}$$

Then, the quadratic constraint

$$\left[\begin{array}{c} \Delta(\Omega_z,T)\star\left[\begin{array}{cc} A_\varepsilon & B_\varepsilon \\ C_\varepsilon & D_\varepsilon \end{array}\right] \\ 1 \end{array}\right]^T \left[\begin{array}{cc} I & 0 \\ 0 & -\eta_{ts} \end{array}\right] \left[\begin{array}{c} \Delta(\Omega_z,T)\star\left[\begin{array}{cc} A_\varepsilon & B_\varepsilon \\ C_\varepsilon & D_\varepsilon \end{array}\right] \\ 1 \end{array}\right] \prec 0$$

is satisfied for all $\Delta(\Omega_z,T) \in \boldsymbol{\Delta_{ts}}$ *if there exists* $W \in \boldsymbol{W_{ts}}$ *such that*

$$\left[\begin{array}{cc} C_\varepsilon & D_\varepsilon \\ 0 & 1 \end{array}\right]^T \left[\begin{array}{cc} I & 0 \\ 0 & -\eta_{ts} \end{array}\right] \left[\begin{array}{cc} C_\varepsilon & D_\varepsilon \\ 0 & 1 \end{array}\right] + \left[\begin{array}{cc} A_\varepsilon & B_\varepsilon \\ I_n & 0 \end{array}\right]^T W \left[\begin{array}{cc} A_\varepsilon & B_\varepsilon \\ I_n & 0 \end{array}\right] \prec 0 \tag{4.15}$$

This result is a straightforward application of Theorem 1.1 in page 28 and Lemma 1.8 in page 44 of [Din05], adapted to our particular case.

Hence, it is possible to compute an upper bound on the thermal sensitivity by computing:

$$SFNL_{ts} \leq \frac{\sqrt{\eta_{ts}}}{SF^{fit}\Omega^{fs}}$$

with η_{SF} the solution of

$$\begin{array}{c} \min\limits_{\eta} \quad \eta \\ \text{such that} \\ \left\{ \begin{array}{c} \exists\, W \in \boldsymbol{W_{ts}}, \\ \left[\begin{array}{cc} C_\varepsilon & D_\varepsilon \\ 0 & 1 \end{array}\right]^T \left[\begin{array}{cc} I & 0 \\ 0 & -\eta \end{array}\right] \left[\begin{array}{cc} C_\varepsilon & D_\varepsilon \\ 0 & 1 \end{array}\right] + \left[\begin{array}{cc} A_\varepsilon & B_\varepsilon \\ I_n & 0 \end{array}\right]^T W \left[\begin{array}{cc} A_\varepsilon & B_\varepsilon \\ I_n & 0 \end{array}\right] \prec 0 \end{array} \right. , \end{array} \tag{4.16}$$

with $\boldsymbol{W_{ts}}$ given by (4.14).

The following section addresses a last case that aims to compute the SFNL from a system model that is obtained by using system identification methods. Such a case implies to work with models whose parameters are only approximately known, then to determine the performance of a system that is inherently uncertain.

4.5 Worst-case SFNL for models obtained by model prediction error identification

Theorem 4.1 allows to compute the scale factor nonlinearity of a controlled MEMS gyroscope through an LMI optimization problem based on a system model. The proposed theorem offers an exact solution for a given reference excitation frequency ω_{exc}. This result relies on the assumption that the values of the model parameters are completely known.

However, a more realistic scenario consists in considering model whose parameters are only approximately known. In fact, in the context of NEXT4MEMS project, the MEMS gyroscope models are obtained using system identification (data-based) methods. More specifically, the modeling is based on the model prediction error framework [Col20, Lju98].

The identification methods based on the model prediction error framework delivers, under the assumption that the system structure is known, a parametric model of the system $G(z,\theta)$. However, because of the presence of noise, and given that the number and the duration of the experiments are finite, the obtained parameters are only the estimates of the true model parameters. Indeed, the obtained parameters are usually different at each experiment.

Hence, the collection of identified parameters, grouped in the so-called identified parameter vector $\widehat{\theta}$, is a normally distributed random variable whose mean value is the collection of the real system parameters, contained in the so-called true parameter vector θ_0. The parameter space is then an ellipsoidal uncertain region $\boldsymbol{U}$ that is shaped by the covariance matrix P_θ, whose estimation is also delivered by the model prediction error method. The true parameter vector is then said to be contained in $\boldsymbol{U}$ with a certain probability level, chosen by the user, which defines the size of the uncertain region.

The uncertainty region $\boldsymbol{U}$ is given by an ellipsoidal set [BGSA01], illustrated in Figure 4.6 and defined as:

$$\boldsymbol{U} = \{\theta \in \mathbb{R}^{n_\theta} | (\theta - \tilde{\theta})^T P_\theta^{-1} \underbrace{(\theta - \tilde{\theta})}_{\delta_U} \leq \alpha\}, \tag{4.17}$$

where $\tilde{\theta}$ is the parameter estimate vector obtained from the identification process, $P_\theta \in \mathbb{R}^{n_\theta \times n_\theta}$ is the covariance matrix of $\tilde{\theta}$ and α is the factor allowing to adjust the probability level.

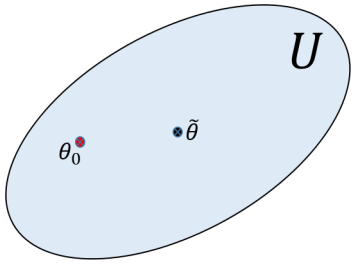

FIGURE 4.6: Ellipsoidal set $\boldsymbol{U}$

Let us then introduce the definition of the worst-case SFNL of uncertain systems.

Definition 4.5 (Worst-case scale factor nonlinearity)**.** *Let the MEMS gyroscope be modeled by a parametric model depending on the uncertain parameter vector θ, which belongs to the set $\boldsymbol{U}$. Then, the worst-case Scale Factor Nonlinearity is the maximal SFNL over the whole uncertainty region $\boldsymbol{U}$, that is*

$$SFNL_{wc} = \sup_{\theta \in \boldsymbol{U}} (SFNL(\theta))$$

with

$$SFNL(\theta) = \max_{\Omega_z \in [\underline{\Omega}_z, \overline{\Omega}_z]} \left(\frac{|z^{fit}(\Omega_z) - z(\Omega_z, \theta)|}{SF^{fit} \Omega^{fs}} \right).$$

Then, the objective is to determine an LMI condition that allows to compute an upper-bound on the maximum modulus of the output error ε_z, for all the angular rates $\Omega_z \in [\underline{\Omega}_z, \overline{\Omega}_z]$ and for all $\theta \in \boldsymbol{U}$.

Similar to the approach used in section 4.3, the output error ε_z, associated to the SFNL, can be computed as the output of an LFT interconnection that now includes not only the parameter Ω_z but also the uncertain vector δ_U, in the case of a SISO system. In the case of MIMO systems, depending on the identification method, it is possible to obtain more than one uncertain vector $\delta_{U1}, ...\delta_{Un}$, associated to the different SISO transfer functions, that belongs to ellipsoidal sets as in (4.17) (Figure 4.6).

The analysis of systems containing uncertain vectors belonging to an ellipsoidal set is adressed, for instance, in [SBBF07], where the results for repeated scalar uncertainties are extended to the case of repeated uncertain vectors, covering the case

of uncertain models obtained through the model prediction error method. More specifically, the authors consider normalized uncertain vectors i.e. $\delta^T\delta \leq 1$. The normalized uncertain vector can be derived from (4.17) as follows: having the uncertain region

$$\boldsymbol{U} = \{\theta \in \mathbb{R}^{n_\theta} | \delta_U^T R \delta_U \leq 1\},$$

with $R = \frac{P_\theta^{-1}}{\alpha}$, and given that the covariance matrix is always symmetric, then R is orthogonally diagonalizable, i.e. $R = V^T E V$, where E is a diagonal matrix. With $\tilde{E}$ being a diagonal matrix whose elements are the square root of the elements of E, we can express the uncertain set $\boldsymbol{\delta_U}$ as follows

$$\boldsymbol{\delta_U} = \{\delta_\theta \in \mathbb{R}^{n_\theta} | \delta_\theta^T \, \delta_\theta \leq 1\},$$

with $\delta_\theta = \tilde{E} V \delta_U$. Then, the matrix $\tilde{E}V$ can be directly integrated in the LTI part of the LFT interconnection.

Hence, ε_z can be computed from an LFT of the form:

$$\varepsilon_z = \Delta \star \begin{bmatrix} A_\varepsilon & B_\varepsilon \\ C_\varepsilon & D_\varepsilon \end{bmatrix}, \tag{4.18}$$

with Δ belonging to the set $\boldsymbol{\Delta}$, given by

$$\boldsymbol{\Delta} = \left\{ \Delta \;\middle|\; \begin{array}{c} \exists\, \Omega_z \in [\underline{\Omega}_z, \overline{\Omega}_z] \\ \forall i = 1, ...n, \;\; \exists\, \Delta_i = I_{n_i} \otimes \delta_{\theta i}, \; \delta_{\theta i} \in \mathbb{R}^{n_{\theta_i}}, \; \delta_{\theta i}^T \delta_{\theta i} \leq 1 \\ \Delta(\theta) = \mathrm{diag}(\Omega_z I, \delta_{\theta 1}, ...\delta_{\theta n}) \end{array} \right\}. \tag{4.19}$$

Then, the worst-case SFNL, given by Definition 4.5, can be computed as:

$$SFNL_{wc} = \frac{\sqrt{\eta_{wc}}}{SF^{fit}\Omega^{fs}}$$

where η_{wc} is the solution of the optimization problem

$$\min_{\eta} \quad \eta$$

$$\text{such that}$$

$$\forall \Delta \in \boldsymbol{\Delta} \quad \left(\Delta \star \begin{bmatrix} A_\varepsilon & B_\varepsilon \\ C_\varepsilon & D_\varepsilon \end{bmatrix}\right) \begin{bmatrix} I & 0 \\ 0 & -\eta \end{bmatrix} \left(\Delta \star \begin{bmatrix} A_\varepsilon & B_\varepsilon \\ C_\varepsilon & D_\varepsilon \end{bmatrix}\right) \prec 0, \;'$$

with $\boldsymbol{\Delta}$ given by (4.19).

Let us then introduce the following theorem that allows to compute an upper bound of the worst-case SFNL in the case of LFT interconnections depending on the parameter Ω_z and repeated uncertain vectors.

Theorem 4.3. *Let be the bounded set* $\boldsymbol{\Delta}$ *defined by* (4.19). *Let be the LFT interconnection*

$$\Delta \star \begin{bmatrix} A_\varepsilon & B_\varepsilon \\ C_\varepsilon & D_\varepsilon \end{bmatrix}.$$

Let the set $\boldsymbol{W_\Omega}$ *be given by*

$$\boldsymbol{W_\Omega} = \left\{ W = W^T \;\middle|\; \begin{array}{c} \exists\ X_D \in \mathbb{R}^{n\times n},\ X_D \succ 0,\ \exists X_G = -X_G^T \in \mathbb{R}^{n\times n}, \\ W = \begin{bmatrix} -2(\underline{\theta}\overline{\theta})X_D & (\underline{\theta}+\overline{\theta})X_D + X_G \\ (\underline{\theta}+\overline{\theta})X_D + X_G^T & -2X_D \end{bmatrix} \end{array} \right\}.$$

Let the W_k, $i \in \{k, ...n\}$ *belong to the set* $\boldsymbol{W_\delta}$ *defined as*

$$\boldsymbol{W_\delta} = \left\{ W = W^T \;\middle|\; \begin{array}{c} \exists\ X_D \in \mathbb{C}^{n\times n},\ X_D = X_D^*,\ X_D \succ 0 \\ \exists\ X_{Gi} \in \mathbb{C}^{n\times n},\ \forall\ i = \{1, ..., n_\delta\},\ X_{Gi} = -X_{Gi}^* \\ W = \left[\begin{array}{c|c} X_D & \sum_{k=1}^{n_\theta} X_{Gi} \otimes e_k^{n_\theta T} \\ \hline \sum_{k=1}^{n_\theta} X_{Gi}^* \otimes e_k^{n_\theta} & -X_D \bigotimes I_{n_\theta} \end{array}\right] \end{array} \right\},$$

with

$$e_k^{n_\theta} = \begin{bmatrix} 0_{1\times(k-1)} & 1 & 0_{1\times(n_\theta-k)} \end{bmatrix}^T.$$

Let $\boldsymbol{W}$ *be the set*

$$\boldsymbol{W} = \left\{ \begin{bmatrix} W_{11} & W_{12} \\ W_{12}^T & W_{22} \end{bmatrix} \;\middle|\; \begin{array}{c} \exists\ W_\Omega \in \boldsymbol{W_\Omega} \\ \forall\ i \in \{1, ..., n\},\ \exists W_{\delta_i} \in \boldsymbol{W_\delta} \\ W_{11} = diag(W_{\Omega_{11}}, W_{\delta_{1,11}}, ..., W_{\delta_{n,11}}), \\ W_{12} = diag(W_{\Omega_{12}}, W_{\delta_{1,12}}, ..., W_{\delta_{n,12}}), \\ W_{22} = diag(W_{\Omega_{22}}, W_{\delta_{1,22}}, ..., W_{\delta_{n,22}}), \end{array} \right\} \tag{4.20}$$

Then, the quadratic constraint

$$\left(\Delta \star \begin{bmatrix} A_\varepsilon & B_\varepsilon \\ C_\varepsilon & D_\varepsilon \end{bmatrix}\right) \begin{bmatrix} I & 0 \\ 0 & -\eta \end{bmatrix} \left(\Delta \star \begin{bmatrix} A_\varepsilon & B_\varepsilon \\ C_\varepsilon & D_\varepsilon \end{bmatrix}\right) \prec 0$$

is satisfied, for all $\Delta \in \boldsymbol{\Delta}$, *if there exists* $W \in \boldsymbol{W}$ *such that*

$$\begin{bmatrix} C_\varepsilon & D_\varepsilon \end{bmatrix}^T \begin{bmatrix} I & 0 \\ 0 & -\eta \end{bmatrix} \begin{bmatrix} C_\varepsilon & D_\varepsilon \end{bmatrix} + \begin{bmatrix} A_\varepsilon & B_\varepsilon \\ I_n & 0 \end{bmatrix}^T W \begin{bmatrix} A_\varepsilon & B_\varepsilon \\ I_n & 0 \end{bmatrix} \prec 0$$

The result is an application of Theorem 1.1 in page 28 and Lemma 1.8 in page 44 of [Din05], combined with an adapted version of Lemma 3.1 in [SBBF07].

The worst-case SFNL upper bound can be then computed as:

$$SFNL_{wc} \leq \frac{\sqrt{\eta_{wc}}}{SF^{fit}\Omega^{fs}}$$

with η_{wc} the solution of

$$\min_{\eta} \quad \eta$$

$$\left\{ \begin{array}{c} \text{such that} \\ \exists\, W \in \boldsymbol{W}, \\ \begin{bmatrix} C_\varepsilon & D_\varepsilon \\ 0 & 1 \end{bmatrix}^T \begin{bmatrix} I & 0 \\ 0 & -\eta \end{bmatrix} \begin{bmatrix} C_\varepsilon & D_\varepsilon \\ 0 & 1 \end{bmatrix} + \begin{bmatrix} A_\varepsilon & B_\varepsilon \\ I_n & 0 \end{bmatrix}^T W \begin{bmatrix} A_\varepsilon & B_\varepsilon \\ I_n & 0 \end{bmatrix} \prec 0 \end{array} \right. ,$$

with $\boldsymbol{W}$ given by (4.20).

The different results, presented along this chapter, allow to determine the different accuracy and robustness performance specifications by solving finite dimensional LMI optimization problems. In the following sections, we implement the introduced set of tools to evaluate the accuracy and sensitivity performance specifications. First, we present an example based on a MEMS gyroscope model. This allows to implement Theorem 4.1 and Theorem 4.2 to respectively determine the SFNL and thermal sensitivity, and compare it with results obtained by Monte Carlo simulations.

Secondly, we address an application case, where the model, as well as its uncertainty region, is obtained by system identification. Then, applying Theorem 4.3, we determine the worst-case SFNL and we compare it with Monte Carlo simulations and experimental results.

4.6 Numerical example: SFNL and thermal sensitivity of a controlled MEMS gyroscope model

In order to illustrate the results introduced along the chapter, let us first consider the study of a controlled MEMS gyroscope model. The nominal system model, as well as the information related to the thermal sensitivity of the parameters, is obtained from a model provided by one of the Next4MEMS industrial partners. The main features of such a model are listed below.

- It is a parametric model that takes the physical structure of the two modes as mass-spring-damper systems. This model also includes non-ideal couplings. The model can be then transformed to the LFT representation given by (B.2).
- It provides a coefficient of the relationship between the resonance frequencies and the temperature, obtained through thermal tests performed in a known range of temperature.
- It also provides a coefficient of an approximated linear relationship between the quality factor Q and the temperature.
- The stiffness couplings are obtained by using the quadrature errors measured during identification (see [OAL+05], [DA09] for quadrature error and their physical interpretation). The damping couplings are considered to be zero.

Part 1: in the first part of the example, we consider the nominal model, that is, the model given for the nominal temperature of $20°C$. Then, we compute the SFNL using the optimization problem (4.10). The LFT interconnection is constructed by using the aforementioned model, as well as one of the designed MIMO LTI controllers [Sag21]. We carried out the analysis for an interval $[-1000, 1000]°/s$, exciting the system at a frequency $\omega_{exc} = \omega_0$, with ω_0 being the resonance frequency of the drive mode, which allows to obtain the best performance.

Then, in order to evaluate the LMI model-based computation of the SFNL, computed by the optimization problem (4.10), we compare it to a Monte Carlo approach.

The Monte Carlo method consists in computing the output error $\varepsilon_z(\Omega_z)$ corresponding to several sampled angular rates Ω_z over the whole set $[-1000, 1000]^\circ/s$, then computing the quantity $|\varepsilon_z(\Omega_z)|/(SF^{fit}\Omega^{fs})$.

The results are illustrated in Figure 4.7. They show that the model-based LMI solution accurately corresponds to the maximal measurement error over the whole range of input angular rates, showing that Theorem 4.1 provides a sufficient and necessary condition to compute the SFNL.

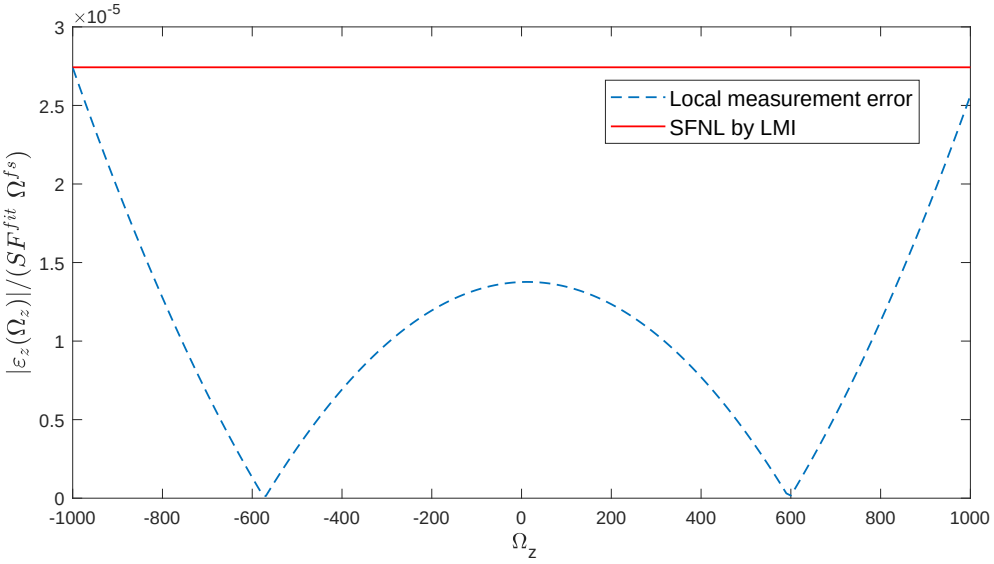

FIGURE 4.7: Comparative of LMI model-based SFNL versus Monte Carlo

Part 2: the second analysis focuses on the thermal sensitivity of the MEMS gyroscope. The effect of the temperature on the different parameters is integrated in the model. The uncertainty is given for a variation of temperature in an interval going from $0°C$ to $40°C$, where $20°C$ is the nominal temperature. Then, solving the optimization problem (4.16), we compute an upper-bound for the thermal sensitivity over the whole interval of tested temperatures.

Then, we compare the results of the LMI-based SFNL thermal sensitivity with those obtained by a Monte Carlo approach. The Monte Carlo (MC) analysis is performed by taking random values of temperature in the interval $[0, 40]°C$ and analytically computing the maximal error over the whole (sampled) angular rate interval $[-1000, 1000]^\circ/s$. The results are summarized in Table 4.1.

Since Theorem 4.2 provides only sufficient conditions, it is important to investigate the possible conservatism introduced by the quadratic separator W. Two indicators allows to evaluate the quality of the worst-case analysis tool.

1. **Upper bound.** The developed method allows to determine an upper-bound on the worst-case scenario. Then, the computed upper-bound must be over all the computed SFNL using the Monte Carlo method. Otherwise, the result indicates a computation error.

2. **Conservatism.** A desired feature in any analysis method is that it gives results that are not excessively conservative. Then, the distance between the computed upper-bound and the worst Monte Carlo result should be reasonable.

We can observe that the first indicator (upper bound) is satisfied since any of the thermal sensitivity bounds obtained by Monte Carlo are over the thermal sensitivity

Specification (method)	Value
SFNL for nominal T (LMI and MC)	$2.7428 \cdot 10^{-5}$
SFNL thermal sensitivity (LMI)	0.0104
SFNL thermal sensitivity (MC)	0.0082

TABLE 4.1: Results of the SFN thermal sensitivity (LMI versus Monte Carlo)

upper bound computed by the proposed LMI optimization. Then, the second indicator (conservatism) can be said to be satisfactory given that the worst-case result obtained by Monte Carlo method is very close to the computed worst-case upper bound.

We can notice that the variations of the temperature have a radical impact on the degradation of obtained performances. The impact of the variations of the resonance frequency are much more critical than the variations of the quality factor. An option to improve the effect of temperature is to obtain fitted functions $z^{fit}(\Omega_z, T)$ for tests performed at different temperatures, which allows an a posteriori compensation. In general, the study of temperature effect and the research of temperature sensing compensation methods is a major topic on the performance improvement of MEMS sensors [PTS13, SEGT00, TSS09, SHC+12, KHC+08, FLW11, GHL+15, FKP+05, PTS12, XCWL09]. In the context of the Next4MEMS project, we propose an adaptive method consisting in a parameter-dependent control that allows to parameterize the controller depending on the estimated drive mode resonance frequency, this topic is addressed in chapter 6.

4.7 Application case: study of the experimental SFNL

Let us now introduce an application case, where we apply the proposed analysis tools in a context that relates the results obtained from the different works carried out in the framework of the Next4MEMS project. First, the models are obtained from experimental data on a MEMS gyroscope and using the identification methods developed in the project. Then, the controllers are synthesized from a simplified version of the model using also methods developed in this project. The MEMS gyroscopes and the development kits that allowed the implementation of the developed methods were provided by our industrial partners.

The objective of this section is to evaluate the performance obtained with one of the controllers that has been experimentally tested. The uncertainty of the obtained models has been integrated in the analysis in order to determine an upper bound on the worst-case performance using the model, the controller and the uncertainties. Then, these results are compared to the experimentally observed results.

4.7.1 Test platform: AS3125-SDK

The operation of a gyroscope is carried out by relying on a whole set of electronic systems and processing units that allow the basic operations of actuation and measurement, as well as the implementation of the control and processing of the signals necessary for the calculation of the rotation speed. The packaging of one of the MEMS gyroscopes used in the project is presented in Figure 4.8.

FIGURE 4.8: MEMS gyroscope packaging

The MEMS gyroscopes were supplied by the company Tronics, which is one of the NEXT4MEMS industrial partners. The MEMS gyroscope packaging contains the mechanical structure of the MEMS modes, as well as the comb-drive actuators and sensors. Furthermore, we employed the AS3125-SDK electronic platform, designed by the society ASYGN, to realize the experimental tests. The functionalities of the test platform are shared between an ASIC (Application-Specific Integrated Circuit) and an FPGA (Field-Programmable Gate Array).

The ASIC contains the charge amplifiers that transform the capacitance variations of the comb-drive sensor into an analog voltage signal, followed by an analog to digital converter (ADC). In the opposite direction, the ASIC contains the digital to analog converters (DAC) for the signals that are send to the gyroscope actuators.

The ASIC communicates with the FPGA, which works as the system processor. The controllers, synchronous demodulation digital filters, and closed-loop computational algorithms are programmed in a development software, then implemented in the FPGA, which allows a flexibility for the implementation of different control and processing strategies.

4.7.2 Model, controllers and uncertainty

The MEMS drive and sense modes were modeled using system identification techniques, that is, data-based modeling. The main used method is the model prediction error. Two models were derived during the modeling stage: a first black-box model of higher order and a second grey-box model of lower order that was obtained from the first model. The objective of deriving a lower-order model was to exploit it in the control design process.

See the PhD manuscript of Kevin Colin for further details of the system identification process in the Next4MEMS project [Col20]. The Bode plot of the reduced model is presented in Figure 4.9.

The MIMO controller is designed using the H_∞ method. Several control objectives are pursuit, for instance, the tracking of the drive mode sinusoidal reference signal, the minimization of the control signal energy, the rejection of the Coriolis force perturbing the sense mode and the attenuation of the effect of noise and unmodeled dynamics. The relationship between the control objectives and the global performances is briefly discussed in Appendix B. The different control objectives are translated into the form of frequency domain constraints that shape the desired closed-loop response. For instance, in Figure 4.10, the drive mode tracking is illustrated in the left part and the sense mode Coriolis rejection in the right part, translating the objective of respectively minimizing the tracking error and the impact of the Coriolis force for a frequecy interval around the drive mode resonance frequency.

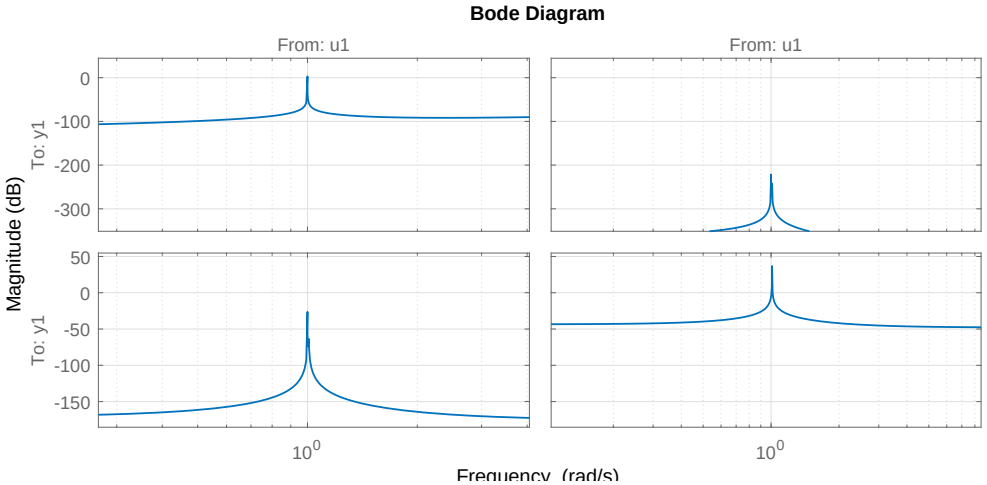

FIGURE 4.9: Bode of black-box identified model (normalized)

The complete details of the control design process used in the Next4MEMS project can be found in the PhD manuscript of Fabricio Saggin [Sag21]. Here, we present some of the closed-loop responses obtained by applying the designed controller.

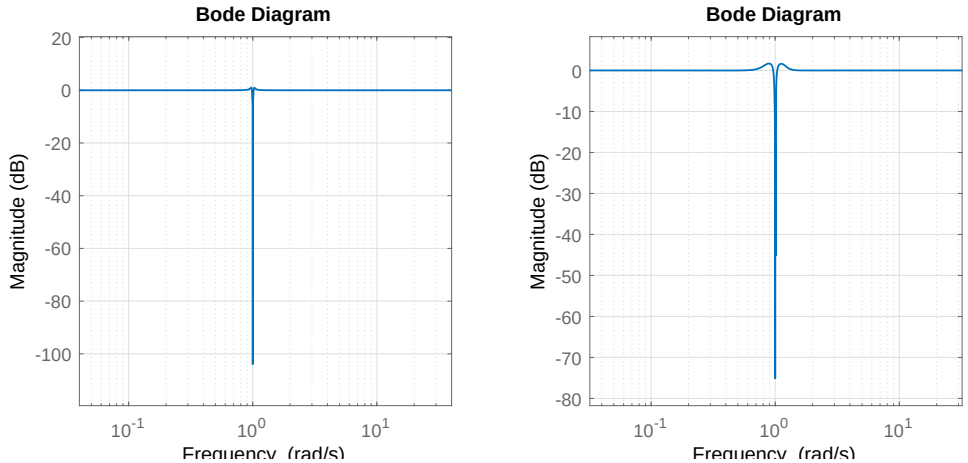

FIGURE 4.10: Closed-loop responses: drive mode tracking error(left) and sense mode Coriolis rejection (right)

As previously mentioned, the model prediction error method allows to determine an uncertainty region on the model parameters estimate. In this case, we consider for the analysis the original black-box model, which is a richer representation of the system dynamics. The identification process gives the model with the parameter estimate, as well as the covariance matrix that can be related to the model uncertainty through the relationship

$$\theta \in U = \{\delta | (\theta - \tilde{\theta})^T R^{-1} (\theta - \tilde{\theta})) < \alpha\},$$

with α a constant associated to the probabilistic confidence interval, here adjusted for a standard deviation of 6σ, that is, a probability level over 99%.

The MEMS resonator is MIMO system with two inputs and two outputs, and it has been identified by using a SISO by SISO approach, that is, each transfer function is identified independently of the others. However, the model uncertainties are

only taken into account for the diagonal transfer functions (drive input to drive output and sense input to sense output), while one of the coupling transfer functions has been considered as nominal (or certain) and the other neglected. This is due to the practical difficulty to identify the coupling (off-diagonal) transfer functions and their corresponding uncertainties since their amplitude and SNR are very weak with respect to the diagonal transfer functions.

4.7.3 Result

We integrate the black-box model, the designed controller and the computed uncertainties of the model in the analysis tool to determine the upper bound on the worst-case SFNL. Since the test room does not dispose of thermal control, the drive mode resonance frequency was observed to present small deviations on an interval of 0.001 Hz. This mismatch between resonance and excitation frequency was also taken into account. Different tests were performed at input angular rates in the interval $[-300, 300]^\circ/s$.

The results are presented in Figure 4.11. The measure errors are given in angular rate units ($^\circ/s$). We compare the experimental results, the errors obtained through Monte Carlo simulations and the upper bound on the worst-case SFNL obtained by solving the LMI optimization problem (4.5).

Let us first compare the worst-case error, obtained by the Monte Carlo and the LMI approaches. Since Theorem 4.3 gives only a sufficient condition, the LMI approach allows to obtain an upper bound on the worst-case error, equals to 12.063, while the maximal error obtained by Monte Carlo is equals to 8.391. It illustrates that the LMI approach actually offers an upper bound on the worst-case error. Indeed, since the Monte Carlo approach is the maximal error over all the simulated configurations, it delivers a lower-bound on the worst-case error. Concerning the experimental results, the LMI upper bound is also validated with respect to the maximal experimental result (9.159).

Then, let us compare the Monte Carlo and the experimental results, focusing on the tested angular rates. In contrast to the LMI approach, which takes into account the whole model set, both Monte Carlo and experimental approaches come to sample the model set and to compute the error for those particular sampled configurations. The Monte Carlo method fixes the tested angular rate and randomly generates values of the uncertain vector, then computes the corresponding error. In this case, we perform 200 random tests for each tested angular rate. Next, the experimental result is equivalent to take a particular point of the model set. In this sense, the Monte Carlo approach should allow to estimate the worst-case error since it allows to test more system configurations than the experimental approach. In order to obtain an equivalent experimental worst-case estimate, it would be necessary to perform a large number of experiments, under very controlled conditions that allows to properly sample the whole model set.

Sometimes, the experimental measure can be greater than the Monte Carlo error, which is possible since the Monte Carlo method allows to estimate the worst-case only with a certain probability level, which implies the possibility of missing a critical scenario.

Even though this first preliminary results offer promising results, additional experimental tests for system identification and control validation might give some insight on the likelihood of the experimental worst-case error.

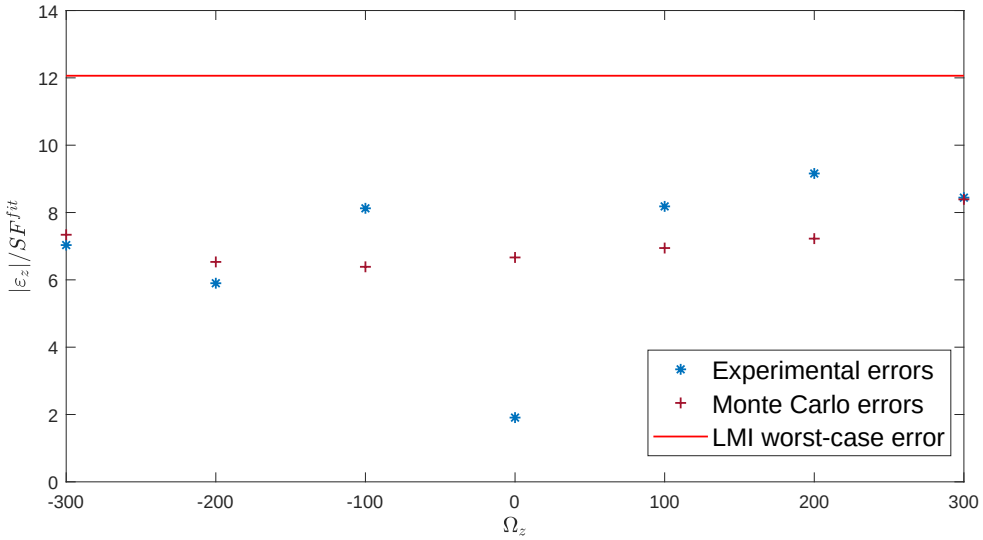

FIGURE 4.11: Comparison of experimental, Monte Carlo and LMI worst-case errors

4.8 Chapter conclusion

In this chapter, we tackle the analysis of the performance specification related to the measurement errors, that is, the bias and the scale factor nonlinearity (SFNL), as well as their thermal sensitivity. The chapter begins by giving formal definitions of the performance specifications. We then introduce an LFT model of the closed-loop system that depends on the input angular rate.

Afterwards, we take into account the effect of synchronous demodulation in the output of the MEMS gyroscope model. We then show how the output error, having a direct connection with the performance specifications, can be computed as the output of a real constant LFT interconnection. We observe that the computation of the SFNL is related to an optimization problem with an infinite number of LMI constraints. The LMI can be solved by replacing the original problem by a finite dimensional optimization problem whose conditions are sufficient and necessary. We discuss that the case involving a single repeated parameter belonging to an interval, which is the case of the nominal SFNL, allows to introduce a quadratic separator that leads to a sufficient and necessary condition.

The result of the SFNL is then extended to two other cases: the computation of the SFNL thermal sensitivity and the computation of the worst-case SFNL for models obtained by system identification (data-based). There equally exist sets of quadratic separators for both cases. However, they only lead to sufficient conditions. The chapter ends by testing the proposed tools on a numerical example and an application case in a real MEMS gyroscope.

Chapter 5

Analysis of Output Noise Level

In chapter 4, we studied some of the main performance specifications on MEMS gyroscopes industry: the bias and the scale factor nonlinearity as well as their thermal sensitivity. The other critical performance indicator concerns the output noise.

To measure the quality of a signal affected by noise, we can consider a comparison between the desired signal and the noise using the Signal to Noise Ratio (SNR), or by setting the signal of interest at zero and evaluating the power of the noise, also known as RMS noise. In both cases, it is necessary to quantify the power of the noise signal.

In the particular case of MEMS sensors, the evaluation of the output noise performance has been standardized, using as main tool the Allan variance method. Based on the study of this particular method method, our objective in this chapter is to propose alternative model-based tools to compute the Allan variance of MEMS gyroscopes.

5.1 Noise in MEMS gyroscopes and the Allan Variance method

In any measurement application, high levels of noise are undesirable since it distorts the exact value of the output signal. In the case of MEMS inertial sensors, output noise can be still more critical. In fact, in many applications, MEMS inertial sensors are integrated to Inertial Measurements Units (IMU) which, even in the absence of the Global Positioning System (GPS), must provide a reliable measure of angular position and linear velocity. Angular position and linear velocity are usually obtained by integrating the angular rate and the acceleration given by the gyroscope and the accelerometer, respectively.

In Figure 5.1, we present two output measurements of a static gyroscope (zero input angular rate), modeled as zero mean Gaussian processes, with two different noise levels characterized by their standard deviation σ_n. Then, in Figure 5.2, we can observe the evolution of the angular positions over the time, obtained by integration of the output angular rate. Ideally, the angular position should be zero, however, we observe that, in the presence of noise, the computed angular position diverges from the real value, even if the mean of the noise process is zero. Secondly, we can see that the magnitude of the accumulated error diverges faster in the presence of a higher noise level. We can then infer how necessary is to establish strong constraints with respect to the observed output noise.

The employed methods to evaluate output noise of MEMS gyroscopes, as well as the test protocols, have been standardized in the *IEEE standard specification format guide and test procedure for coriolis vibratory gyros* [IEE04], whose methods and protocols can also be found in the *IEEE standard specification format guide and test procedure for single axis interferometric fiber optic gyros* [IEE06]. More general standard

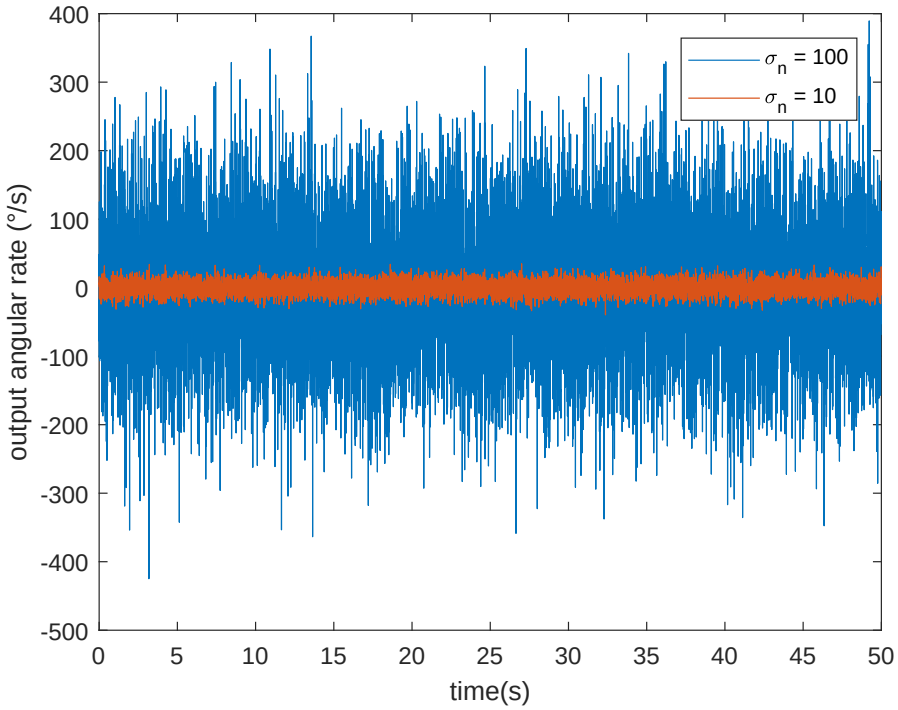

FIGURE 5.1: Noise of output angular rate

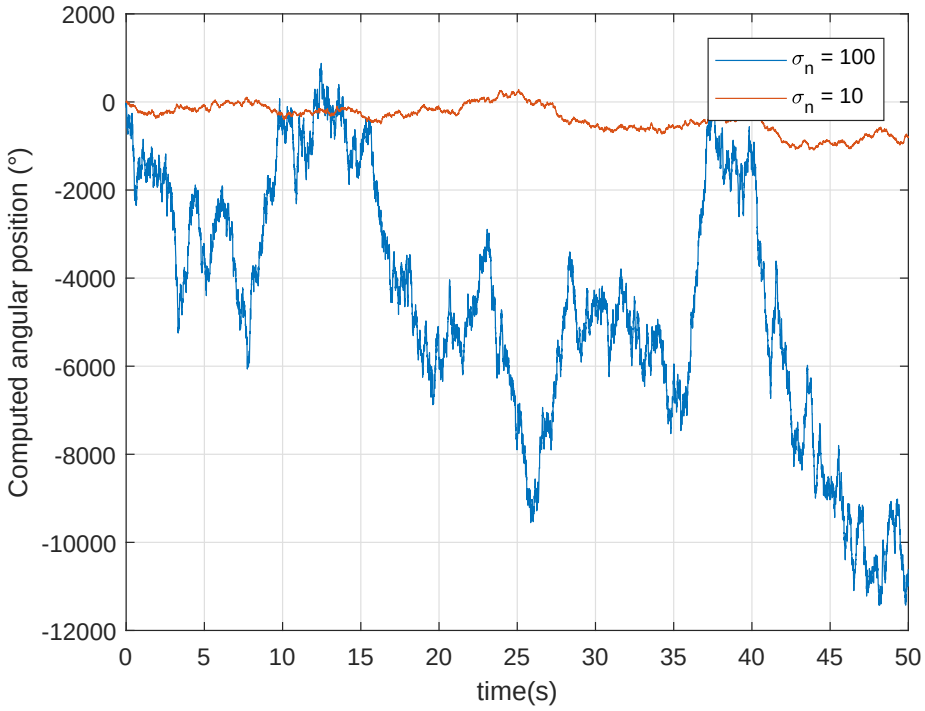

FIGURE 5.2: Computed angular position

definitions of inertial sensors can be found in *IEEE Standard for Sensor Performance Parameters Definition* [IEE18].

The standard procedure to evaluate output noise performance of MEMS inertial sensors (accelerometers and gyroscopes) is the Allan variance method. The Allan variance was introduced in 1966 by David W. Allan [All66] to study the stability of atomic clocks. Then, in the eighties, it started to be applied on the measurement of output noise of inertial sensors [Teh83].

The Allan variance is a time domain characterization that allows to identify properties of a random signal whose frequency content is richer than the one that can be detected, for instance, by using the Root Mean Square (RMS) noise identification.

Since the Allan variance is a characteristic of a signal, the first step to apply this method to MEMS gyroscopes consists in performing a long measurement, usually of some hours, of the noisy gyroscope output $\Omega(t)$, with the input set to zero (no angular motion). Then, we compute the Allan variance, defined as follows.

Definition 5.1 (Allan variance)**.** *Let $y(t)$ be the realization of an ergodic random signal. Then, the Allan variance $\sigma_y^2(T)$ is defined as*

$$\sigma_y^2(T) = \frac{1}{2}\left\langle \left(\overline{y}_T(t+T) - \overline{y}_T(t)\right)^2 \right\rangle \tag{5.1}$$

with $\langle\rangle$ denoting the averaging operation given by

$$\langle f(t)\rangle = \lim_{T_e\to\infty} \frac{1}{T_e}\int_{-T_e/2}^{T_e/2} f(t)dt,$$

and $\overline{y}_T(t)$ the local average of $y(t)$ over an interval T, defined as

$$\overline{y}_T(t) = \frac{1}{T}\int_t^{t+T} y(\tau)d\tau. \tag{5.2}$$

Remark: The computation of the Allan variance is based on the obtained experimental data, which is usually in discrete-time. However, in this chapter we focus on the continuous-time evaluation, which is more suitable to the proposed Allan variance estimation methods.

Finally, we obtain the Allan deviation $\sigma_y(T)$ by computing the square root of the Allan variance. The values are plotted on a semilogarithmic scale graphic of the Allan deviation as a function of the local averaging time T, which is shown on Figure 5.3.

As mentioned before, the RMS value, that can be seen as the classical probabilistic variance of a stationary and ergodic random signal, does not allow to completely characterize the frequency content of correlated random signals. In Figure 5.3 we can observe that the Allan deviation plot presents straight lines of different slopes, each of them characterizing different frequency components, as $1/\nu$ and $1/\nu^2$, in the spectrum of the measured signal. The Allan variance is not the only possible characterization of output noise. In fact, other variances such as the Picinbono and Hadamard variances [Gag98, Bau71] allow to identify the presence of higher order noise components, for instance $1/\nu^3$. However, the Allan variance is, in general, sufficient to evaluate the random signals that we usually find in MEMS gyroscopes.

There are two main types of noise that are of interest in MEMS gyroscopes standards. First, in Figure 5.3, we can observe an interval where the Allan deviation $\sigma_y(T)$ has a linear behavior with a slope of -1/2. This indicates the presence of a

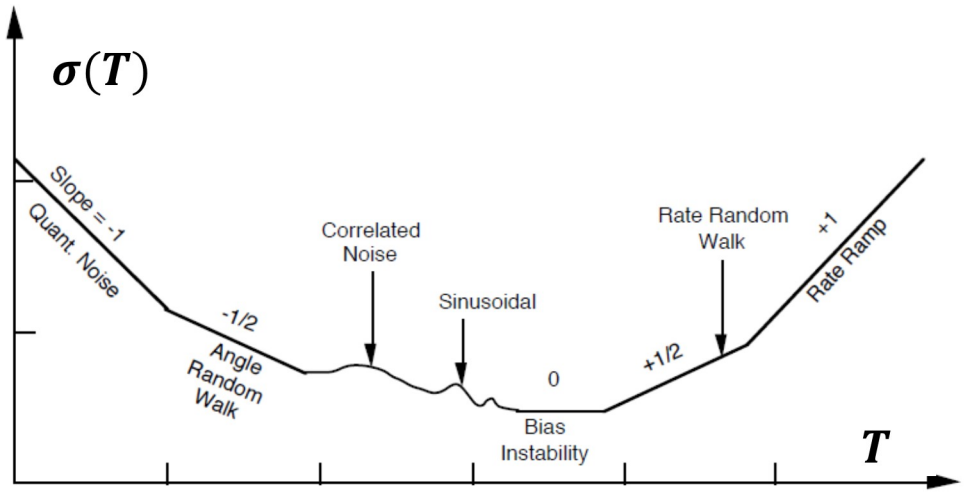

FIGURE 5.3: Allan deviation plot (adapted from [IEE06])

white noise component in the sensor output and it is usually named as *Angle Random Walk* in the MEMS community. Secondly, the *Bias Instability* is defined as the lower point in the Allan Deviation plot, which can sometimes appear as a line of zero slope. Bias Instability can be caused by Flicker noise ($1/f$ noise) or by slow bias changes over long time measurements.

To summarize, some of the main motivations to implement the Allan variance on MEMS gyroscopes are the following.

- It responds to the need of a standard method to discriminate and measure different types of noise that we find in MEMS gyroscope measures.
- Although Allan variance may diverge for some types of noise, it is well adapted for the noise usually found in MEMS sensors: white noise and $1/\nu$ noise.
- Its implementation, computation and interpretation are relatively simple.

We can find several works devoted to the application of the Allan variance method to the study of output noise in MEMS inertial sensors [SHC+12, DVS+17], in some cases including also the effect of temperature [TSS09, VBH12, Hou04] or comparing complex stochastic models with experimental results [PS10].

However, Bias Instability is frequently detected at very high values of the local averaging time (T >30 minutes). Since the Allan variance is computed from the difference of at least two averaged intervals, the duration of the experiments must be greater than twice the maximal T to be plotted. Therefore, the implementation of the Allan variance method demands to perform considerably long experiments, as well as the corresponding data processing to compute the Allan variance plot.

As discussed in chapter 2, long experimentation is probably not the most efficient alternative for performance validation in a control design process, mainly in the step where several controllers and control strategies are to be evaluated. Then, our objective in this chapter is to propose a complementary approach that, instead of computing the Allan variance from an experimental measure, allows to estimate the same performance indicator using an approach based on the concept of generator filter, hereafter called model-based Allan variance estimation. That is, we aim to compute the Allan variance by analyzing the model of the system that generates the signal to be evaluated.

To this end, it is possible to carry out an experimental step, only few times, at the beginning of the control process, within the system identification process. The purpose is to identify the generator filter, detecting its behavior over long times, and then evaluate the Allan variance using the properties of the generator filter model, as it is introduced in section 5.3.

Therefore, once system identification is applied, it is possible to obtain the characteristics of the noise processes in the system, as well as the model of the gyroscope itself. We can thus change the configuration of the controlled gyroscope: to study open-loop or closed-loop behavior, to test the designed controllers with different parameters or structures, or to consider control techniques that imply more important modifications of the feedback loop. It is then possible to compute the Allan variance without performing any additional experiment and to compare different control strategies at some given operation conditions.

We can also enhance the model by considering different working conditions, modeling errors and environmental changes, that is, including uncertainty. In this case, we can consider a robustness analysis that offers a guarantee of a worst-case Allan variance, despite the variations of the test conditions, allowing to prove the robustness of the controlled system with respect to output noise performance. The worst-case Allan variance will be presented in section 5.4.

A final crucial aspect, is the fact that the gyroscope output is the in-phase component obtained by applying synchronous demodulation. The presence of a demodulator introduces in the generator filter a time-varying phenomenon that modifies the power spectral density of the output signal. Hence, it is necessary to determine how the Allan variance can be computed from a system model when synchronous demodulation is included in it. This question is tackled in section 5.5.

To summarize, the following problems must be addressed in order to construct a model-based method for the estimation of the Allan variance in MEMS gyroscopes.

- Formally establish the relationship between the performance indicator (Allan variance) and the characteristics of the signal to be evaluated (section 5.2).
- Determine how to compute the Allan variance using a generator filter approach: for the nominal case (section 5.3) and for the uncertain case (section 5.4).
- Determine how to compute the Allan variance using a generator filter that includes demodulation. (section 5.5).

Once the previous problems have been solved, in section 5.6, the developed tools are implemented to estimate the Allan variance of a MEMS gyroscope, and it is then compare it to experimental results.

5.2 Allan variance in the frequency domain

In order to provide an equivalent measure estimation, the first step is to understand which are the properties of a noisy signal that the Allan variance describes. To this end, we introduce below a result that relates the Power Spectral Density (PSD) of the signal of interest to its Allan variance [BCC+71, Hou04].

Theorem 5.1. *Let y be a stationary and ergodic random signal whose Power Spectral Density is S_y. Then, the Allan variance $\sigma_y^2(T)$ is given by*

$$\sigma_y^2(T) = \int_{-\infty}^{+\infty} |H_{All_T}(\nu)|^2 S_y(\nu) d\nu \tag{5.3}$$

with

$$H_{All_T}(\nu) = \sqrt{2}\frac{\sin^2(\pi T\nu)}{\pi T\nu}. \tag{5.4}$$

Proof. The averaged output $\overline{y}_T(t)$, defined by Equation (5.2), can be seen as the convolution product between the signal $y(t)$ and the impulse response h_{Ave_T} of a linear filter (Figure 5.4), given by

$$h_{Ave_T}(t) = \frac{1}{T} rect\left(\frac{t + T/2}{T}\right) \tag{5.5}$$

where $rect(\cdot)$ is the rectangle function.

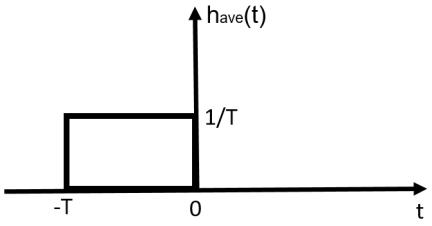

FIGURE 5.4: Impulse response of h_{Ave_T}

Let us define the signal d_T as follows

$$\forall\ t \in \mathbb{R} \quad d_T(t) = \frac{1}{\sqrt{2}}\left(\overline{y}_T(t+T) - \overline{y}_T(t)\right) \tag{5.6}$$

which can be seen as the response to a signal y of a linear filter h_{All} whose impulse response (Figure 5.5) is:

$$h_{All_T}(t) = \frac{1}{\sqrt{2}T}\left(rect\left(\frac{t + 3T/2}{T}\right) - rect\left(\frac{t + T/2}{T}\right)\right). \tag{5.7}$$

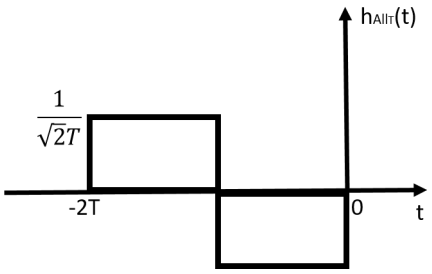

FIGURE 5.5: Impulse response

Then, the Allan variance is equal to the application of the averaging operator to the square of the signal $d_T(t)$, which is actually the expression of the power signal of

d_T:

$$\sigma_y^2(T) = P_{d_T} = \lim_{T_e \to \infty} \frac{1}{T_e} \int_{-T_e/2}^{+T_e/2} d_T^2(t)dt. \tag{5.8}$$

The power P_{d_T} can be also computed in the frequency domain by integrating the Power Spectral Density (PSD) of d_T as follows

$$\sigma_y^2(T) = P_{d_T} = \int_{-\infty}^{+\infty} S_{d_T}(\nu)d\nu \tag{5.9}$$

with S_{d_T} the PSD of d_T. Now, as mentioned above, the signal d_T is the output of the convolution product between the impulse response h_{All_T} and the signal y. Hence, it is possible to establish a relationship between the PSD of y and the Allan variance, given by the expression

$$\sigma_y^2(T) = P_{d_T} = \int_{-\infty}^{+\infty} |H_{All_T}(\nu)|^2 S_y(\nu)d\nu \tag{5.10}$$

where H_{All_T} is the frequency response of the filter with impulse response h_{All_T}. Therefore, the link between the signal y and the Allan variance $\sigma_y^2(T)$ is given by the frequency response $H_{All_T}(\nu)$ of some particular filter, hereafter referred to as *Allan filter*.

Now, assuming y and $\overline{y}$ to be stationary and ergodic, we have the power of d_T given by:

$$P_{d_T} = R_{d_T}(0) = R_{\overline{y}}(0) - R_{\overline{y}}(T)$$

with R_{d_T} and $R_{\overline{y}}$ respectively the autocorrelation functions of d_T $\overline{y}$.

As the autocorrelation function is the inverse Fourier transform of the PSD, we obtain

$$\begin{aligned} P_{d_T} &= \mathcal{F}^{-1}[S_{\overline{y}}](0) - \mathcal{F}^{-1}[S_{\overline{y}}](T) \\ &= \int_{-\infty}^{+\infty} \left(1 - e^{2\pi j\nu T}\right) S_{\overline{y}}(\nu)d\nu \end{aligned}$$

With the Fourier transform of (5.5), and since $S_{\overline{y}}(\nu) = |H_{ave_T}(\nu)|^2 S_y(\nu)$, we have $S_{\overline{y}}(\nu) = sinc^2(T\nu)S_y(\nu)$. Then

$$\begin{aligned} P_{d_T} &= \int_{-\infty}^{+\infty} \left(1 - e^{2\pi j\nu T}\right) sinc^2(T\nu)S_y(\nu)d\nu \\ &= -\int_{-\infty}^{+\infty} e^{\pi j\nu T}\left(e^{\pi j\nu T} - e^{-\pi j\nu T}\right) sinc^2(T\nu)S_y(\nu)d\nu \\ &= -2j\int_{-\infty}^{+\infty} e^{\pi j\nu T}\sin(\pi\nu T)sinc^2(T\nu)S_y(\nu)d\nu \end{aligned}$$

Then, using the fact that, for a parameter θ and an odd function $f(\nu)$,

$$\int_{-\infty}^{+\infty} e^{j\theta\nu}f(\nu)d\nu = 2j\int_0^{\infty} \sin(\theta\nu)f(\nu)d\nu,$$

we have

$$P_{d_T} = 4\int_0^{+\infty} \sin^2(\pi\nu T)sinc^2(T\nu)S_y(\nu)d\nu. \tag{5.11}$$

Replacing the function $sinc(\cdot)$ by its definition, and with $\sigma_y^2(T) = P_{d_T}$, we obtain that the Allan variance is given by

$$\sigma_y^2(T) = 4\int_0^\infty \frac{\sin^4(\pi T\nu)}{(\pi T\nu)^2} S_y(\nu)d\nu \tag{5.12}$$

Now, since the function inside the integral of (5.12) is even (because S_y is even), we can rewrite the expression as

$$P_{d_T} = \sigma^2(T) = \int_{-\infty}^{+\infty} 2\frac{\sin^4(\pi T\nu)}{(\pi T\nu)^2} S_y(\nu)d\nu.$$

Then, using the interpretation of the filtered signal as in the expression (5.3), we can identify the magnitude of the Allan filter frequency response H_{All_T} as

$$|H_{All_T}(\nu)| = \sqrt{2}\frac{\sin^2(\pi T\nu)}{|\pi T\nu|}. \tag{5.13}$$

□

Remark: In general, the relation (5.12) is not a one-to-one mapping, thus no reverse formula exists. However, for some particular random processes, it is possible to find conditions allowing an inversion of the relation (5.12) [Gre98].

The magnitude of the frequency responses $H_{All_T}(\nu)$, for different averaging times T, are compared in Figure 5.6 . We can observe that $h_{All_T}(T)$ behaves as a kind of bandpass filter whose bandwidth is adjusted by the averaging interval T.

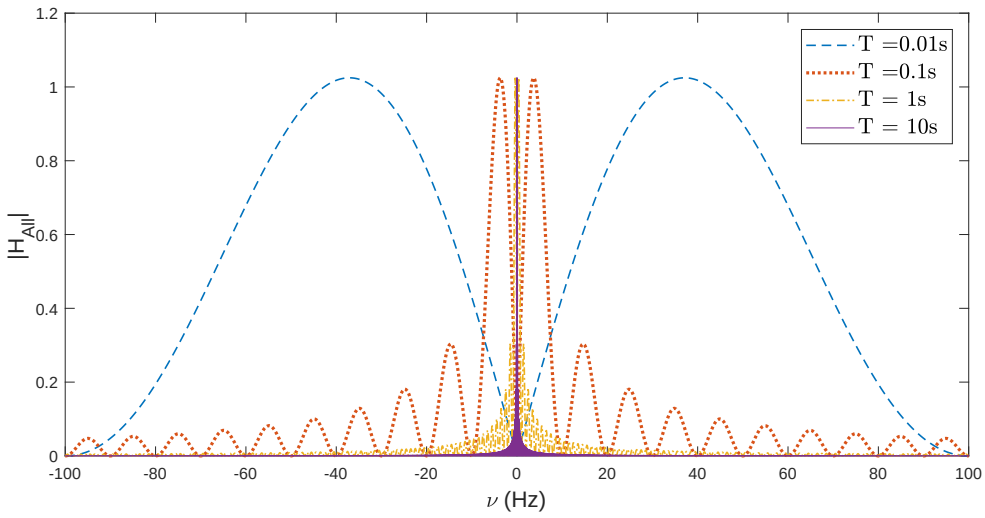

FIGURE 5.6: Frequency responses of Allan filter h_{All}

5.3 LTI Model-based Allan variance

We have discussed how the Allan variance of a signal y can be interpreted as the computation of the power of an output signal d_T that is generated by the signal of interest y passing through a particular filter, here referred to as Allan filter, with magnitude of frequency response $|H_{All_T}(j\omega)|$. Now, the Allan variance is a characterization of a signal, while our objective here is to propose an alternative method

to compute the Allan variance by using the characteristics of the system model that generates the signal of interest.

To this purpose, we propose to consider a generator filter approach. This approach consists in modeling the main characteristics of a given signal as the output of as system model (or generator filter) that is excited by a well-known excitation input signal (white noise, Dirac impulse). Then, the system model somehow shapes the output signal of interest. Indeed, this is one of the principles in which rely many communication applications [DM10], as well as the modeling based on system identification [Lju98].

Concerning the input signal, we are usually interested in using canonical signals, that is, signals whose properties can be easily modeled. In this case, we need a framework that allows to model random signals. In system identification theory it is common to use the spectral factorization to model many classes of correlated noises as filtered white noise. To know more about the exact conditions in which this is possible, see [Lju98, Roz67]. White noise is characterized by having a constant PSD, that is, for an input white noise w, we have that $S_w(\nu) = \sigma_w^2$, making it a suitable candidate to generate random signals.

Then, the PSD $S_n(\nu)$ of correlated noises n can be accurately modeled by introducing fictitious filters such that $S_n(\nu) = |N_n(\nu)|^2\sigma_w^2$, which are usually integrated in the system model. Hence, as illustrated in Figure 5.7, it is possible to build an extended system G_e that contains both system and noise models which, excited by white a noise vector w, generate the output signal to be evaluated. Then, applying the Allan filter at the output, we have

$$d_T = H_{All_T}(s)G_e(s)w. \tag{5.14}$$

To be structurally coherent with the application to MEMS gyroscope described in chapter 2, let us assume that this model is a Multi-Input Single-Output (MISO) system.

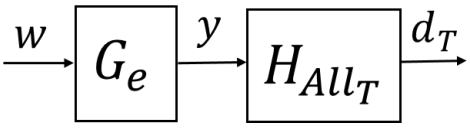

FIGURE 5.7: Extended system G_e for Allan variance computation

Disposing of a system model to characterize the noisy output signal, we have to determine an appropriate model-based system performance measure to estimate the Allan variance. Such a result is introduced in the following subsection.

5.3.1 Allan variance and the $\mathcal{H}_2$ system performance

In this section, we present how, using a generator filter approach to model a noisy signal y, we can compute the Allan variance of this signal by using the properties of the system model and the input signal.

Let us introduce the following theorem that establishes a relationship between the Allan variance of a random output signal and the $\mathcal{H}_2$ norm of the MISO system, driven by white noise, that generates such a signal.

Theorem 5.2. *Let $G_e(s)$ be a MISO convolution system, $G_e(s) = \begin{bmatrix} G_{e_1}(s) & \cdots & G_{e_{n_w}}(s) \end{bmatrix}$, and let the system input w be a vector of normalized white noise with spectrum matrix*

$\Phi(\nu) = \sigma_w^2 I_{n_w}$. Then, with $y = G_e(s)w$, the Allan variance $\sigma_{G_e w}(T)$ of y is given by

$$\sigma_{G_e w}(T) = \sigma_w^2 \| H_{All_T} G_e \|_2^2$$

with $\| H_{All_T} G_e \|_2^2$ the square of the $\mathcal{H}_2$ norm of $H_{All_T}(s)G_e(s)$, written as

$$\| H_{All_T} G_e \|_2^2 = \frac{1}{2\pi} \int_{-\infty}^{+\infty} |H_{All_T}(j\omega)|^2 \left(|G_{e_1}(j\omega)|^2 + |G_{e_2}(j\omega)|^2 + ... + |G_{e_{n_w}}(j\omega)|^2 \right) d\omega. \tag{5.15}$$

Proof. According to Theorem 5.1, the Allan variance is defined as the power of the output signal d_T,

$$\sigma_{G_e w}(T) = P_{d_T} = \frac{1}{2\pi} \int_{-\infty}^{+\infty} S_{d_T}(\omega) d\omega$$

The PSD $S_{d_T}(\omega)$ is the output signal of a MISO system excited by noise, in such case $S_{d_T}(\omega)$ is defined as

$$S_{d_T}(\omega) = H_{All_T}(j\omega) G_e(j\omega) \Phi_w(\omega) G_e(j\omega)^* H_{All_T}(j\omega)^* \tag{5.16}$$

where Φ_w is the spectrum matrix defined as the Fourier transform of the covariance matrix, related to the autocorrelation function of w [Lju98].

Since all the elements of w are white noise signals that are not correlated between them, we have that the spectra matrix $\Phi_w(\omega)$ is

$$\Phi_w(\omega) = \sigma_w^2 I_{n_w}.$$

Then, with $H_{All_T}(j\omega)$ being a scalar function, while G_e is a MISO system, we have that

$$\begin{aligned} S_{d_T}(\omega) &= H_{All_T}(j\omega) G_e(j\omega) \Phi_\omega(\omega) G_{e_T}(j\omega)^* H_{All_T}(j\omega)^* & (5.17) \\ &= \sigma_w^2 |H_{All_T}(j\omega)|^2 \left(|G_{e_1}(j\omega)|^2 + |G_{e_2}(j\omega)|^2 + ... + |G_{e_{n_w}}(j\omega)|^2 \right). & (5.18) \end{aligned}$$

Then, by computing the power P_{d_T} from (5.18) we can directly identify Equation (5.15). □

Hence, we can note that the Allan variance is directly related to the $\mathcal{H}_2$ norm of a system $(H_{All_T} G_e)$ containing the generator filter and the Allan filter. Furthermore, assuming that the system $H_{All_T} G_e$ admits a state-space representation (A, B, C, D), we can state the following theorem adapted from the classical result to compute the $\mathcal{H}_2$-norm of LTI systems [ZD98].

Theorem 5.3. *Let G_e be an LTI MISO system, let the system $H_{All_T} G_e$ admits the state-space representation (A, B, C, D) with $D = 0$, and let the system input w be a vector of normalized white noise signals with spectrum matrix $\Phi(\nu) = \sigma_w^2 I_{n_w}$. Then, with $y = G_e(s)w$, the Allan variance $\sigma_{G_e w}(T)$ of y is given by*

$$\sigma^2_{G_e w}(T) = \sigma_w^2 Tr \left(B^T G_O B \right) \tag{5.19}$$

where Tr denotes the trace of a matrix and G_O is a solution of the equation

$$A^T G_O + G_O A + C^T C = 0.$$

Proof. From Theorem 5.2, we have the Allan variance given by the product of σ_w^2 and the squared $\mathcal{H}_2$ norm of the system $H_{All_T}G_e$:

$$\|H_{All_T}G_e\|_2^2 = \frac{1}{2\pi}\int_{-\infty}^{+\infty} |H_{All_T}(j\omega)|^2 \left(|G_{e1}(j\omega)|^2 + |G_{e2}(j\omega)|^2 + ... + |G_{en_w}(j\omega)|^2\right) d\omega$$

Then, denoting $G_{e_T} = H_{All_T}G_e$, previous equation can be rewritten as

$$\|G_{e_T}\|_2^2 = \frac{1}{2\pi}\text{Tr}\left(\int_{-\infty}^{\infty} G_{e_T}(j\omega)^* G_{e_T}(j\omega) d\omega\right) \tag{5.20}$$

Applying the Parseval equality, the squared $\mathcal{H}_2$ norm of G_{e_T} can be also written as

$$\|G_{e_T}\|_2^2 = \text{Tr}\left(\int_0^{\infty} G_{e_T}(t)^T G_{e_T}(t) dt\right) \tag{5.21}$$

where $G_{e_T}(t)$ corresponds to the impulse response of G_{e_T}. Assuming that G_{e_T} has the state-space realization (A, B, C, D), the system G_{e_T} can have a finite $\mathcal{H}_2$ norm only if its transfer function $G_{e_T}(s)$ is strictly proper, that is $D = 0$. Then, $G_{e_T}(t)$ is given by

$$G_{e_T}(t) = \mathcal{L}^{-1}\{C(sI - A)^{-1}B\} = Ce^{At}B. \tag{5.22}$$

(5.21) then becomes

$$\begin{aligned}
\|G_{e_T}\|_2^2 &= \text{Tr}\left(\int_0^{\infty} (Ce^{At}B)^T Ce^{At}B dt\right) \\
&= \text{Tr}\left(B^T \int_0^{\infty} e^{A^T t} C^T C e^{At} dt B\right) \\
&= \text{Tr}\left(B^T G_O B\right)
\end{aligned}$$

with $G_O = \int_0^{\infty} e^{A^T t} C^T C e^{At} dt$ being the observability gramian, which is a solution of the Lyapunov equation

$$A^T G_O + G_O A + C^T C = 0.$$

□

Remark: The $\mathcal{H}_2$ norm computation, as introduced here, can be interpreted as: with the system G_{e_T} having zero initial conditions $x(0) = 0$ at the instant $t = 0^-$, we apply a Dirac impulse at $t = 0$. Then, at the instant $t = 0^+$ the input $w(t)$ becomes 0 for $t > 0$, and the initial conditions switch to $x(0) = B$, the system then evolves as an autonomous system with non zero initial conditions. Finally, Tr $\left(B^T G_O B\right)$ comes to quantify the observed energy at the output of such autonomous system.

To summarize, the previous result tells us that the Allan variance of a signal can be obtained by constructing a generator system G_{e_T} using the frequency response of the Allan filter; then computing the $\mathcal{H}_2$ norm of the obtained a system. This computation is performed under the consideration that G_{e_T} has a state-space representation (A, B, C, D) with $D = 0$.

However, the Allan filter, whose frequency response $H_{All_T}(\nu)$ is defined in (5.4), is given by a non rational transfer function, hence, it does not admit a state-space representation (A, B, C, D), making not possible to directly apply Theorem 5.3 to determine the Allan variance.

Degree m	Padé Approximant $R(s)$
0	1
1	$\frac{1+\frac{1}{2}sT}{1-\frac{1}{2}sT}$
2	$\frac{1+\frac{1}{2}sT+\frac{1}{12}(sT)^2}{1-\frac{1}{2}sT+\frac{1}{12}(sT)^2}$
3	$\frac{1+\frac{1}{2}sT+\frac{1}{10}(sT)^2+\frac{1}{120}(sT)^3}{1-\frac{1}{2}sT+\frac{1}{10}(sT)^2-\frac{1}{120}(sT)^3}$

TABLE 5.1: Table of different order Padé approximants

Therefore, in order to recast the computation of the Allan variance into a tractable problem, we propose to replace the Allan filter by an approximated Allan filter whose transfer function is rational.

5.3.2 Rational Allan filter design using Padé approximation

Using the impulse response $h_{All_T}(t)$, given in Equation (5.7), and since the phase has no impact on the Allan variance computation, we can consider a causal version $h_{AllC_T}(t)$ of the Allan filter by introducing a delay in the original impulse response: $h_{AllC_T}(t) = h_{All_T}(t - 2T)$. Then, applying the Laplace transform to $h_{AllC_T}(t)$, we obtain

$$H_{AllC_T}(s) = \frac{1}{T\sqrt{2}\,s}\left(e^{-sT} - 1\right)^2. \tag{5.23}$$

We can observe that the obtained function $H_{AllC_T}(s)$ contains an exponential function of Ts, then, it is not rational on s.

In this work, we propose to apply the Padé approximation of finite order m to the exponential function of (5.23) [GVL96], allowing then to approximate $H_{AllC_T}(s)$ to rational functions of s, thus to the transfer function of a finite-dimensional system.

We can then obtain an approximated Allan filter whose transfer function has the form

$$H_{AllP_T}(s) = \frac{1}{T\sqrt{2}\,s}\left(R(s) - 1\right)^2. \tag{5.24}$$

with $R(s)$ being a rational functions of s. In Table Table 5.1 we show the obtained functions $R(s)$ depending on the chosen order m.

In Figure 5.8, we present the frequency response of some approximated Allan filters H_{AllP_T}. We take different degrees for the Padé approximants $R(s)$ of the exponential function and we compare them to the exact frequency response of H_{All_T}.

It is also interesting to analyze the absolute and relative frequency response errors of the Allan filter approximations, which are respectively shown in Figure 5.9 and Figure 5.10. We can observe that the errors are small for low frequencies. Then, they increase as the frequency becomes higher. Ii is important to notice that the bandwidth for which the absolute and relative errors remain low depends on the chosen order for the Padé approximation.

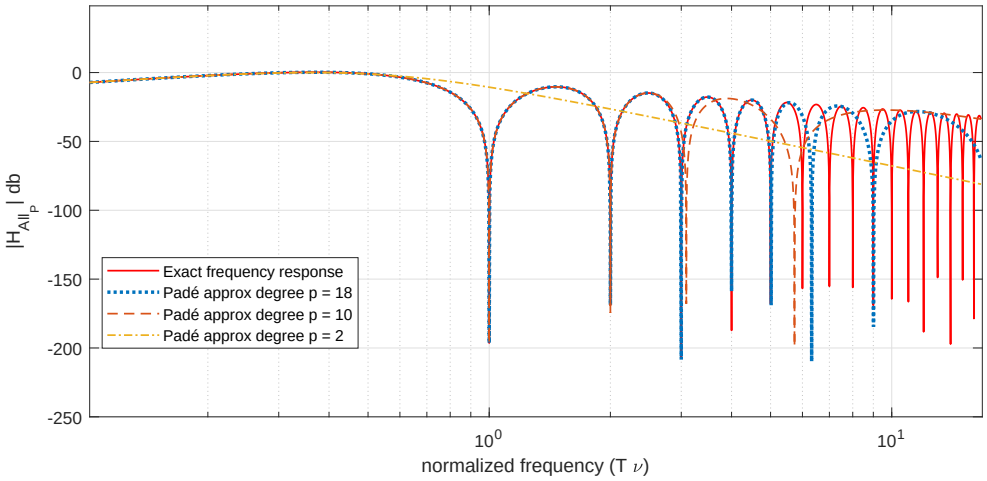

FIGURE 5.8: Frequency response of Allan filter and approximated Allan filters

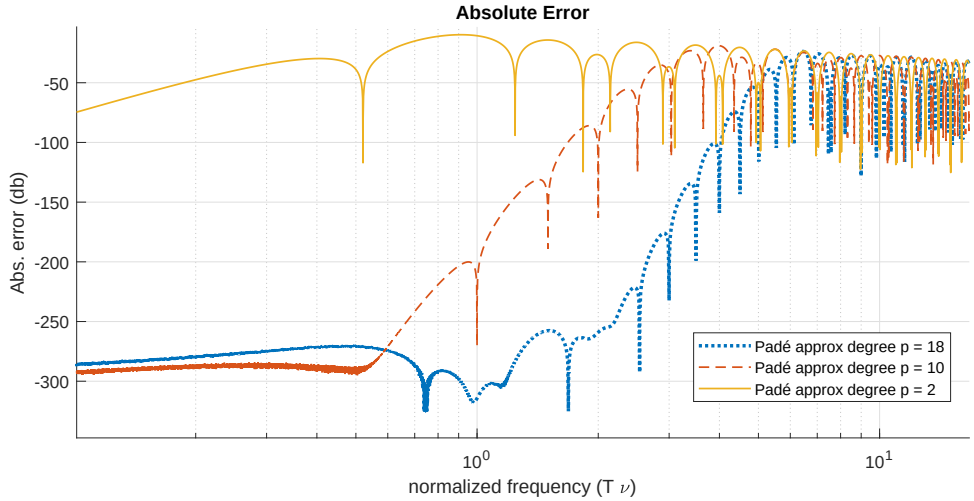

FIGURE 5.9: Absolute error of the approximated Allan filters

The question about how to choose an adequate Padé approximation order m for each depends on the frequency response of the generator filter G_e. In general, the model G_e that produces the signal y is a system whose frequency response has a limited bandwidth of interest. Hence, the idea is to use the frequency domain information of the generator system and to determine the frequency range where the response of the system is relevant. Then, we can select a Padé approximation order that allows to minimize the error in this frequency interval and thus to preserve the important information.

5.3.3 Example

In order to show the convenience of the proposed approach for the filter approximation, we investigate the characterization of two different classes of noise : white noise (or angular random walk in MEMS jargon) and $1/\nu^2$ noise (or rate random walk).

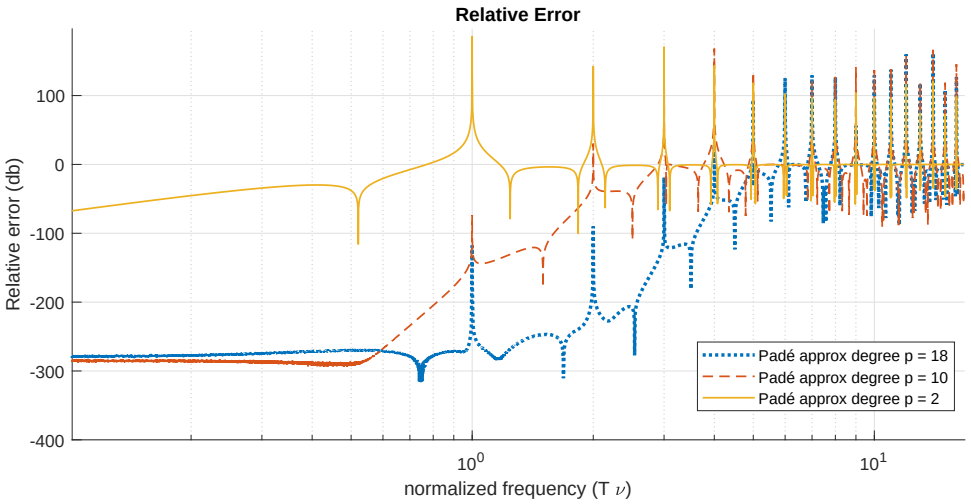

FIGURE 5.10: Relative error of the approximated Allan filters

For the sake of simplicity and without loss of generality, the signal of interest is generated by a generator filter with one input. We choose these two random signals because their analytic Allan variance is well defined. We then compare the analytic solution with the results obtained for different approximated Allan filters.

White noise

The first case considers that the output signal y is white noise. As we previously introduced in this chapter, white noise has a constant PSD $S_y(\nu) = \sigma_y^2$. Here we set $\sigma_y^2 = 1$ for the sake of simplicity. Then, the analytic Allan variance is obtained as follows (see equations (5.4) and (5.12)):

$$\begin{aligned}\sigma_y^2(T) &= 4\int_0^\infty \frac{\sin^4(\pi T\nu)}{(\pi T\nu)^2} S_y(\nu)d\nu \\ &= 4\sigma_y^2\int_0^\infty \frac{\sin^4(\pi T\nu)}{(\pi T\nu)^2} d\nu \\ &= \frac{4}{\pi T}\int_0^\infty \frac{\sin^4(u)}{(u)^2} du\end{aligned}$$

where $u = \pi T\nu$. Then, with

$$\int_0^\infty \frac{\sin^4(u)}{(u)^2} du = \frac{\pi}{4}$$

we have that the Allan deviation is

$$\sigma_y(T) = \frac{1}{\sqrt{T}}.$$

Now, in order to compute the model-based Allan variance, we have that the generator filter G_e is an unitary gain, while the input white noise has an unitary PSD $\sigma_w^2 = 1$. Hence, the Allan variance is reduced to be the $\mathcal{H}_2$ norm of the approximated Allan filter H_{AllP_T}.

We show in Figure 5.11 the Allan plot obtained with the approximated Allan filters with different degrees of approximation, and we compare them with the exact solution. We can observe that all the results show a linear relation of the Allan deviation with respect to the averaging time, with a slope of -1/2.

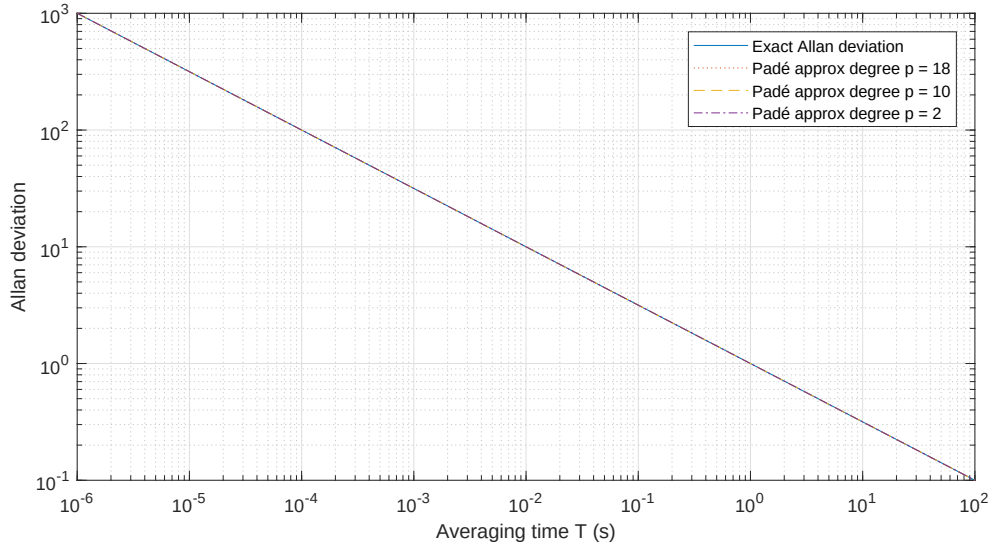

FIGURE 5.11: Allan deviation plot for an white noise

$1/\nu^2$ noise

Secondly, we consider a rate random walk characterized by a PSD of the form $S_n = k/\nu^2$.

Setting $S_y = \frac{k}{\nu^2} = \frac{1}{\nu^2}$, the analytic Allan variance is given by

$$\begin{aligned}\sigma_y^2(T) &= 4\int_0^\infty \frac{\sin^4(\pi T\nu)}{(\pi T\nu)^2} S_y(\nu)d\nu \\ &= 4k\int_0^\infty \frac{\sin^4(\pi T\nu)}{\pi^2 T^2\nu^4} d\nu \\ &= 4\pi T\int_0^\infty \frac{\sin^4(u)}{(u)^4} du\end{aligned}$$

where $u = \pi T\nu$. Then, with

$$\int_0^\infty \frac{\sin^4(u)}{(u)^4} du = \frac{\pi}{3}$$

we obtain the Allan deviation

$$\sigma(T) = 2\pi\sqrt{\frac{T}{3}}.$$

Then, the filter generator G_e that produces a signal whose PSD is $1/\nu^2$ has the form of an integrator

$$G_e(s) = \frac{1}{s}.$$

However, an integrator is not a stable system which does not have a finite $\mathcal{H}_2$ norm, making impossible the computation of the Allan variance.

To address this issue, we can approximate the integrator by a quasi-integrator, that is, a first order low-pass filter whose pole is very close to zero, this in order to guarantee a finite $\mathcal{H}_2$ system norm. Hence, the generator filter expression is

$$H_{in}(s) = \frac{2\pi}{s + \omega_c} \quad \text{with } \omega_c << 1.$$

Similarly, we present in Figure 5.12 the Allan plots obtained with the proposed approach and compared to the analytic solution, we observe that our approach shows the same linear relation of the Allan deviation as the analytic solution, with a slope of 1/2.

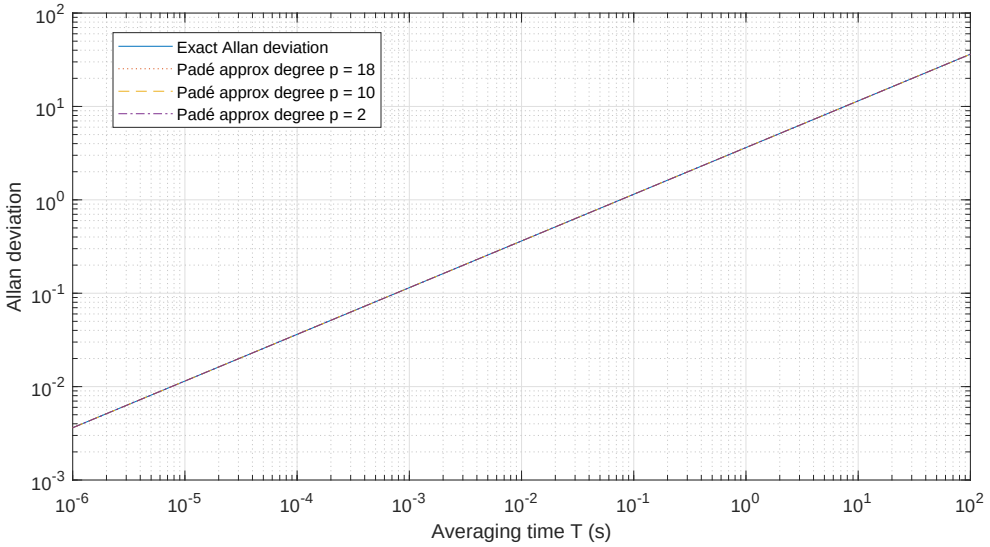

FIGURE 5.12: Allan deviation plot for an white noise for a rate random walk noise

The obtained results for the two cases under consideration offer very accurate estimations of the analytic Allan variance, even for low order Padé approximations.

5.4 Worst-case Allan variance of uncertain systems

In the previous sections, we introduce the definition of the Allan variance, which is a characteristic of a signal. We discussed how this indicator can be interpreted as the power of a filtered signal, as shown in Figure 5.13 a), which is also a signal feature. Then, we demonstrated that, when the signal of interest is the output of a system, we can compute a model-based Allan variance by computing the $\mathcal{H}_2$ norm of the system generating the signal, which brings the Allan variance from a signal characteristic to a system one (Figure 5.13 b).

Now, as we mentioned in the previous chapters, MEMS gyroscopes are systems that are naturally uncertain. In such a case, we do not have a single model, but a whole set of models that represents the real system in some particular configuration. Hence, we need to determine how to define the Allan variance in this context. As we represent on Figure 5.13 c), the uncertain system can be modeled by the LFT $\Delta \star H_T$. Then, since we aim to guarantee a certain noise performance level characterized

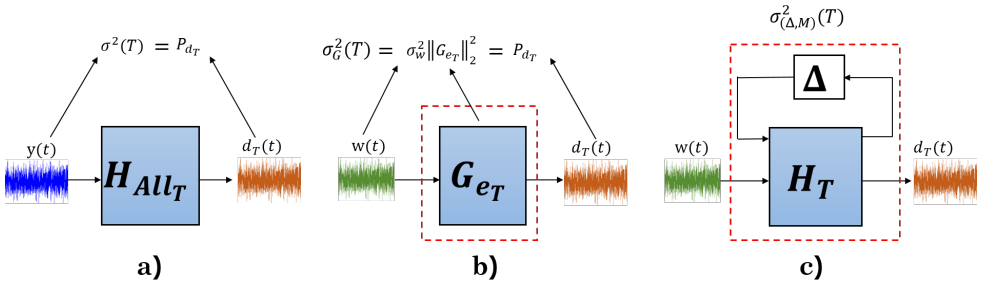

FIGURE 5.13: Computation of the Allan variance. a) Allan variance from a noise. b) Allan variance from a nominal system model. c) Worst-case Allan variance from an uncertain system model.

by the Allan variance, we need to determine, for all the possible existing models generated by all $\Delta \in \mathbf{\Delta}$, what would be the Allan variance in the worst-case scenario. We define then a worst-case Allan variance $\sigma_{(\Delta,H_T)}(T)$ as follows.

Definition 5.2 (Worst-case Allan variance)**.** *Let $H_T(s)$ be a stable LTI system, and let $\mathbf{\Delta}$ be a set of bounded and causal operators. Then, the worst-case Allan variance of the uncertain interconnection $\mathbf{\Delta} \star H_T$ is given by*

$$\sigma_{(\mathbf{\Delta},H_T)}(T) = \sup_{\Delta \in \mathbf{\Delta}} \sigma_{\Delta \star M}(T). \tag{5.25}$$

That is to say, whatever the system model derived from the set $\mathbf{\Delta}$, the Allan variance of the output signal will be equal to or less than $\sigma_{(\mathbf{\Delta},H_T)}(T)$.

With an appropriate measure of the Allan variance adapted to the context of uncertain systems, our objective now is to introduce a method to compute such a quantity, or more precisely, an upper bound of the worst-case Allan variance.

Following the nominal case, we need to translate the generator filter notion to the uncertain case. The properties of the input signal do not change when dealing with an a uncertain system, so we only need a framework that offers a measure of the worst-case $\mathcal{H}_2$ norm for uncertain systems. In chapter 3, we mentioned that the IQC approach makes possible to investigate different performance measures, including $\mathcal{H}_2$ performance. Let us then introduce an IQC theorem that computes the $\mathcal{H}_2$ norm of uncertain systems using a state-space resolution, which can be directly linked to the worst-case Allan variance.

Theorem 5.4. *Let H_T be the stable LTI system*

$$H_T = \begin{bmatrix} H_{qp} & H_{qw} \\ h_{dp} & h_{dw} \end{bmatrix},$$

and let $\mathbf{\Delta}$ be a set of causal and bounded operators. Let be a set of factorizable multipliers $\mathbf{\Pi} = \{\Pi | \exists M \in \boldsymbol{M}, \Pi = \Psi^* M \Psi, \forall \Delta \in \mathbf{\Delta}, \Delta \in IQC(\Pi)\}$, with $\boldsymbol{M} \in \mathbb{S}^\bullet$ and $\Psi \in \mathcal{RH}_\infty$. Let the system input w be a vector of normalized white noise signals with spectrum matrix $\Phi(\nu) = \sigma_w^2 I_{n_w}$.

Assume that

1. *for all $\tau \in [0,1]$, for all $\Delta \in \mathbf{\Delta}$, $\tau\Delta \star H_T$ is well-posed;*
2. *for all $\tau \in [0,1]$, for all $\Delta \in \mathbf{\Delta}$ and for all $\Pi \in \mathbf{\Pi}$, $\tau\Delta \in IQC(\Pi)$.*

Then, $\mathbf{\Delta} \star H_T$ is robustly stable and guarantees an $\mathcal{H}_2$ norm less than γ^2 if there exist $M \in \boldsymbol{M}$ and $P \in \mathbb{S}^\bullet$ satisfying

$$\begin{bmatrix} I & 0 \\ A & B_1 \\ C_1 & D_{11} \\ C_2 & D_{21} \end{bmatrix}^T \begin{bmatrix} 0 & P & 0 & 0 \\ P & 0 & 0 & 0 \\ 0 & 0 & M & 0 \\ 0 & 0 & 0 & I \end{bmatrix} \begin{bmatrix} I & 0 \\ A & B_1 \\ C_1 & D_{11} \\ C_2 & D_{21} \end{bmatrix} \prec -\varepsilon I \tag{5.26}$$

and

$$Tr(B_2^T P B_2) < \gamma^2, \tag{5.27}$$

with

$$\left[\begin{array}{c|c|c} \Psi & 0 & 0 \\ 0 & I & 0 \end{array}\right] \left[\begin{array}{cc} H_{qp} & H_{qw} \\ I & 0 \\ \hline H_{dp} & H_{dw} \\ \hline 0 & I \end{array}\right] \sim \begin{bmatrix} A & B_1 & B_2 \\ C_1 & D_{11} & 0 \\ C_2 & D_{21} & 0 \end{bmatrix}. \tag{5.28}$$

Moreover, we guarantee a worst-case Allan variance $\sigma_{(\mathbf{\Delta} \star H_T)w}(T)$ upper-bounded by

$$\sigma_{(\mathbf{\Delta} \star H_T)w}(T) \leq \gamma^2 \sigma_w^2. \tag{5.29}$$

Proof. From Theorem 5.2, we have the Allan variance which is given by the product of the PSD σ_w^2 and the $\mathcal{H}_2$ norm of the system G_{e_T}, here represented by the LFT representation $d_T = (\mathbf{\Delta} \star H_T)w$.

To compute the $\mathcal{H}_2$ norm of a MISO uncertain system, we here consider a deterministic interpretation, related to the impulse response of the system [VSK16]. To do so, we consider the following virtual experiment, illustrated in Figure 5.14.

- Let consider an impulse input in one channel at a time, denoted as $w^j = \delta e_j$ for $j = 1, ..., n_w$, with δ the normalized Dirac impulse distribution and e_j the jth unit vector.
- In the frequency domain, the obtained output $\widehat{d}_T(j\omega)$ for each excited input is $\widehat{d}_T^j(j\omega) = H_{dw}(j\omega)e_j$, which is the jth column of $H_{dw}(j\omega)$.
- In the time domain, $d^j(t)$ is the observed impulse response when the jth input is excited by a Dirac impulse.
- Then, the $\mathcal{H}_2$ performance is measured as the sum of the energy observed at the output of the system for each excited input, once at a time. Thus, the $\mathcal{H}_2$ performance constraint $\|H_{dw}(j\omega)\|_2^2 < \gamma^2$ is translated into the following signal energy constraint:

$$\frac{1}{2\pi} \sum_{j=1}^{n_w} \int_{-\infty}^{\infty} |\widehat{d}_T^j(j\omega)|^2 d\omega = \sum_{j=1}^{n_w} \int_0^{\infty} |d_T^j(t)^T|^2 dt < \gamma^2.$$

- For robust $\mathcal{H}_2$ performance, we denote the internal responses of the LFT interconnection as p^j, q^j.

Now, let us prove that, if conditions (5.26) and (5.27) are satisfied, then the $\mathcal{H}_2$ norm is bounded by γ.

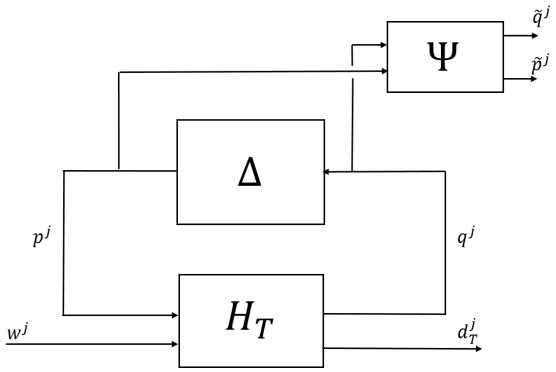

FIGURE 5.14: IQC H_2 performance virtual experiment

If we respectively multiply condition (5.26) at the right and the left by $col(x^j(t), p^j(t))$ and its transpose, we obtain:

$$\begin{bmatrix} x^j(t) \\ \dot{x}^j(t) \\ \begin{bmatrix} \tilde{q}^j(t) \\ \tilde{p}^j(t) \end{bmatrix} \\ d_T^j(t) \end{bmatrix}^T \begin{bmatrix} 0 & P & 0 & 0 \\ P & 0 & 0 & 0 \\ 0 & 0 & M & 0 \\ 0 & 0 & 0 & I \end{bmatrix} \begin{bmatrix} x^j(t) \\ \dot{x}^j(t) \\ \begin{bmatrix} \tilde{q}^j(t) \\ \tilde{p}^j(t) \end{bmatrix} \\ d_T^j(t) \end{bmatrix} < -\varepsilon(x^j(t)^T x^j(t) + p^j(t)^T p^j(t)),$$

since

$$\begin{bmatrix} I & 0 \\ A & B_1 \\ C_1 & D_{11} \\ C_2 & D_{21} \end{bmatrix} \begin{bmatrix} x^j(t) \\ p^j(t) \end{bmatrix} = \begin{bmatrix} x^j(t) \\ Ax^j(t) + B_1 p^j(t) \\ C_1 x^j(t) + D_{11} p^j(t) \\ C_2 x^j(t) + D_{21} p^j(t) \end{bmatrix} = \begin{bmatrix} x^j(t) \\ \dot{x}^j(t) \\ \begin{bmatrix} \tilde{q}^j(t) \\ \tilde{p}^j(t) \end{bmatrix} \\ d_T^j(t) \end{bmatrix},$$

with $col(\tilde{q}^j(t), \tilde{p}^j(t)) = \Psi[col(q^j(t), p^j(t))](t)$. Developing the matrix products we have:

$$\begin{bmatrix} x^j(t) \\ \dot{x}^j(t) \end{bmatrix}^T \begin{bmatrix} 0 & P \\ P & 0 \end{bmatrix} \begin{bmatrix} x^j(t) \\ \dot{x}^j(t) \end{bmatrix} + \begin{bmatrix} \tilde{q}^j(t) \\ \tilde{p}^j(t) \end{bmatrix}^T M \begin{bmatrix} \tilde{q}^j(t) \\ \tilde{p}^j(t) \end{bmatrix} + d_T^j(t)^T d_T^j(t) < 0,$$

which leads to the condition

$$\begin{aligned} &x^j(t)^T P \dot{x}^j(t) + \dot{x}^j(t)^T P x^j(t) + \begin{bmatrix} \tilde{q}^j(t) \\ \tilde{p}^j(t) \end{bmatrix}^T M \begin{bmatrix} \tilde{q}^j(t) \\ \tilde{p}^j(t) \end{bmatrix} + d_T^j(t)^T d_T^j(t) \\ &= \frac{d}{dt} x^j(t)^T P x^j(t) + \begin{bmatrix} \tilde{q}^j(t) \\ \tilde{p}^j(t) \end{bmatrix}^T M \begin{bmatrix} \tilde{q}^j(t) \\ \tilde{p}^j(t) \end{bmatrix} + d_T^j(t)^T d_T^j(t) < 0 \end{aligned}$$

Then, if we integrate over $[0, T_e]$, we infer for $T_e \to \infty$ that the quadratic integral term involving $\tilde{q}^j$ and $\tilde{p}^j$ is positive as defined by the IQC for the operator Δ. Then we obtain

$$\lim_{T_e \to \infty} \left(\int_0^{T_e} d_T^j(t)^T d_T^j(t) dt - x^j(0)^T P x^j(0) + x^j(T_e)^T P x^j(T_e) \right) < 0$$

Since $x(T_e) \to 0$ for $T_e \to \infty$ we finally obtain

$$\int_0^\infty d_T^j(t)^T d_T^j(t) dt < x^j(0)^T P x^j(0) \tag{5.30}$$

With the input of a jth channel w^j being an impulse, we have that the initial state is $x^j(0) = 0$ for $t \leq 0^-$, and suddenly, for $t = 0^+$ the initial state is given by $x^j(0) = B_w e_j$. Therefore, we have that

$$\sum_{j=1}^{n_w} \int_0^\infty d_T^j(t)^T d_T^j(t) dt \leq \sum_{j=1}^{n_w} x^j(0) P x^j(0) = \sum_{j=1}^{n_w} e_j^T B_w^T P B_w e_j = \mathrm{Tr}(B_w^T P B_w) < \gamma^2$$

□

The previous result allows us to extend the system-based computation of the Allan variance to the case of uncertain systems and some types of time-varying systems, which can be an useful tool to face the case where the model contains synchronous demodulation, but other approaches can be also considered. This is discussed in the following section.

5.5 Model-based Allan variance of demodulated signals

In the previous sections, we solve some problems that allow us to propose a method to compute the Allan variance of a signal by using the model of the system generating it. However, the system under study in this memoir demands to determine the Allan variance of a signal coming from a synchronous demodulation operation.

Hence, this last problem can be summarized as: given a modulated signal y that can be decomposed into its two components, an in-phase y_i and a quadrature y_q component, how to compute the Allan variance of the in-phase component by using the characteristics of the system model? Considering this problem as an extension of the previous ones, the in-phase signal can be modeled as

$$y_i = F_L(s)\ \cos(\omega_0 t)\ G_e(s) w \tag{5.31}$$

where $G_e(s)$ and w are respectively the extended system and the input white noise, as defined in section 5.3, while $F_L(s)$ is a low-pass filter associated to the synchronous demodulation.

We then propose two different approaches to perform such an analysis.

1. An IQC approach using the catalog of harmonic multipliers introduced in chapter 3. This approach makes possible to naturally deal with uncertainties and harmonic parameters simultaneously.

2. A stochastic approach using properties of random and modulated signals in order to establish an LTI system such that its Allan variance is equivalent to the Allan variance of the system containing synchronous demodulation.

5.5.1 Approach 1: IQC approach with harmonic multipliers

The IQC approach can be seen as a simple extension of the IQC theorem for $\mathcal{H}_2$ performance combined with the set of multipliers for a harmonic parameter proposed in chapter 3. Let us introduce a Theorem, using the state-space resolution, to compute the $\mathcal{H}_2$ performance of a harmonically time-varying system.

Theorem 5.5 (Allan variance upper bound for harmonic TV systems)**.** *Let H_T be a stable LTI system having the state-space realization*

$$\left[\begin{array}{c|cc} A & B_p & B_w \\ \hline C_q & D_{qp} & 0 \\ C_z & D_{zp} & 0 \end{array}\right].$$

Let be the harmonic set $\boldsymbol{\Delta}_{\boldsymbol{H}}^{\boldsymbol{\omega_0}}$ defined by (3.27), with θ^{ω_0} given by (3.28). Let be the set of multipliers $\underline{\boldsymbol{\Pi}}_{\boldsymbol{\theta}}$ given by (3.43) with $\Psi \in \mathcal{RH}_\infty^{\bullet\times\bullet}$ having the minimal state-space realization $(A_\Psi, B_\Psi, C_\Psi, D_\Psi)$.

Then, $\boldsymbol{\Delta}_{\boldsymbol{\theta}}^{\boldsymbol{\omega_0}} \star H_T$ is robustly stable and guarantees an $\mathcal{H}_2$ norm less than γ^2 if it is well-posed and if there exist $M_D \in \boldsymbol{M_D}$ and $P \in \mathbb{S}^\bullet$ satisfying

$$\begin{bmatrix} I & 0 \\ A & B_1 \\ C_1 & D_{11} \\ C_2 & D_{21} \end{bmatrix}^T \begin{bmatrix} 0 & P & 0 & 0 \\ P & 0 & 0 & 0 \\ 0 & 0 & \tilde{M}_D & 0 \\ 0 & 0 & 0 & I \end{bmatrix} \begin{bmatrix} I & 0 \\ A & B_1 \\ C_1 & D_{11} \\ C_2 & D_{21} \end{bmatrix} \prec 0 \tag{5.32}$$

and

$$Tr(B_w P B_w) < \gamma^2 \tag{5.33}$$

with $\tilde{M}_D = diag(\frac{1}{2}M_D, \frac{1}{2}M_D, -2M_D)$ and

$$A = \begin{bmatrix} A_\Psi & \omega_0 I & 0 & B_\Psi C_q \\ -\omega_0 I & A_\Psi & 0 & 0 \\ 0 & 0 & A_\Psi & 0 \\ 0 & 0 & 0 & A \end{bmatrix}, B_1 = \begin{bmatrix} B_\Psi D_{qp} \\ 0 \\ B_\Psi \\ B_p \end{bmatrix},$$
$$C_1 = \begin{bmatrix} 2C_\Psi & 0 & 0 & 2D_\Psi C_q \\ 0 & 2C_\Psi & 0 & 0 \\ 0 & 0 & C_\Psi & 0 \end{bmatrix}, D_{11} = \begin{bmatrix} 2D_\Psi D_{qp} \\ 0 \\ D_\Psi \end{bmatrix}.,$$
$$C_2 = \begin{bmatrix} 0 & 0 & 0 & C_z \end{bmatrix} \qquad , D_{21} = D_{zp}.$$

Moreover, with the input being a white noise vector, we ensure a worst-case Allan variance $\sigma_{(\boldsymbol{\Delta}\star H_T)w}(T)$ upper-bounded by

$$\sigma_{(\boldsymbol{\Delta}\star H_T)w}(T) \leq \gamma^2 \sigma_w^2.$$

Proof. The proof is a direct consequence of Theorem 5.4, using the set of multipliers $\underline{\boldsymbol{\Pi}}_{\boldsymbol{\theta}}$ of (3.43), and using its state-space representation, given in Lemma 3.4. □

Remark: An alternative approach to compute the worst-case Allan variance, based on the IQC framework, might be to consider a frequency-domain solution to compute the worst-case $\mathcal{H}_2$ performance (in contrast to the state-space computation introduced in Theorem 5.5). Determining the robust $\mathcal{H}_2$ performance can be computed, for instance, using the approach proposed in [Pag99, Pag96]. This approach is based on frequency gridding techniques and, since frequency-gridding solutions were proposed in section 3.5.2 for the analysis of harmonically time-varying systems, both approaches might be combined.

An advantage of such a frequency-domain approach is that it might allow to reduce the conservatism that is implied by the multiplier factorization. However, a very dense gridding can be necessary, depending on the analyzed system, to obtain an accurate result. Hence, this approach might lead to consume considerably high computational and time resources.

5.5.2 Approach 2: Equivalent LTI system

This second approach exploits the characteristics of random modulated signals. Indeed, as we mention in chapter 2 and chapter 4, the signals of the MEMS closed-loop systems usually have a spectrum that is highly concentrated around a resonance frequency ω_0. Then, the system output, before demodulation, has a PSD that allows to model it as a modulated random signal.

The definition of pure modulated signals is introduced in subsection 2.1.4, where the assumption of pure modulated signals allows to derive some of the main results concerning synchronous demodulation.

Such an assumption is equally necessary to model y as a modulated signal. Moreover, in this case, y needs to be also assumed as a wide-sense stationary (WSS) random signal. Let us then adopt an assumption adapted to the context of random signals.

Assumption 5.1. *Let the output y of a system model to be a random modulated signal, defined as a wide sense stationary (WSS) signal whose Power Spectral Density S_y has a limited bandwidth $2W$ around a frequency ω_0, with $W < \omega_0$,*

$$S_y(\omega) = 0 \quad \forall\, \omega \ \in]-\omega_0 + W, \omega_0 - W[\cup]\omega_0 + W, \infty[\cup]-\infty, -\omega_0 - W[, \tag{5.34}$$

Under Assumption 5.1, we can prove that y can be exactly decomposed into its in-phase y_i and quadrature y_q signals. Furthermore, the expression of the Power Spectral Density S_y allows in the sequel to recast the computation of the Allan variance of y_i (the signal of interest) as the computation of the $\mathcal{H}_2$ norm of a fictitious LTI system.

To this end, we need to introduce some results related to modulated random signals, which will be useful for the final theorem, this result is taken from [Lat70] (Chapter 5, page 326), complemented with some results of [Pap83].

Theorem 5.6. *Let y be a modulated wide-sense stationary signal of bandwidth $2W$ centered at ω_0.*

Then, there exists wide-sense stationary signals y_i and y_q of bandwidth $2W$ centered at 0 such that

$$y(t) = y_i(t)\cos(\omega_0 t) + y_q(t)\sin(\omega_0 t).$$

Furthermore,

- $$\begin{cases} y_i(t) &= y(t)\cos(\omega_0 t) + \check{y}(t)\sin(\omega_0 t) \\ y_q(t) &= y(t)\sin(\omega_0 t) - \check{y}(t)\cos(\omega_0 t) \end{cases}, \tag{5.35}$$

  with $\check{y}(t) = \frac{1}{\pi t} * y(t)$ being the Hilbert transform of $y(t)$.

- $$S_{y_i}(\omega) = \begin{cases} S_y(\omega + \omega_0) + S_y(\omega - \omega_0) & |\omega| < W \\ 0 & |\omega| \geq W \end{cases} \tag{5.36}$$

The proof is given in Appendix C.

In Assumption 5.1, the wide sense stationary of y is directly verified since y is the response of an LTI system G_e to a white noise vector input w, and given that white noise is a class of Wide Sense Stationary (WSS) signals, then the filtered output y is also a WSS signal.

In contrast, since $G_e(s)$ is a rational function of the frequency, the Power Spectral Density S_y cannot be exactly zero as specified in (5.34). In this sense, Assumption

5.1 cannot be completely satisfied, so its pertinence needs to be verified by observing the frequency response of the generator filter.

Next, according to subsection 2.1.4, y_i can be obtaining by adopting Assumption 2.1 that considers an ideal synchronous demodulation, that is, a multiplication by $2\cos(\omega_0)$ followed of an ideal low-pass filter of the form

$$F_L(j\omega) = \text{rect}\left(\frac{\omega}{2W}\right). \tag{5.37}$$

Then, under the previous assumptions, the Allan variance of y_i can be computed using the $\mathcal{H}_2$ norm of an LTI system, as it is stated in the following theorem.

Theorem 5.7. *Let be $y = G_e w$, with w being a vector of normalized white noise signals, and assume that y satisfies Assumption 5.1. Let y_i be the in-phase component of y using demodulation under Assumption 2.1. Then, the Allan variance of the in-phase component y_i is given by*

$$\sigma_{y_i}(T) = \sigma_w^2 \| \left(F(s+j\omega_0) + F(s-j\omega_0)\right) G_e(s) \|_2^2 \tag{5.38}$$

with $F(s) = H_{All_T}(s)F_L(s)$, H_{All_T} given by (5.4) and $F_L(s)$ given by (5.37).

Proof. Under Assumption 5.1, we have that y is a WSS random signal with bandwidth $2W$ and centered around ω_0. From Theorem 5.6, we have that y can be expressed as

$$y(t) = y_i(t)\cos(\omega_0 t) + y_q(t)\sin(\omega_0 t)$$

and that

$$S_{y_i}(\omega) = \begin{cases} S_y(\omega+\omega_0) + S_y(\omega-\omega_0) & |\omega| < W \\ 0 & |\omega| > W \end{cases}$$

Applying the low-pass filter $F_L(s)$ under Assumption 2.1, the DSP S_{y_i} is given by

$$S_{y_i} = |F_L(j\omega)|^2 (S_y(\omega+\omega_0) + S_y(\omega-\omega_0))$$

.

From Theorem 5.1, we have that the Allan variance of y_i is given by the power of the output signal d_T, given by y_i filtered by H_{All_T}. Taking $F(s) = H_{All_T}(s)F_L(s)$, we obtain

$$\begin{aligned} P_{d_T} &= \int_{-\infty}^{\infty} |F(j\omega)|^2 (S_y(\omega+\omega_0) + S_y(\omega-\omega_0)) d\omega \\ &= \int_{-\infty}^{\infty} |F(j\omega)|^2 S_y(\omega+\omega_0) d\omega + \int_{-\infty}^{\infty} |F(j\omega)|^2 S_y(\omega-\omega_0) d\omega. \end{aligned}$$

Since the integrals goes from $-\infty$ to ∞, a frequency shift of the involved transfer functions does not modify the result of the integral. Then, we can perform a change of variable, obtaining

$$P_{d_T} = \int_{-\infty}^{\infty} (|F(j(\omega+\omega_0))|^2 + |F(j(\omega-\omega_0))|^2) S_y(\omega) d\omega.$$

Note that, since $|F(j(\omega-\omega_0))|^2 S_y(\omega)$ and $|F(j(\omega+\omega_0))|^2 S_y(\omega)$ are disjoint, we have

$$P_{d_T} = \int_{-\infty}^{\infty} |F(j(\omega+\omega_0)) + F(j(\omega-\omega_0))|^2 S_y(\omega) d\omega.$$

Since $F(s)$ has a limited bandwidth, and it is centered at zero, the modulated filter $(F(j(\omega+\omega_0)) + F(j(\omega-\omega_0)))$ can indeed be expressed as the frequency response of an LTI system with real coefficients (Lemma 3.4).

Finally, with $S_y = \sigma_w^2(|G_{e1}j(\omega)|^2 + ... + |G_{en_w}(j\omega)|^2)$, we have from Theorem 5.2 that the Allan variance of y_i is given by

$$\sigma_{y_i}(T) = \sigma_w^2 \|(F(j(\omega+\omega_0)) + F(j(\omega-\omega_0)))G_e\|_2^2$$

□

Furthermore, if we assume that $F(s)$ has a state-space representation with real matrices, hence $F^{\omega_0}(s) = (F(s+\omega_0) + F(s-\omega_0))$ also has one, and we can state the following theorem that allows to compute the Allan variance of y_i by using the state space representation of a particular LTI system.

Theorem 5.8. *Let be $y = G_e w$, with w being a vector of normalized white noise, and assume that y satisfies Assumption 5.1. Let y_i be the in-phase signal of y, obtained by using demodulation under Assumption 2.1. Let G_e be a MISO convolution system admitting the state-space realization (A_G, B_G, C_G, D_G) with $D_G = 0$, and let the system $F = H_{All_T} F_L$ with the state-space representation (A_F, B_F, C_F, D_F). Then, the Allan variance of y_i is given by*

$$\sigma_{y_i}(T) = \sigma_w^2 Tr\left(B^T G_O B\right) \tag{5.39}$$

where Tr denotes the trace of a matrix, G_O is a solution of the equation

$$A^T G_O + G_O A + C^T C = 0$$

and

$$A = \begin{bmatrix} A_F & \omega_0 I & B_F C_G \\ -\omega_0 I & A_F & 0 \\ 0 & 0 & A_G \end{bmatrix}, B = \begin{bmatrix} B_F D_G \\ 0 \\ B_G \end{bmatrix},$$
$$C = \begin{bmatrix} 2C_F & 0 & 2D_F C_G \end{bmatrix}.$$

Proof. From Lemma 3.4, we have that for a given system with transfer function $F(s)$ and admitting the state-space representation (A_F, B_F, C_F, D_F), then the modulated system $(F(s+\omega_0) + F(s-\omega_0)$ has the state space representation

$$\left[\begin{array}{cc|c} A_F & \omega_0 I & B_F \\ -\omega_0 I & A_F & 0 \\ \hline 2C_F & 0 & 2D_F \end{array}\right].$$

Hence, with $y = G_e w$, we have from Theorem 5.7 and Theorem 5.3 that the Allan variance of y_i is given by (5.39).

□

Summarizing, the previous results allow to obtain the Allan variance of the in-phase component of a purely modulated signal by computing the $\mathcal{H}_2$ performance of a system, under the assumption that the system has a state-space representation. Nevertheless, as we discussed in subsection 5.3.1, the Allan filter is not a rational function of s. To cope with this issue, we can design approximated Allan filters, as we proposed in subsection 5.3.2 using a Padé approximation. In the case of demodulated signals, the equivalent LTI approach is possible by assuming an ideal synchronous demodulation, which contains an ideal low-pass filter. However, an ideal low-pass filter is an infinite dimensional system that does not have a state-space realization. Hence, in an applicative context, it is necessary to verify if the implementation of a non-ideal filter offers reasoneable results with respect to those obtained by adopting Assumption 2.1 .

In the application context of MEMS gyroscopes, we can observe from chapter 2 that Assumption 5.1 is a plausible one given the considerable high quality factor of the MEMS resonators, as well as the roll-off enforced by the controller for the frequencies outside the bandwidth of interest. Furthermore, when we implement synchronous demodulation in practice, it contains a non-ideal low-pass filter F_L, which is usually an LTI filter having a real state-space realization.

In the following example, we will observe that, despite the considered assumptions, Approach 2 allows to obtain an accurate estimation of the in-phase signal Allan variance, even when it is obtained from a resonating system whose output is not a purely modulated signals, s well as applying non-ideal synchronous demodulation.

5.5.3 Example

Let us present an example to compare the proposed methods. We consider a simple model $G_e(s)$ being a second order system with resonance frequency $\omega_0 = 1500Hz$ and a quality factor $Q = 100$. The implemented synchronous demodulation filter is a Butterworth low-pass filter of fifth order and cut-off frequency $\omega_c = 200Hz$. The obtained results, and its comparison with results obtained in simulation, are presented in Figure 5.15.

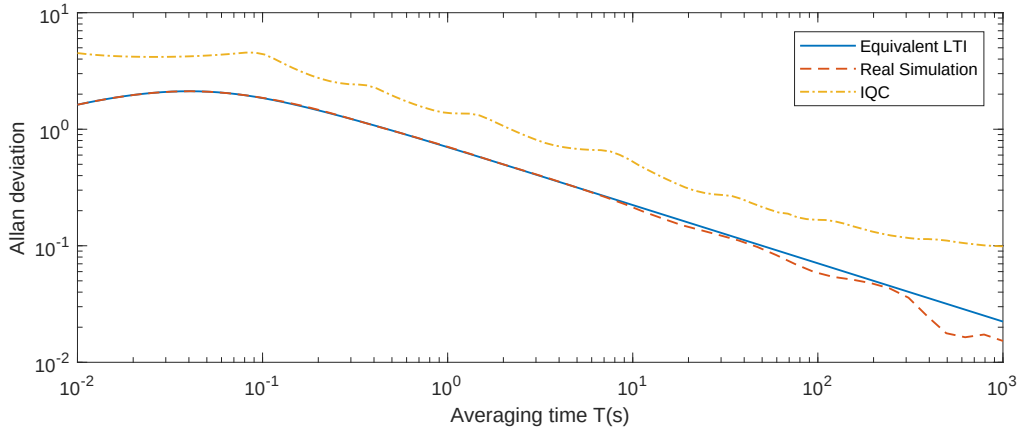

FIGURE 5.15: Comparison of simulation and estimation of Allan variance

We can observe that the proposed IQC approach offers an upper bound to the result obtained by simulating the system with an approximated Allan filter at the output and computing the power of the final output signal. The conservatism of the results can be reduced by adjusting the poles of the chosen basis Ψ according to the averaging time T, hence to the interval of frequencies to be analyzed.

In contrast, in spite of the adopted assumptions, the equivalent LTI approach offers very accurate results with respect to the actual Allan variance, showing their pertinence in the case of poorly-damped resonators corresponding to the closed-loop response of MEMS gyroscopes.

5.6 Application to MEMS gyroscope

In this last section, we present an application case where we apply the proposed analysis tools to an experimentally tested MEMS gyroscope. Similar to the application case of chapter 4, we exploit other results of the Next4MEMS project: the system models obtained through system identification methods [Col20] and the designed MIMO controllers [Sag21].

The MEMS gyroscopes and the development platform used for the experimental tests are provided by our industrial partners, and they are described in section 4.7 (application case for the measurement errors).

In Figure 5.16, we illustrate a schematic representation of the extended system used to compute the Allan variance of the gyroscope output z_i. The main elements of the system are the noise models N_{in}, the closed-loop MEMS model G_s, the cosine function representing the extraction of the in-phase signal, the low-pass filter of the demodulation F_L and finally the Allan filter H_{All_T}.

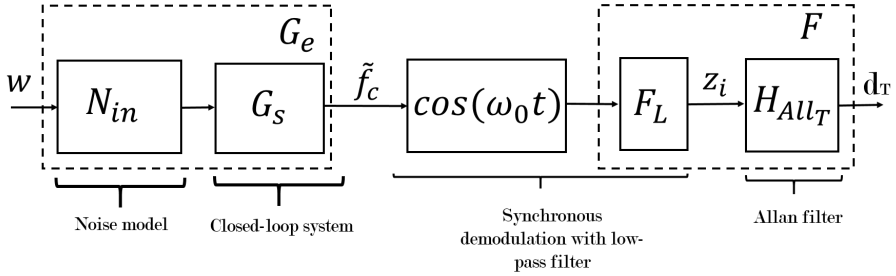

FIGURE 5.16: Equivalent system

The measured noise is presented in Figure 5.17. We can observe that it presents a long-term bias drift. Then, we apply a deterministic compensation of bias so that the measured noise can be considered as a stationary signal, which is a necessary assumption to apply the model-based computation of the Allan variance of stochastic signals. The compensated measure is shown in Figure 5.18.

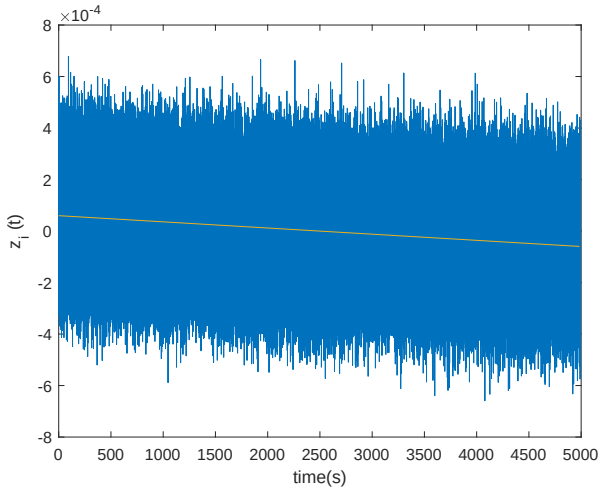

FIGURE 5.17: Measured output

Then, we compare the Allan variance obtained by two approaches. First, we compute the Allan variance by directly applying Definition 5.1 on the measured output z_i, implemented in discrete-time. Second, we apply Theorem 5.8 to compute the

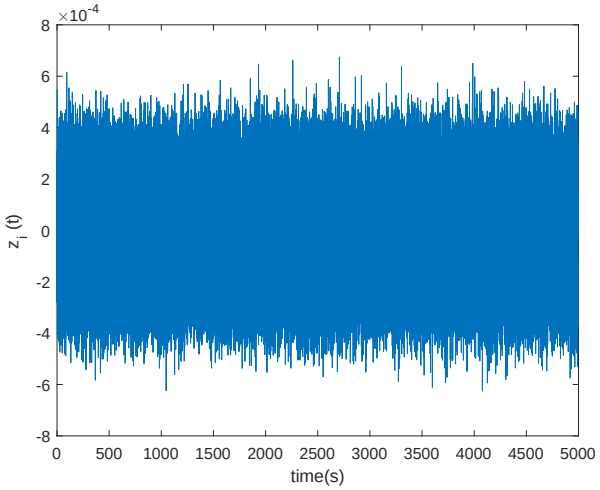

FIGURE 5.18: Compensated output

model-based Allan variance. The results are presented in Figure 5.19, where we can observe a close similarity on both computed Allan variances. Since the LTI approach is not a worst-case one, in this case it is possible to obtain a result that do not upper-bound the experimental result. The estimation errors can then be caused by the non-idealities inducing other non-stochastic processes (small bias drifts), modeling errors, the pure modulated assumption, the non-ideal filters, among other phenomena.

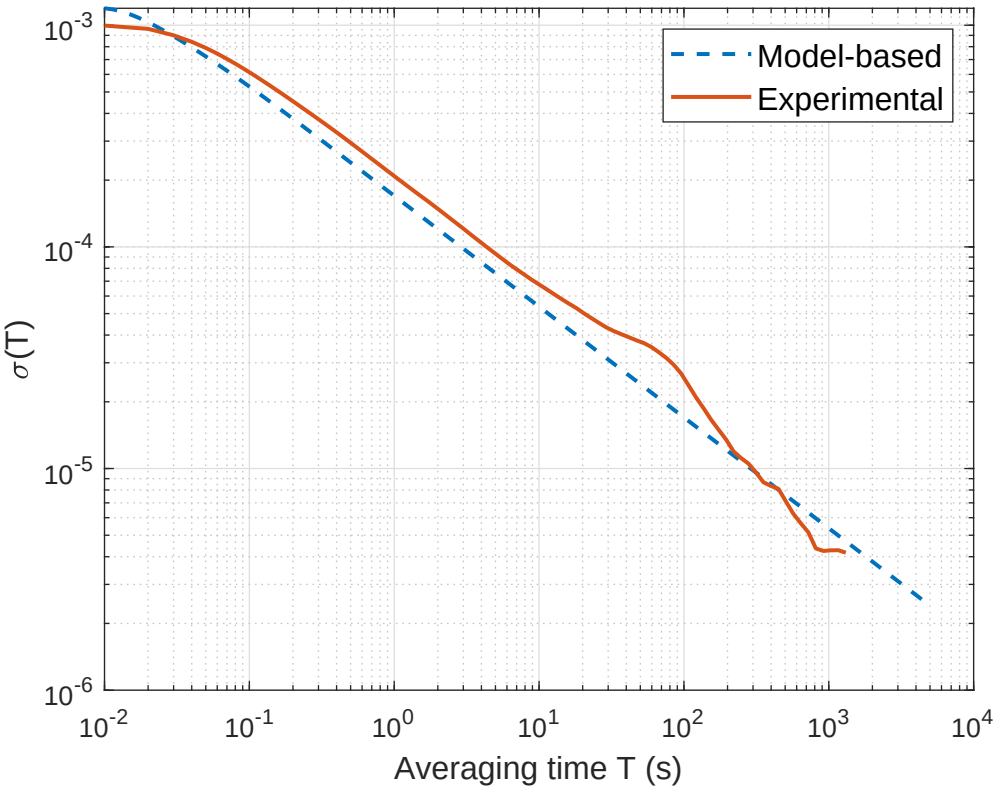

FIGURE 5.19: Comparison of Allan deviation results

5.7 Chapter conclusion

In this chapter, we address the analysis of the output noise. The standard method to evaluate the noise in MEMS gyroscopes is the Allan variance method. In order to translate the Allan variance method into a model-based method, several problems are tackled. First, the Allan variance can be interpreted as the computation of the power of the output of a system filtered by a so-called Allan filter. Then, using the notion of generating filter, the properties of the system characterized by the Allan variance are translated to the properties of the system generating the signal, finding a relationship between the Allan variance of the output signal and $\mathcal{H}_2$ performance of the generating system. Moreover, since the Allan filter, used to compute the Allan variance, is an infinite-dimensional system, we propose a Padé approximation to obtain a finite-dimensional Allan filter. The results are then extended to the worst-case Allan variance of uncertain systems. Finally, we address the problem of computing the Allan variance of a system containing synchronous demodulation. To this purpose, two methods are proposed; an IQC-based method, employing the proposed harmonic multipliers, and a method based on an equivalent LTI system, based on the properties of random modulated signals.

Chapter 6

Analysis methods for alternative control strategies

All along this manuscript, we study the problem of how to efficiently evaluate the global performances of MEMS gyroscopes, having as main objective to integrate this validation step in the control design process. In chapter 2, we introduce the application under study (gyroscopes MEMS) and the problem of evaluating performances when non-ideal phenomena arise. In chapter 3, we introduce the theoretical framework that can offer solutions to the performance validation problem, providing analysis tools for uncertain and harmonically time-varying systems, which can describe the main non-idealities in MEMS gyroscopes. Then, in chapter 4 and chapter 5 we formalize the global performance specifications into mathematical criteria that can be tested using the proposed analysis tools, introducing then the corresponding analysis conditions.

The proposed analysis solutions focus on offering a general framework that allows to model the main uncertain and time-varying features of MEMS gyroscopes, then to evaluate the stability and performance specifications by testing formal mathematical conditions. This set of tools was developed in a flexible form, such that they can be applied independently of the adopted control strategy. In order to introduce the main concepts, we mainly focused on an LTI MIMO direct control strategy, which leads us to a linear feedback control loop.

Now, in some cases, the control solutions can also modify the structure of the closed-loop system, adding elements that are nonlinear or time-varying. In such cases, although the proposed analysis solutions remain valid, it is necessary to provide supplementary tools that allow a performance analysis adapted to the new control solutions. Within the scope of the Next4MEMS project, two interesting and innovative control solutions were developed: a phasor-based control and a parameter-dependent control. Each of them demand the development of adequate analysis tools that are presented in this chapter. Both control strategies are designed by adopting some assumptions that, while reasonable, require a post-design analysis to ensure that stability and performance specifications are achieved in the absence of such assumptions.

First, in section 6.1, we introduce the phasor-based control, which relies in two assumptions: 1) the closed-loop internal signals, that are tracked and rejected in the closed-loop, are pure modulated signals in the sense of Definition 2.1; 2) the synchronous demodulation implemented in the closed-loop is assumed to be ideal. However, the real case, containing non pure modulated signals and non-ideal demodulation, degenerates the stability and performance guarantees. We then propose a stability analysis tool that, by modeling the system as a harmonically time-varying one, allows to test the stability of the control loop.

Then, in section 6.2, we describe the implementation of a discrete-time parameter-dependent control. This control approach exploits the structure of the drive mode resonator to design a controller that can be easily adapted to the resonance frequency changes using a simple frequency normalization. The controller design is possible by adopting some assumptions. First, the normalization technique uses the characteristics of the system in continuous time. However, we will observe that when this method is applied to design a discrete-time controller, the structure of the system does not allow a straightforward normalization, requiring to design the controller from a "fictitious" model. Secondly, the resonance frequency is a slowly time-varying parameter that it is assumed to be uncertain and time-invariant. Finally, it is assumed that the resonance frequency can be perfectly measured in real-time, without any error between the measure and the real value of the resonance frequency. We will observe that, without such assumptions, we need to face a robustness analysis problem that involves a non-rational dependency on the uncertain parameters.

6.1 Stability analysis of a phasor-based control strategy with non-ideal synchronous demodulation

During the years of development of MEMS gyroscopes, different approaches using concepts from different communities have been proposed (subsection 2.1.3). Traditionally, the literature has been mainly dominated by approaches using AGC + PLL strategies. These strategies have the advantage of implementing controllers whose structure is relatively simple, for instance, PI controllers in the simplest cases. Moreover, the control system employs sampling and processing frequencies that are much lower those used with direct control approaches, which are necessarily higher than the resonance frequency of the drive mode resonator. The biggest drawback of this type of architectures is that it requires the implementation of modulators and demodulators inside the loop, as well as a transformation from "in-phase" and "quadrature" signals to "amplitude" and "phase" signals, which implies an additional nonlinear operation.

On the other hand, the so-called direct control approaches have the advantage of operating in a more classical closed-loop architecture from the point of view of the control theory, which makes it possible to offer formal guarantees of stability, performance and robustness. This control approach allows a more systematic control design process to achieve the desired control objectives. Nevertheless, a drawback of this control approach is the necessity of controllers that, a priori, have more complex structures, and therefore consume more processing resources. In addition, they operate at frequencies that are close to (even higher than) the resonance frequency, which also requires higher sampling frequencies. This may find limitations in the context of inertial sensors, as the processor and sampler capabilities in embedded electronics may be limited for cost and space reasons.

Within the scope of the Next4MEMS project, one of the proposed strategies aims to merge the advantages of both solutions, that is, to propose a solution that allows to implement simpler controllers at low-frequencies, while giving formal stability and performance guarantees. This strategy is introduced in the following subsection.

6.1.1 Phasor-based control with ideal synchronous demodulation

The phasor-based control design is presented in details in [SSK20]. In this section, we describe some of the general concepts about the phasor-based modeling in an ideal

case, followed by the problems that arise when it is implemented, which implies to consider a non-ideal case for which an additional stability analysis is necessary.

The purpose of the phasor-based model is that, given an LTI plant, the controller allows to track reference signals and reject disturbances that are pure modulated signals in the sense of Definition 2.1, that is, signals whose spectrum is concentrated around the excitation frequency $\omega_{exc} \approx \omega_0$ and contained in the interval $[\omega_{exc} - W, \omega_{exc} + W]$ (for the positive frequencies), with $W < \omega_{exc}$. Let us begin by introducing the definition of the phasor associated to a modulated signal.

Definition 6.1. *Let the modulated signal $z(t)$ be given by*

$$z(t) = Z(t)\cos(\omega_{exc}t + \Phi_z(t),$$

where ω_{exc} is the harmonic frequency, here assumed to be constant, while $Z(t)$ and $\Phi_z(t)$ respectively are the instant amplitude and phase of the modulated signal. Then, the phasor associated to the signal z is defined as the couple (Z, ϕ_z) and it is usually expressed in the form of the complex phasor:

$$\underline{z}(t) = Z(t)e^{j\Phi_z(t)}$$

.

The advantage of considering a control strategy that works with the phasor instead of directly with the modulated signal is that the controller operates at frequencies that are much lower than the bandwidth of the modulated signals. For this reason, the amplitude-phase control strategies (see subsection 2.1.3) are probably the most popular in the MEMS community.

Let the MEMS resonator modes being modeled as the LTI plant with real state-space representation

$$G : \begin{cases} \dot{x}(t) = Ax(t) + Bu(t) \\ y(t) = Cx(t) + Du(t) \end{cases}, \tag{6.1}$$

where the input u and output y are pure modulated signals.

The difference with respect to the classical phasor-based approaches is based on the fact that the plant output y, being a modulated signal, written as

$$y(t) = Y(t)\cos(\omega_{exc}t + \Phi_y(t),$$

can be equivalently expressed as

$$y(t) = y_R(t)\cos(\omega_{exc}t) - y_I(t)\sin(\omega_{exc}t). \tag{6.2}$$

Then, the phasor-based approach proposed in [SSK20] control the real and imaginary parts of the phasor instead of the amplitude and phase of it. This rather simple change allows to get rid of the nonlinear operations (in the closed-loop) that are necessary to obtain the amplitude and phase from a modulated signal.

Hence, according to the strategy of [SSK20], the phasor-based controller is an LTI controller that operates with the real and imaginary part of the phasor associated to the modulated signals. This controller has the following state-space representation:

$$K : \begin{cases} \dot{x}_k(t) &= A_k x_k(t) + B_k\, s2p(y(t)) + B_k^r y_r(t) \\ u(t) &= p2s(C_k x_k(t) + D_k s2p(y(t)) + D_k^r y_r(t)) \end{cases}, \tag{6.3}$$

where $s2p$ and $p2s$ are respectively the signal-to-phasor and phasor-to-signal transformations. More specifically, given the modulated signal (6.2), the $s2p$ operation

extracts the real and imaginary parts of the associated phasor, that is

$$s2p(y(t)) = \begin{bmatrix} y_R(t) \\ y_I(t) \end{bmatrix}.$$

On the other hand, $p2s$ operation constructs a pure modulated signal u from the real and imaginary parts of its phasor, that is

$$p2s\left(\begin{bmatrix} u_R(t) \\ u_I(t) \end{bmatrix}\right) = u_R(t)\cos(\omega_{exc}t) - u_I(t)\sin(\omega_{exc}t).$$

Note that, in this case, all the internal signals of the closed-loop system are pure modulated signals.

The $s2p$ and $p2s$ transformations imply to introduce in the feedback-loop some operation that are not LTI. Nevertheless, as presented in [SSK20], in case of ideal operation of $s2p$ and $p2s$, the phasor-based control design method that computes the state-space matrices (A_k, B_k, C_k, D_k), such that the closed-loop system is stable and achieve tracking and disturbance rejection performances, is recast as a standard H_∞ problem.

The control design method is based on the fact that the plant G, from the perspective of the controller, can be seen as

$$G : \begin{cases} \dot{x}(t) & = Ax(t) + B\ p2s\left(\begin{bmatrix} u_R(t) \\ u_I(t) \end{bmatrix}\right) \\ \begin{bmatrix} y_R(t) \\ y_I(t) \end{bmatrix} & = s2p\left(Cx(t) + D\ p2s\left(\begin{bmatrix} u_R(t) \\ u_I(t) \end{bmatrix}\right)\right) \end{cases}, \tag{6.4}$$

Then, G can be rewritten as an equivalent LTI system G_{cp} whose input and output are the real and imaginary parts of the modulated signals [SACKS20]. This system has the state-space representation:

$$G_{cp} : \begin{cases} \begin{bmatrix} \dot{x}_R(t) \\ \dot{x}_I(t) \end{bmatrix} & = \begin{bmatrix} A & \omega_{exc}I \\ -\omega_{exc}I & A \end{bmatrix}\begin{bmatrix} x_R(t) \\ x_I(t) \end{bmatrix} + \begin{bmatrix} B & 0 \\ 0 & B \end{bmatrix}\begin{bmatrix} u_R(t) \\ u_I(t) \end{bmatrix} \\ \begin{bmatrix} y_R(t) \\ y_I(t) \end{bmatrix} & = \begin{bmatrix} C & 0 \\ 0 & C \end{bmatrix}\begin{bmatrix} x_R(t) \\ x_I(t) \end{bmatrix} + \begin{bmatrix} D & 0 \\ 0 & D \end{bmatrix}\begin{bmatrix} u_R(t) \\ u_I(t) \end{bmatrix} \end{cases}. \tag{6.5}$$

Therefore, the global closed-loop system can be seen as a global LTI system, represented in Figure 6.2.

Regarding the implementation, the $p2s$ transformation can be straightforwardly implemented by respectively multiplying u_R and u_I by cosine and sine functions (modulation).

Now, as pointed out in subsection 2.1.4, the $s2p$ operation is implemented using synchronous demodulation, as represented in Figure 6.1, where

$$\begin{cases} y_c(t) & = y_R(t) + \underbrace{y_R(t)\cos(2\omega_{exc}t) - y_I(t)\sin(2\omega_{exc}t)}_{\delta_{y_R}} \\ y_s(t) & = y_I(t) \underbrace{-y_R(t)\sin(2\omega_{exc}t) - y_I(t)\cos(2\omega_{exc}t)}_{\delta_{y_I}} \end{cases} \tag{6.6}$$

Since y is assumed to be a pure modulated signal, the spectra of y_R and y_I are contained in the frequency interval $[0, W]$, while the spectra of δ_{y_R} and δ_{y_I} are limited

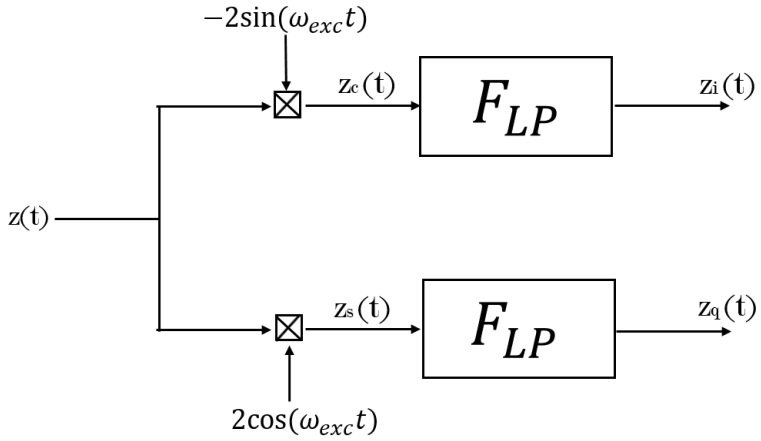

FIGURE 6.1: Implementation of $s2p$: synchronous demodulation

to the frequency range $[2\omega_{exc} - W, 2\omega_{exc} + W]$.

With the demodulation low-pass filter F_{LP} being an ideal filter with cut-off frequency $\omega_c < \omega_0$, we have that:

$$\begin{cases} y_c^{LP}(t) & = y_R(t) \\ y_s^{LP}(t) & = y_I(t) \end{cases} \tag{6.7}$$

completing the LTI closed-loop represented in Figure 6.2.

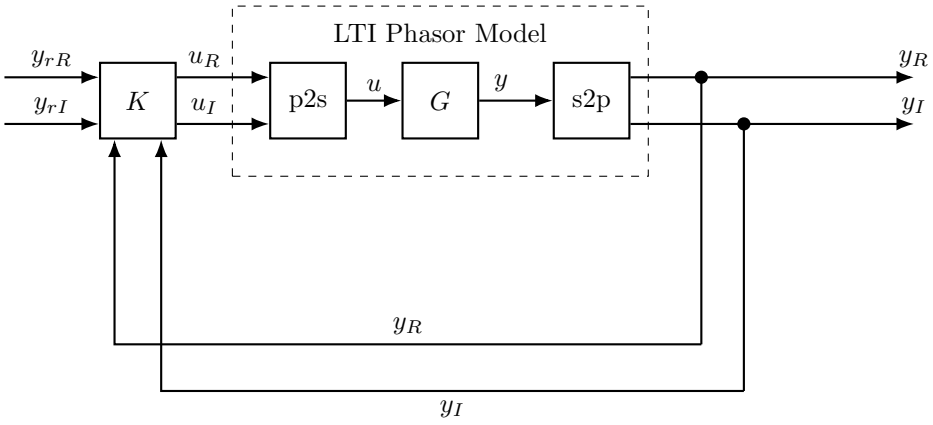

FIGURE 6.2: Ideal closed-loop phasor control

6.1.2 Analysis with non-ideal synchronous demodulation

The phasor control ensures stability and performance of the closed-loop system under the assumption that the synchronous demodulation in the loop is ideal and that the internal signals are pure modulated signals. Now, if F_{LP} is no longer an ideal low-pass filter, we have that

$$\begin{cases} y_c^{LP}(t) & \neq y_R(t) \\ y_s^{LP}(t) & \neq y_I(t) \end{cases} \tag{6.8}$$

Hence, our objective is to analyze if the closed-loop system remains stable when F_{LP} is not an ideal filter. Note that the equations (6.6) can be expressed as:

$$\begin{bmatrix} y_c(t) \\ y_s(t) \end{bmatrix} = \left(I_2 + \underbrace{\begin{bmatrix} \cos(2\omega_{exc}t) & -\sin(2\omega_{exc}t) \\ -\sin(2\omega_{exc}t) & -\cos(2\omega_{exc}t) \end{bmatrix}}_{R(t)} \right) \begin{bmatrix} y_R(t) \\ y_I(t) \end{bmatrix}, \tag{6.9}$$

where $R(t)$ is a full-block harmonic function whose structure is similar to a time-varying rotation matrix. Then, with F_{LP} being a non-ideal low-pass filter, the demodulated signals are given by

$$\begin{bmatrix} \widehat{y}_R(t) \\ \widehat{y}_I(t) \end{bmatrix} = \begin{bmatrix} F_{LP}(y_c)(t) \\ F_{LP}(y_s)(t) \end{bmatrix}. \tag{6.10}$$

Then, the non-ideal synchronous demodulation is, as illustrated in Figure 6.3, modeled by the ideal $s2p$ transformation, followed by an interconnection with a time-varying rotation operator $R(t)$ that represents the remaining components at $2\omega_{exc}$, then followed by the F_{LP}.

Remark. Replacing the ideal assumption of $\widehat{y}_R = y_R$ and $\widehat{y}_I = y_I$ by the equation (6.10) covers the two following non-ideal cases: 1) the synchronous demodulation filters F_{LP} are non-ideal; 2) the internal signals of the closed-loop are not pure modulated signals, that is, they do not have a limited bandwidth for instance in the presence of noise.

The components that are contained in $R(t)$, oscillating at twice the frequency ω_0, will be propagated through the closed-loop. This is a phenomenon that cannot be considered in the controller design process, yet it can have an effect on the stability of the system. In fact, it has been observed that in the presence of this high frequency oscillations, the stability of the system can be compromised for certain cut-off frequencies of the low-pass filters in the demodulator.

Now, since the plant phasor model, the phasor-based controller, and the low-pass filters F_{LP} are all linear, then, the non-ideal feedback phasor model, including the high frequency harmonic oscillationts can be modeled as a Linear Harmonically Time-Varying (LHTV) system $(M, R(t))$, defined in (3.31), where M represents the LTI part of the closed-loop system, given by

$$M = G_{cp}KF_{LP}(I - G_{cp}KF_{LP})^{-1},$$

while the function $R(t)$ is given by

$$R(t) = \begin{bmatrix} \cos(2\omega_{exc}t) & -\sin(2\omega_{exc}t) \\ -\sin(2\omega_{exc}t) & -\cos(2\omega_{exc}t) \end{bmatrix}.$$

Then, assessing the stability of the phasor-based closed-loop system with non-ideal synchronous demodulation can be considered as the stability analysis of a Linear Harmonically Time-Varying (LHTV) system. Therefore, this problem can be analyzed by using the catalog of multipliers proposed in chapter 3.

First, the phasor-based closed-loop can be equivalently recast as the feedback interconnection $(\tilde{M}_{full}, \theta^{2\omega_{exc}}_{full_s}(t))$, with $\theta^{2\omega_{exc}}_{full_s}(t)$ a singular full-block harmonic operator

$$\theta^{2\omega_{exc}}_{full_s}(t) = \begin{bmatrix} \cos(2\omega_{exc}t) & \sin(2\omega_{exc}t) \\ -\sin(2\omega_{exc}t) & \cos(2\omega_{exc}t) \end{bmatrix},$$

and

$$\tilde{M}_{full} = \begin{bmatrix} 1 & 0 \\ 0 & -1 \end{bmatrix} M,$$

allowing to employ the set of

- multipliers for full block harmonic operators in the singular case, denoted $\mathbf{\Pi}_{\boldsymbol{\theta Rs}}^{2\omega_{exc}}$ (3.67).

Furthermore, the interconnection can be also rearranged as the equivalent LHTV system $(\tilde{M}_{SD}, \theta_{SD}^{2\omega_{exc}}(t))$, with

$$\theta_{SD}^{2\omega_{exc}}(t) = \begin{bmatrix} \cos(2\omega_{exc}t) I_2 & 0 \\ 0 & \sin(2\omega_{exc}t) I_2 \end{bmatrix} q(t).$$

and

$$\tilde{M}_{SD} = \begin{bmatrix} 1 & 0 \\ 0 & 1 \\ 0 & 1 \\ 1 & 0 \end{bmatrix} M \begin{bmatrix} 1 & 0 & -1 & 0 \\ 0 & -1 & 0 & -1 \end{bmatrix}.$$

This second representation allows to test the stability by employing other three sets of harmonic multipliers:

- multipliers for single repeated harmonic oscillations $\mathbf{\Pi}_{\boldsymbol{\theta}}^{2\omega_{exc}}$, given by (3.35);
- multipliers for coupled harmonic oscillations $\mathbf{\Pi}_{\boldsymbol{\theta SD}}^{2\omega_{exc}}$, (3.55);
- multipliers for arbitrarily time-varying parameters $\mathbf{\Pi}_{\boldsymbol{TV}}$, (3.32).

In order to quantify the conservatism of the different sets of multipliers, we replace θ^{ω_0} by $\alpha\theta^{\omega_0}$, $\alpha > 0$. Then we evaluate the maximal amplitude of oscillations α for which each set of multipliers can ensure the stability. Physically speaking, we can observe that if $\alpha \geq 1$, then the multiplier can guarantee the stability of the real closed-loop system.

The non-ideal filters F_{LP} are designed as first-order linear filters with cut-off frequency $\omega_c = 67.3 rad/s$, which is close to the nominal instability of the closed-loop gyroscope under consideration. The results are summarized in Table 6.1. We can compare the conservatism associated to each set of multipliers. First, the set of multipliers that leads to the best results is the coupled harmonics set $\mathbf{\Pi}_{\boldsymbol{\theta SD}}$, given by (3.55). Comparing with the sets of multipliers for single-repeated harmonic $\mathbf{\Pi}_{\boldsymbol{\theta}}$, as expected, the set of $\mathbf{\Pi}_{\boldsymbol{\theta SD}}$ is less conservative since the former includes information about the phase-shift between harmonic oscillations. In both cases, the inclusion of the non-diagonal functions X_G radically reduces the conservatism of the analysis results, confirming its relevance and the interest for future developments.

In the other extreme, the set of multipliers for arbitrarily-fast time-varying parameters $\mathbf{\Pi}_{\boldsymbol{TV}}$ is by far the most conservative set of multipliers, which it is expected given that these multipliers are not frequency-dependent. Finally, the case of the set for full-block (singular) harmonic operators $\mathbf{\Pi}_{fullS}$, although it is a set of frequency-dependent multipliers and it integrates the structure of the operator, showed to be a more conservative set than $\mathbf{\Pi}_{\boldsymbol{\theta SD}}$ and $\mathbf{\Pi}_{\boldsymbol{\theta}}$. This results suggests that, it might be interesting to further investigate its relationship with other sets of multipliers, looking for the possibility of finding larger sets of multipliers for full-block (singular) harmonic operators.

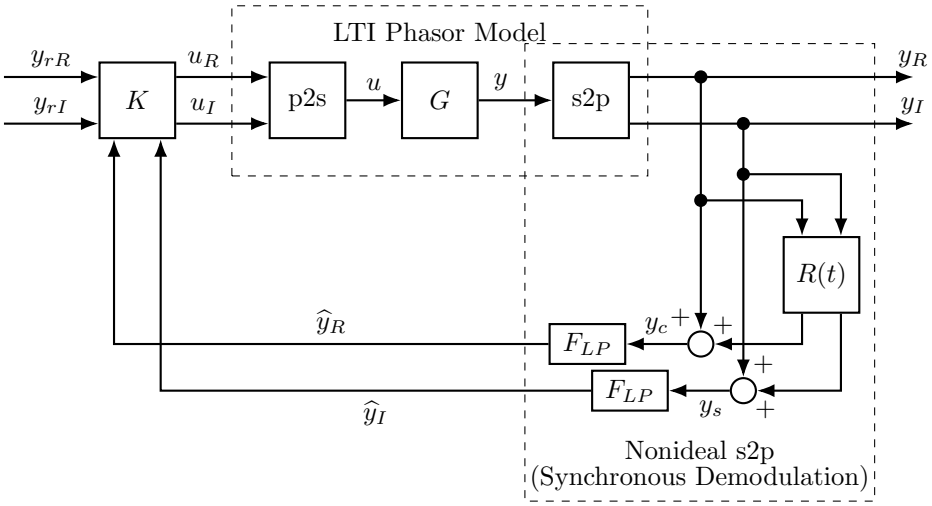

FIGURE 6.3: Non-ideal closed-loop phasor control

Multiplier set	α max (only with X_D)	α max (with X_D and X_G)
$\mathbf{\Pi}_{\theta}^{2\omega_{esx}}$: single repeated harm.	1.1621	3.5156
$\mathbf{\Pi}_{\theta SD}^{2\omega_{exc}}$: coupled harmonics	1.1719	4.7656
$\mathbf{\Pi}_{\theta Rs}^{2\omega_{exc}}$: full-block singular	0.9766	0.9863
$\mathbf{\Pi}_{TV}$: arbitrarily TV	0.2891	0.2891
Simulation	≈ 5.1	≈ 5.1

TABLE 6.1: Results of the non-ideal phasor closed-loop analysis

6.2 Analysis of the discrete-time implementation of a parameter dependent adaptative controller

In this section, we introduce a parameter-dependent control strategy that aims to improve the tracking performance of the MEMS drive mode. In chapter 2, we discuss that the main objective of the drive mode control is to maintain a constant amplitude of the oscillations. Furthermore, we also mention that a secondary objective is to maintain an excitation frequency close to the resonance frequency of the drive mode oscillator. Indeed, exciting the system at the resonance frequency simultaneously allows to minimize the tracking error, to reduce the energy consumption and to improve the signal to noise ratio. Hence, the objective of the parameter-dependent control is to ensure an accurate excitation at the resonance frequency.

Changes in temperature make difficult the achievement of this objective because they introduce a frequency shift of the drive mode resonance frequency, causing a mismatch with respect to the reference excitation frequency, thus an important gain reduction. The proposed MIMO direct control consists in designing a controller that can ensure a certain level of performance for a frequency range around the drive mode resonance frequency, then the controller can compensate the lost of gain due to the frequency shifting. Nevertheless, as we can observe in the example illustrated in Figure 6.4, the optimal drive-mode tracking performance is degraded when the resonance frequency derives from its nominal value. Furthermore, additional practical problems might arise in such situation, such as noise amplification, energy consumption or saturation of the control signals.

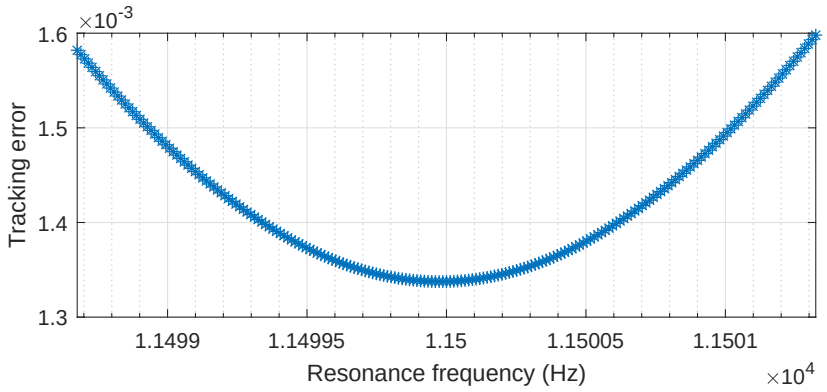

FIGURE 6.4: Impact of resonance frequency variations on the tracking error

Even though the variations of temperature are considerably slower than the dynamics of the system, they end up causing very important performance deterioration through the drifts of the resonance frequency. In this context, an optimal control strategy should be able to adapt the reference signal and the controller when the resonance frequency ω_0 changes.

Within the Next4MEMS project, some techniques for the estimation of the resonance frequency have been explored, considering mainly the implementation of the extremum seeking method and the recursive system identification, see [Mor21]. Using these methods, it is possible to obtain a real-time estimate of the resonance frequency during the operation, and thus to exploit it by updating the corresponding control variables.

The control design method exploits the system structure to propose a simple adaptative control strategy [SACKS20]. This control strategy uses a parameterization of the controller that has a linear dependency on the excitation frequency, which comes to perform a frequency normalization of the controller. This design method relies on three main assumptions:

1. the design method, proposed for continuous time, remains valid when implemented in discrete-time;

2. the slowly varying resonance frequency is modeled as a time-invariant parameter;

3. the resonance frequency can be perfectly measured in real time and without errors.

Nevertheless, these assumptions are not completely respected in a real implementation, which implies that formal guarantees of stability and performance cannot be given. It is then necessary to perform an analysis to validate designed controller using a more realistic model. However, as it will be introduced in the following, the associated analysis problem presents a particular characteristic: the model does not rationally depend on the uncertain parameters. This issue is addressed by proposing an approximation-based approach that offers formal stability and performance guarantees.

6.2.1 Analysis of the discrete-time implementation of parameter dependent controller with non-ideal resonance frequency estimation

The general objective of this section is to propose a method that evaluates if a discrete time parameter-dependent control ensures the stability and the tracking performance of the closed-loop system.

The drive mode is modeled by a discrete-time system with state-space representation:

$$G^d_{\omega_0} : \left\{ \begin{array}{rcl} x((k+1)T_s) & = & e^{\omega_0 e^{AT_s}} x(kT_s) + (e^{\omega_0 e^{AT_s}} - I)A^{-1}Bu(kT_s) \\ y(kT_s) & = & Cx(kT_s) + Du(kT_s) \end{array} \right. , \tag{6.11}$$

where ω_0 is the resonance frequency of the drive mode, T_s the sampling frequency and A, B, C, D the state-pace matrices of the continuos time and normalized drive mode system model, see [SACKS20]. Given that the variations of the resonance frequency are mainly caused by changes of temperature, which are considerably slower than the main dynamics of the system, ω_0 is assumed to be a time-invariant uncertain parameter, that is

$$\omega_0 \in [\underline{\omega}_0, \overline{\omega}_0].$$

The parameter-dependent controller $K^c_{\tilde{\omega}_0}$ is designed in a continuous-time space, linked to the discrete-time space via the bilinear transform (or Tustin method). The controller is synthesized by employing a simplified fictitious plant model with similar characteristics to those of $G^d_{\omega_0}$ [SACKS20]. The obtained controller has the state-space representation:

$$K^c_{\tilde{\omega}_0} : \left\{ \begin{array}{rcl} \dot{x}_K(t) & = & g(\tilde{\omega}_0)A_K x_K(t) + g(\tilde{\omega}_0)B_{Kr} y_r(t) + g(\tilde{\omega}_0)B_K y(t) \\ u(t) & = & C_K x_K(t) + D_{Kr} y_r(t) + D_K y(t) \end{array} \right. . \tag{6.12}$$

where $\tilde{\omega}_0$ is the measure of the resonance frequency ω_0 and

$$g(\omega) = \frac{2}{T_s} \tan\left(\frac{\omega T_s}{2}\right).$$

In the sequel, the mismatch between the measured resonance frequency $\tilde{\omega}_0$ and the actual resonance frequency ω_0 is the denoted ω_m, which is assumed to belong to the interval $[-\overline{\omega}_m, \overline{\omega}_m]$.

Since the controller is designed from a simplified model of the plant, we can not formally ensure that the obtained controller will meet the desired closed-loop stability and performance requirements. We then aim to analyze the stability and the performance of the closed-loop system by considering a plant that better corresponds to the real system. Furthermore, removing the perfect measurement assumption implies that both the reference excitation frequency and the parameterization of the parameter-dependent controller might have a mismatch ω_m with respect to the actual resonance frequency ω_0. The analysis problem is then stated as follows.

Problem 6.1. *Let be a closed-loop system, consisting in the interconnection of the continuous-time controller $K^c_{\tilde{\omega}_0}$ and the continuous time plant $G^c_{\omega_0}$, obtained by applying the bilinear transform to $G^d_{\omega_0}$. Test if the closed-loop system is stable and achieves some tracking performance level*

$$|T^c_{y_r \to \varepsilon}(j\, g(\omega_0 + \omega_m))| \leq \eta, \tag{6.13}$$

for all $\omega_0 \in [\underline{\omega}_0, \overline{\omega}_0]$ and for all $\omega_m \in [-\overline{\omega}_m, \overline{\omega}_m]$, with $T^c_{y_r \to \varepsilon}$ denoting the transfer function associating the reference signal to the tracking error.

Indeed, since the system input is a sinusoidal reference signal with excitation frequency given by the measured resonance frequency $g(\omega_0+\omega_m)$, then the tracking error is given by the harmonic response of $T^c_{y_r\to\varepsilon}$ at the frequency $g(\omega_0+\omega_m)$.

Since the bilinear transform maps the left half of the Laplace complex plane to the inner part of the unitary circle in the Z complex plane, then, ensuring the system stability in continuous-time implies also the system stability in discrete-time. Furthermore, the tracking performance tested in continuous-time is strictly equivalent to the discrete-time tracking performance:

$$|T^d_{y_r\to\varepsilon}(e^{j(\omega_0+\omega_m)T_s})| \leq \eta.$$

Then, without loss of generality, we address here the analysis problem in continuous-time.

We can observe, in (6.11), that the discrete-time plant $G^d_{\omega_0}$ has a linear dependency on the exponential function e^{ω_0}, which contains the parameter of interest. Moreover, any LTI discrete-time system can be expressed as the LFT interconnection of a constant matrix and the Z-domain delay operator, then $G^d_{\omega_0}$ can be represented as the following LFT:

$$G^d_{\omega_0} = e^{\omega_0} I \star \left(z^{-1} I \star M^d_G\right). \tag{6.14}$$

with

$$M^d_G = \begin{bmatrix} 0 & I & -A^{-1}B \\ e^{AT_s} & 0 & e^{AT_s}A^{-1}B \\ C & 0 & D \end{bmatrix}$$

Then, applying the bilinear transform to pass the system into continuous-time comes to replace z by $\frac{1+\frac{sT_s}{2}}{1-\frac{sT_s}{2}}$. We then obtain the continuous-time LFT plant, given by

$$G^c_{\omega_0} = e^{\omega_0} I \star \left(\frac{1-\frac{sT_s}{2}}{1+\frac{sT_s}{2}} I \star M^d_G\right) = e^{\omega_0} I \star M^c_G(s), \tag{6.15}$$

with

$$M^c_G(s): \left\{ \begin{bmatrix} \dot{\zeta}(t) \\ q_e(t) \\ y(t) \end{bmatrix} = \begin{bmatrix} -\frac{2}{T_s} I & \frac{4}{T_s} I & -\frac{4}{T_s} A^{-1}B \\ e^{AT_s} & -e^{AT_s} & 2e^{AT_s}A^{-1}B \\ C & -C & CA^{-1}B + D \end{bmatrix} \begin{bmatrix} \zeta(t) \\ p_e(t) \\ u(t) \end{bmatrix} \right.$$

Now, the evaluation of the tracking performance presents a difficulty. In fact, the performance condition (6.13) demands to be tested at the frequency $g(\omega_0+\omega_m)$, for all $\omega_0 \in [\underline{\omega}_0, \overline{\omega}_0]$ and for all $\omega_m \in [-\overline{\omega}_m, \overline{\omega}_m]$, implying an infinite number of constraints.

However, note that (6.13) can be radically simplified by considering a frequency normalization of $T^c_{y_r\to\varepsilon}$, i.e. taking $\omega_n = \omega / g(\omega_0+\omega_m)$, obtaining then the following tracking performance condition:

$$|T^c_{(y_r\to\varepsilon)_n}(j\cdot 1)| \leq \eta. \tag{6.16}$$

where $T^c_{(y_r\to\varepsilon)_n}$ denotes the normalized version of the system $T^c_{y_r\to\varepsilon}$.

As a consequence, the controller and the plant need to be normalized. Note that, since the controller $K^c_{\tilde{\omega}_0}$ is linearly parameterized by $g(\omega_0+\omega_m)$, then its normalize

version K_n^c is straightforwardly obtained:

$$K_n^c : \left\{ \begin{array}{rcl} \dot{x}_K(t_n) & = & A_K x_K(t_n) + B_{Kr} y_r(t_n) + B_K y(t_n) \\ u(t_n) & = & C_K x_K(t_n) + D_{Kr} y_r(t_n) + D_K y(t_n) \end{array} \right. . \tag{6.17}$$

In the other hand, normalization of the continuous-time plant is a transformation that implies a linear dependency on the function $\frac{1}{g(\omega_0+\omega_m)} I$, the normalized plant can then be expressed as the LFT system

$$G_n^c(s_n) = \text{diag}\left(\frac{1}{g(\omega_0+\omega_m)} I, e^{\omega_0} I \right) \star M_{Gn}^c(s_n). \tag{6.18}$$

with

$$M_{Gn}^c(s_n) : \left\{ \begin{bmatrix} \dot{\zeta}(t_n) \\ q_e(t_n) \\ q_g(t_n) \\ y(t_n) \end{bmatrix} = \begin{bmatrix} 0 & 0 & I & 0 \\ e^{AT_s} & -e^{AT_s} & 0 & 2e^{AT_s} A^{-1} B \\ -\frac{2}{T_s} I & \frac{4}{T_s} I & 0 & -\frac{4}{T_s} A^{-1} B \\ C & -C & 0 & CA^{-1}B + D \end{bmatrix} \begin{bmatrix} \zeta(t_n) \\ p_e(t_n) \\ p_g(t_n) \\ u(t_n) \end{bmatrix} \right.$$

Finally, the global closed-loop system $T^c_{(y_r \to \varepsilon)_n}$ can be represented as an LFT system, illustrated in Figure 6.5, given by:

$$T^c_{(y_r \to \varepsilon)_n}(s_n) = \text{diag}\left(\frac{1}{g(\omega_0+\omega_m)} I, e^{\omega_0} I \right) \star M_\mu(s_n). \tag{6.19}$$

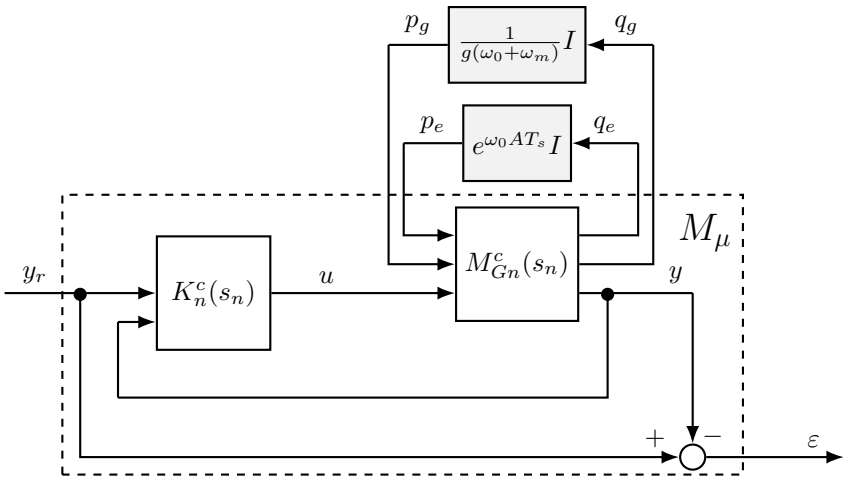

FIGURE 6.5: Analysis model in normalized pseudo-continuous time

Then, we can test the robust stability of systems modeled as LFT interconnections by using Theorem 3.1. Since both ω_0 and ω_m are time-invariant parametric uncertainties, we can employ the set of multipliers $\mathbf{\Pi_{TI}}$, given by (3.33), to characterize each of them. We can then construct a set of multipliers for the combinaton of the two uncertainties, as indicated in subsection 3.4.2.

If the robust stability is verified, then, testing the robust performance, defined by the constraint (6.16), is a particular version of Theorem 3.2 that consists on testing (3.15) at only one sampled frequency $\omega = 1$ rad/s.

However, in order to apply Theorem 3.1 and the particular version of Theorem 3.2, it is required to consider an LFT model where the uncertain parameters appear in a diagonal structure, i.e. $\text{diag}(\delta_1 I_{\delta_1}, ..., \delta_n I_{\delta_n})$. This is always possible if the

dependency of the function on the uncertain parameters is rational. However, this is not actually the case since the dependency of e^{ω_0} and $1/g(\omega_0+\omega_m)$ is nonrational with respect to ω_0 and ω_m.

Therefore, we introduce a solution based on a Taylor approximation that allows to transform e^{ω_0} and $1/g(\omega_0+\omega_m)$ into functions that rationally depend on ω_0 and ω_m. Furthermore, the proposed method allows to model the approximation errors as supplementary uncertainties, providing then sufficient stability and performance guarantees.

In order to establish an LFT model that can be analyzed, we propose to approximate the nonrational functions e^{ω_0} and $1/g(\omega_0+\omega_m)$ by rational functions of the uncertain parameters. The proposed approach is based on a Taylor approximation series. However, any approximation produces an error between the original function and the approximated one. Hence, it is important to take into account such approximation error in order to do not neglect its impact on the system stability and performance.

Let us introduce the following lemma that allows to embed nonrational function of an uncertain parameter into an LFT representation whose uncertain block contains the parameter of interest, as well as the approximation errors in the form of addtional uncertainties.

Lemma 6.1. *Let be a nonrational matrix function $F(\theta)\in\mathbb{R}^{n_q\times n_q}$ depending on a parameter θ, with θ taking values in a finite interval $[\underline{\theta},\overline{\theta}]$ and with nominal value $\theta_c=(\overline{\theta}+\underline{\theta})/2$. If $F(\theta)$ is derivable $(d+1)$ times, then: $\forall\,\theta\in[\underline{\theta},\overline{\theta}]$, $\exists\,\Delta_{RF}\in\mathbb{R}^{n_q\times n_q}$, $\overline{\sigma}(\Delta_{RF})\leq R_{maxF}$ such that $F(\theta)=diag(\delta_\theta I_{(d\times n_q)},\Delta_{RF})\star N_F$ with $\delta_\theta=\theta-\theta_c$,*

$$N_F=\begin{bmatrix} 0 & \dots & 0 & 0 & I_{n_q}\\ I_{(d\times n_q)-1} & & 0 & 0 & 0\\ 0 & \dots & 0 & 0 & I_{n_q}\\ F_1 & \dots & F_d & I_{n_q} & F_0\end{bmatrix}, \tag{6.20}$$

$F_0=F(\theta_c)$, $F_k=\frac{1}{k!}\frac{d^kF}{d\theta^k}(\theta_c)\;\forall\,k\in\{1,\dots,d\}$, *and*

$$R_{maxF}=\frac{D}{(d+1)!}\,(\delta_{max\theta})^{d+1}$$

with $D\geq\|\frac{d^{(d+1)}F}{d\theta^{(d+1)}}(\theta_\xi)\|\;\forall\,\theta_\xi\in[\underline{\theta},\overline{\theta}]$, *and* $\delta_{max\theta}=\frac{(\overline{\theta}-\underline{\theta})}{2}$.

Proof. Using a Taylor series approximation, $F(\theta)$ can be developed as:

$$F(\theta)=F_0+\sum_{k=1}^{d}\delta_\theta^kF_k\;+R_F(\theta), \tag{6.21}$$

where $R_F(\theta)$ is the residual or approximation error. Since the residual $R_F(\theta)$ is bounded by R_{maxF}, it can be modeled as a block uncertainty, i.e. Δ_{RF} such that $\overline{\sigma}(\Delta_{RF})\leq R_{maxF}$.

Using the fact that $\delta_\theta^n=\prod_{k=1}^{n}\delta_\theta$, we have that $F(\theta)$ can be written as

$$F(\theta)=F_0+\delta_\theta(F_1+\delta_\theta(F_2+\delta_\theta(...(F_d))))\;+\Delta_{RF}.$$

Then, defining $p_1 = \delta_\theta q_1, ..., p_d = \delta_\theta q_d$ and $p_{(d+1)} = \Delta_{RF} q_{(d+1)}$, the expression $z = F(\theta)w$ can be written as

$$z = F_0 w + F_1 p_1 + ... + F_d p_d + p_{(d+1)}$$

with

$$\begin{bmatrix} q_1 \\ q_2 \\ \vdots \\ q_d \\ q_{(d+1)} \\ z \end{bmatrix} = \begin{bmatrix} 0 & \cdots & 0 & 0 & 0 & I_{n_q} \\ I_{n_q} & \cdots & 0 & 0 & 0 & 0 \\ \vdots & \ddots & \ddots & \ddots & \ddots & \vdots \\ 0 & \cdots & I_{n_{qe}} & 0 & 0 & 0 \\ 0 & \cdots & 0 & 0 & 0 & I_{n_q} \\ F_1 & \cdots & F_{(d-1)} & F_d & I_{n_q} & F_0 \end{bmatrix} \begin{bmatrix} p_1 \\ \vdots \\ p_{(d-1)} \\ p_d \\ p_{(d+1)} \\ w \end{bmatrix}$$

□

It is important to note that the application of Lemma 6.1 implies a trade-off between the size of the LFT representation, which depends on the truncation order d, and the size of the approximation error $R(\theta)$, related to the conservatism of the analysis result.

Using the Lemma 6.1, the original system with nonrational dependency can be recast as a system with rational dependency. This new system can then be exploited for analysis using classical results of the robustness analysis framework. Let us then introduce the following Theorem that allows to test the stability and the tracking performance given by the transfer $T^c_{(y_r \to \varepsilon)_n}$, implying the tracking performance of $T^c_{y_r \to \varepsilon}$.

Theorem 6.1. *Let be the LFT system given by (6.19). Let* $\mathbf{\Delta}$ *be the set defined by:*

$$\mathbf{\Delta} = \left\{ \Delta \;\middle|\; \begin{array}{c} \exists\, \delta_{\omega_0} \in [\underline{\omega}_0, \overline{\omega}_0],\ \exists\, \delta_{\omega_m} \in [-\overline{\omega}_m, \overline{\omega}_m], \\ \exists\, \delta_{Rg} \in [-R_{maxg}, R_{maxg}],\ \exists\, \delta_{R_e} \in [-R_{maxe}, R_{maxe}] \\ \\ \Delta = diag(\delta_{\omega_0} I_{(d\times n_{qg})+(d\times n_{qe})}, \delta_{\omega_m} I_{d\times n_{qg}}, \delta_{Rg} I_{n_{qg}}, \delta_{Re} I_{n_{qe}}) \end{array} \right\}. \tag{6.22}$$

Let N be given by

$$\begin{bmatrix} 0 & \dots & 0 & 0 & \dots & 0 & 0 & \dots & 0 & 0 & 0 & I_{n_{qg}} & 0 \\ I_{(d\times n_{qg})-1} & & 0 & 0 & \dots & 0 & 0 & \dots & 0 & 0 & 0 & 0 & 0 \\ 0 & \dots & 0 & 0 & \dots & 0 & 0 & \dots & 0 & 0 & 0 & 0 & I_{n_{qe}} \\ 0 & \dots & 0 & I_{(d\times n_{qe})-1} & & 0 & 0 & \dots & 0 & 0 & 0 & 0 & 0 \\ 0 & \dots & 0 & 0 & \dots & 0 & 0 & \dots & 0 & 0 & 0 & I_{n_{qg}} & 0 \\ 0 & \dots & 0 & & 0 & & 0 & I_{(d\times n_{qg})-1} & 0 & 0 & 0 & 0 & 0 \\ 0 & \dots & 0 & 0 & \dots & 0 & 0 & \dots & 0 & 0 & 0 & I_{n_{qg}} & 0 \\ 0 & \dots & 0 & & 0 & & 0 & I_{(d\times n_{qg})-1} & 0 & 0 & 0 & 0 & 0 \\ 0 & \dots & 0 & 0 & \dots & 0 & 0 & \dots & 0 & 0 & 0 & I_{n_{qg}} & 0 \\ 0 & \dots & 0 & 0 & \dots & 0 & 0 & \dots & 0 & 0 & 0 & 0 & I_{n_{qe}} \\ g_1 I_{n_{qg}} & \dots & g_d I_{n_{qg}} & & 0 & & 0 & g_1 I_{n_{qg}} & \dots & g_d I_{n_{qg}} & I_{n_{qg}} & 0 & g_0 I_{n_{qg}} & 0 \\ 0 & \dots & 0 & e_1 I_{n_{qe}} & \dots & e_d I_{n_{qe}} & 0 & \dots & 0 & 0 & I_{n_{qe}} & 0 & e_0 I_{n_{qe}} \end{bmatrix} \tag{6.23}$$

with $e_0 = e^{\omega_{0c}}$, $e_k = \frac{1}{k!}\frac{d^k e^{\omega_0}}{d\omega_0}(\omega_{0c})\ \forall\, k \in \{1, \dots, d\}$, $\omega_{0c} = (\overline{\omega}_0 + \underline{\omega}_0)/2$ *and*

$$R_{maxe} = \frac{D_e}{(d+1)!}\left(\delta_{max\omega_0}\right)^{d+1}$$

with $D_e \geq |\frac{d^{(d+1)}e^{\omega_0}}{d\omega_0^{(d+1)}}(\omega_0)| \; \forall \; \omega_0 \in [\underline{\omega}_0, \overline{\omega}_0]$, *and* $\delta_{max\omega_0} = \frac{(\overline{\omega}_0 - \underline{\omega}_0)}{2}$, $g_0 = \frac{1}{g(\omega_{0c})}$, $g_k = \frac{1}{k!}\frac{d^k(1/g)}{d\omega_0^k}(\omega_{0c}) \; \forall \; k \in \{1, \ldots, d\}$, *and*

$$R_{maxg} = \frac{D_g}{(d+1)!}\left(\delta_{max\omega_0} + \delta_{max\omega_m}\right)^{d+1}$$

with $D_g \geq |\frac{d^k(1/g)}{d\omega_0}(\omega_0 + \omega_m)| \; \forall \; \omega_0 \in [\underline{\omega}_0, \overline{\omega}_0]$, *and* $\forall \; \omega_m \in [-\overline{\omega}_m, \overline{\omega}_m]$, *and with* $\delta_{max\omega_0} = \frac{(\overline{\omega}_0 - \underline{\omega}_0)}{2}$, $\delta_{max\omega_m} = \overline{\omega}_m$.

Then, if the LFT system $\Delta \star (N \star M_\mu)$ *is stable and ensures*

$$|\Delta \star (N \star M_\mu(j \times 1))| \leq \eta, \tag{6.24}$$

for all $\Delta \in \mathbf{\Delta}$, *then,* $T^c_{(y_r \to \varepsilon)_n}$ *and* $T^c_{y_r \to \varepsilon}$ *are stable and satisfy conditions* (6.13) *and* (6.16) $\forall \; \omega_0 \in [\underline{\omega}_0, \overline{\omega}_0]$ *and* $\forall \; \omega_m \in [-\overline{\omega}_m, \overline{\omega}_m]$.

Proof. When we apply Lemma 6.1 to $e^{\omega_0} I_{n_{qe}}$, we have the Taylor approximation

$$e^{\omega_0} I_{n_{qe}} = e_0 I_{n_{qe}} + \sum_{k=1}^{d} \delta^k_{\omega_0} e_k I_{n_{qe}} \; + R_e(\omega_0),$$

with $e_0 = e^{\omega_{0c}}$, $e_k = \frac{1}{k!}\frac{d^k e^{\omega_0}}{d\omega_0}(\omega_{0c}) \; \forall \; k \in \{1, \ldots, d\}$, $\omega_{0c} = (\overline{\omega}_0 + \underline{\omega}_0)/2$, $R_e(\omega_0)$ the diagonal matrix $r_e(\omega_0) I_{n_{qe}}$ and $r_e(\omega_0)$ the scalar residual of the Taylor approximation of e^{ω_0}.

Then, the bounded residual can be modeled as the structured uncertainty $\Delta_{Re} = \delta_{Re} I_{n_{qe}}$, $|\delta_{Re}| \leq R_{maxe}$, with

$$R_{maxe} = \frac{D_e}{(d+1)!}\left(\delta_{max\omega_0}\right)^{d+1}$$

with $D_e \geq |\frac{d^{(d+1)}e^{\omega_0}}{d\omega_0^{(d+1)}}(\omega_0)| \; \forall \; \omega_0 \in [\underline{\omega}_0, \overline{\omega}_0]$, and $\delta_{max\omega_0} = \frac{(\overline{\omega}_0 - \underline{\omega}_0)}{2}$,

We then obtain a rational function represented by the LFT $\mathrm{diag}(\delta_{\omega_0} I_{n_{qe}}, \delta_{Re} I_{n_{qe}}) \star N_e$, with

$$N_e = \begin{bmatrix} 0 & \ldots & 0 & 0 & I_{n_{qe}} \\ I_{(d \times n_{qe})-1} & & 0 & 0 & 0 \\ 0 & \ldots & 0 & 0 & I_{n_{qe}} \\ e_1 I_{n_{qe}} & \ldots & e_d I_{n_{qe}} & I_{n_{qe}} & e_0 I_{n_{qe}} \end{bmatrix}, \tag{6.25}$$

Then, for the approximation of $1/g(\tilde{\omega}_0) I_{n_{qg}}$, we have the Taylor approximation

$$\frac{1}{g(\tilde{\omega}_0)} I_{n_{qg}} = g_0 I_{n_{qg}} + \sum_{k=1}^{d} \delta^k_{\tilde{\omega}_0} g_k I_{n_{qg}} + R_g(\tilde{\omega}_0) I_{n_{qg}}, \tag{6.26}$$

with $g_0 = \frac{1}{g(\tilde{\omega}_{0c})}$, $g_k = \frac{1}{k!}\frac{d^k(1/g)}{d\omega_0^k}(\tilde{\omega}_{0c}) \; \forall \; k \in \{1, \ldots, d\}$. Since $\tilde{\omega}_0 = \omega_0 + \omega_m$, we have that $\tilde{\omega}_{0c} = \omega_{0c} + \omega_{mc}$ with $\omega_{mc} = (-\overline{\omega}_m + \overline{\omega}_m)/2 = 0$, then $\tilde{\omega}_{0c} = \omega_{0c}$.

Next, we have

$$\delta_{\tilde{\omega}_0} = (\tilde{\omega}_0 - \tilde{\omega}_{0c}) = \underbrace{\omega_0 - \omega_{0c}}_{\delta_{\omega_0}} + \underbrace{\omega_m - 0}_{\delta_{\omega m}}.$$

Then, the equation (6.26) becomes

$$\frac{1}{g(\omega_0+\omega_m)}I_{n_{qg}} = g_0 I_{n_{qg}} + \sum_{k=1}^{d}\delta_{\omega_0}^k g_k I_{n_{qg}} + \sum_{k=1}^{d}\delta_{\omega_m}^k g_k I_{n_{qg}} + R_g(\omega_0+\omega_m)I_{n_{qg}},$$

with $R_g(\omega_0+\omega_m)$ the diagonal matrix $r_g(\omega_0+\omega_m)I_{n_{qg}}$ and $r_g(\omega_0+\omega_m)$ the scalar residual of the Taylor approximation of $1/g(\omega_0+\omega_m)$.

Then, the bounded residual can be modeled as the structured uncertainty $\Delta_{Rg} = \delta_{Rg}I_{n_{qe}}$, $|\delta_{Rg}| \leq R_{maxg}$, with

$$R_{maxg} = \frac{D_g}{(d+1)!}\left(\delta_{max\omega_0} + \delta_{max\omega_m}\right)^{d+1}$$

with $D_g \geq |\frac{d^k(1/g)}{d\omega_0}(\omega_0+\omega_m)| \;\forall\; \omega_0 \in [\underline{\omega}_0, \overline{\omega}_0]$ and $\forall\; \omega_m \in [-\overline{\omega}_m, \overline{\omega}_m]$, and with $\delta_{max\omega_0} = \frac{(\overline{\omega}_0-\underline{\omega}_0)}{2}$, $\delta_{max\omega_m} = \overline{\omega}_m$.

We can then obtain the LFT $\text{diag}(\delta_{\omega_0}I, \delta_{\omega_m}I, \delta_{Rg}I) \star N_g$, with

$$N_g = \begin{bmatrix} 0 & \dots & 0 & 0 & \dots & 0 & 0 & I_{n_{qg}} \\ I_{(d\times n_{qg})-1} & & 0 & 0 & \dots & 0 & 0 & 0 \\ 0 & \dots & 0 & 0 & \dots & 0 & 0 & I_{n_{qg}} \\ 0 & \dots & 0 & I_{(d\times n_{qg})-1} & & 0 & 0 & 0 \\ 0 & \dots & 0 & 0 & \dots & 0 & 0 & I_{n_{qg}} \\ g_1 I_{n_{qg}} & \dots & g_d I_{n_{qg}} & g_1 I_{n_{qg}} & \dots & g_d I_{n_{qg}} & I_{n_{qg}} & g_0 I_{n_{qg}}. \end{bmatrix} \tag{6.27}$$

Then, the global LFT is given by

$$\text{diag}(\delta_{\omega_0}I, \delta_{\omega_m}I, \Delta_{Rg}I, \delta_{\omega_0}I, \Delta_{Re}) \star \text{diag}(N_g, N_e). \tag{6.28}$$

Rearranging the resulting LFT interconnection to regroup the diagonal repeated δ_{ω_0} in a single block, we obtain the global LFT

$$\underbrace{\text{diag}(\delta_{\omega_0}I, \delta_{\omega_m}I, \Delta_{Rg}I, \Delta_{Re})}_{\Delta} \star N, \tag{6.29}$$

with N given by (6.23). Finally, we have that $(\Delta \star N) \star M_\mu = \Delta \star (N \star M_\mu)$.

Finally, since the approximation errors are upper-bounded, ensuring the robust stability and robust performance of $\Delta \star (N \star M_\mu)$, respectively using Theorem 3.1 and Theorem 3.2 with the set of multipliers (3.33), also implies the robust stability and robust performance of (6.19). □

As previously mentioned, the robust stability of the LFT system (6.24), for the structured set $\mathbf{\Delta}$ given by (6.22), can be tested using Theorem 3.1 and constructing multipliers in the set (3.33) for the different parametric uncertainties.

Then, if the robust stability is guaranteed for all $\Delta \in \mathbf{\Delta}$, we can evaluate the robust performance condition, given by (6.16), by testing condition (3.15) of Theorem 3.2, for $\omega = 1$.

Remark: The previous results allows to test two of the design assumptions:

- the controller, designed from a simplified fictitious model, ensures the stability and the tracking performance when it is implemented in the real system for all $\omega_0 \in [\underline{\omega}_0, \overline{\omega}_0]$;

- in the presence of a mismatch between the measured and actual resonance frequencies, the controller can ensure the stability and the performance tracking for all $\omega_0 \in [\underline{\omega}_0, \overline{\omega}_0]$ and for all $\omega_m \in [-\overline{\omega}_m, \overline{\omega}_m]$.

Furthermore, all along this section, we have emphazised that the resonance frequency ω_0 is modeled as a time-invariant uncertainty, which it is not true since the frequency changes with the temperature, thus it is actually a slowly time-varying parameter. However, the application of the IQC theorems (Theorem 3.1 and Theorem 3.2) with the set of multipliers (3.33) is also valid when applied to uncertain parameters that are slowly time-varying [CT95]. Therefore, the conditions of Theorem Theorem 6.1 can be also applied when the parameters ω_0 and ω_m are slowly time-varying, which is the case of MEMS gyroscopes application.

6.2.2 Example

Let us introduce an example to illustrate how the estimation error of the resonance frequency can affect the tracking error. The discrete-time drive mode system is given by the state-space representation (6.11), with

$$A = \begin{bmatrix} 0 & 1 \\ -1 & -1/Q \end{bmatrix}, \quad B = \begin{bmatrix} 0 \\ 1 \end{bmatrix}, \quad C = \begin{bmatrix} k & 0 \end{bmatrix}, \quad D = 0,$$

$k = 0.05$, $Q = 2000$, $T_s = 16 \cdot 10^{-6}$s and $\omega_0 \in [2\pi \cdot 11 \cdot 10^3,\ 2\pi \cdot 12 \cdot 10^3]$ rad s^{-1}. The controller is designed by following the method presented in [SACKS20], and the complete closed loop system analysis LFT system is given by (6.19).

Now, in order to cast the system in an LFT form with a rational dependency on the uncertain parameters, we apply Lemma 6.1 to $e^{\omega_0} I$ and $1/g(\widehat{\omega}_0) I$. We apply a Taylor approximation order $d = 2$ for both functions. Then, the transformation of the exponential function gives a maximal approximation error $R_{maxe} = 2.226 \cdot 10^{-5}$, while the inverse of $g(\omega)$ gives a maximal approximation error $R_{maxg} = 2.640 \cdot 10^{-8}$. The approximation errors are then integrated as the upper-bounds of the uncertainties representing these residuals.

We can then construct the uncertain set $\mathbf{\Delta}$ and the LFT system $\Delta \star (N \star_\mu)$ by applying Theorem 6.1, obtaining the set

$$\mathbf{\Delta} = \{\Delta \,|\Delta = \text{diag}(\delta_{\omega_0} I_8, \delta_{\omega_m} I_4, \delta_{Rg} I_2, \delta_{Re} I_2)\},$$

.

Next, robust stability is tested by applying Theorem 3.1 and constructing multipliers in the set $\mathbf{\Pi_{TI}}$ given by (3.33), observing that stability is not compromised for any frequency ω_0 and for any frequency mismatch ω_m.

Then, we investigate the impact of different maximal measure mismatches $\overline{\omega}_m$ on the tracking performance specification defined in (6.16), for all $\omega_m \in [-\overline{\omega}_m, \overline{\omega}_m]$ and for all $\omega_0 \in [2\pi \cdot 11 \cdot 10^3,\ 2\pi \cdot 12 \cdot 10^3]$ rad/s.

The performance analysis is computed through an LMI optimization problem associated to the particular case of testing condition (3.15) of Theorem 3.2 for $\omega = 1$. The result gives an upper-bound η in the worst-case tracking error performance, defined by condition (6.16).

The obtained results are shown in Figure 6.6. For the sake of illustration, we present a normalized tracking error $\tilde{\eta}$ such that $\tilde{\eta}$ is lower than one if the performance specification is met and greater than one if not. We can first observe the case of a perfect estimation of ω_0, this by observing the performance obtained for $\overline{\omega}_m = 0$.

We have that, with a perfect measure, the tracking performance is $\tilde{\eta} = 0.6219$, which shows that the discrete-time controller ensures performance for all $\omega_0 \in [\underline{\omega}_0, \overline{\omega}_0]$ when there is no error on the resonance frequency estimation.

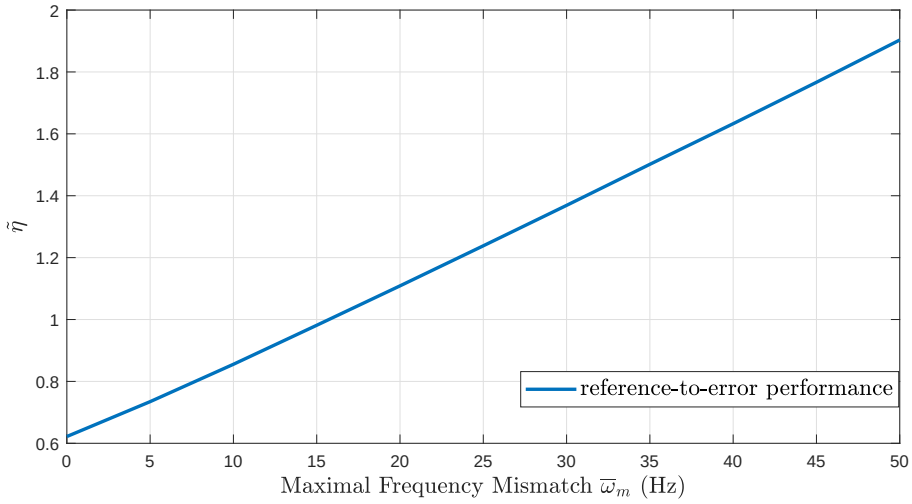

FIGURE 6.6: Variation of performance with respect to $\omega_{m_{max}}$.

Then, we can see that $\tilde{\eta}$ approximately increases 160% for a maximal mismatch frequency of 2 π 50 rad/s, which demonstrates how performance is deteriorated when the measure of the resonance frequency is not accurate. In order to determine the maximal mismatch for which the performance criterion is satisfied, we must observe the value $\overline{\omega}_m$ for which $\tilde{\eta} = 1$. We can conclude, for this example, that the designed discrete-time controller ensures the tracking performance specification for all $\omega_0 \in [\underline{\omega}_0, \overline{\omega}_0]$ and for all $\omega_m \in [-\overline{\omega}_m, \overline{\omega}_m]$, tolerating a maximal measure error $\overline{\omega}_m$ of 2 π 15.763 rad/s. In a real application, such a frequency mismatch is a very unlikely scenario. Concluding that the discrete-time implementation of a parameter-dependent controller is an attractive and simple strategy for the improvement of the global performance objectives in MEMS gyroscopes.

6.3 Chapter conclusion

In this chapter, we propose some analysis tools for control strategies that inherently induce in the system some properties going beyond an LTI closed-loop system. First, we tackle the stability analysis of a phasor-based control strategy with non-ideal synchronous demodulation. This type of a system is a natural test-bench where we could test the harmonic multipliers that were proposed in this work. The improvement of the analysis results offered by the coupled harmonic multipliers with respect to the single repeated multipliers is visible, showing that the integration of the phase-shift information is relevant. In contrast, the full-block multipliers showed up a more significant conservatism, leaving an open question about their pertinence and the research of alternative multipliers. Then, we address the performance analysis of the discrete-time implementation of a parameter-dependent controller. From an analysis point of view, this problem leads to the analysis of an uncertain system that does not rationally depends on the parametric uncertainties. To cope with this, we propose a Taylor-based approximation of the non-rational functions, allowing to recast the problem as the analysis of an LFT system that rationally depends on the

uncertain parameters and the approximation error, allowing to formally ensure the robust performance.

Chapter 7

Conclusions and perspectives

In this chapter, we present some conclusions about the research work presented all along this manuscript. Afterwards, some suggestions for future work are introduced, concerning both the application to MEMS gyroscopes and further researches in the analysis of Linear Harmonically Time-Varying systems.

7.1 Conclusions

The main objective of this work is the development of efficient and systematic methods for the pre-experimental performance validation of MEMS gyroscopes. To this purpose, we adopt a model-based approach by applying different tools of the System Analysis theory. Given the uncertain and harmonically time-varying nature, the approaches of the Robust Control framework, such as the IQC approach, were particularly relevant. Based on a general review of the MEMS gyroscopes operation and the performance validation problem (chapter 2), three large classes of problems were addressed: the analysis of LHTV systems (chapter 3), the model-based computation of the main MEMS performance specifications (chapter 4 and chapter 5) and the validation of control strategies beyond the scope of the LTI control (chapter 6).

Analysis of LHTV systems. We define an LHTV system as a linear system that contains one or several parameters that are Harmonically Time-Varying (HTV) i.e. that vary as sinusoidal functions of the time. For the stability and performance analysis, we adopted the IQC approach since allows to simultaneously consider the uncertain and LHTV nature of MEMS gyroscopes. A key step to apply the main IQC theorems is to characterize the input-output relationships of the element under consideration (an uncertainty, a time-varying parameter, etc.). This is done by verifying if all the elements in the uncertain set satisfy an IQC defined by a set of so-called multipliers. The chosen set of multipliers plays a central in the conservatism of the analysis results. Therefore, it is particularity important, for a given uncertain set, to construct a set of multipliers that sufficiently characterizes the main features of this uncertain set.

In some cases, a proper choice of multipliers can lead to exact analysis conditions. For instance, a widely studied case, coming from the μ-analysis framework [Doy82, FTD91], is the characterization of a repeated parametric uncertainty, where the concepts related to the frequency domain multipliers are addressed under the denomination of $D - G$ scalings. The D scaling characterizes the bounded nature of the uncertain parameter, making it a valid candidate to derive analysis conditions. Nevertheless, it is the introduction of the G scaling, characterizing the fact that the

uncertain parameter belong to the set of reals, which radically reduced the conservatism of the analysis results, even providing sufficient and necessary conditions is some cases [MIF00].

Regarding the case of a repeated HTV parameter, a frequency domain multiplier has been introduced in the catalog of multipliers of [MR97] (without available proof in the literature). Investigating this result, we deduce that the construction of sets of multipliers for HTV parameters is possible by using a modulation-commutation property. However, the harmonic multiplier of [MR97] only introduces a D scaling. Therefore, a major contribution of our work consisted in searching and constructing a harmonic G scaling that significantly reduces, as in the case of parametric uncertainties, the conservatism of the LHTV systems analysis. In order to illustrate the reduction of conservatism provided by the harmonic off-diagonal function, we test it in the numerical example of section 3.5.2, concerning the Mathieu-Hill equations, observing that the inclusion of the off-diagonal functions radically reduces the conservatism of the analysis results.

This result is then extended to the case of LHTV systems containing several HTV parameters that oscillate at the same frequency but with a phase-shift between them, covering the case of synchronous demodulation. The innovation of this class of multipliers is that, in addition to frequency and amplitude, it also integrates the information about the phase-shift between the harmonic oscillations. The application of this sets of multipliers to the phasor-based control analysis shows that the integration of the the phase-shift in the multiplier has a positive impact on the reduction of conservatism. A final extension concerned the analysis of HTV full-block structures, covering, for instance, the case of two-dimensional rotation operators. Nevertheless, this result presented an important degree of conservatism that it was not expected.

Concerning the implementation of the IQC theory, the direct application of the main IQC stability and performance theorems implies the resolution of infinite dimensional optimization problems. Hence, in order to obtain tractable solutions, two possible approaches can be adopted to obtain a finite dimensional problem: a state-space solution and a frequency domain solution. In the case of LTI uncertain systems, these two results are well-known [VSK16, FTD91]. However, the application of these techniques in the case of LHTV systems is more delicate. The state-space solution is derived by applying the Kalman-Yakubovich-Popov (KYP) Lemma [Ran96], relating a frequency domain inequality to an LMI constraint. The major difficulty to apply this type of solution is that it is necessary to find a suitable parameterization of the harmonic multipliers. Hence, as another contribution, we introduce a particular parameterization, admitting a real state-space realization, for the harmonic D scaling harmonic multipliers. The frequency-domain solution is based on the use of a griding of the frequency axis, similar to the approach employed in μ-analysis. However, harmonic multipliers impose particular constraints between different frequencies. We have therefore proposed a systematic method that allows to construct the griding and to establish the analysis conditions, as well as to execute the associated optimization algorithm.

Model-based computation of the performance specifications. The SFNL is defined as the largest measurement error over the whole range of input angular rates, where each gyroscope output is measured for a constant angular rate at the steady-state. Given the class of input reference signal, the application of the (ideal) synchronous demodulation, and the dependency of the output error on the angular rate, modeled

as an uncertain parameter, the computation of the SFNL is reduced to a robust optimization problem. Then, applying the Robust control results of [Din05], the model-based computation of the SFNL provides a sufficient and necessary condition, which is illustrated through a numerical example. The results are then extended to the study of the SFNL thermal sensitivity and the worst-case SFNL of identified models. The model-based computation of the worst-case SFNL of an identified model was compared to experimental results, showing that the model-based computation allows to establish a worst-case performance in a real application case, with a slight conservatism.

The Allan variance is the standard method to classify and quantify the stochastic processes of the output noise. To derive model-based computation methods for the Allan variance, we adopt a filter generator approach. We first address the problem of computing the Allan variance by considering that the output signal is generated by an LTI system, showing that the Allan variance can be recast as the $\mathcal{H}_2$ performance of an extended system, consisting in the series connection of the generator filter and the so-called Allan filter. Since the Allan filter is an infinite dimensional system, we proposed a Padé approximation of the Allan filter, showing that the approximated Allan filter allows to accurately compute the Allan variance of some common stochastic processes. The result was then extended to the MEMS gyroscopes, modeled as an LTI closed-loop system whose output is then applied to a synchronous demodulator. To tackle this problem, we propose two approaches: an IQC-based approach and an equivalent LTI approach based on a random modulated signal assumption. Both approaches were compared on a numerical example, observing that the equivalent LTI approach, in spite of the adopted assumptions, offers very accurate results, while the IQC-based approach shows an important conservatism, probably related to the application of an IQC state-space solution employing an only on-diagonal multiplier. Finally, the equivalent LTI approach was tested in an application case, showing the important accuracy of the model-based Allan variance with respect to the experimental results.

Validation of alternative control strategies. Since these classes of control strategies are designed by adopting some appropriate but strong assumptions, special analysis tools were developed to verify the stability and the performance of these control solutions in a more realistic scenario. The first case concerns the stability analysis of a phasor-based control with non-ideal synchronous demodulation, which can be directly modeled as an LHTV system. Then, using the set of IQC tools developed for the analysis of this class of systems, we were able to verify the stability of this control strategy. The second case concerns the discrete-time implementation of a parameter-dependent control strategy, considering a non-ideal estimation of the resonance frequency. This problem leads us to the analysis of an uncertain system with a non-rational dependency on the uncertainty. Then, using a Taylor-based approximation of the non-rational function, and modeling the approximation error as a additional uncertainty, it was possible to validate the tracking performance of this control strategy, as well as to determine the relationship between the estimation error and the obtained performance.

7.2 Future work

In this memoir, we address a certain number of problems that were solved at different levels. Some of them offering rather complete solutions, other that need to be

completed, and some of them remaining as open questions to be explored. Depending on the interest of the reader, we classify the suggestions of future work in two main classes: perspectives for MEMS gyroscopes and perspectives for the analysis of LHTV systems.

7.2.1 Model-based evaluation of MEMS gyroscopes

On the extension of the model-based Allan variance to the study of the bias instability

The proposed methods for the model-based computation of the Allan variance provided some satisfactory results for the study of the output noise of MEMS gyroscopes. However, in the MEMS community, the Allan variance is also employed to evaluate the bias drift in a long-time scale. We can detect to different time-scales, the short-term scale allows to directly evaluate evaluate the effects of the control system, as it has been investigated in this work, and a long-term scale where the influence of the control system is harder to observe and the effect of the bias-drift becomes important.

Hence, the variation of bias along the time is a non-stochastic phenomena that has an important contribution on the observed Allan variance, mainly for long averaging times. Then, a first open question is to find out the relationship between a signal that contains a non-stochastic component and its computed Allan variance. The second issue is the development of a model-based approach, requiring to explore the long-term dynamics. It is likely that the bias drift is due to changes in temperature that introduce slow variations of the system parameters. Then, it can be necessary to perform an identification experience over a long time scale in order to adjust the model parameters and their possible variations. Then, if the system is proven to have slowly time-varying parameters, it is possible to exploit the IQC-based methods, using the corresponding multipliers, for the computation of the worst-case Allan variance on the long-time scale.

On the performance analysis of the phasor-based control

The model-based computation of the main performance specifications was derived by considering a series configuration of the closed-loop system and the synchronous demodulator. Then, we address the stability analysis of the phasor-based control, based on a feedback LHTV system. Therefore, considering the modular structure of the IQC approach, all the obtained analysis tools can be combined to extend the analysis of the phasor-based control to the evaluation of the performance specifications.

On the integration of nonlinear phenomena

The analysis of some of the most relevant nonlinear phenomena of MEMS gyroscopes was not explored in this work. Probably, the main nonlinear phenomena in MEMS gyroscopes are the spring-softening and spring-hardening, observed as the variation of the resonance frequency with respect to the amplitude of the drive-mode oscillations. Complete models in the literature [EKT+11, ST17] show that the spring-hardening and softening are caused by electrostatic parasitic phenomena and large deflections in the silicon beams. In these models, they appear as the square or

the cube of the drive-mode position. Then, it is necessary to determine the appropriate analysis tool. The IQC framework allows the analysis of systems containing some particular classes of nonlinearities such as monotone nonlinearites, which could cover the case of a cubic nonlinearity.

Among the control architectures that were exploited during the project, we have an approach based on a $\Sigma - \Delta$ control, embedding the controller and the analog to digital converter in a single system. This type of architecture introduces a relay in the closed-loop, which can be modeled as the sign function. Then, the analysis of such an architecture demand the use of tools for nonlinear analysis such as the analysis of piecewise systems. A solid framework for the application of the IQC approach to the analysis of uncertain piecewise affine systems was established in [Wai18]. Therefore, the combination of these results and those obtained in this memoir offers a promising perspective to address the analysis of this control architecture.

Finally, a second control architecture that requires the analysis of nonlinear operations in the system, is the classical amplitude-phase control. Since this control architecture shares some similarities with the phasor-based approach, the latter can be a started point to systematically derive a solution.

7.2.2 Analysis of LHTV systems

On the study of harmonic multipliers conservatism

It has been proved that the frequency-dependent multipliers for one repeated parametric uncertainty allow to obtain necessary and sufficient analysis conditions. Reviewing the case of a multiplier for a single repeated HTV parameter, we can observe that the multipliers for a parametric uncertainty are a particular case of the multipliers for an HTV parameter (when the harmonic frequency is equal to zero). The construction of the harmonic multipliers allow to directly determine the sufficient conditions. In contrast, the observation of necessary conditions is much less intuitive. A review of the necessity of classical multipliers for a parametric uncertainty in different cases might allow a better understanding on the conservatism of harmonic multipliers, as well as some insights for possible improvements.

On the mystery of the full-block harmonic multipliers

The analysis results of the different harmonic multipliers show that the full-block harmonic (singular case) multipliers are considerably more conservative than the other classes of multipliers. This is not intuitive since full-block harmonic multipliers seem to represent a closer characterization of the operator under study. It is then necessary to further investigate the main features of the full-block HTV operators and to determine how their structure can be translated in the construction of a less conservative set of multipliers. Indeed, we detect that in some cases, a multiplier with a full-block structure leads to a class of multipliers that could not be exploited in an efficient analysis test. Going in the opposite direction, it might be interesting to clarify the question of which are the characteristics that make the other classes of multipliers less conservative than the full-block ones.

On the research of better state-space solutions

In order to obtain tractable analysis conditions, an efficient option is to derive state-space solutions for LHTV systems. The application of the KYP lemma to obtain the

state-space solution requires sets of multipliers that admit a suitable parameterization. This issue is partially solved by finding a parametrization of the harmonic multipliers containing only the on-diagonal functions X_D. Nevertheless, this subset of multipliers is considerably more conservative than the full harmonic multipliers, containing also the off-diagonal functions X_G. Indeed, this issue implied an important limitation of the IQC-based computation of the Allan Variance since the efficient computation of the $\mathcal{H}_2$ performance is solved in state-space.

The main challenge is to find a parameterization for the complete multiplier is that the off-diagonal functions are particular periodic functions of the frequency, then infinite-dimensional functions that do not admit a state-space realization. The big advantage of the state-space solution with respect to the frequency-domain one [Pag99] is the efficiency since the number of decision variables is, in general, much lower. Then, it is necessary to look for possible relaxations, approximations or modifications of the off-diagonal functions X_G in order to obtain a harmonic multiplier that can be completely parameterized and that better optimizes the trade-off between efficiency and conservatism.

Appendix A

Proofs of Chapter 3

A.1 Proof of Theorem 3.6

Proof. **Part 1: $\tilde{\boldsymbol{X}}_{\boldsymbol{D}}(\boldsymbol{j\omega})$.** The input-output relation of θ^{ω_0} given by (3.29) can be rewritten in its exponential form:

$$p_1(t) = \frac{1}{2}\left(e^{j(\omega_0 t+\phi)} + e^{-j(\omega_0 t+\phi)}\right) q_1(t)$$
$$p_2(t) = \frac{1}{2}\left(e^{j(\omega_0 t+\phi+\psi)} + e^{-j(\omega_0 t+\phi+\psi)}\right) q_2(t).$$

Using the same approach as in the proof of the set of multipliers (3.35), we define the internal signals

$$p_{up}(t) = \theta_{up}(t)q_{up}(t) = e^{j\omega_0 t}\begin{bmatrix} I_{n_{q_1}} & 0 \\ 0 & e^{j\psi}I \end{bmatrix} e^{j\phi} q_{up}(t)$$

and

$$p_{low}(t) = \theta_{low}(t)q_{low}b(t) = e^{-j\omega_0 t}\begin{bmatrix} I_{n_{q_1}} & 0 \\ 0 & e^{-j\psi}I \end{bmatrix} e^{-j\phi} q_{low}(t),$$

with $p = \frac{1}{2}(p_{up} + p_{low})$. A schematic representation is shown in Figure A.1.

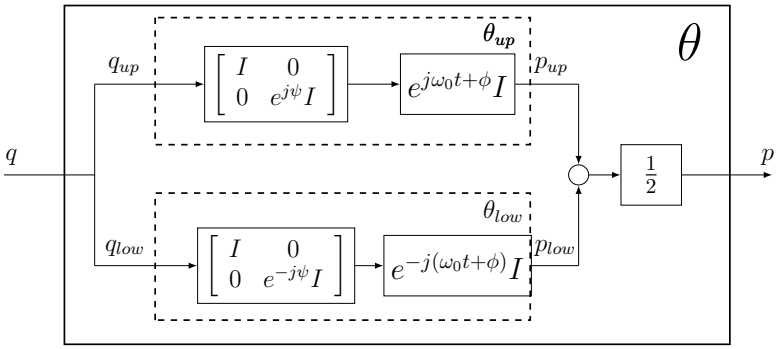

FIGURE A.1: Representation of the exponential form of $\theta^{\omega_0}(t)$

Similar to multipliers of (3.35), we first consider the upper branch with the operator θ_{up} with input and output signals denoted q_{up} and p_{up}, respectively.

The operator θ_{up} is equivalent to $\tilde{\theta}_{up} = T^{-1}T\theta_{up}$, with $T(j\omega)$ a complex invertible matrix function (Figure A.2 b)). We define the signal $\tilde{p}_{up}$ as

$$\widehat{\tilde{p}}_{up}(j\omega) = T(j\omega)\begin{bmatrix} I & 0 \\ 0 & e^{j\psi}I \end{bmatrix} \widehat{\tilde{q}}_{up}(j(\omega-\omega_0))e^{j\phi}$$

The direct commutation between θ_{up} and T does not give an equivalent operator because of the modulation property, as well as the change implied by the matrix commutation between T and the phase matrix $(\text{diag}(I, e^{j\psi}I))$. Then, in order to preserve the equivalence, we introduce the commutation-modulation, as shown in Figure 3.7 c). We look then to maintain the same intermediate signal $\tilde{p}$. To this end, we need to satisfy the equality

$$T(j\omega)\begin{bmatrix} I & 0 \\ 0 & e^{j\psi}I \end{bmatrix}\widehat{\tilde{q}}_{up}(j(\omega-\omega_0)) = \begin{bmatrix} I & 0 \\ 0 & e^{j\psi}I \end{bmatrix}\tilde{T}(j(\omega-\omega_0))\widehat{q}_{up}(j(\omega-\omega_0)),$$

which is the case for

$$\tilde{T}(j\omega) = \begin{bmatrix} I & 0 \\ 0 & e^{-j\psi}I \end{bmatrix} T(j(\omega+\omega_0)) \begin{bmatrix} I & 0 \\ 0 & e^{j\psi}I \end{bmatrix}. \tag{A.1}$$

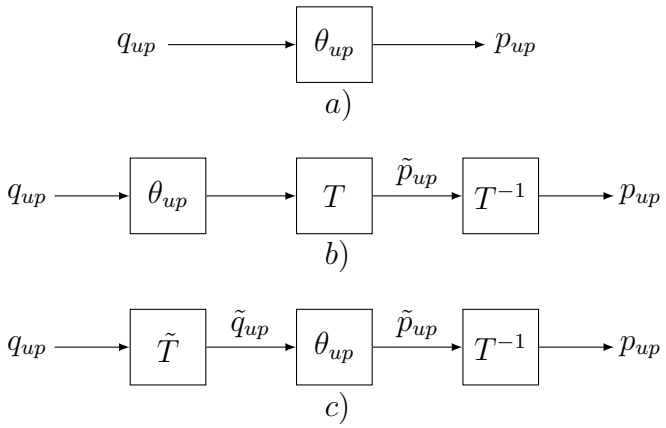

FIGURE A.2: Equivalent representation of θ_{up}

Then, knowing that θ_{up} is bounded, i.e. $|\overline{\sigma}(\theta_{up})| \leq 1$, combined with the relations $\tilde{q} = \tilde{T}q$ and $\tilde{p} = Tp$ and the Parseval equality, leads us to the frequency domain inequality

$$\int_{-\infty}^{\infty} \widehat{p}_{up}(j\omega)^* T(j\omega)^* T(j\omega)\widehat{p}_{up}(j\omega)d\omega \leq \int_{-\infty}^{\infty} \widehat{q}_{up}(j\omega)^* \tilde{T}(j\omega)^* \tilde{T}(j\omega)\widehat{q}_{up}(j\omega)d\omega.$$

We define $X_D(j\omega) = T(j\omega)^* T(j\omega)$, which implies that $X_D(j\omega) = X_D(j\omega)^* \succ 0$. Similarly, for $X_{D+}(j\omega) = T(j(\omega+\omega_0))^* T(j(\omega+\omega_0))$ and $X_{D-}(j\omega) = T(j(\omega-\omega_0))^* T(j(\omega-\omega_0))$. We also define

$$\tilde{X}_{D+}(j\omega) = \tilde{T}(j\omega)^*\tilde{T}(j\omega) = \begin{bmatrix} I & 0 \\ 0 & e^{-j\psi}I \end{bmatrix} X_{D+}(j\omega) \begin{bmatrix} I & 0 \\ 0 & e^{j\psi}I \end{bmatrix},$$

to obtain the inequality

$$\int_{-\infty}^{\infty} \widehat{p}_{up}(j\omega)^* X_D(j\omega)\widehat{p}_{up}(j\omega)d\omega \leq \int_{-\infty}^{\infty} \widehat{q}_{up}(j\omega)^* \tilde{X}_{D+}(j\omega)\widehat{q}_{up}(j\omega)d\omega. \tag{A.2}$$

Performing the same procedure for the lower branch, we define

$$\tilde{X}_{D-}(j\omega) = \begin{bmatrix} I & 0 \\ 0 & e^{j\psi}I \end{bmatrix} X_{D-}(j\omega) \begin{bmatrix} I & 0 \\ 0 & e^{-j\psi}I \end{bmatrix},$$

giving the inequality

$$\int_{-\infty}^{\infty} \widehat{p}_{low}(j\omega)^* X_D(j\omega) \widehat{p}_{low}(j\omega) d\omega \leq \int_{-\infty}^{\infty} \widehat{q}_{low}(j\omega)^* \tilde{X}_{D-}(j\omega) \widehat{q}_{low}(j\omega) d\omega. \quad \text{(A.3)}$$

Adding inequalities (A.2) and (A.3) and using $q_{up} = q_{low} = q$, $2p = p_{up} + p_{low}$ and the same convex argument used in the proof of Theorem 3.3 (page 59), we obtain the functions $X_D(j\omega)$ of the set $\mathbf{\Pi}^{\omega_0}_{\theta SD}$, given in (3.55).

Second part: $X_G(j\omega)$. We consider the following frequency equality constraint

$$\int_{-\infty}^{\infty} \begin{bmatrix} \widehat{q}(j\omega) \\ \widehat{p}(j\omega) \end{bmatrix}^* \begin{bmatrix} 0 & X_G(j\omega) \\ X_G(j\omega)^* & 0 \end{bmatrix} \begin{bmatrix} \widehat{q}(j\omega) \\ \widehat{p}(j\omega) \end{bmatrix} d\omega = 0 \quad \text{(A.4)}$$

with $X_G(j\omega)$ being a complex-valued matrix function. We then aim to find out the necessary properties of $X_G(j\omega)$ such that equality constraint is satisfied for

$$\widehat{p}(j\omega) = \frac{1}{2} \left(\begin{bmatrix} I & 0 \\ 0 & e^{-j\psi} I \end{bmatrix} \widehat{q}(j(\omega + \omega_0)) e^{-j\phi} + \begin{bmatrix} I & 0 \\ 0 & e^{j\psi} I \end{bmatrix} \widehat{q}(j\omega - j\omega_0) e^{j\phi} \right)$$

.

Then replacing $\widehat{p}(j\omega)$ in (A.13), the equality becomes:

$$\begin{aligned}
&\int_{-\infty}^{\infty} \widehat{q}(j\omega)^* X_G(j\omega) \begin{bmatrix} I & 0 \\ 0 & e^{-j\psi} I \end{bmatrix} \widehat{q}((j\omega + \omega_0)) e^{-j\phi} d\omega \\
+ &\int_{-\infty}^{\infty} \widehat{q}(j\omega)^* X_G(j\omega) \begin{bmatrix} I & 0 \\ 0 & e^{j\psi} I \end{bmatrix} \widehat{q}(j(\omega - \omega_0)) e^{j\phi} d\omega \\
+ &\int_{-\infty}^{\infty} \widehat{q}(j(\omega + \omega_0))^* \begin{bmatrix} I & 0 \\ 0 & e^{j\psi} I \end{bmatrix} X_G(j\omega)^* \widehat{q}(j\omega) e^{j\phi} d\omega \\
+ &\int_{-\infty}^{\infty} \widehat{q}(j(\omega - \omega_0))^* \begin{bmatrix} I & 0 \\ 0 & e^{-j\psi} I \end{bmatrix} X_G(j\omega)^* \widehat{q}(j\omega) e^{-j\phi} d\omega = 0
\end{aligned}$$

Since the integrals are evaluated from $-\infty$ to ∞, a frequency shift does not modify the integrals. We can then perform a change of variable in two of the four integrals, getting

$$\begin{aligned}
&\int_{-\infty}^{\infty} \widehat{q}(j\omega)^* X_G(j\omega) \begin{bmatrix} I & 0 \\ 0 & e^{-j\psi} I \end{bmatrix} \widehat{q}((j\omega + \omega_0)) e^{-j\phi} d\omega \\
+ &\int_{-\infty}^{\infty} \widehat{q}(j(\omega + \omega_0))^* X_G(j(\omega + \omega_0)) \begin{bmatrix} I & 0 \\ 0 & e^{j\psi} I \end{bmatrix} \widehat{q}(j\omega) e^{j\phi} d\omega \\
+ &\int_{-\infty}^{\infty} \widehat{q}(j(\omega + \omega_0))^* \begin{bmatrix} I & 0 \\ 0 & e^{j\psi} I \end{bmatrix} X_G(j\omega)^* \widehat{q}(j\omega) e^{j\phi} d\omega \\
+ &\int_{-\infty}^{\infty} \widehat{q}(j\omega)^* \begin{bmatrix} I & 0 \\ 0 & e^{-j\psi} I \end{bmatrix} X_G(j(\omega + \omega_0))^* \widehat{q}(j(\omega + \omega_0)) e^{-j\phi} d\omega = 0
\end{aligned}$$

Regrouping the obtained terms, we get:

$$\int_{-\infty}^{\infty} \begin{bmatrix} \widehat{q}(j\omega) \\ \widehat{q}(j(\omega + \omega_0)) \end{bmatrix}^* \begin{bmatrix} 0 & \tilde{X}_G(j\omega) \\ \tilde{X}_G(j\omega)^* & 0 \end{bmatrix} \begin{bmatrix} \widehat{q}(j\omega) e^{j\phi} \\ \widehat{q}(j(\omega + \omega_0)) e^{-j\phi} \end{bmatrix} d\omega = 0$$

with

$$\tilde{X}_G(j\omega)^* = X_G(j(\omega + j\omega_0)) \begin{bmatrix} I & 0 \\ 0 & e^{j\psi} I \end{bmatrix} + \begin{bmatrix} I & 0 \\ 0 & e^{j\psi} I \end{bmatrix} X_G(j\omega)^*$$

which is equals to zero, for all $q \in \mathcal{L}_2^{n_q}$, only if

$$\forall \omega \in \mathbb{R}, \qquad X_G(j(\omega + \omega_0)) = - \begin{bmatrix} I & 0 \\ 0 & e^{j\phi} I \end{bmatrix} X_G(j\omega)^* \begin{bmatrix} I & 0 \\ 0 & e^{-j\phi} I \end{bmatrix}$$

□

A.2 Proof of Lemma 3.5

Proof. Considering the parameterization $X_D(j\omega) = \Psi(j\omega)^* M_D \Psi(j\omega)$, with $M_D \in \mathbb{S}^\bullet$ and $\Psi \in \mathcal{RH}_\infty^{\bullet \times n_q}$, we obtain

$$\begin{aligned} X_D(j(\omega + \omega_0)) &= \Psi(j(\omega + \omega_0))^* M_D \underbrace{\Psi(j(\omega + \omega_0))}_{\Psi_+} \\ X_D(j(\omega - \omega_0)) &= \Psi(j(\omega - \omega_0))^* M_D \underbrace{\Psi(j(\omega - \omega_0))}_{\Psi_-}. \end{aligned}$$

Then, we denote $\tilde{\Psi}_+ = \Psi_+ \begin{bmatrix} I & 0 \\ 0 & e^{j\psi} I \end{bmatrix}$ and $\tilde{\Psi}_- = \Psi_- \begin{bmatrix} I & 0 \\ 0 & e^{-j\psi} I \end{bmatrix}$. Hence, the upper-left block of the multiplier Π in the set of (3.55) is expressed as follows

$$\tilde{X}_{D+} + \tilde{X}_{D-} = \tilde{\Psi}_+^* M_D \tilde{\Psi}_+ + \tilde{\Psi}_-^* M_D \tilde{\Psi}_-,$$

which can be rewritten as

$$\begin{aligned} \tilde{X}_{D+} + \tilde{X}_{D-} = &\frac{1}{2} \left[\tilde{\Psi}_+ + \tilde{\Psi}_-\right]^* M_D \left[\tilde{\Psi}_+ + \tilde{\Psi}_-\right] \\ &+ \frac{1}{2} \left[-j(\tilde{\Psi}_+ + \tilde{\Psi}_-)\right]^* M_D \left[-j(\tilde{\Psi}_+ + \tilde{\Psi}_-)\right]. \end{aligned}$$

Then, combining this factorization with that of X_D, we can easily obtain the final factorization (3.56) of Π. □

A.3 Proof of Theorem 3.8

Proof. **Part 1: $\tilde{X}_D(j\omega)$.** The input-output relation of θ^{ω_0} given by (3.64) can be rewritten in its exponential form, with $p(t) = \frac{1}{2}\left(p_{up}(t) + p_{low}(t)\right)$ and

$$\begin{aligned} p_{up}(t) &= \underbrace{\begin{bmatrix} I & e^{j\psi_1} I \\ e^{j\psi_2} I & -e^{j(\psi_1+\psi_2)} I \end{bmatrix}}_{\Phi_{up}} e^{j(\omega_0 t + \phi)} q(t) \\ p_{low}(t) &= \underbrace{\begin{bmatrix} I & e^{-j\psi_1} I \\ e^{-j\psi_2} I & -e^{-j(\psi_1+\psi_2)} I \end{bmatrix}}_{\Phi_{low}} e^{-j(\omega_0 t + \phi)} q(t). \end{aligned} \tag{A.5}$$

Similar to the derivation of previous sets of harmonic multipliers, we first investigate the upper branch, with the operator θ_{up} with input and output signals respectively denoted q_{up} and p_{up}.

In frequency domain, the signal p_{up} is defined as

$$\widehat{p}_{up}(j\omega) = \begin{bmatrix} I & e^{j\psi_1}I \\ e^{j\psi_2}I & -e^{j(\psi_1+\psi_2)}I \end{bmatrix} \widehat{q}_{up}(j(\omega-\omega_0))e^{j\phi}$$

The operator θ_{up} is equivalent to $\tilde{\theta}_{up} = T^{-1}T\theta_{up}$, with $T(j\omega)$ a complex invertible matrix function, let us then define the signal $\widehat{\tilde{p}}_{up}(j\omega) = T(j\omega)\tilde{p}_{up}(j\omega)$ (Figure A.3 b)). In order to commute θ_{up} as shown in Figure A.3 c), the following must be satisfied

$$\begin{aligned}\widehat{\tilde{p}}_{up}(j\omega) &= T(j\omega)\begin{bmatrix} I & e^{j\psi_1}I \\ e^{j\psi_2}I & -e^{j(\psi_1+\psi_2)}I \end{bmatrix} \widehat{\tilde{q}}_{up}(j(\omega-\omega_0))e^{j\phi} \\ &= \begin{bmatrix} I & e^{j\psi_1}I \\ e^{j\psi_2}I & -e^{j(\psi_1+\psi_2)}I \end{bmatrix} \underbrace{\tilde{T}(j(\omega-\omega_0))\widehat{q}_{up}(j(\omega-\omega_0))}_{\widehat{\tilde{q}}_{up}(j(\omega-\omega_0))} e^{j\phi},\end{aligned}$$

Using modulation commutation properties, and the inverse of the non-singular phase matrix Φ_{up}, we obtain

$$\tilde{T}_1(j\omega) = \begin{bmatrix} I & e^{j\psi_1}I \\ e^{j\psi_2}I & -e^{j(\psi_1+\psi_2)}I \end{bmatrix}^{-1} T(j(\omega+\omega_0)) \begin{bmatrix} I & e^{j\psi_1}I \\ e^{j\psi_2}I & -e^{j(\psi_1+\psi_2)}I \end{bmatrix}, \tag{A.6}$$

and using the explicit expression of the matrix inverse, we have

$$\tilde{T}_1(j\omega) = \frac{1}{-2e^{j(\psi_1+\psi_2)}} \begin{bmatrix} -e^{j(\psi_1+\psi_2)} & -e^{j\psi_1}I \\ -e^{j\psi_2}I & I \end{bmatrix} T(j(\omega+\omega_0)) \begin{bmatrix} I & e^{j\psi_1}I \\ e^{j\psi_2}I & -e^{j(\psi_1+\psi_2)}I \end{bmatrix}. \tag{A.7}$$

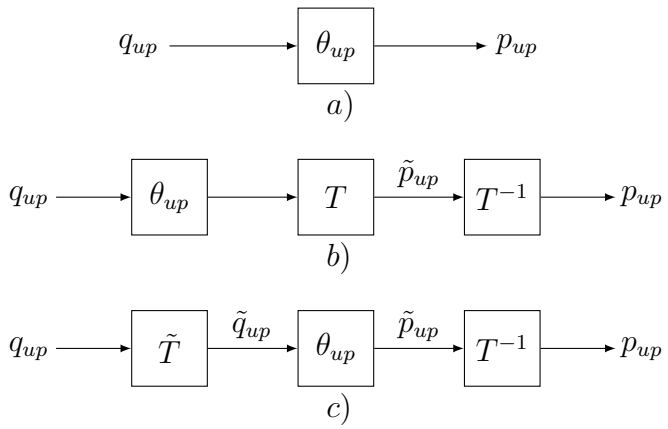

FIGURE A.3: Equivalent representation of θ_{up}

Then, knowing that θ_{up} is bounded, i.e. $|\overline{\sigma}(\theta_{up})|^2 \leq 2$, combined with Parseval's equality, leads us to the frequency domain inequality

$$\int_{-\infty}^{\infty} \widehat{\tilde{p}}_{up}(j\omega)^* \widehat{\tilde{p}}_{up}(j\omega)d\omega \leq 2\int_{-\infty}^{\infty} \widehat{\tilde{q}}_{up}(j\omega)^* \widehat{\tilde{q}}_{up}(j\omega)d\omega,$$

which is expressed in terms of $\widehat{p}(j\omega)$ and $\widehat{q}(j\omega)$, by using the relations $\widehat{\tilde{q}}(j\omega) = \tilde{T}(j\omega)\widehat{q}(j\omega)$ and $p_{up}(j\omega) = T^{-1}(j\omega)\widehat{\tilde{p}}_{up}(j\omega)$, as

$$\int_{-\infty}^{\infty} \widehat{p}_{up}(j\omega)^* T(j\omega)^* T(j\omega)\widehat{p}_{up}(j\omega)d\omega \leq \mathbf{2}\int_{-\infty}^{\infty} \widehat{q}_{up}(j\omega)^* \tilde{T}(j\omega)^* \tilde{T}(j\omega)\widehat{q}_{up}(j\omega)d\omega,$$

where the product $\tilde{T}(j\omega)^*\tilde{T}(j\omega)$ is given by

$$\begin{aligned}\tilde{T}(j\omega)^*\tilde{T}(j\omega) =& \frac{\mathbf{1}}{\mathbf{4}}\begin{bmatrix} I & e^{-j\psi_2}I \\ e^{-j\psi_1}I & -e^{-j(\psi_1+\psi_2)}I \end{bmatrix} T(j(\omega+\omega_0))^* \begin{bmatrix} -e^{-j(\psi_1+\psi_2)}I & -e^{-j\psi_2}I \\ -e^{-j\psi_1}I & I \end{bmatrix} \\ & \cdot \begin{bmatrix} -e^{j(\psi_1+\psi_2)}I & -e^{j\psi_1}I \\ -e^{j\psi_2}I & I \end{bmatrix} T(j(\omega+\omega_0)) \begin{bmatrix} I & e^{j\psi_1}I \\ e^{j\psi_2}I & -e^{j(\psi_1+\psi_2)}I \end{bmatrix}\end{aligned} \tag{A.8}$$

since $|-2e^{j(\psi_1+\psi_2)}|^2 = 4$. Now, let us focus on the following matrix product

$$\begin{aligned}\begin{bmatrix} -e^{-j(\psi_1+\psi_2)}I & -e^{-j\psi_2}I \\ -e^{-j\psi_1}I & I \end{bmatrix}\begin{bmatrix} -e^{j(\psi_1+\psi_2)}I & -e^{j\psi_1}I \\ -e^{j\psi_2}I & I \end{bmatrix} &= \begin{bmatrix} \mathbf{2}I & e^{-j\psi_2}-e^{-j\psi_2}I \\ e^{j\psi_2}-e^{j\psi_2}I & \mathbf{2}I \end{bmatrix} \\ &= \mathbf{2}\begin{bmatrix} I & 0 \\ 0 & I \end{bmatrix}.\end{aligned} \tag{A.9}$$

Please note that (A.9) is a consequence of the combination of the phases ψ_1 and ψ_2, the chosen structure is actually necessary to satisfy the inversibility of the phase matrices Φ_{up} and Φ_{low} as well as the diagonal structure of (A.9).

Hence, we obtain

$$\begin{aligned}&\int_{-\infty}^{\infty} \widehat{p}_{up}(j\omega)^* T(j\omega)^* T(j\omega)\widehat{p}_{up}(j\omega)d\omega \leq \\ &2\times\frac{1}{4}\times 2\int_{-\infty}^{\infty} \widehat{q}_{up}(j\omega)^* E_1 T(j(\omega+\omega_0))^* T(j(\omega+\omega_0))E_2\widehat{q}_{up}(j\omega)d\omega,\end{aligned} \tag{A.10}$$

with

$$E_1 = \begin{bmatrix} I & e^{-j\psi_2}I \\ e^{-j\psi_1}I & -e^{-j(\psi_1+\psi_2)}I \end{bmatrix}$$

and

$$E_2 = \begin{bmatrix} I & e^{j\psi_1}I \\ e^{j\psi_2}I & -e^{j(\psi_1+\psi_2)}I \end{bmatrix}.$$

We define $X_D(j\omega) = T(j\omega)^*T(j\omega)$, which implies that $X_D(j\omega) = X_D(j\omega)^* \succ 0$. Similarly for $X_{D+} = T(j(\omega+\omega_0))^*T(j(\omega+\omega_0))$ and $X_{D-} = T(j(\omega-\omega_0))^*T(j(\omega-\omega_0))$. We also define

$$\tilde{X}_{D+} = \tilde{T}(j\omega)^*\tilde{T}(j\omega) = \begin{bmatrix} I & e^{-j\psi_2}I \\ e^{-j\psi_1}I & -e^{-j(\psi_1+\psi_2)}I \end{bmatrix} X_{D+} \begin{bmatrix} I & e^{j\psi_1}I \\ e^{j\psi_2}I & -e^{j(\psi_1+\psi_2)}I \end{bmatrix},$$

to obtain the inequality

$$\begin{aligned}&\int_{-\infty}^{\infty} \widehat{p}_{up}(j\omega)^* X_D(j\omega)\widehat{p}_{up}(j\omega)d\omega \leq \\ &\int_{-\infty}^{\infty} \widehat{q}_{up}(j\omega)^* \tilde{X}_{D+}(j\omega)\widehat{q}_{up}(j\omega)d\omega.\end{aligned} \tag{A.11}$$

Performing the same procedure for the lower branch, we define

$$\tilde{X}_{D-} = \begin{bmatrix} I & e^{j\psi_2}I \\ e^{j\psi_1}I & -e^{j(\psi_1+\psi_2)}I \end{bmatrix} X_{D-} \begin{bmatrix} I & e^{-j\psi_1}I \\ e^{-j\psi_2}I & -e^{-j(\psi_1+\psi_2)}I \end{bmatrix},$$

giving the inequality

$$\begin{aligned}&\int_{-\infty}^{\infty} \widehat{p}_{low}(j\omega)^* X_D(j\omega)\widehat{p}_{low}(j\omega)d\omega \leq \\ &\int_{-\infty}^{\infty} \widehat{q}_{low}(j\omega)^* \tilde{X}_{D-}(j\omega)\widehat{q}_{low}(j\omega)d\omega.\end{aligned} \tag{A.12}$$

Adding inequalities (A.11) and (A.12), then using $q_{up} = q_{low} = q$, $2p = p_{up} + p_{low}$ and the same convex argument used in the proof of Theorem 3.3 (page 59), we obtain the functions $\tilde{X_D}(j\omega)$ of the set of multipliers (3.66).

Second part: $X_G(j\omega)$. We consider the following frequency equality constraint

$$\int_{-\infty}^{\infty} \begin{bmatrix} \widehat{q}(j\omega) \\ \widehat{p}(j\omega) \end{bmatrix}^* \begin{bmatrix} 0 & X_G(j\omega) \\ X_G(j\omega)^* & 0 \end{bmatrix} \begin{bmatrix} \widehat{q}(j\omega) \\ \widehat{p}(j\omega) \end{bmatrix} d\omega = 0 \tag{A.13}$$

with $X_G(j\omega)$ being a complex-valued matrix function. We then aim to find out the necessary properties of $X_G(j\omega)$ such that equality constraint is satisfied for

$$\begin{aligned}\widehat{p}(j\omega) = \frac{1}{2}\Bigg(&\begin{bmatrix} I & e^{-j\psi_1}I \\ e^{-j\psi_2}I & -e^{-j(\psi_1+\psi_2)}I \end{bmatrix} \widehat{q}(j(\omega+\omega_0))e^{-j\phi} \\ &+ \begin{bmatrix} I & e^{j\psi_1}I \\ e^{j\psi_2}I & -e^{j(\psi_1+\psi_2)}I \end{bmatrix} \widehat{q}(j\omega - j\omega_0)e^{j\phi}\Bigg).\end{aligned}$$

Then replacing $\widehat{p}(j\omega)$ in (A.13), the equality becomes:

$$\begin{aligned}&\frac{1}{2}\int_{-\infty}^{\infty} \widehat{q}(j\omega)^* X_G(j\omega) \begin{bmatrix} I & e^{-j\psi_1}I \\ e^{-j\psi_2}I & -e^{-j(\psi_1+\psi_2)}I \end{bmatrix} \widehat{q}((j\omega+\omega_0))e^{-j\phi}d\omega \\ &+\frac{1}{2}\int_{-\infty}^{\infty} \widehat{q}(j\omega)^* X_G(j\omega) \begin{bmatrix} I & e^{j\psi_1}I \\ e^{j\psi_2}I & -e^{j(\psi_1+\psi_2)}I \end{bmatrix} \widehat{q}(j(\omega-\omega_0))e^{j\phi}d\omega \\ &+\frac{1}{2}\int_{-\infty}^{\infty} \widehat{q}(j(\omega+\omega_0))^* \begin{bmatrix} I & e^{j\psi_1}I \\ e^{j\psi_2}I & -e^{j(\psi_1+\psi_2)}I \end{bmatrix} X_G(j\omega)^* \widehat{q}(j\omega)e^{j\phi}d\omega \\ &+\frac{1}{2}\int_{-\infty}^{\infty} \widehat{q}(j(\omega-\omega_0))^* \begin{bmatrix} I & e^{-j\psi_1}I \\ e^{-j\psi_2}I & -e^{-j(\psi_1+\psi_2)}I \end{bmatrix} X_G(j\omega)^* \widehat{q}(j\omega)e^{-j\phi}d\omega = 0\end{aligned}$$

Since the integrals are evaluated from $-\infty$ to ∞, a frequency shift does not modify the integrals. We can then perform a change of variable in two of the four integrals, getting

$$\frac{1}{2}\int_{-\infty}^{\infty}\widehat{q}(j\omega)^* X_G(j\omega)\begin{bmatrix} I & e^{-j\psi_1}I \\ e^{-j\psi_2}I & -e^{-j(\psi_1+\psi_2)}I \end{bmatrix}\widehat{q}((j\omega+\omega_0))e^{-j\phi}d\omega$$
$$+\frac{1}{2}\int_{-\infty}^{\infty}\widehat{q}(j(\omega+\omega_0))^* X_G(j(\omega+\omega_0))\begin{bmatrix} I & e^{j\psi_1}I \\ e^{j\psi_2}I & -e^{j(\psi_1+\psi_2)}I \end{bmatrix}\widehat{q}(j\omega)e^{j\phi}d\omega$$
$$+\frac{1}{2}\int_{-\infty}^{\infty}\widehat{q}(j(\omega+\omega_0))^*\begin{bmatrix} I & e^{j\psi_1}I \\ e^{j\psi_2}I & -e^{j(\psi_1+\psi_2)}I \end{bmatrix}X_G(j\omega)^*\widehat{q}(j\omega)e^{j\phi}d\omega$$
$$+\frac{1}{2}\int_{-\infty}^{\infty}\widehat{q}(j\omega)^*\begin{bmatrix} I & e^{-j\psi_1}I \\ e^{-j\psi_2}I & -e^{-j(\psi_1+\psi_2)}I \end{bmatrix}X_G(j(\omega+\omega_0))^*\widehat{q}(j(\omega+\omega_0))e^{-j\phi}d\omega = 0$$

Regrouping the obtained terms, we get:

$$\int_{-\infty}^{\infty}\begin{bmatrix}\widehat{q}(j\omega)\\ \widehat{q}(j(\omega+\omega_0))\end{bmatrix}^*\begin{bmatrix}0 & \tilde{X}_G(j\omega)\\ \tilde{X}_G(j\omega)^* & 0\end{bmatrix}\begin{bmatrix}\widehat{q}(j\omega)e^{j\phi}\\ \widehat{q}(j(\omega+\omega_0))e^{-j\phi}\end{bmatrix}d\omega = 0$$

with

$$\tilde{X}_G(j\omega)^* = X_G(j\omega+j\omega_0)\begin{bmatrix} I & e^{j\psi_1}I \\ e^{j\psi_2}I & -e^{j(\psi_1+\psi_2)}I \end{bmatrix} + X_G(j\omega)^*\begin{bmatrix} I & e^{j\psi_2}I \\ e^{j\psi_1}I & -e^{j(\psi_1+\psi_2)}I \end{bmatrix}$$

which is equals to zero, , for all $q \in \mathcal{L}_2^{n_q}$,, only if

$$\forall\omega\in\mathbb{R},\ X_G(j(\omega+\omega_0)) = \begin{bmatrix} I & e^{j\psi_2}I \\ e^{j\psi_1}I & -e^{j(\psi_1+\psi_2)}I \end{bmatrix}\frac{X_G(j\omega)^*}{2e^{j(\psi_1+\psi_2)}}\begin{bmatrix} -e^{j(\psi_1+\psi_2)}I & -e^{j\psi_1}I \\ -e^{j\psi_2}I & I \end{bmatrix}$$

□

A.4 Proof of Theorem 3.9

Proof. **Part 1: $X_D(j\omega)$.** The input-output relation of θ^{ω_0} given by (3.65) can be rewritten in its exponential form,, with $p(t) = \frac{1}{2}\left(p_{up}(t) + p_{low}(t)\right)$ and

$$\begin{aligned} p_{up}(t) &= \underbrace{\begin{bmatrix} I & e^{j\psi_1}I \\ -e^{j\psi_1}I & -e^{j2\psi_1}I \end{bmatrix}}_{\Phi_{up}} e^{j(\omega_0 t+\phi)}q(t) \\ p_{low}(t) &= \underbrace{\begin{bmatrix} I & e^{-j\psi_1}I \\ -e^{-j\psi_1}I & -e^{-j2\psi_1}I \end{bmatrix}}_{\Phi_{low}} e^{-j(\omega_0 t+\phi)}q(t). \end{aligned} \tag{A.14}$$

In this case the phase matrices Φ_{up} and Φ_{low} are singular. Singularity of the phase matrices implies that they are of degenerated rank, allowing the following decomposition. (Figure A.5)

$$p_{up} = \begin{bmatrix} I_{n_{q_1}} \\ -e^{j\psi_1}I_{n_{q_2}} \end{bmatrix} e^{j(\omega_0 t+\phi)} \begin{bmatrix} I_{n_{q_1}} & e^{j\psi_1}I_{n_{q_2}} \end{bmatrix}$$
$$p_{low} = \begin{bmatrix} I_{n_{q_1}} \\ -e^{-j\psi_1}I_{n_{q_2}} \end{bmatrix} e^{-j(\omega_0 t+\phi)} \begin{bmatrix} I_{n_{q_1}} & e^{-j\psi_1}I_{n_{q_2}} \end{bmatrix}$$

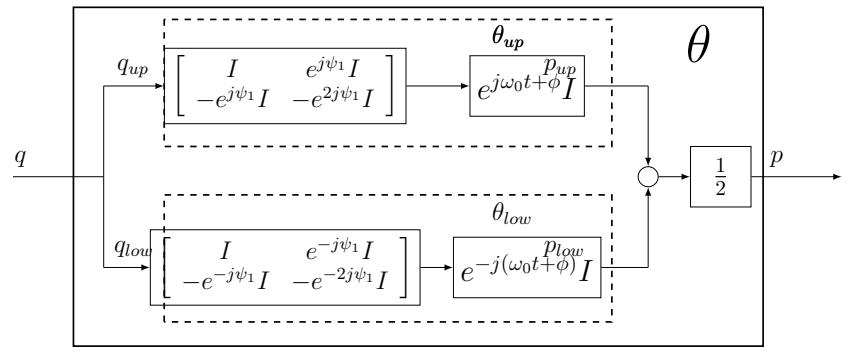

FIGURE A.4: Representation of the exponential form of $\theta^{\omega_0}(t)$

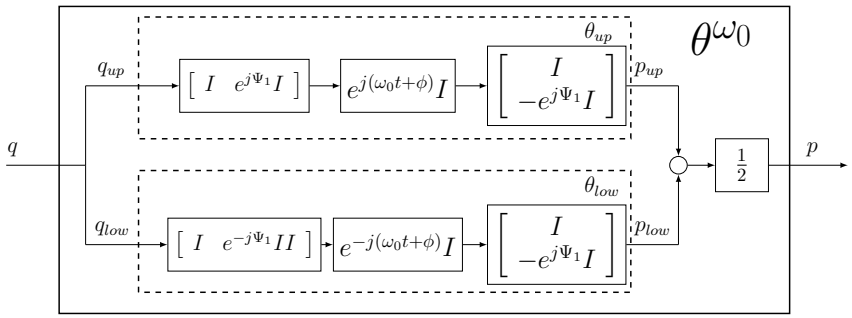

FIGURE A.5: Representation of the decomposed exponential form of $\theta^{\omega_0}(t)$

Let us first study the signals p_{up} and q_{up} of the upper branch. We perform a first commutation-modulation between modulation operator and an invertible matrix function $\tilde{t}$ such that p_{up} remains unchanged, that is represented on Figure A.6. As we have presented in the derivation of previous harmonic multipliers, this is

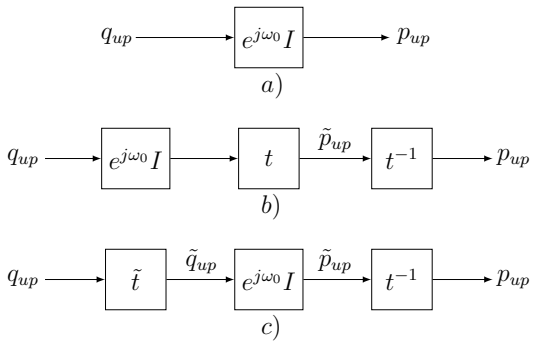

FIGURE A.6: Equivalent representation of θ_{up}

possible by using the modulation Lemma F.2, with

$$\tilde{t}(j\omega) = t(j(\omega - \omega_0)) \in \mathbb{C}^{n_{q_1} \times n_{q_1}}.$$

Then, we perform the second commutation with the tall matrices as shown on Figure A.7.

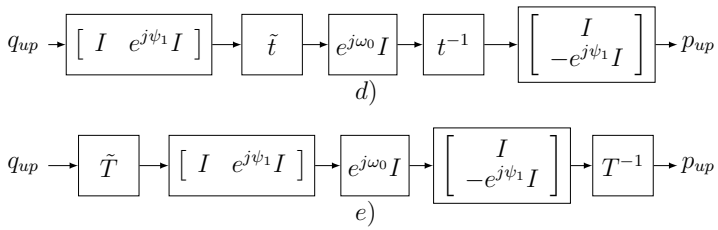

FIGURE A.7: Second commutation of θ_{up}

We denote the obtained matrices as $\tilde{T}(j\omega) = \begin{bmatrix} t(j(\omega-\omega_0)) & 0 \\ 0 & t(j(\omega-\omega_0)) \end{bmatrix}$ and $T^{-1}(j\omega) = \begin{bmatrix} t^{-1}(j\omega) & 0 \\ 0 & t^{-1}(j\omega) \end{bmatrix}$

Exploiting the bounded nature of θ_{up}, i.e. $|\theta_{up}|^2 \leq 4$ and using the Parseval's equality, we obtain frequency-domain integral inequality

$$\begin{aligned} &\int_{-\infty}^{\infty} \widehat{p}_{up}(j\omega)^* T(j\omega)^* T(j\omega) \widehat{p}_{up}(j\omega) d\omega \leq \\ &4 \int_{-\infty}^{\infty} \widehat{q}_{up}(j\omega)^* \tilde{T}(j\omega)^* \tilde{T}(j\omega) \widehat{q}_{up}(j\omega) d\omega \end{aligned} \tag{A.15}$$

We can then define the operator

$$X_D(j\omega) = T(j\omega)^* T(j\omega) = \begin{bmatrix} t(j\omega)^* t(j\omega) & 0 \\ 0 & t(j\omega)^* t(j\omega) \end{bmatrix} = \begin{bmatrix} x_D(j\omega) & 0 \\ 0 & x_D(j\omega) \end{bmatrix}$$

with $x_D(j\omega) = x_D(j\omega)^* \succ 0$. and also for

$$\begin{aligned} X_{D+} &= T(j(\omega+\omega_0))^* T(j(\omega+\omega_0)), \\ X_{D-} &= T(j(\omega-\omega_0))^* T(j(\omega-\omega_0)). \end{aligned}$$

This yields to the inequality

$$\begin{aligned} &\int_{-\infty}^{\infty} \widehat{p}_{up}(j\omega)^* X_D(j\omega) \widehat{p}_{up}(j\omega) d\omega \leq \\ &\int_{-\infty}^{\infty} \widehat{q}_{up}(j\omega)^* \tilde{X}_{D-}(j\omega) \widehat{q}_{up}(j\omega) d\omega. \end{aligned} \tag{A.16}$$

Similarly, we obtain for the lower branch the inequality

$$\begin{aligned} &\int_{-\infty}^{\infty} \widehat{p}_{low}(j\omega)^* X_D(j\omega) \widehat{p}_{low}(j\omega) d\omega \leq \\ &\int_{-\infty}^{\infty} \widehat{q}_{low}(j\omega)^* \tilde{X}_{D+}(j\omega) \widehat{q}_{low}(j\omega) d\omega \end{aligned} \tag{A.17}$$

Adding inequalities (A.16) and (A.17), then using $q_{up} = q_{low} = q$, $2p = p_{up} + p_{low}$ and the convex argument, we get to an IQC defined by a multiplier belonging to the set

$$\mathbf{\Pi} = \left\{ \Pi : \Pi(j\omega) = \begin{bmatrix} 2X_{D+}(j\omega) + 2X_{D-}(j\omega) & 0 \\ 0 & -X_D(j\omega) \end{bmatrix} \right\} \tag{A.18}$$

with $X_D(j\omega)$ being Hermitian-valued and positive definite, and

$$X_{D+}(j\omega) = \begin{bmatrix} x_D(j(\omega+\omega_0)) & 0 \\ 0 & x_D(j(\omega+\omega_0)) \end{bmatrix},$$

$$X_{D-}(j\omega) = \begin{bmatrix} x_D(j(\omega-\omega_0)) & 0 \\ 0 & x_D(j(\omega-\omega_0)) \end{bmatrix}.$$

Part 2: $X_G(j\omega)$. We consider the following frequency equality constraint

$$\int_{-\infty}^{\infty} \begin{bmatrix} \widehat{q}(j\omega) \\ \widehat{p}(j\omega) \end{bmatrix}^* \begin{bmatrix} 0 & X_G(j\omega) \\ X_G(j\omega)^* & 0 \end{bmatrix} \begin{bmatrix} \widehat{q}(j\omega) \\ \widehat{p}(j\omega) \end{bmatrix} d\omega = 0 \tag{A.19}$$

with $X_G(j\omega)$ being a complex-valued matrix function. We then aim to find out the structure and constraints of $X_G(j\omega)$ such that equality is satisfied for

$$\begin{aligned} p(t) \;=\; & \tfrac{1}{2}\Bigg(\begin{bmatrix} I_{n_{q_1}} \\ -e^{j\psi_1} I_{n_{q_2}} \end{bmatrix} e^{j(\omega_0 t+\phi)} \begin{bmatrix} I_{n_{q_1}} & e^{j\psi_1} I_{n_{q_2}} \end{bmatrix} \\ & + \begin{bmatrix} I_{n_{q_1}} \\ -e^{j\psi_1} I_{n_{q_2}} \end{bmatrix} e^{-j(\omega_0 t+\phi)} \begin{bmatrix} I_{n_{q_1}} & e^{-j\psi_1} I_{n_{q_2}} \end{bmatrix} \Bigg) q(t) \end{aligned} . \tag{A.20}$$

Developing the equality by replacing $\widehat{p}(j\omega)$, we obtain

$$\begin{aligned} 0 &= \int_{-\infty}^{\infty} \widehat{q}(j\omega)^* X_G(j\omega)\widehat{p}(j\omega) + \widehat{p}(j\omega)^* X_G(j\omega)^* \widehat{q}(j\omega) \\ &= \int_{-\infty}^{\infty} \widehat{q}(j\omega)^* X_G(j\omega) \begin{bmatrix} I \\ -e^{j\psi_1} I \end{bmatrix} \begin{bmatrix} I & e^{j\psi_1} I \end{bmatrix} \widehat{q}(j(\omega-\omega_0)))e^{-j\phi} d\omega \\ &\quad + \int_{-\infty}^{\infty} \widehat{q}(j\omega)^* X_G(j\omega) \begin{bmatrix} I \\ -e^{-j\psi_1} I \end{bmatrix} \begin{bmatrix} I & e^{-j\psi_1} I \end{bmatrix} \widehat{q}(j(\omega+\omega_0))e^{j\phi} d\omega \\ &\quad + \int_{-\infty}^{\infty} \widehat{q}(j(\omega-\omega_0))^* \begin{bmatrix} I \\ -e^{-j\psi_1} I \end{bmatrix} \begin{bmatrix} I & e^{-j\psi_1} I \end{bmatrix} X_G(j\omega)^* \widehat{q}(j\omega)e^{j\phi} d\omega \\ &\quad + \int_{-\infty}^{\infty} \widehat{q}(j(\omega+\omega_0))^* \begin{bmatrix} I \\ -e^{j\psi_1} I \end{bmatrix} \begin{bmatrix} I & e^{j\psi_1} I \end{bmatrix} X_G(j\omega)^* \widehat{q}(j\omega)e^{-j\phi} d\omega \end{aligned} \tag{A.21}$$

Applying a frequency shift to the pertinent integrals, we obtain

$$\begin{aligned} 0 &= \int_{-\infty}^{\infty} \widehat{q}(j(\omega+\omega_0))^* X_G(j(\omega+\omega_0)) \begin{bmatrix} I \\ -e^{j\psi_1} I \end{bmatrix} \begin{bmatrix} I & e^{j\psi_1} I \end{bmatrix} \widehat{q}(j\omega))e^{-j\phi} d\omega \\ &\quad + \int_{-\infty}^{\infty} \widehat{q}(j\omega)^* X_G(j\omega) \begin{bmatrix} I \\ -e^{-j\psi_1} I \end{bmatrix} \begin{bmatrix} I & e^{-j\psi_1} I \end{bmatrix} \widehat{q}(j(\omega+\omega_0))e^{j\phi} d\omega \\ &\quad + \int_{-\infty}^{\infty} \widehat{q}(j\omega)^* \begin{bmatrix} I \\ -e^{-j\psi_1} I \end{bmatrix} \begin{bmatrix} I & e^{-j\psi_1} I \end{bmatrix} X_G(j(\omega+\omega_0))^* \widehat{q}(j(\omega+\omega_0))e^{j\phi} d\omega \\ &\quad + \int_{-\infty}^{\infty} \widehat{q}(j(\omega+\omega_0))^* \begin{bmatrix} I \\ -e^{j\psi_1} I \end{bmatrix} \begin{bmatrix} I & e^{j\psi_1} I \end{bmatrix} X_G(j\omega)^* \widehat{q}(j\omega)e^{-j\phi} d\omega \end{aligned} \tag{A.22}$$

Then regrouping the terms, we have

$$\begin{aligned}0 = \int_{-\infty}^{\infty} \widehat{q}(j\omega)^* \Bigg(& X_G(j\omega) \begin{bmatrix} I \\ -e^{-j\psi_1} I \end{bmatrix} \begin{bmatrix} I & e^{-j\psi_1} I \end{bmatrix} \\ & + \begin{bmatrix} I \\ -e^{-j\psi_1} I \end{bmatrix} \begin{bmatrix} I & e^{-j\psi_1} I \end{bmatrix} X_G(j(\omega+\omega_0))^* \Bigg) \widehat{q}(j(\omega+\omega_0)) e^{-j\phi} \\ & + \widehat{q}(j(\omega+\omega_0))^* \Bigg(X_G(j(\omega+\omega_0)) \begin{bmatrix} I \\ -e^{j\psi_1} I \end{bmatrix} \begin{bmatrix} I & e^{j\psi_1} I \end{bmatrix} \\ & + \begin{bmatrix} I \\ -e^{j\psi_1} I \end{bmatrix} \begin{bmatrix} I & e^{j\psi_1} I \end{bmatrix} X_G(j\omega)^* \Bigg) \widehat{q}(j\omega) e^{j\phi} d\omega \end{aligned} \tag{A.23}$$

Let us introduce the following function $X_G(j\omega)$

$$X_G(j\omega) = \begin{bmatrix} x_G(j\omega) & 0 \\ 0 & x_G(j(\omega+\omega_0))^* \end{bmatrix},$$

from where we obtain the conditions

$$\begin{bmatrix} x_G(j\omega) & x_G(j\omega)e^{-j\psi_1} \\ -x_G(j(\omega+\omega_0))^* e^{-j\psi_1} & -x_G(j(\omega+\omega_0))^* e^{-j2\psi_1} \end{bmatrix} + \begin{bmatrix} x_G(j(\omega+\omega_0))^* & -e^{-j\psi_1} x_G(j(\omega+2\omega_0)) \\ e^{-j\psi_1} x_G(j(\omega+\omega_0))^* & -e^{-j2\psi_1} x_G(j(\omega+2\omega_0)) \end{bmatrix} = 0$$

and

$$\begin{bmatrix} x_G(j(\omega+\omega_0)) & x_G(j(\omega+\omega_0))e^{j\psi_1} \\ -x_G(j(\omega+2\omega_0))^* e^{j\psi_1} & -x_G(j(\omega+2\omega_0))^* e^{j2\psi_1} \end{bmatrix} + \begin{bmatrix} x_G(j\omega)^* & -e^{j\psi_1} x_G(j(\omega+\omega_0)) \\ e^{j\psi_1} x_G(j\omega)^* & -e^{j2\psi_1} x_G(j(\omega+\omega_0)) \end{bmatrix} = 0.$$

Observing element by element, this implies the constraints

$$\begin{aligned} x_G(j\omega) &= -x_G(j(\omega+\omega_0))^* \\ x_G(j\omega) &= x_G(j(\omega+2\omega_0)) \\ x_G(j(\omega+\omega_0))^* &= x_G(j(\omega+\omega_0))^* \\ x_G(j(\omega+\omega_0))^* &= -x_G(j(\omega+2\omega_0)) \\ x_G(j(\omega+\omega_0)) &= -x_G(j\omega)^* \\ x_G(j(\omega+\omega_0)) &= x_G(j(\omega+\omega_0)) \\ x_G(j(\omega+2\omega_0))^* &= x_G(j\omega)^* \\ x_G(j(\omega+2\omega_0))^* &= -x_G(j(\omega+\omega_0)), \end{aligned}$$

which are actually different versions of the same single constraint

$$x_G(j\omega) = -x_G(j(\omega+\omega_0))^*. \tag{A.24}$$

Hence, introducing the functions $X_G(j\omega)$ and their constraints, we finally obtain the sets of multipliers $\mathbf{\Pi}^{\omega_0}_{\theta Rs}$, given in (3.67). □

Appendix B

Proofs and elements of chapter 4

B.1 Least Square linear regression and relationship with scale factor error

From Definition G.2, $SFNL$ is defined using the differences between the measures $z(\Omega_z)$ and the value of the straight fitted line $z^{fit}(\Omega_z)$ at Ω_{z_i}. To do so, we need first to define how Ω^{fit} is obtained. First, the fitted function z^{fit} is expressed as a function of the desired linear function, evaluated in the measured points Ω_{z_i}. The set of equations are listed as follows

$$\begin{aligned} z_{-N} &= B^{fit} + SF^{fit}\Omega_{z_{-N}} \\ &\vdots \\ z_0 &= B^{fit} + SF^{fit}\Omega_{z_0} \\ z_1 &= B^{fit} + SF^{fit}\Omega_{z_1} \\ &\vdots \\ z_N &= B^{fit} + SF^{fit}\Omega_{z_N}. \end{aligned}$$

This can be written in vector form as

$$\underbrace{\begin{bmatrix} z_{-N} \\ \vdots \\ z_0 \\ z_1 \\ \vdots \\ z_N \end{bmatrix}}_{F} = \underbrace{\begin{bmatrix} 1 \\ \vdots \\ 1 \\ 1 \\ \vdots \\ 1 \end{bmatrix}}_{I_{M\times 1}} B^{fit} + \underbrace{\begin{bmatrix} \Omega_{z_{-N}} \\ \vdots \\ \Omega_{z_0} \\ \Omega_{z_1} \\ \vdots \\ \Omega_{z_N} \end{bmatrix}}_{X} SF^{fit}.$$

Then, the residual r_i is defined as the difference between each measure $\tilde{\Omega}_z$ and the corresponding point of Ω_z^{fit}. The concatenation of all the residuals in a vector R can be then expressed as

$$R = I_{M\times 1}B^{fit} + SF^{fit}X - Z$$

where Z is the column vector containing al the measured points.

Then, the linear regression is computed by using the least squares method, that

is, by minimizing the sum of the squared residuals. We can then introduce the function S of the sum of the squared residuals as

$$S = R^T R = [I_{M\times 1} B^{fit} + SF^{fit} X - Z]^T [I_{M\times 1} B^{fit} + SF^{fit} X - Z] \tag{B.1}$$

Then, S is minimized by computing the derivatives with with respect to B^{fit} and to SF^{fit}, then setting the gradients to zero to obtain

$$\begin{aligned}
\frac{\partial S}{\partial B^{fit}} &= 2MB^{fit} + 2(SF^{fit} - 1)X^T I_{M\times 1} + 2E_{SF}^T I_{M\times 1} = 0 \\
\frac{\partial S}{\partial B^{fit}} &= 2MB^{fit} X^T I_{M\times 1} + 2(SF^{fit} - 1)X^T X + 2X^T E_{SF} = 0.
\end{aligned}$$

B.1.1 LFT model of MEMS gyroscope

The complete closed-loop system can be represented as the LFT system, illustrated in Figure B.1, with G_{Ω_z} defined as

$$G_{\Omega_z} = \Omega_z \; I_2 \star M_G(s) : \left\{ \begin{array}{rcl} p & = & \Omega_z I_2 \, q \\ \begin{bmatrix} q \\ x \\ y \end{bmatrix} & = & M_G(s) \begin{bmatrix} p \\ u_x \\ u_y \end{bmatrix} \end{array} \right. \tag{B.2}$$

and $M_G(s)$ given by

$$M_G(s) = \left\{ \begin{array}{cc} M_G^{11}(s) & M_G^{12}(s) \\ M_G^{21}(s) & M_G^{22}(s) \end{array} \right\} : \left\{ \begin{array}{rcl} \begin{bmatrix} \dot{x}(t) \\ \ddot{x}(t) \\ \dot{y}(t) \\ \ddot{y}(t) \end{bmatrix} & = & A \begin{bmatrix} x(t) \\ \dot{x}(t) \\ y(t) \\ \dot{y}(t) \end{bmatrix} + B \begin{bmatrix} p(t) \\ u_x(t) \\ u_y(t) \end{bmatrix} \\ \begin{bmatrix} q(t) \\ x(t) \\ y(t) \end{bmatrix} & = & C \begin{bmatrix} x(t) \\ \dot{x}(t) \\ y(t) \\ \dot{y}(t) \end{bmatrix} + D \begin{bmatrix} p(t) \\ u_x(t) \\ u_y(t) \end{bmatrix} \end{array} \right. .$$

with

$$A = \begin{bmatrix} 0 & 1 & 0 & 0 \\ -\frac{k_{xx}}{m_x} & -\frac{d_{xx}}{m_x} & -\frac{k_{xy}}{m_x} & -\frac{d_{xy}}{m_x} \\ 0 & 0 & 0 & 1 \\ -\frac{k_{yx}}{m_y} & -\frac{d_{yx}}{m_y} - \frac{2m_x}{m_y} & -\frac{k_{yy}}{m_y} & -\frac{d_{yy}}{m_y} \end{bmatrix}$$

$$B = \begin{bmatrix} 0 & 0 & 0 & 0 \\ \frac{2m_y}{m_x} & 0 & 1 & 0 \\ 0 & 0 & 0 & 0 \\ 0 & -\frac{2m_x}{m_y} & 0 & 1 \end{bmatrix},$$

$$C = \begin{bmatrix} 0 & 1 & 0 & 0 \\ 0 & 0 & 0 & 1 \\ 1 & 0 & 0 & 0 \\ 0 & 0 & 1 & 0 \end{bmatrix}, \quad D = \begin{bmatrix} 0 & 0 \\ 0 & 0 \\ 0 & 0 \\ 0 & 0 \end{bmatrix}$$

In the other hand, the designed MIMO LTI controller has the state-space representation.

$$K(s) = \left\{ \begin{array}{cc} K^{11}(s) & K^{12}(s) \\ K^{21}(s) & K^{22}(s) \end{array} \right\} : \left\{ \begin{array}{rcl} \dot{x}_k(t) & = & A_k x_k(t) + B_k \left[\begin{array}{c} x(t) \\ y(t) \\ x_r(t) \end{array} \right] \\ \left[\begin{array}{c} u_x(t) \\ u_y(t) \\ \tilde{f}_c(t) \end{array} \right] & = & C_k x_k(t) + D_k \left[\begin{array}{c} x(t) \\ y(t) \\ x_r(t) \end{array} \right] \end{array} \right.$$

where $x_r(t)$ is the the reference signal $x_r(t) = A\sin(\omega_{exc}t)$.

Then, the closed-loop system, as illustrated in Figure B.1, is given by

$$H_{\Omega_z} = \Omega_z \; I_2 \star M_H(s) : \left\{ \begin{array}{rcl} p & = & \Omega_z \, q \\ \left[\begin{array}{c} q \\ \tilde{f}_c \end{array} \right] & = & M_H(s) \left[\begin{array}{c} p \\ x_r \end{array} \right] \end{array} \right.$$

where

$$M_H(s) = M_G(s) \star K(s) = \left[\begin{array}{cc} M_H^{11}(s) & M_H^{12}(s) \\ M_H^{21}(s) & M_H^{22}(s) \end{array} \right]. \tag{B.3}$$

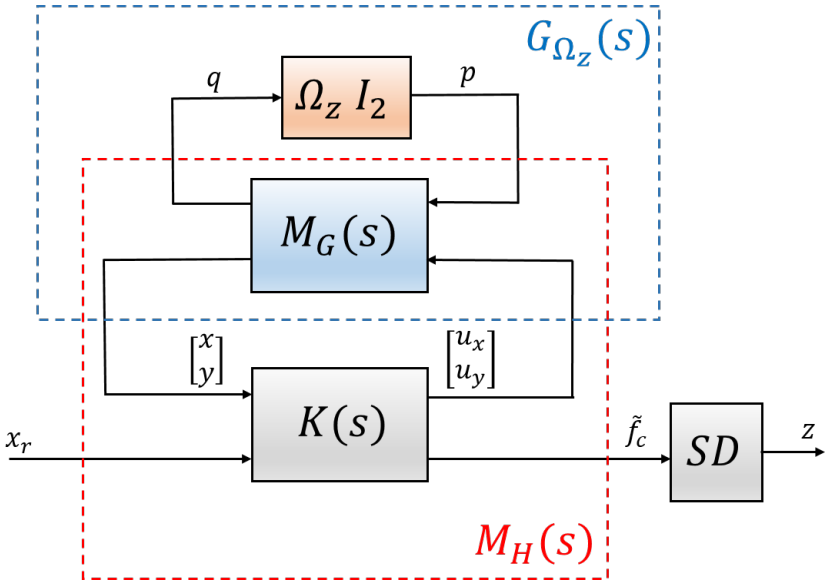

FIGURE B.1: LFT of the MEMS closed-loop system

Since H_{Ω_z} can be represented by the LFT system $\Omega_z I_2 \star M_H$, the gyroscope output z can thus be computed as the imaginary part of a constant complex LFT with unitary input, that is:

$$\begin{aligned} z &= \Im\{H_{\Omega_z}(j\omega_{exc})\} \\ &= \Im\{\Omega_z \; I_2 \star M_H(j\omega_{exc})\} \cdot 1. \end{aligned}$$

To extract the imaginary part of the LFT, we have that, for a complex matrix A, $\Im\{A\} = (A - (A^*)^T)/2j$, hence

$$\Im\{\Omega_z \; I_2 \star M_H(j\omega_{exc})\} \cdot 1 = \frac{1}{2j}\left((\Omega_z I_2 \star M_H) - (\Omega_z I_2 \star (M_H^*)^T)\right) \cdot 1.$$

Then, with M_H given by (B.3), we have that the imaginary part of $\Omega_z\ I_2 \star M_H(j\omega_{exc})$ can be also expressed as the output of an LFT, illustrated in Figure B.2, and given by:

$$z = \Im\{\Omega_z\ I_2 \star M_H(j\omega_{exc})\} = (\Omega_z I_4 \star \tilde{M}_H) \cdot 1 \tag{B.4}$$

with

$$\tilde{M}_H = \left[\begin{array}{cc|c} M_H^{11}(j\omega_{exc}) & 0 & M_H^{12}(j\omega_{exc}) \\ 0 & (M_H^{11}(j\omega_{exc})^*)^T & (M_H^{12}(j\omega_{exc})^*)^T \\ \hline \frac{1}{2j}M_H^{21}(j\omega_{exc}) & -\frac{1}{2j}(M_H^{21}(j\omega_{exc})^*)^T & \frac{1}{2j}(M_H^{22}(j\omega_{exc}) - (M_H^{21}(j\omega_{exc})^*)^T) \end{array}\right]$$

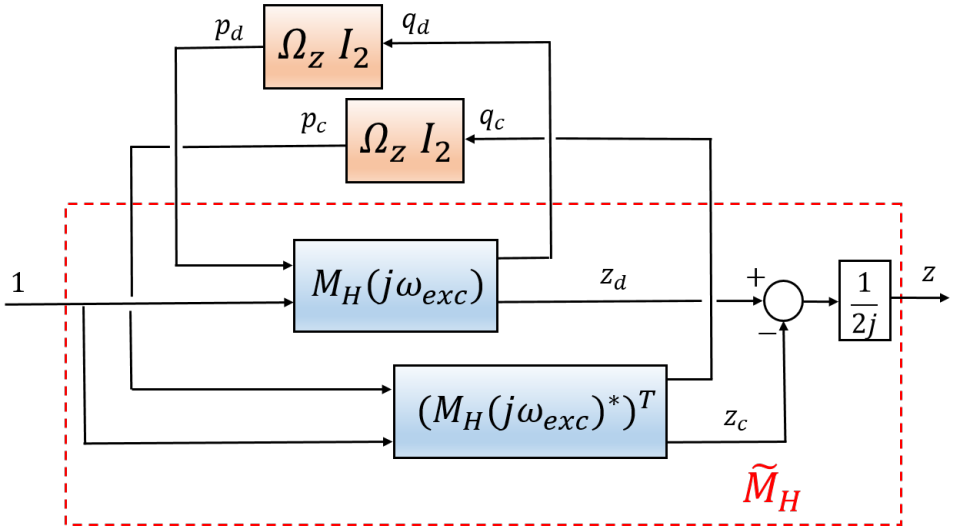

FIGURE B.2: LFT for the computation of the output z

B.2 Relationships between the control design objectives and the global performance specifications

This section is a note that aims to establish a link between the control design criteria and the global performance specifications.

Given the tracking error of the drive mode at steady-state

$$\varepsilon_t(t) = x_r(t) - x(t)$$

its derivative with respect to time is

$$\dot{\varepsilon}_t(t) = \dot{x}_r(t) - \dot{x}(t).$$

Hence, the real Coriolis force, defined in terms of the tracking error is given by

$$\begin{aligned} f_c(t) &= -k_c\Omega_z\dot{x} \\ &= -k_c\Omega_z(\dot{x}_r(t) - \dot{\varepsilon}_t(t)) \end{aligned}$$

where $k_c \approx 2m_x$.

Then, with the estimated Coriolis force being $\tilde{f}_c$, the estimation error is defined as

$$\varepsilon_e(t) = f_c(t) - \tilde{f}_c(t),$$

from where we can express the estimation of the Coriolis force as

$$\tilde{f}_c(t) = -k_c\Omega_z\dot{x}_r(t) + k_c\Omega_z\dot{\varepsilon}_t(t) - \varepsilon_e(t).$$

Now, the output is extracted by applying synchronous demodulation. We have that for a harmonic signal of amplitude A, its derivative amplitude is $\omega_{exc}A$, then, the demodulated gyroscope output is approximately given by

$$\tilde{f}_c \approx k_c\Omega_z\omega_{exc} - k_c\Omega_z\omega_{exc}E_t - E_e,$$

where E_t and E_e are respectively the amplitudes of the tracking and estimation errors.

Then, neglecting any change of units, the fitted constant SF^{fit} that somehow relates the output units (Newtons of Coriolis force) to the input the angular rate, is approximately equal to

$$SF^{fit} \approx k_c\omega_{exc}$$

Then, the measured angular rate is approximately

$$\tilde{\Omega}_z \approx \Omega_z + \Omega_z E_t - \frac{E_e}{k_c\omega_{exc}}.$$

We can observe that both tracking and estimation errors contributes to a deviation of the measured angular rate from the actual input angular rate. This measurement error is partially mitigated by the fitting process, which somehow operates as a calibration process to compensate the "predictable" measurement errors.

Appendix C

Proofs of chapter 5

C.1 Proof of Theorem 5.6

Step 1. Let us prove that, if y is a wide-sense stationary signal of bandwidth $2W$ centered at ω_0, then there exists y_i and y_q such that

$$y(t) = y_i(t)\cos(\omega_0 t) + y_q(t)\sin(\omega_0 t).$$

and

$$\left\{ \begin{array}{ll} y_i(t) & = y(t)\cos(\omega_0 t) + \check{y}(t)\sin(\omega_0 t) \\ y_q(t) & = y(t)\sin(\omega_0 t) - \check{y}(t)\cos(\omega_0 t) \end{array} \right. ,$$

Lemma C.1. *Let us introduce $z(t)$ such that*

$$S_z(\omega) = \left\{ \begin{array}{ll} 4S_y(\omega) & \omega > 0 \\ 0 & \omega < 0 \end{array} \right.$$

with z known as the analytic signal associated to y. Then,

$$z(t) = y(t) + j\check{y}(t)$$

with

$$\check{y}(t) = \frac{1}{\pi t} * y(t) = \frac{1}{\pi}\int_{-\infty}^{\infty} \frac{y(\tau)}{t-\tau} d\tau$$

that is, $\check{y}(t)$ is the Hilbert transform of $y(t)$.

Proof. z can be interpreted as the output of a convolution system whose input is y, and whose frequency response $H(j\omega)$ is $1 + \mathrm{sgn}(\omega)$. As a consequence of $S_z = |H(\omega)|^2 S_y$, then

$$S_z(\omega) = (1 + \mathrm{sgn}(\omega))^2 S_y(\omega)$$

that is

$$\left\{ \begin{array}{lcll} S_z(\omega) & = & 4S_y(\omega) & \omega > 0 \\ S_z(\omega) & = & 0 & \omega > 0 \end{array} \right. ,$$

now

$$\begin{array}{rcl} z(j\omega) & = & y(j\omega) + \mathrm{sgn}(\omega) y(j\omega) \\ & = & y(j\omega) + j \underbrace{(-j\mathrm{sgn}(\omega))}_{\check{H}(\omega)} y(j\omega) \end{array} \qquad \text{(C.1)}$$

then

$$z(t) = y(t) + j\check{y}(t)$$

with $\check{y} = \check{h}(t) * y(t)$ and $\check{h}(t) = \mathcal{F}^{-1}[\check{H}(\cdot)]$, that is

$$\check{h}(t) = \frac{1}{\pi t}$$

□

Note that, if $y(t) \in \mathbb{R}$, then $\check{y}$ also belongs to $\mathbb{R}$, while $z(t)$ is a complex signal.

Step 2. Let us prove that $y(t) = y_i(t)\cos(\omega_0 t) + y_q(t)\sin(\omega_0 t)$.
Developing $z(t)e^{-j\omega_0 t}$, we have

$$\begin{aligned} z(t)e^{-j\omega_0 t} &= (y(t) + j\check{y}(t))(\cos(\omega_0 t) - j\sin(\omega_0 t)) \\ &= \underbrace{y(t)\cos(\omega_0 t) + \check{y}(t)\sin(\omega_0 t)}_{y_i(t)} - j\underbrace{y(t)\sin(\omega_0 t) - \check{y}(t)\cos(\omega_0 t)}_{y_q(t)}, \end{aligned}$$

Then, multiplying the expression of $y_i(t)$ by $\cos(\omega_0 t)$, and the expression of $y_q(t)$ by $\sin(\omega_0 t)$, and adding both, we obtain

$$y(t) = y_i(t)\cos(\omega_0 t) + y_q(t)\sin(\omega_0 t).$$

Step 3. Let us prove that $y_i(t)$ is a WSS signal. We can determine a WSS as a random signal

- whose average and variance are independent of the instant t.
- whose autocorrelation function between the instants t and $t+\tau$, depends only on τ.

Average and variance can be trivially verified. In the following, we prove that the autocorrelation of y_i depends only on τ,, showing that y_i WSS.
First, the correlation between two signals $a(t)$ and $b(t)$ is here defined as

$$R_{ab}(t, t+\tau) = \int_{-\infty}^{\infty}\int_{-\infty}^{\infty} a(t)b(t+\tau)p(a, b, t, t+\tau)dadb.$$

where $p(a, b, t, t+\tau)$ is the probability function between $a(t)$ and $b(t+\tau)$.

Lemma C.2. *Let $y(t)$ be band-limited random signal, and let $\check{y}(t)$ be the Hilbert transform of $y(t)$. Then,*

$$\begin{aligned} S_{\check{y}}(\omega) &= S_y(\omega) \\ R_{\check{y}}(\tau) &= R_y(\tau). \end{aligned}$$

Furthermore,

$$\begin{aligned} S_{y\check{y}}(\omega) &= -j\ sgn(\omega)S_y(\omega) \\ S_{\check{y}y}(\omega) &= j\ sgn(\omega)S_y(\omega) \end{aligned}$$

hence

$$S_{y\check{y}}(\omega) = -S_{\check{y}y}(\omega)$$
$$R_{y\check{y}}(\tau) = -R_{\check{y}y}(\tau).$$

Proof. In the frequency domain, the Hilbert transform $\check{y}(j\omega)$ can be seen as the response of a filter with frequency response $\check{H}(\omega) = -j \ \operatorname{sgn}(\omega)$ to the input signal $y(j\omega)$. We can easily observe that

$$|\check{H}|^2(\omega) = 1$$

Hence,

$$S_{\check{y}}(\omega) = |\check{H}|^2(\omega)S_y(\omega) = S_y(\omega)$$

Then, the cross Power Spectral Density between an input y and the output $\check{y}$, following the expression for correlation, is given by $S_{y\check{y}}(\omega) = \check{H}(\omega)S_y(\omega)$, hence

$$S_{y\check{y}}(\omega) = -j \operatorname{sgn}(\omega)S_y(\omega)$$

Then, for two real signals a and b, we have that $S_{ab}(\omega) = S_{ba}(-\omega)$. Therefore

$$S_{\check{y}y}(\omega) = S_{y\check{y}}(-\omega) = -j \operatorname{sgn}(-\omega)S_y(-\omega) = j \operatorname{sgn}(\omega)S_y(\omega).$$

Concluding then

$$S_{\check{y}y}(\omega) = -S_{y\check{y}}(\omega).$$

Finally, autocorrelation and cross correlation relationships are obtained by respectively applying the inverse Fourier transform to the PSDs and CPSDs. □

Computing the autocorrelation function of $y_i(t)$, expressed as in (5.35):

$$\begin{aligned} R_{y_i}(t, t+\tau) = \int_{-\infty}^{\infty}\int_{-\infty}^{\infty} & (y(t)\cos(\omega_0 t) + \check{y}(t)\sin(\omega_0)t)) \\ & ((y(t+\tau)\cos(\omega_0(t+\tau)) + \check{y}(t+\tau)\sin(\omega_0(t+\tau))) \\ & p(y, \check{y}, t, t+\tau)p(\check{y}, y, t, t+\tau)dyd\check{y} \end{aligned}$$

which is developed as follows

$$\begin{aligned} R_{y_i}(t, t+\tau) = & \cos(\omega_0(t+\tau))\cos(\omega_0 t)\int_{-\infty}^{\infty} y(t)y(t+\tau)p(y, t, t+\tau)dy \\ & + \sin(\omega_0(t+\tau))\sin(\omega_0 t)\int_{-\infty}^{\infty} \check{y}(t)\check{y}(t+\tau)p(\check{y}, t, t+\tau)d\check{y} \\ & + \sin(\omega_0(t+\tau))\cos(\omega_0 t)\int_{-\infty}^{\infty}\int_{-\infty}^{\infty} y(t)\check{y}(t+\tau)p(y, \check{y}, t, t+\tau)dyd\check{y} \\ & + \cos(\omega_0(t+\tau))\sin(\omega_0 t)\int_{-\infty}^{\infty}\int_{-\infty}^{\infty} \check{y}(t)y(t+\tau)p(\check{y}, y, t, t+\tau)dyd\check{y}, \end{aligned}$$

which gives

$$\begin{aligned} R_{y_i}(t,t+\tau) =& \cos(\omega_0(t+\tau))\cos(\omega_0 t)R_y(\tau) \\ &+ \sin(\omega_0(t+\tau))\sin(\omega_0 t)R_{\check{y}}(\tau) \\ &+ \sin(\omega_0(t+\tau))\cos(\omega_0 t)R_{y\check{y}}(\tau) \\ &+ \cos(\omega_0(t+\tau))\sin(\omega_0 t)R_{\check{y}y}(\tau). \end{aligned}$$

Using the trigonometric identities $\cos(A)\cos(B) = \frac{1}{2}(\cos(A-B)+\cos(A+B))$, $\sin(A)\sin(B) = \frac{1}{2}(\cos(A-B)-\cos(A+B))$, $\cos(A)\sin(B) = \frac{1}{2}(\sin(A+B)-\sin(A-B))$ and $\sin(A)\cos(B) = \frac{1}{2}(\sin(A+B)+\sin(A-B))$, with $A = \omega_0(t+\tau)$ and $B = \omega_0 t$, we obtain

$$\begin{aligned} R_{y_i}(t,t+\tau) =& \frac{1}{2}R_y(\tau)(\cos(\omega_0\tau)+\cos(\omega_0(2t+\tau))) \\ &+ \frac{1}{2}R_{\check{y}}(\tau)(\cos(\omega_0\tau)-\cos(\omega_0(2t+\tau))) \\ &+ \frac{1}{2}R_{y\check{y}}(\tau)(\sin(\omega_0(2t+\tau))+\sin(\omega_0\tau)) \\ &+ R_{\check{y}y}(\tau)\sin(\omega_0(2t+\tau))-\sin(\omega_0\tau). \end{aligned}$$

Reorganizing the terms as factors of cosine and sine functions, we have

$$\begin{aligned} R_{y_i}(t,t+\tau) =& \frac{1}{2}\left((R_y(\tau)+R_{\check{y}}(\tau))\cos(\omega_0\tau)+(R_{y\check{y}}(\tau)-R_{\check{y}y}(\tau))\sin(\omega_0\tau)\right) \\ &+ \frac{1}{2}\left((R_y(\tau)-R_{\check{y}}(\tau))\cos(\omega_0(2t+\tau))+(R_{y\check{y}}(\tau)+R_{\check{y}y}(\tau))\sin(\omega_0(2t+\tau))\right). \end{aligned}$$

Using the PSD and CPSD relationships of Lemma C.2, we have

$$R_{y_i}(\tau) = R_y(\tau)\cos(\omega_0\tau) + R_{y\check{y}}(\tau)\sin(\omega_0\tau) \tag{C.2}$$

Hence, $y_i(t)$ is a wide sense stationary signal.

Step 4. Let us prove that

$$S_{y_i}(\omega) = S_y(\omega+\omega_0) + S_y(\omega-\omega_0) \qquad |\omega| < W.$$

Given that $y_i(t)$ is a wide sense stationary signal, we can obtain its PSD by applying the Fourier transform to its autocorrelation function R_{y_i}, as follows

$$S_{y_i}(\omega) = \frac{1}{2}\left[S_y(\omega+\omega_0)+S_y(\omega-\omega_0)\right] \tag{C.3}$$

$$+ \frac{1}{2}\left[S_y(\omega+\omega_0)\mathrm{sgn}(\omega+\omega_0) - S_y(\omega-\omega_0)\mathrm{sgn}(\omega-\omega_0)\right] \tag{C.4}$$

Since the PSD $S_y(\omega)$ is a passband even function, we can rewrite it from a low pass PSD $S_l(\omega)$ (**??**) as follows:

$$S_y(\omega) = S_l(\omega-\omega_0) + S_l(-\omega-\omega_0)$$

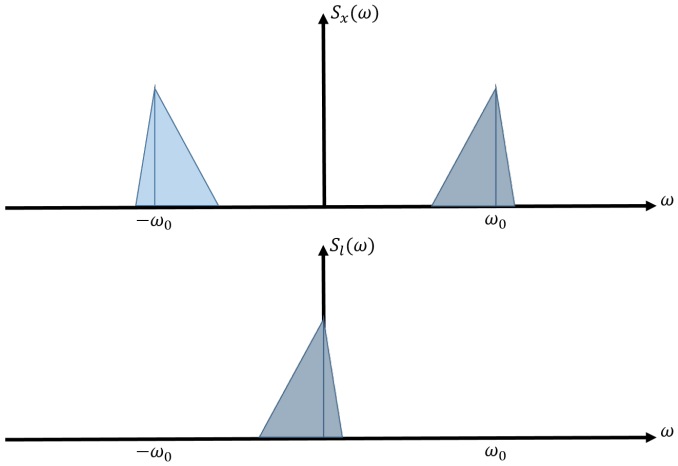

FIGURE C.1: DSP $S_l(\omega)$

Therefore, we have that

$$S_y(\omega+\omega_0) = S_l(\omega) + S_l(-\omega-2\omega_0) \tag{C.5}$$
$$S_y(\omega-\omega_0) = S_l(-\omega) + S_l(\omega-2\omega_0) \tag{C.6}$$
$$S_y(\omega+\omega_0)\text{sgn}(\omega+\omega_0) = S_l(\omega) - S_l(-\omega-2\omega_0) \tag{C.7}$$
$$S_y(\omega-\omega_0)\text{sgn}(\omega-\omega_0) = -S_l(-\omega) + S_l(\omega-2\omega_0) \tag{C.8}$$

Substituting (C.8) in (C.4), we obtain

$$S_{y_i}(\omega) = S_l(\omega) + S_l(-\omega)$$

Finally, we can identify that

$$S_l(\omega) + S_l(-\omega) = \begin{cases} S_y(\omega+\omega_0) + S_y(\omega-\omega_0) & |\omega| < \omega_b \\ 0 & |\omega| > \omega_b \end{cases} \tag{C.9}$$

Appendix D

Résumé étendu : Chapitre 1. Introduction générale

D.1 Contexte et motivations

D.1.1 Gyroscopes MEMS

Un gyroscope est un dispositif qui mesure la vitesse angulaire d'un objet par rapport à un référentiel. L'acronyme MEMS signifie "Micro Electro-Mechanical Systems". La taille microscopique des gyroscopes MEMS permet de les intégrer dans des systèmes embarqués compacts et légers. Ils présentent également l'avantage de consommer beaucoup moins d'énergie et d'être moins chers que les gyroscopes de grande taille. Néanmoins, la mise en œuvre des gyroscopes MEMS dans des applications qui exigent des spécifications de haute performance reste assez limitée. Si la micro-taille des gyroscopes MEMS peut être avantageuse dans certains cas, elle présente néanmoins plusieurs inconvénients, tels que des imperfections de fabrication, une sensibilité élevée aux conditions environnementales, un rapport signal sur bruit plus faible, etc.

Afin d'élargir le champ d'application des gyroscopes MEMS, leur précision et leur fiabilité doivent être améliorées. Cependant, il est souhaitable qu'ils conservent l'un de leurs principaux avantages : un prix attractif. Les boucles de commande à rétroaction jouent un rôle crucial comme alternative pour obtenir d'importantes améliorations de performance. En effet, les boucles de commande peuvent être conçues de manière à garantir spécifiquement une certaine précision tout en améliorant la robustesse par rapport à l'incertitude du système. De plus, l'amélioration des boucles de commande implémentées ne nécessite pas de modification significative des caractéristiques matérielles des gyroscopes MEMS, ce qui permet d'aborder correctement le compromis entre performance et faible coût.

D.1.2 Le projet Next4MEMS

Le projet Next4MEMS est une initiative de plusieurs acteurs français de l'industrie de la microélectronique et des capteurs inertiels. L'enjeu du projet Next4MEMS est d'établir une industrie française des MEMS inertiels au silicium, compétitive et durable, répondant à la plupart des besoins de haute performance. Ce projet est soutenu par BPI France (la banque française d'investissement public) dans le cadre du pôle de compétitivité Minalogic "PSPC" (Projet de Recherche et Développement Structurants pour la Compétitivité).

Ce programme de doctorat est réalisé au sein du Laboratoire Ampère, dont l'objectif est de proposer une méthodologie systématique pour le processus de conception des

commandes. Le but d'un tel processus est de fournir systématiquement des solutions de commande qui améliorent les spécifications de performance globale et de robustesse des gyroscopes MEMS.

D.1.3 Le processus de conception de la commande

Le processus de conception de la commande adopté pour le Next4MEMS est décrit ci-après. La première étape consiste à dériver un modèle qui décrit le comportement du système réel. Ce modèle doit être aussi précis que possible tout en conservant une structure relativement simple, adaptée à la conception des correcteurs. Ensuite, l'étape de conception de la commande développe des stratégies de commande pour atteindre les spécifications requises. Ensuite, des techniques de commande adaptatives peuvent être nécessaires pour compenser l'effet de la température sur le comportement du système. Enfin, l'objectif de l'étape de validation est d'évaluer si le système en boucle fermée peut garantir certaines propriétés souhaitées lorsqu'il est mis en œuvre sur le système réel. L'objectif de ce travail est de proposer des méthodes efficaces pour réaliser l'étape de validation du système dans le cadre du processus de conception des commandes. Ce mémoire se concentre sur le problème de la validation pré-expérimentale de la performance basée sur un modèle plutôt que sur la procédure de validation expérimentale qui nécessite généralement un investissement important en temps et en ressources.

D.2 Approche de la recherche et contributions

Pour fournir des méthodes de validation pré-expérimentale, il est nécessaire d'adopter une approche basée sur le modèle qui, du point de vue de la théorie de l'automatique, est liée au problème de l'analyse du système. Les gyroscopes MEMS peuvent être considérés comme une classe particulière de systèmes incertains et temps-variants. En effet, la présence d'une démodulation synchrone dans le système se manifeste par l'introduction d'un ou plusieurs paramètres à temps-variants harmoniques (HTV), c'est-à-dire des paramètres qui varient comme des fonctions sinusoïdales dans le domaine temporel d'une fréquence donnée. Ceci implique une motivation majeure pour aborder formellement l'analyse des systèmes linéaires temps-variants harmoniques (LHTV). De plus, nous devons dériver des critères d'analyse précis pour l'évaluation des performances.

D.2.1 Analyse des systèmes LHTV

Nous définissons un système LHTV comme un système linéaire qui contient un ou plusieurs paramètres temps-variants harmoniques (HTV), c'est-à-dire qui varient comme des fonctions sinusoïdales dans le domaine temporel d'une fréquence donnée. Pour aborder formellement l'analyse des systèmes LHTV, nous adoptons l'approche des contraintes quadratiques intégrales (IQC) : [MR97, Sei14, VSK16, CS15]. Ce cadre théorique est adapté à l'analyse des gyroscopes MEMS, permettant de considérer simultanément sa nature incertaine et temps-variante, ainsi que d'étudier les spécifications de précision, de sensibilité et de bruit de sortie.

Une étape clé pour appliquer le cadre IQC est de caractériser les relations entrée-sortie de l'élément problématique, appartenant à un ensemble incertain, par une contrainte quadratique intégrale qui est définie par un ensemble de fonctions, appelées *multiplieurs*. Le choix approprié d'un ensemble de multiplieurs est crucial pour réduire le conservatisme des résultats de l'analyse. Pour aborder l'analyse des

systèmes LHTV, en réduisant le conservatisme des résultats, nous généralisons et améliorons à la fois les ensembles de multiplieurs pour une incertitude paramétrique répétée et des paramètres temps-variants arbitrairement rapides (ou $D-G$ scalings) [FTD91, MIF00, LTVD00]), ainsi que l'ensemble de multiplieurs proposé dans [MR97] pour un paramètre HTV répété. De plus, certaines extensions doivent être développées pour les cas de systèmes contenant plusieurs paramètres HTV qui oscillent à la même fréquence, mais avec un déphasage entre eux.

D.2.2 Spécifications de performance basées sur des modèles

Non-linéarité du Facteur d'échelle

La spécification de précision la plus importante est la non-linéarité du facteur d'échelle (SFNL). La SFNL quantifie l'erreur maximale de mesure du gyroscope sur toute la gamme des vitesses angulaires dans laquelle le gyroscope fonctionne. Le calcul basé sur le modèle de la SFNL, étant donné la classe particulière de signaux d'entrée et l'application de la démodulation synchrone à la sortie, est réduit à un problème d'optimisation robuste. Ensuite, une partie de notre contribution s'est concentrée sur la visite et l'adaptation des outils d'analyse disponibles, principalement dérivés de la théorie de la commande robuste, pour calculer efficacement le SFNL des gyroscopes MEMS.

Bruit de sortie et variance d'Allan

La méthode standard pour évaluer le bruit de sortie des gyroscopes MEMS est la méthode de la variance d'Allan [All66, SHC+12]. Cette méthode permet de classer et de quantifier les différents processus stochastiques qui sont contenus dans le bruit de sortie du gyroscope. Afin de fournir un ensemble de méthodes basées sur le modèle pour calculer efficacement la variance d'Allan, nous adoptons une approche de filtre générateur, qui consiste à caractériser les propriétés du signal de sortie à travers les propriétés du modèle du système qui le génère, qui est à son tour excité par une classe particulière de signaux bien connus, par exemple, un bruit blanc. Le premier problème consistait à étudier le cas d'un bruit de sortie généré par un modèle LTI. Ensuite, pour orienter le calcul de la variance d'Allan basé sur un modèle dans le contexte des gyroscopes MEMS, il est nécessaire de considérer le problème où le signal est généré par un système LTI, représentant la boucle fermée commandée, suivi par un démodulateur synchrone. Ceci nécessite de déterminer quel est l'effet de la démodulation synchrone sur la densité spectrale de puissance (DSP) du signal de sortie. Nous proposons deux solutions : une basée sur les concepts de signaux aléatoires modulés [Lat70, Pap83] et une seconde dans une perspective IQC.

D.2.3 Validation de la conception de la commande

Un intérêt majeur dans le développement de nos outils d'analyse de système est la validation de stratégies de commande alternatives qui nécessitent des architectures plus complexes que la commande LTI classique. Nous abordons l'analyse d'une commande basée sur les phaseurs qui nécessite l'implémentation de modulateurs et de démodulateurs dans la boucle fermée [SSK20]. La conception de la commande est effectuée en supposant une démodulation synchrone idéale. Cependant, il peut s'agir d'une hypothèse forte. Dans un cas de mise en œuvre, où la démodulation synchrone réelle n'est pas idéale, il n'est plus possible de supposer que le système n'est pas LTI mais LHTV. Nous étudions ensuite la stabilité de la commande

basée sur les phaseurs avec une démodulation synchrone non idéale en appliquant l'ensemble des outils que nous développons pour l'analyse des systèmes LHTV. Une autre stratégie de commande du projet Next4MEMS consiste en l'implémentation en temps discret d'un correcteur dépendant des paramètres [SACKS20]. Cette stratégie de commande utilise des méthodes en temps continu et consiste à estimer un paramètre du système en temps réel, puis à l'utiliser pour mettre à jour le paramétrage du correcteur. Cependant, l'implémentation en temps discret et les erreurs d'estimation posent des problèmes qui sont négligés dans le processus de conception de la commande. Ce problème nous amène à analyser un système incertain qui a une dépendance non rationnelle sur les paramètres incertains, ce qui peut être abordé en utilisant une approximation proposée basée sur Taylor et des outils d'analyse de robustesse.

Appendix E

Résumé étendu : Chapitre 2. Validation des performances des gyroscopes MEMS

Ce chapitre présente le principe de fonctionnement d'un gyroscope MEMS mesurant la vitesse angulaire par rapport à un référentiel fixe, ceci en considérant un fonctionnement idéal. Ensuite, les stratégies de commande utilisées pour répondre aux exigences de fonctionnement des gyroscopes MEMS sont passées en revue. Les spécifications standard qui indiquent la qualité d'un gyroscope sont ensuite introduites. Dans les sections suivantes, nous présentons quelques-unes des principales non-idéalités que l'on trouve dans les micro gyroscopes et leurs effets. Enfin, nous présentons le processus de validation du système, ce qui permet d'énoncer les principaux objectifs et problèmes qui sont abordés dans ce travail.

E.1 Description du système

Les gyroscopes sont des dispositifs qui mesurent la vitesse angulaire d'un objet soumis à un mouvement de rotation par rapport à un axe donné. L'acronyme MEMS signifie "Micro Electro-Mechanical Systems". Parmi les gyroscopes MEMS, nous présenterons ici les gyroscopes MEMS dits vibratoires (résonants). La résonance permet d'améliorer radicalement le rapport signal sur bruit (SNR).

E.1.1 Principe mécanique

Le cœur des gyroscopes MEMS est une structure micro-mécanique composée de deux systèmes ressort-masse orthogonaux faiblement amortis. La masse m_x ne peut être déplacée linéairement que dans la direction x en appliquant une force F_x, c'est ce qu'on appelle le mode drive. De même, la masse m_y ne peut être déplacée que sur une direction y orthogonale au mode d'entraînement en appliquant une force F_y, on parle de mode sense.

Les deux masses sont liées à une structure fixe au moyen de poutres en silicium. Il existe alors des éléments de rigidité et d'amortissement entre les masses et la structure fixe Figure E.1. Le système peut alors être modélisé comme deux systèmes masse-ressort-amortisseur indépendants comme suit :

$$\begin{aligned} m_x\ddot{x}(t) + d_{xx}\dot{x}(t) + k_{xx}x(t) &= F_x(t) \\ m_y\ddot{y}(t) + d_{yy}\dot{y}(t) + k_{yy}y(t) &= F_y(t) \end{aligned} \tag{E.1}$$

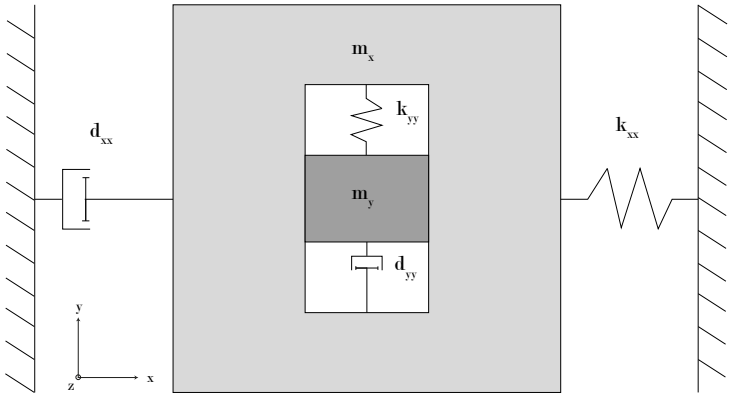

FIGURE E.1: Représentation schématique des modes drive et sense du MEMS.

avec k_{xx} et k_{yy} respectivement les constantes de rigidité du mode drive et du mode sense, tandis que d_{xx} et d_{yy} sont les coefficients d'amortissement correspondants.

Or, lorsque cette structure mécanique est soumise à un mouvement de rotation par rapport à l'axe z (orthogonal aux deux modes) à une vitesse angulaire $Omega_z$, si l'on applique une force F_x pour induire un mouvement oscillatoire sur la masse m_x, l'effet Coriolis se produit transférant l'énergie du mode drive au mode sense. Ceci fait apparaître sur le mode sense une force de Coriolis F_{cy} proportionnelle à la vitesse angulaire Ω_z, et donc un couplage entre le mode drive et le mode sense. Il existe également une force de Coriolis F_{cx} qui peut perturber les vibrations du mode drive. Les deux forces de Coriolis décrites sont définies comme suit :

$$\begin{aligned} F_{cy}(t) &= -2m_x\dot{x}(t)\Omega_z \\ F_{cx}(t) &= 2m_y\dot{y}(t)\Omega_z \end{aligned} \tag{E.2}$$

Cependant, l'effet de F_{cx} est souvent minimisé. En incluant les équations (2.4) dans (2.1), nous obtenons l'équation complète d'un micro-gyroscope idéal :

$$M\ddot{r}(t) + D\dot{r}(t) + Kr(t) = C\dot{r}(t) + F(t) \tag{E.3}$$

avec les vecteurs des signaux

$$r(t) = \begin{bmatrix} x(t) \\ y(t) \end{bmatrix}, \qquad F(t) = \begin{bmatrix} F_x(t) \\ F_y(t) \end{bmatrix},$$

et les matrices de paramètres

$$M = \begin{bmatrix} m_x & 0 \\ 0 & m_y \end{bmatrix}, \quad D = \begin{bmatrix} d_{xx} & 0 \\ 0 & d_{yy} \end{bmatrix}, \quad K = \begin{bmatrix} k_{xx} & 0 \\ 0 & k_{yy} \end{bmatrix}, \quad C = \begin{bmatrix} 0 & 2m_y\Omega_z \\ -2m_x\Omega_z & 0 \end{bmatrix}.$$

Ainsi, en présence d'un effet de Coriolis, il est possible d'obtenir indirectement la vitesse angulaire Ω_z en mesurant la force de Coriolis F_{cy} en mode sense. Pour cela, il faut simultanément induire l'effet de Coriolis et estimer la force de Coriolis.

Ces deux objectifs sont atteints en utilisant des stratégies de commande en boucle fermée qui sont présentées dans ce qui suit.

E.1.2 Actionnement et détection

Actionnement

Nous avons présenté le principe mécanique d'un gyroscope MEMS. Comme nous l'avons mentionné, les modes peuvent être pilotés par l'application de forces externes. Pour cela, il faut prévoir un mécanisme d'excitation. La méthode d'excitation la plus courante est l'actionneur électrostatique (ou capacitif) : [Sau08a, EKT+11].

Détection

La mesure des déplacements des modes drive et sense est effectuée en utilisant l'actionneur en peigne en mode passif. Le déplacement de x induit un changement de la capacité C_x, qui peut être converti en un signal de tension en utilisant un amplificateur de charge [Sau08a].

E.1.3 Commande en boucle fermée

Mode Drive

La force de Coriolis F_{cy} est générée en induisant un déplacement oscillatoire du mode drive. Pour cela, il est nécessaire d'appliquer une force F_x telle que le mode drive maintienne des oscillations d'amplitude constante à l'état d'équilibre, par exemple,

$$x(t) = A_x \sin(\omega_{exc} t).$$

Ensuite, la force de Coriolis F_{cy} affectant le mode sense est donnée par

$$F_{cy}(t) = -2m_x A_x \omega_{exc} \cos(\omega_{exc} t)\Omega_z.$$

Par conséquent, les objectifs de contrôle du mode drive peuvent être résumés comme suit :

- maintenir une amplitude constante A_x des oscillations ;
- exciter le mode drive à une fréquence ω_{exc} qui tend à être égale à la fréquence de résonance ω_0 du résonateur.

Plusieurs stratégies de commande ont été développées pour atteindre ces objectifs. Puisque l'application exige la commande de signaux sinusoïdaux, nous pouvons les classer en deux approches générales : les approches basées sur l'enveloppe qui consistent à commander l'enveloppe du signal sinusoïdal, habituellement en commandant l'amplitude et la phase [Sau08b, RCRW09, MVG01] ou le phaseur associé au signal [SSK20] ; et les approches de commande directe, qui consistent à commander directement les signaux sinusoïdaux.

Mode sense

Ensuite, avec l'effet de Coriolis induit, une force de Coriolis F_{cy} perturbe le mode sense, l'objectif est maintenant d'obtenir une estimation précise de cette force de Coriolis, et par conséquent, de la vitesse angulaire Ω_z. L'approche la plus courante est estimer la force de Coriolis en boucle fermée. Cette approche consiste à concevoir

une stratégie de commande qui maintient la position du mode sense $y(t)$ proche de zéro. Ensuite, la force F_y appliquée par le correcteur s'opposera à la force de Coriolis F_{cy} afin de conserver la référence zéro, à savoir

$$F_y \approx -F_{cy},$$

ce qui permet d'obtenir presque directement une estimation de la force de Coriolis.

Quelques stratégies de commande du projet NEXT4MEMS

Trois approches principales, développées dans le cadre de ce projet, seront analysées dans ce document.

1. **Commande directe MIMO :** cette approche peut être regroupée parmi les solutions de commande directe, les deux modes drive et sense sont asservis en commandant directement les signaux sinusoïdaux impliqués, ce qui permet de mettre en œuvre une architecture de commande linéaire classique. Ce type de commande sera considéré pour l'analyse effectuée dans les Appendix G et Appendix H.
2. **Commande basée phaseur :** cette stratégie commande les parties réelles et imaginaires du phasor associé aux signaux sinusoïdaux dans la boucle. Cette approche est analysée dans Appendix I.
3. **Commande dépendant d'un paramètre :** Cette dernière approche consiste en un simple correcteur linéaire dépendant d'un paramètre qui, face à une dérivation de la fréquence de résonance du MEMS, peut facilement adapter sa dynamique par de simples normalisations de fréquence. Cette dernière approche est analysée dans Appendix I.

E.1.4 Démodulation synchrone

Indépendamment de la stratégie de commande adoptée, à la sortie du mode sense, nous récupérons une estimation de la force de Coriolis, approximativement donnée par

$$\tilde{f}_c(t) \approx 2m_x A_x \omega_{exc} \cos(\omega_{exc} t)\Omega_z,$$

Par suite, la sortie en boucle fermée est une oscillation harmonique dont l'amplitude donne une estimation de Ω_z.

Enfin, afin d'extraire du signal modulé l'amplitude désirée, il est nécessaire d'appliquer la *démodulation synchrone*.

Démodulation synchrone idéale

Lorsqu'un certain signal $\tilde{z}$ présente un spectre fortement concentré autour d'une fréquence particulière ω_0, le signal peut être considéré comme un signal modulé, défini comme suit.

Definition E.1 (Signal modulée pur)**.** *On dit d'un signal $\tilde{z}$ qu'il est un signal modulé pur si sa densité spectrale de puissance S_z a une largeur de bande limitée $2W$ autour d'une fréquence ω_0, avec $W < \omega_0$, soit*

$$S_z(\omega) = 0 \quad \forall\, \omega \ \in]-\omega_0 + W, \omega_0 - W[\cup]\omega_0 + W, \infty[\cup]-\infty, -\omega_0 - W[, \tag{E.4}$$

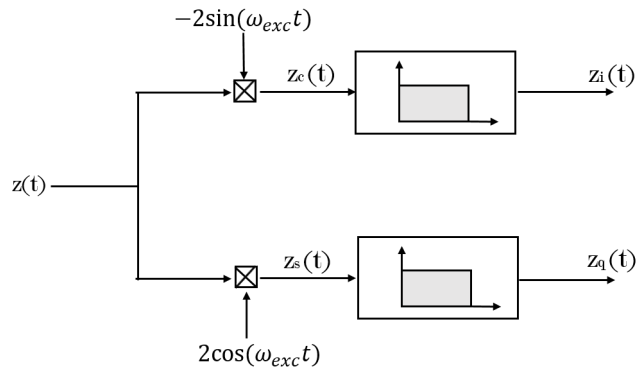

FIGURE E.2: Représentation schématique de la démodulation synchrone idéale

Ensuite, en supposant que le signal z est un signal modulé pur au sens de la définition E.1, il peut être exprimé comme suit

$$\tilde{z}(t) = z_i(t)\cos(\omega_0 t) - z_q(t)\sin(\omega_0 t) \tag{E.5}$$

où $z(t)$ est le signal modulé, $z_i(t)$ sa composante en phase et $z_q(t)$ sa composante en quadrature.

Ensuite, l'objectif de la démodulation synchrone est d'extraire ces deux composantes du signal modulé. Pour ce faire, comme le montre la Figure E.2, nous multiplions d'abord le signal modulé d'entrée $z(t)$ par une fonction cosinus et une fonction sinus. Ensuite, les signaux résultants z_c et z_i passent par des filtres passe-bas. Introduisons l'hypothèse suivante relative à un filtre passe-bas idéal dans le démodulateur synchrone.

Assumption E.1 (Filtre passe-bas idéal)**.** *Un filtre passe-bas est idéal si, pour une fréquence de coupure W, il est donné par*

$$F_L(j\omega) = rect\left(\frac{\omega}{2W}\right), \tag{E.6}$$

où $rect(\cdot)$ est la fonction rectangle et $W < \omega_0$ est la bande passante du filtre passe-bas.

Par conséquent, si nous supposons le filtre passe-bas idéal, les signaux z_{cf} et zcs à la sortie du démodulateur seront donnés par

$$z_{cf}(t) = z_i(t) \tag{E.7}$$
$$Nz_{sf}(t) = z_q(t), \tag{E.8}$$

en obtenant alors les composantes en phase et en quadrature.

Extraction de la force de Coriolis

Pour un signal de référence de mode drive de la forme $x_r(t) = A_r \sin(\omega_{exc} t)$, la sortie modulée est approximativement donnée par

$$\tilde{z}(t) \approx \tilde{f}_c \cos(\omega_{exc} t). \tag{E.9}$$

Alors, $\tilde{z}$ est un signal modulé pur particulier au sens de la définition 2.1. Ensuite, en appliquant une démodulation synchrone à $\tilde{z}$ dans (**??**), on obtient la sortie du

gyroscope z, donnée par la composante en phase z_i, donnée par

$$z = z_i \approx \tilde{f}_c.$$

E.2 De la sortie du gyroscope à la vitesse angulaire mesurée

La dernière étape consiste à obtenir la vitesse angulaire Ω_z à partir de la sortie du démodulateur synchrone, ci-après dénommée z. Pour établir la relation entre la sortie du gyroscope et la vitesse angulaire affichée, l'approche la plus courante consiste à effectuer une première procédure expérimentale. Plusieurs essais sont effectués sur toute la gamme des vitesses angulaires d'entrée. Ensuite, en utilisant des approches de régression linéaire [TWY17], une fonction linéaire z^{fit} est obtenue et définie comme suit

$$z^{fit}(\Omega_z) = SF^{fit}\Omega_z + B^{fit}. \tag{E.10}$$

En utilisant la fonction ajustée, il est possible d'obtenir la vitesse angulaire mesurée à afficher par la relation suivante :

$$\tilde{\Omega}_z = \frac{z - B^{fit}}{SF^{fit}}. \tag{E.11}$$

E.3 Spécifications des performances du gyroscope

Dans cette section, nous donnerons une brève introduction sur les spécifications de performance standard pour les gyroscopes MEMS [IEE04, IEE06, IEE18]. Ces spécifications de performance seront examinées en détail dans les chapitres suivants (Appendix G et Appendix H).

Considérons un gyroscope MEMS auquel on applique une vitesse angulaire Ω_z en entrée et dont on obtient une mesure z en sortie. Dans le cas idéal, la relation entrée-sortie est donnée par l'expression :

$$z^{idal} = SF\ \Omega_z$$

où z^{idal} est la sortie idéale et SF est le facteur d'échelle.

Les déviations par rapport à une mesure idéale peuvent être caractérisées à l'aide de deux types d'erreurs.

- **Biais :** la moyenne sur un temps donné de la sortie du gyroscope mesurée dans des conditions données, sans corrélation avec la rotation d'entrée.

Il n'existe pas de spécification particulière concernant le biais dans des conditions nominales. Cependant, le biais est facilement affecté par les changements environnementaux, principalement causés par les changements de température. Par conséquent, nous sommes intéressés par sa sensibilité thermique

- **Sensibilité thermique du biais :** rapport entre une variation du biais et une variation de la température.

Une autre erreur est une mesure de l'écart par rapport au facteur d'échelle idéal à la température nominale.

- **Non-linéarité du facteur d'échelle :** écart maximal, aux conditions nominales, de la droite qui définit la relation entrée-sortie nominale sur toute la gamme des vitesses angulaires de fonctionnement.

Tout comme le biais, l'erreur du facteur d'échelle est également sensible aux variations de température, ce qui nécessite de considérer sa sensibilité thermique.

- **Sensibilité thermique du facteur d'échelle :** rapport entre une variation du facteur d'échelle et une variation de la température.

Enfin, les dernières spécifications de performance concernent le niveau de bruit que l'on retrouve à la sortie du capteur. Elles sont principalement évaluées en utilisant la variance d'Allan. Cette méthode et les spécifications respectives seront présentées en détails dans Appendix H.

E.4 Non-idéalités dans les gyroscopes MEMS : sources d'incertitude

E.4.1 Dispersion de fabrication

Les limites des techniques de fabrication peuvent affecter les propriétés géométriques, électrostatiques et matérielles des dispositifs MEMS. Cela se traduit par des écarts importants par rapport aux valeurs nominales des paramètres en raison des tolérances de fabrication élevées. Le résultat est alors une limitation des propriétés de performance et de robustesse atteignables [AS08].

E.4.2 Aniso élasticité

En pratique, on peut trouver une imperfection qui induit un décalage angulaire entre les axes de la poutre et ceux du mode [SSP+06]. Ce type de phénomène induit un couplage élastique entre les modes drive et sense ; on parle alors d'anisoélasticité. Ces forces aniso élastiques peuvent être modélisées en introduisant des éléments non diagonaux dans la matrice de rigidité.

E.4.3 Amortissement non idéal

L'amortissement est associé à la dissipation d'énergie des systèmes mécaniques, provenant généralement de la friction mécanique ou de la viscosité du gaz entourant la structure mécanique. Dans les gyroscopes vibrants MEMS, l'effet de l'amortissement visqueux est prédominant par rapport à la friction structurelle.

Il est possible de regrouper les différents phénomènes d'amortissement et d'anisoélasticité en introduisant des termes non diagonaux dans le modèle mécanique des MEMS.

E.4.4 Sensibilité à l'environnement

En plus des imperfections de fabrication inhérentes, les variations des conditions environnementales ont un effet perturbateur sur la dynamique des gyroscopes MEMS. Plusieurs recherches ont été menées pour étudier l'impact de la température sur le facteur de qualité Q et la fréquence de résonance ω_0 [XCWL09, CSL+12, SEGT00, FKP+05, GHL+15].

E.4.5 Bruit

Le bruit thermique mécanique est la principale source rapportée de comportement stochastique : [Gab93, ALM99, Lel06, KM13]. Ce type de bruit se comporte comme un bruit blanc gaussien, dont la densité spectrale de puissance (DSP) est proportionnelle à la température.

D'autres types de bruit présents dans les capteurs inertiels sont présentés dans [IEE04]. Dans la pratique de la communauté MEMS, une importance remarquable a été accordée au bruit $1/\nu$, considéré comme la cause principale de l'*instabilité du biais*.

E.5 Validation de la conception de la commande

Les différentes stratégies de commande proposées dans le cadre du projet Next4MEMS sont basées sur des modèles qui sont des versions simplifiées du système réel. Il est donc nécessaire de procéder à une étape de validation des performances. Dans ce travail, nous proposons une approche pré-expérimentale basée sur le modèle pour la validation. Comme il existe des erreurs entre le modèle et le système, il est nécessaire de valider la commande par rapport à ces erreurs et à d'autres sources d'incertitude, c'est-à-dire d'évaluer la robustesse du système en boucle fermée. La plupart de la littérature se concentre sur les méthodes de Monte Carlo [ZTSL10, WHGS16]. A notre connaissance, la seule tentative d'utilisation d'une approche pire-cas se trouve dans [DZG07]. Néanmoins, l'analyse est basée sur les marges de stabilité classiques en utilisant différentes valeurs de paramètres, y compris minimales et maximales, ce qui ne constitue pas une garantie formelle de robustesse. Il existe une lacune évidente à combler, qui exige de proposer des méthodes alternatives pour tester, dans le processus de conception de la commande, la robustesse des gyroscopes MEMS en utilisant des méthodes plus fiables et efficaces.

E.6 Formulation du problème de recherche

Compte tenu des différents concepts et problèmes qui ont été introduits et discutés dans ce chapitre, l'objectif principal de ce travail peut être énoncé comme suit.

Étant donnée une stratégie de commande proposée pour un gyroscope MEMS qui répond aux spécifications de performance requises pour un modèle nominal ou un modèle simplifié, comment évaluer efficacement si les diverses spécifications de performance sont respectées malgré la présence de phénomènes non modélisés.

Les approches pire-cas issues de la théorie de la commande robuste et de l'analyse des systèmes développent des outils qui nous permettent d'analyser des systèmes soumis à des éléments "problématiques" en énonçant le problème sous la forme d'un critère mathématique. Différentes méthodes d'analyse permettent de tester une variété de propriétés de stabilité et de performance. Dans ce contexte, l'objectif général de validation des performances, en utilisant une approche pire-cas basée sur un modèle, implique de résoudre trois problèmes implicites de nature différente.

1. Comment déterminer une représentation appropriée du système réel ?
2. Comment interpréter les spécifications de performance standard ?
3. Comment tester la propriété désirée de façon efficace ?

Appendix F

Résumé étendu : Chapitre 3. Analyse des systèmes incertains et temps-variants harmoniques

Comme les gyroscopes MEMS sont des systèmes qui ont naturellement tendance à être incertains, il est nécessaire d'adopter un cadre approprié pour faire face à cette classe de problème d'analyse. La commande robuste robuste offre plusieurs outils d'analyse qui peuvent être des candidats appropriés pour nos objectifs. Par conséquent, la première partie de ce chapitre présente les principaux concepts et méthodes théoriques qui sont exploités dans ce travail, en se concentrant principalement sur l'approche des contraintes quadratiques intégrales (IQC). Dans Appendix E, nous présentons la démodulation synchrone, qui introduit dans le modèle des paramètres qui varient comme des fonctions sinusoïdales dans le domaine temporel d'une fréquence donnée. Nous appelons cette classe de systèmes les systèmes linéaires (incertains) temps-variants harmoniques (LHTV). Par conséquent, la deuxième partie de ce chapitre se concentre sur l'extension des outils d'analyse IQC existants à l'analyse des systèmes LHTV.

F.1 Stabilité et performance entrée-sortie

La première propriété intéressante d'un système à analyser est la stabilité, qui consiste à évaluer si l'opérateur représentant le système est borné. Nous considérons ici la notion de stabilité $\mathcal{L}_2$-gain qui est définie comme suit.

Definition F.1 (Stabilité $\mathcal{L}_2$-gain)**.** *Soit le système $G : \mathcal{L}_{2e}^{n_w} \to \mathcal{L}_{2e}^{n_z}$, avec une entrée w et une sortie z. On dit que G est $\mathcal{L}_2$-gain stable s'il existe un certain $\gamma > 0$ tel que*

$$\int_0^\infty |z(t)|^2 dt \leq \gamma^2 \int_0^\infty |w(t)|^2 dt \quad \forall\, w \in \mathcal{L}_2^{n_w}. \tag{F.1}$$

D'après la définition F.1, nous pouvons observer qu'une quantité (γ) est obtenue en testant simplement la stabilité $\mathcal{L}_2$-gain. Il est donc également possible d'évaluer les performances en utilisant le $\mathcal{L}_2$-gain.

Definition F.2 (performance $\mathcal{L}_2$-gain)**.** *Soit le système stable au sens du $\mathcal{L}_2$-gain $G : \mathcal{L}_{2e}^{n_w} \to \mathcal{L}_{2e}^{n_z}$. La performance $\mathcal{L}_2$-gain de G est le plus petit γ tel que (F.1) est satisfait.*

F.2 Représentation des systèmes incertains

F.2.1 Transformation linéaire fractionaire (LFT)

La représentation LFT décrit l'interconnexion par rétroaction de deux opérateurs. Dans l'analyse de la robustesse, il s'agit généralement d'un système LTI bien connu $G(s)$, appelé "système nominal", et d'un opérateur bloc Δ contenant tous les "éléments problématiques" du système, par exemple, les incertitudes, les paramètres variant dans le temps et les non-linéarités (Figure F.1). Nous désignons la représentation LFT par $\Delta \star G$, qui est définie par les équations :

$$\begin{aligned} \begin{bmatrix} q(s) \\ z(s) \end{bmatrix} &= \underbrace{\begin{bmatrix} G_{qp}(s) & G_{qw}(s) \\ G_{zp}(s) & G_{zw}(s) \end{bmatrix}}_{G(s)} \begin{bmatrix} p(s) \\ w(s) \end{bmatrix} \\ p(s) &= \Delta(q)(s) \end{aligned} \tag{F.2}$$

où $G \in \mathcal{RH}_\infty^{(n_p+n_w)\times(n_q+n_z)}$ est un système LTI stable, et $\Delta : \mathcal{L}_{2e}^{n_q} \to \mathcal{L}_{2e}^{n_p}$ peut être un opérateur quelconque borné et causal.

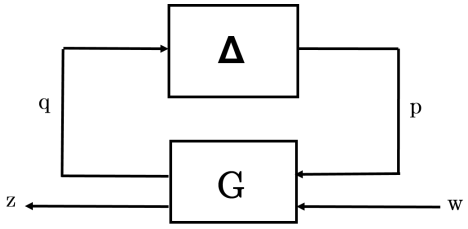

FIGURE F.1: Représentation LFT $\Delta \star G$

L'incertitude est introduite lorsque Δ appartient à un ensemble $\mathbf{\Delta}$ qui décrit la nature et la structure des éléments incertains. L'ensemble $\mathbf{\Delta}$ génère toute une famille de modèles $\mathbf{\Delta} \star G$ tels qu'il existe un élément Δ dans l'ensemble $\mathbf{\Delta}$ pour lequel $\mathbf{\Delta} \star G$ décrit la dynamique du système réel. Introduisons maintenant la définition d'un système incertain sous représentation LFT.

Definition F.3 (Système incertain)**.** *Soit $G \in \mathcal{RH}_\infty^{(n_p+n_w)\times(n_q+n_z)}$ un système LTI stable, et soit $\mathbf{\Delta}$ un ensemble d'opérateurs bornés et causaux. Alors, un système incertain $z = (\mathbf{\Delta} \star G)w$ est défini comme :*

$$\exists\, \Delta \in \mathbf{\Delta} \begin{cases} \begin{bmatrix} q(s) \\ z(s) \end{bmatrix} &= \underbrace{\begin{bmatrix} G_{qp}(s) & G_{qw}(s) \\ G_{zp}(s) & G_{zw}(s) \end{bmatrix}}_{G(s)} \begin{bmatrix} p(s) \\ w(s) \end{bmatrix} \\ p(s) &= \Delta(q)(s). \end{cases} \tag{F.3}$$

En utilisant cette définition des systèmes incertains, les notions de stabilité et de performance, qui ont été données pour un système général, doivent être adaptées au cas des ensembles de modèles. Pour ce faire, nous introduisons la notion de *robustesse* dans la section suivante.

F.3 Stabilité robuste et performance robuste

F.3.1 Stabilité robuste

Considérons d'abord l'interconnexion de rétroaction interne (G_{qp}, Δ) représentée dans Figure F.2 et définie par

$$\begin{aligned} q &= G_{qp}(s)p + q_{in} \\ p &= \Delta(q) + p_{in} \end{aligned} \tag{F.4}$$

avec $G_{qp} \in \mathcal{RH}_\infty^{n_p \times n_q}$ un système LTI stable et Δ un opérateur borné et causal, des signaux internes $q \in \mathcal{L}_{2e}^{n_q}$ et $p \in \mathcal{L}_{2e}^{n_p}$, et des perturbations $q_{in} \in \mathcal{L}_{2e}^{n_q}$, $p_{in} \in \mathcal{L}_{2e}^{n_q}$. Avant de définir la stabilité, il faut que l'interconnexion (G_{qp}, Δ) ait la propriété *bien posée*, c'est-à-dire que $(I - G_{qp}\Delta)$ a un inverse causal [ZD98]. Nous pouvons maintenant définir la stabilité de l'interconnexion (G_{sp}, Δ), également appelée stabilité interne.

Definition F.4 (Stabilité interne)**.** *Soit l'interconnexion de rétroaction bien posée (G_{qp}, Δ) définie par (F.4). On dit de l'interconnexion (G_{qp}, Δ) qu'elle est $\mathcal{L}_2$-gain stable par rapport à Δ si elle est bien posée et s'il existe un certain α tel que*

$$\|q\|_2^2 + \|p\|_2^2 \leq \alpha^2(\|q_{in}\|_2^2 + \|p_{in}\|_2^2) \quad \forall\, q_{in} \in \mathcal{L}_{2e}^{n_q},\ p_{in} \in \mathcal{L}_{2e}^{n_p} \tag{F.5}$$

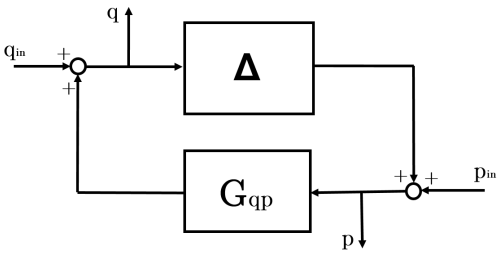

FIGURE F.2: Interconnexion de rétroaction (G_{qp}, Δ)

Décrivons maintenant une interconnexion incertaine $(G_{qp}, \mathbf{\Delta})$ comme :

$$\exists\, \Delta \in \mathbf{\Delta} \left\{ \begin{array}{rl} q(s) & = G_{qp}(s)p + q_{in} \\ p & = \Delta(q) + p_{in}. \end{array} \right. . \tag{F.6}$$

À partir de la définition F.4, et en utilisant l'interconnexion incertaine donnée par (F.6), nous pouvons introduire une définition formelle de la stabilité robuste.

Definition F.5 (Stabilité robuste)**.** *Soit G_{qp} un système LTI stable, et soit $\mathbf{\Delta}$ un ensemble d'opérateurs bornés et causaux. Alors, le système incertain $(G_{qp}, \mathbf{\Delta})$, défini par (F.6), est dit robuste en stabilité si (G_{qp}, Δ) est bien posé et a la stabilité interne pour tout $\Delta \in \mathbf{\Delta}$.*

F.3.2 Performance robuste

Considérons le système incertain représenté comme le système LFT $\mathbf{\Delta} \star G$ défini par (F.3). Comme pour la définition de la stabilité, la LFT $\Delta \star G$ doit être bien posée.

Definition F.6 (Performance $\mathcal{L}_2$-gain robuste)**.** *. Soit G un système LTI stable, et soit $\mathbf{\Delta}$ un ensemble d'opérateurs bornés et causaux. Alors, $\mathbf{\Delta} \star G$, défini par (F.3), a un $\mathcal{L}_2$-gain robuste de γ s'il est robustement stable et si γ est le plus petit scalaire tel que, pour tout $\Delta \in \mathbf{\Delta}$, $\Delta \star G$ satisfait la condition (F.1).*

F.4 Analyse des systèmes LFT

Étant donné que les gyroscopes MEMS sont des systèmes contenant un nombre important d'éléments incertains et temps-variants, et étant donné que nous visons à valider différents critères de performance, la flexibilité et l'efficacité du cadre IQC le rendent adapté à la poursuite de nos objectifs, il sera donc l'approche principale utilisée dans ce mémoire.

F.4.1 Approche des contraintes quadratiques intégrales (IQC)

L'approche IQC proposée par Megretski et Rantzer dans [MR97] permet d'étudier la stabilité et la performance d'une large classe de systèmes incertains, temps-variants et non linéaires sous une représentation LFT. Nous considérons ici les systèmes décrits par l'interconnexion définie dans (F.4), avec G étant un système LTI, et $\Delta \in \mathbf{\Delta}$ le bloc contenant les incertitudes et les éléments temps-variants. L'idée sous-jacente est de caractériser les principales propriétés de l'ensemble d'incertitudes $\mathbf{\Delta}$ aussi précisément que possible. Pour cela, nous considérons le mapping $p = \Delta(q)$ et nous contraignons les relations entrée-sortie de Δ à travers une IQC. Énonçons la définition d'une IQC.

Definition F.7 (Contrainte quadratique intégrale)**.** *Soit* $\Pi : j\mathbb{R} \to \mathbb{C}^{(n_q+n_p)\times(n_q+n_p)}$ *un opérateur affine, hermitienne et borné. Alors, on dit que* Δ *satisfait le IQC défini par* Π *(*$\Delta \in IQC(\Pi)$*) si, pour tout* $q \in \mathcal{L}_2^{n_q}$*,*

$$\int_{-\infty}^{\infty} \begin{bmatrix} \widehat{q}(j\omega) \\ \widehat{p}(j\omega) \end{bmatrix}^* \underbrace{\begin{bmatrix} \Pi_{11}(j\omega) & \Pi_{12}(j\omega) \\ \Pi_{12}(j\omega)^* & \Pi_{22}(j\omega) \end{bmatrix}}_{\Pi(j\omega)} \begin{bmatrix} \widehat{q}(j\omega) \\ \widehat{p}(j\omega) \end{bmatrix} d\omega \geq 0. \tag{F.7}$$

avec $\widehat{p}(j\omega)$ *et* $\widehat{q}(j\omega)$ *les transformées de Fourier de respectivement* p *et* q*, et* $p = \Delta(q)$*.*

L'opérateur Π définissant l'IQC est généralement connu sous le nom de multiplieur. Pour évaluer la propriété de robustesse, nous devons construire un ensemble de multiplieurs $\mathbf{\Pi}$, définis comme suit.

Definition F.8 (Ensemble de multiplicateurs)**.** *Soit* $\mathbf{\Delta}$ *un ensemble d'opérateurs bornés et causaux. Considérons la Contrainte Quadratique Intégrale donnée par* (F.7)*. Nous définissons alors un ensemble de multiplicateurs* $\mathbf{\Pi}$ *comme suit*

$$\mathbf{\Pi} = \left\{ \; \Pi(j\omega) \;\middle|\; \Delta \in IQC(\Pi) \; \forall \; \Delta \in \mathbf{\Delta} \; \right\} \tag{F.8}$$

Stabilité robuste

Énonçons maintenant une version adaptée du principal théorème de stabilité de l'IQC introduit par Megretski et Rantzer dans [MR97].

Theorem F.1. *Soit* G_{qp} *un système LTI stable, soit* $\mathbf{\Delta}$ *un ensemble d'opérateurs bornés et causaux, et soit* $(G_{qp}, \mathbf{\Delta})$ *défini par* (F.6)*. L'ensemble* $\mathbf{\Pi}$ *est défini par* (F.8)*.*
Supposons que

1. *pour tout* $\tau \in [0,1]$*, pour tout* $\Delta \in \mathbf{\Delta}$*, l'interconnexion* $(G_{qp}, \tau\Delta)$ *est bien posée ;*
2. *pour tout* $\tau \in [0,1]$*, pour tout* $\Delta \in \mathbf{\Delta}$ *et pour tout* $\Pi \in \mathbf{\Pi}$*,* $\tau\Delta \in IQC(\Pi)$ *;*

Alors, l'interconnexion $(G_{qp}, \mathbf{\Delta})$ *est stable de manière robuste s'il existe un* $\Pi \in \mathbf{\Pi}$ *et un* $\epsilon > 0$ *satisfaisant l'inégalité du domaine fréquentiel*

$$\begin{bmatrix} G_{qp}(j\omega) \\ I \end{bmatrix}^* \Pi(j\omega) \begin{bmatrix} G_{qp}(j\omega) \\ I \end{bmatrix} \preceq -\epsilon I \quad \text{pour tout } \omega \in \overline{\mathbb{R}}. \tag{F.9}$$

La démostration est disponible dans le travail original [MR97]. Le choix approprié de l'ensemble $\mathbf{\Pi}$ est un point crucial dans l'analyse de robustesse.

Performance robuste

Pour aborder l'analyse de performance robuste, considérons le système LFT incertain $z = (\mathbf{\Delta} \star G)w$ défini dans (F.3), avec le système nominal G contenant le canal de performance qui à z associe le signal d'entrée w.

Introduisons alors la version adaptée suivante du théorème de performance IQC, ici introduit pour le cas de la performance $\mathcal{L}_2$-gain.

Theorem F.2. *Soit* G *un système LTI stable, soit* $\mathbf{\Delta}$ *un ensemble d'opérateurs bornés et causaux, et soit* $\mathbf{\Delta} \star G$ *défini par* (F.3). *Soit l'ensemble* $\mathbf{\Pi}$ *défini par* (F.8), *et soit*

$$\Pi^{perf} = \begin{bmatrix} I & 0 \\ 0 & -\gamma^2 I \end{bmatrix}.$$

Supposons que

1. *pour tout* $\tau \in [0,1]$, *pour tout* $\Delta \in \mathbf{\Delta}$, $\Delta \star G$ *est bien posé ;*
2. *pour tout* $\tau \in [0,1]$, *pour tout* $\Delta \in \mathbf{\Delta}$ *et pour tout* $\Pi \in \mathbf{\Pi}$, $\tau\Delta \in IQC(\Pi)$ *;*

Alors, $\mathbf{\Delta} \star G$ *est stable de manière robuste et a une performance* $\mathcal{L}_2$*-gain robuste inférieure à* γ *s'il existe* $\Pi \in \mathbf{\Pi}$ *et* $\epsilon > 0$ *satisfaisant l'inégalité du domaine fréquentiel*

$$\begin{bmatrix} G_{qp}(j\omega) & G_{qw}(j\omega) \\ I & 0 \\ G_{zp}(j\omega) & G_{zw}(j\omega) \\ 0 & I \end{bmatrix}^* \begin{bmatrix} \Pi(j\omega) & 0 \\ 0 & \Pi^{perf} \end{bmatrix} \begin{bmatrix} G_{qp}(j\omega) & G_{qw}(j\omega) \\ I & 0 \\ G_{zp}(j\omega) & G_{zw}(j\omega) \\ 0 & I \end{bmatrix} \preceq -\epsilon I \quad \forall\, \omega \in \overline{\mathbb{R}}. \tag{F.10}$$

La démonstration de ce théorème se trouve dans [MR97, VSK16].

F.4.2 Conditions de dimension finie

Malgré l'importance de Theorem F.1 et Theorem F.2 pour tester la stabilité robuste et la performance robuste, telles qu'elles ont été présentées, les conditions de test (F.9) et (F.10) sont des problèmes d'optimisation de dimension infinie. En fait, l'ensemble des multiplicateurs $\mathbf{\Pi}$ qui satisfait l'IQC (F.7) appartient à un espace fonctionnel de dimension infinie. De plus, les conditions (F.9) et (F.10) doivent être satisfaites pour tout $\omega \in \mathbb{R}$, c'est-à-dire que nous devons satisfaire un nombre infini de contraintes. Pour faire face à ce problème, deux approches possibles peuvent être exploitées pour établir des conditions de dimension finie sous la forme de problèmes d'optimisation convexe sous contraintes LMI.

Solution dans l'espace d'état. La solution dans l'espace d'état est l'approche proposée par Megretski et Rantzer dans [MR97]. Pour résoudre le problème, nous devons d'abord contraindre l'ensemble choisi de multiplicateurs $\mathbf{\Pi}$ à un ensemble fini de fonctions rationnelles complexes et propres, c'est-à-dire $\mathbf{\Pi} \in \mathcal{RL}_\infty$. Dans ce mémoire, nous considérons des ensembles de multiplicateurs qui peuvent être paramétrés comme $\mathbf{\Pi} = \{\Pi | \exists M \in \boldsymbol{M}, \Pi = \Psi M \Psi\}$, avec $\boldsymbol{M} \in \mathbb{S}^\bullet$ étant un ensemble de matrices symétriques réelles et $\Psi \in \mathcal{RH}_\infty^{\bullet \times n_p}$ une matrice de fonction de transfert généralement appelée base. En utilisant la paramétrisation introduite, et en considérant $H = \Psi \begin{bmatrix} G \\ I \end{bmatrix}$, nous pouvons exploiter le lemme de Kalman-Yakubovich-Popov (KYP) pour transformer les inégalités du domaine fréquentiel (F.9) et (F.10) en une seule condition LMI impliquant des matrices d'espace d'état qui satisfont (F.9) et (F.10) pour tout $\omega \in \overline{\mathbb{R}}$.

Lemma F.1 (Kalman-Yakubovich-Popov)**.** *Soit $H \in \mathcal{RL}_\infty^{\bullet \times \bullet}$ ayant la réalisation minimale de l'espace d'état (A,B,C,D) avec $A \in \mathbb{R}^{n_h \times n_h}$, et soit $M \in \mathbb{S}^\bullet$. Alors, les deux affirmations suivantes sont équivalentes*

1. *$H(j\omega)^* M H(j\omega) \prec 0 \; \forall \omega \in \overline{\mathbb{R}}$.*
2. *Il existe une matrice $P \in \mathbb{S}^{n_h \times n_h}$ telle que*

$$\begin{bmatrix} I & 0 \\ A & B \\ C & D \end{bmatrix}^T \begin{bmatrix} 0 & P & 0 \\ P & 0 & 0 \\ 0 & 0 & M \end{bmatrix} \begin{bmatrix} I & 0 \\ A & B \\ C & D \end{bmatrix} \prec 0. \tag{F.11}$$

Compte tenu des résultats précédents, énonçons alors le corollaire suivant concernant l'analyse de stabilité.

Corollary F.1. *Soit G_{qp} un système LTI stable, soit $\mathbf{\Delta}$ un ensemble d'opérateurs bornés et causaux, soit $(G_{qp}, \mathbf{\Delta})$ défini par (F.6). Soit $\boldsymbol{M} \subset \mathbb{S}^\bullet$ and soit $\mathbf{\Pi} = \{\Pi | \forall \Delta \in \mathbf{\Delta} \; \Delta \in IQC(\Pi) \exists M \in \boldsymbol{M}, \Pi = \Psi M \Psi\}$ avec $\Psi \in \mathcal{RH}_\infty$, et soit $\Psi \begin{bmatrix} G_{qp} \\ I \end{bmatrix}$ ayant la réalisation minimale de l'espace d'état $\begin{bmatrix} A & B \\ C & D \end{bmatrix}$*

Supposons que

1. *pour tout $\tau \in [0,1]$, pour tout $\Delta \in \mathbf{\Delta}$, l'interconnexion $(G_{qp}, \tau\Delta)$ est bien posée ;*
2. *pour tout $\tau \in [0,1]$, pour tout $\Delta \in \mathbf{\Delta}$ et pour tout $\Pi \in \mathbf{\Pi}$, $\tau\Delta \in IQC(\Pi)$;*

Alors, l'interconnexion $(G_{qp}, \mathbf{\Delta})$ est stable de manière robuste s'il existe $M \in \boldsymbol{M}$, $P \in\in \mathbb{S}^\bullet$ et $\epsilon > 0$ satisfaisant

$$\begin{bmatrix} I & 0 \\ A & B \\ C & D \end{bmatrix}^T \begin{bmatrix} 0 & P & 0 \\ P & 0 & 0 \\ 0 & 0 & M \end{bmatrix} \begin{bmatrix} I & 0 \\ A & B \\ C & D \end{bmatrix} \preceq -\epsilon I \tag{F.12}$$

La solution dans l'espace d'état pour le théorème IQC de la performance $\mathcal{L}_2$-gain robuste suit une procédure similaire.

Solution dans le domaine fréquentiel On peut également envisager, avec une certaine prudence, une solution directe dans le domaine fréquentiel. Cette approche s'inspire des résultats classiques du cadre de la μ-analyse [FTD91], où l'indicateur

μ était calculé dans le domaine fréquentiel en considérant un maillage fréquentiel. Tout d'abord, il est nécessaire de définir un ensemble fini de fréquences à tester $\mathbf{\Omega} = \{\omega_1, ..., \omega_i, ..., \omega_n\}$.

Une fois défini $\mathbf{\Omega}$, on teste la Condition (F.9) ou la Condition (F.10) pour le nombre fini de fréquences contenues dans l'ensemble $\mathbf{\Omega}$. En effet, pour une fréquence donnée $\omega \in \mathbf{\Omega}$, les conditions (F.9) et (F.10) deviennent des contraintes LMI complexes qui peuvent être décomposées en conditions LMI réelles et résolues efficacement.

F.5 Systèmes incertains et temps-variants harmoniques

Dans un gyroscope MEMS, le lien entre les signaux modulés internes interagissant avec le résonateur et la sortie du capteur basse fréquence est le processus de démodulation synchrone. Les MEMS peuvent alors être modélisés comme l'interconnexion d'un système linéaire stationnaire et de certains paramètres temps-variants harmoniques (HTV) (paramètres qui varient comme des fonctions sinusoïdales dans le domaine temporel d'une certaine fréquence harmonique), appelés systèmes linéaires temps-variants harmoniques (LHTV). En outre, nous avons mentionné que les capteurs MEMS sont des systèmes qui ont naturellement tendance à être incertains. Nous avons donc besoin d'un cadre compatible à la fois avec les incertitudes et les paramètres HTV.

F.5.1 Description du système

Considérons les systèmes temps-variants harmoniques et incertains qui peuvent être décrits comme des interconnexions de rétroaction incertaines. Pour des raisons de clarté, dans cette section, nous nous concentrons exclusivement sur les systèmes temps-variants harmoniques à phase incertaine. Étant donné que les approches présentées sont basées sur le cadre IQC, l'inclusion d'autres incertitudes peut être facilement réalisée.

Définissons d'abord l'ensemble $\mathbf{\Delta_H^{\omega_0}}$ des opérateurs temps-variants harmoniques.

Étant donné $\omega_0 > 0$,

$$\mathbf{\Delta_H^{\omega_0}} = \left\{ \Delta_H^{\omega_0} : \mathcal{L}_{2e}^{k_\theta} \to \mathcal{L}_{2e}^{k_\theta} \;\middle|\; \exists\, \phi \in [0, 2\pi[, \quad ; \forall t, \quad ; \Delta_H^{\omega_0}(q)(t) = \theta^{\omega_0}(t) q(t) \right\} \tag{F.13}$$

où θ^{ω_0} représente l'opérateur harmonique à étudier. Nous analysons ici deux cas d'opérateurs harmoniques.

1. Paramètre harmonique unique répété

$$\theta^{\omega_0}(t) = \cos(\omega_0 t + \phi) I_{n_q} \tag{F.14}$$

où ϕ est une phase incertaine.

2. Paramètres harmoniques couplés

$$\theta^{\omega_0}(t) = \begin{bmatrix} \cos(\omega_0 t + \phi) I_{n_q} & 0 \\ 0 & \cos(\omega_0 t + \phi + \psi) I_{n_q} \end{bmatrix} \tag{F.15}$$

où ψ est un déphasage connu entre deux paramètres harmoniques, tandis que ϕ est une phase incertaine.

En utilisant les ensembles définis précédemment, nous pouvons donner une définition formelle d'un système incertain et temps-variant harmonique

Definition F.9 (Système incertain et temps-variant harmonique)**.** *Soit $G_{qp} \in \mathcal{RH}_\infty^{(n_p)\times(n_q)}$ un système LTI stable, et soit $\boldsymbol{\Delta_H^{\omega_0}}$ l'ensemble défini par (F.13). Un système incertain et temps-variant harmonique est défini comme suit :*

$$\exists\, \Delta_H^{\omega_0} \in \boldsymbol{\Delta_H^{\omega_0}},\ \ (G_{qp}, \boldsymbol{\Delta_H^{\omega_0}}) = \left\{ \begin{array}{ll} q & = G_{qp}(s)p + q_{in} \\ p & = \Delta_H^{\omega_0}(q) + p_{in}. \end{array} \right. \tag{F.16}$$

Dans les sous-sections suivantes, nous présentons les multiplicateurs IQC du domaine fréquentiel, ainsi que les méthodes de solution, pour les cas susmentionnés de systèmes incertains et temps-variants harmoniques.

F.5.2 Multiplicateur IQC pour un paramètre HTV répété

Commençons par le système temps-variant harmonique le plus simple, contenant un seul paramètre harmonique répété, donné par l'ensemble (F.13) avec $\theta^{\omega_0}(t)$ défini par (F.14). Observons d'abord les ensembles incertains pour lesquels des multiplicateurs ont déjà été obtenus. Nous pouvons considérer l'ensemble des paramètres incertains répétés définis comme $\boldsymbol{\Delta_{TI}} = \{\delta I_{n_q} | \delta \in \mathbb{R},\ |\delta| \leq 1\}$, et l'ensemble des paramètres temps-variants arbitrairement rapides $\boldsymbol{\Delta_{TV}} = \{\delta I_{n_q} | \delta : \mathbb{R} \to \mathbb{R}, |\delta(t)| \leq 1\}$. Une première observation évidente est que $\boldsymbol{\Delta_\theta^{\omega_0}} \subset \boldsymbol{\Delta_{TV}}$. En outre, notez que si nous fixons la fréquence d'oscillation ω_0 à zéro, alors $\theta^{\omega_0}(t) = \theta^0(t) = \cos(\phi)$ avec $\phi \in [0, 2\pi[$, c'est-à-dire un paramètre incertain borné par un. Par conséquent, $\boldsymbol{\Delta_{TI}} = \boldsymbol{\Delta_\theta^0} \subset \boldsymbol{\Delta_{TV}}$. Par conséquent, l'ensemble des multiplicateurs $\boldsymbol{\Pi_{TV}}$, défini par

$$\boldsymbol{\Pi_{TV}} = \left\{ \Pi_{TV} \;\middle|\; \begin{array}{c} \exists\, X_D \ /\ X_D = X_D^T \succ 0, \\ \\ \exists\, X_G \ /\ X_G = -X_G^T, \\ \\ \Pi_{TV} = \left[\begin{array}{cc} X_D & X_G \\ X_G^T & -X_D \end{array} \right] \end{array} \right\} \tag{F.17}$$

satisfait à $\delta \in IQC(\boldsymbol{\Pi_{TV}}\ \ \forall \delta \in \boldsymbol{\Delta_{TV}},\ \ \forall \Pi_{TV} \in \boldsymbol{\Pi_{TV}}$. Cet ensemble satisfait également $\theta^{\omega_0} \in IQC(\Pi_{TV})\ \forall \theta^{\omega_0} \in \boldsymbol{\Delta_H^{\omega_0}},\ \forall \Pi_{TV} \in \boldsymbol{\Pi_{TV}}$ avec θ^{ω_0} donné par (F.14). Cet ensemble de multiplicateurs constants (indépendants de la fréquence) peut alors être utilisé pour tester la stabilité robuste des systèmes LHTV avec un paramètre HTV répété. Cependant, ce choix peut être trop restrictif. Maintenant, il existe l'ensemble $\boldsymbol{\Pi_{TI}}$:

$$\boldsymbol{\Pi_{TI}} = \left\{ \Pi_{TI}(j\omega) \;\middle|\; \begin{array}{c} \exists\, X_D(j\omega) \ /\ X_D(j\omega) = X_D(j\omega)^* \succ 0, \\ \\ \exists\, X_G(j\omega) \ /\ X_G(j\omega) = -X_G(j\omega)^*, \\ \\ \Pi_{TI}(j\omega) = \left[\begin{array}{cc} X_D(j\omega) & X_G(j\omega) \\ X_G(j\omega)^* & -X_D(j\omega) \end{array} \right] \end{array} \right\}. \tag{F.18}$$

$\boldsymbol{\Pi_{TI}}$ est un ensemble dépendant de la fréquence, alors un ensemble plus large incluant $\boldsymbol{\Pi_{TV}}$, c'est-à-dire $\boldsymbol{\Pi_{TV}} \in \boldsymbol{\Pi_{TI}}$, ce qui peut réduire radicalement le conservatisme. Dans le cas des paramètres HTV, cependant, l'ensemble $\boldsymbol{\Pi_{TI}}$ ne peut être

utilisé que pour le cas particulier $\omega_0 = 0$. Par conséquent, la question suivante se pose : est-il possible de trouver un ensemble de multiplicateurs dépendant de la fréquence qui satisfasse une IQC pour un paramètre HTV répété ? En prenant la forme exponentielle complexe $\cos(\omega_0 t) = \frac{1}{2}(e^{j\omega_0 t} + e^{-j\omega_0 t})$, nous trouverons $e^{j\omega_0 t} I$ au lieu de δI trouvé pour les incertitudes paramétriques. Ceci nous amène à la propriété de modulation, qui est donnée par le produit d'un signal, dans le domaine temporel, par l'opérateur de modulation $e^{j\omega_0 t}$. Énonçons alors le lemme suivant concernant la modulation des signaux et des systèmes.

Lemma F.2 (Modulation)**.** *Soit $T(s)$ un système LTI stable, avec un signal d'entrée $q \in \mathcal{L}_2^\bullet$ et un signal de sortie donné, dans le domaine fréquentiel, par $\widehat{p}(j\omega) = T(j\omega)\widehat{q}(j\omega)$. Ensuite, l'application de l'opérateur de modulation $e^{j\omega_0 t}$ à la sortie, donne le signal $\tilde{p}(t) = e^{j\omega_0 t} T(q(\cdot))(t)$ dans le domaine temporel, et produit la réponse en fréquence modulée*

$$\widehat{\tilde{p}}(j\omega) = T(j(\omega - \omega_0))\widehat{q}(j(\omega - \omega_0)). \tag{F.19}$$

En exploitant ce lemme, nous pouvons maintenant énoncer le théorème suivant qui introduit une nouvelle classe de multiplicateurs qui satisfont l'IQC (F.7) pour le cas d'un paramètre HTV répété.

Theorem F.3. *Soit l'ensemble $\mathbf{\Delta}_H^{\omega_0}$, défini dans (F.13) avec $\theta^{\omega_0}(t)$ donné par (F.14). Ensuite, l'IQC (F.7) est satisfaite avec Π appartenant à l'ensemble des multiplicateurs*

$$\mathbf{\Pi}_{\boldsymbol{\theta}}^{\boldsymbol{\omega_0}} = \left\{ \Pi \;\middle|\; \begin{array}{c} \exists\, X_D(j\omega) \;/\; X_D(j\omega) = X_D(j\omega)^* \succ 0, \\ \\ \exists\, X_G(j\omega) \;/\; X_G(j\omega) = -X_G(j\omega + j\omega_0)^*, \\ \\ \Pi = \begin{bmatrix} X_{D+}(j\omega) + X_{D-}(j\omega) & X_G(j\omega) \\ X_G(j\omega)^* & -2X_D(j\omega) \end{bmatrix} \\ \\ X_{D+} = X_D(j(\omega + \omega_0)) \\ X_{D-} = X_D(j(\omega - \omega_0)) \end{array} \right\} \tag{F.20}$$

La démonstration complète se trouve dans chapter 3.

Avec l'ensemble des multiplicateurs donnés par (F.20), nous pouvons énoncer des conditions de stabilité IQC pour les système LHTV avec un paramètre HTV répété.

Theorem F.4. *Soit G_{qp} un système LTI stable, soit $\mathbf{\Delta}_H^{\omega_0}$ l'ensemble défini par (3.27), avec θ^{ω_0} donné par (3.28). Soit l'ensemble des multiplicateurs $\mathbf{\Pi}_{\boldsymbol{\theta}}^{\boldsymbol{\omega_0}}$ donné par (F.20). Alors, l'interconnexion $(G_{qp}, \mathbf{\Delta}_H^{\omega_0})$ est stable de manière robuste s'il existe $\Pi \in \mathbf{\Pi}_{\boldsymbol{\theta}}^{\boldsymbol{\omega_0}}$ et $\epsilon > 0$ satisfaisant, $\forall\, \omega \in \overline{\mathbb{R}}$,*

$$\begin{bmatrix} G_{qp}(j\omega) \\ I \end{bmatrix}^* \begin{bmatrix} X_D(j(\omega - \omega_0)) + X_D(j(\omega + \omega_0)) & X_G(j\omega) \\ X_G(j\omega)^* & -2X_D(j\omega) \end{bmatrix} \begin{bmatrix} G_{qp}(j\omega) \\ I \end{bmatrix} \preceq -\epsilon I \tag{F.21}$$

Comme pour les théorèmes de subsection F.4.1, le test de la condition de stabilité de Theorem F.4 exige de tester la faisabilité du problème sous un nombre infini de contraintes LMI, ce qui peut être transformé en un test qui peut être résolu en utilisant soit des solutions dans l'espace d'état, soit des solutions dans le domaine fréquentiel.

Solution dans le domaine fréquentiel

La solution dans le domaine fréquentiel consiste à échantillonner l'axe des fréquences et à tester la condition (F.9) pour les points de fréquence sélectionnés. Notre procédure est également basée sur cette idée, cependant, elle doit être étendue au cas des systèmes LHTV. Une première difficulté dans le maillage des fréquences est de choisir la fréquence maximale ω_{max} à échantillonner puisque la condition (F.9) implique de tester aussi les fréquences qui tendent vers l'infini. Comme le système nominal G est supposé être LTI et stable, sa fonction de transfert est donc une fonction propre ou strictement propre de s remplacée par $j\omega$, ce qui conduit à deux scénarios possibles.

1. $\overline{\sigma}(G(j\omega)) \to 0$ lorsque $\omega \to \infty$. Alors, la condition (F.9) converge vers la condition $\Pi_{22}(j\omega) \prec 0$, qui est toujours satisfaite pour les multiplicateurs caractérisant des opérateurs bornés.

2. $G(j\omega) \to G_\infty$ lorsque $\omega \to \infty$, avec G_∞ étant une matrice constante. Alors, il existe une fréquence ω_{max} telle que pour toute fréquence $\omega \geq \omega_{max}$ le système nominal tend vers G_∞, ce qui implique de tester les mêmes conditions pour toutes les $\omega \geq \omega_{max}$.

Dans le cas des multiplicateurs harmoniques, nous avons une dépendance à la fréquence harmonique ω_0. Ensuite, nous définissons le pas minimal du maillage ω_u comme une fraction de ω_0 : $\omega_u = \omega_0/N_u$, où N_u est le nombre de points de grille. Nous définissons la fréquence maximale à tester ω_{max} comme une proportion linéaire de ω_0 : $\omega_{max} = N_{max}\omega_0$, avec N_{max} étant un entier positif. Ensuite, la grille de fréquences obtenue constitue l'ensemble fini :

$$\mathbf{\Omega_s} = \{-N_{max}\omega_0, ..., -\omega_u, 0, \omega_u, ..., N_{max}\omega_0\}\,. \tag{F.22}$$

Le test de la condition (F.9) pour chaque fréquence de l'ensemble $\mathbf{\Omega_s}$ générera une contrainte LMI complexe à tester.

Une autre différence par rapport au maillage classique, est que, dans la μ-analyse, les scalings du multiplieur obtenus pour une fréquence spécifique sont indépendants des mêmes scalings à une autre fréquence. Alors que dans le cas de multiplicateurs harmoniques induisant la propriété de modulation, les fonctions $X_D(j\omega)$ et $X_G(j\omega)$ imposent des conditions inter-fréquences. Par exemple, si nous voulons tester la condition (F.9) pour une fréquence particulière $\omega_i \in \mathbf{\Omega_s}$ en utilisant un multiplicateur harmonique, nous devons considérer $G(j\omega_i)$ et construire la fonction complexe $X_D(j\omega_i) = X_{D_i}$, mais aussi $X_D(j(\omega_i + \omega_0)) = X_{D_{i+N_u}}$ et $X_D(j(\omega_i - \omega_0))X_{D_{i-N_u}}$. Ces dernières fonctions seront ensuite utilisées dans la même condition (F.9) mais aux fréquences $\omega_{i+/-N_u}$. De plus, nous devons échantillonner les fréquences positives et négatives étant donné le manque de propriétés lorsque ω est remplacé par $-\omega$.

Les fonctions $X_G(j\omega)$ sont des cas particuliers de fonctions périodiques, dont la périodicité dépend de l'ensemble des multiplicateurs. Pour illustrer leur construction, considérons les multiplicateurs harmoniques pour un seul paramètre harmonique répété. Nous devons définir la fonction $X_G(j\omega_k) = X_{Gk}$ uniquement pour un intervalle $[0, \omega_0[$ puisque $X_G(j\omega) = -X_G(j(\omega + \omega_0))^* = X_G(j(\omega + 2\omega_0))$, voir Fig. F.3.

Enfin, le problème d'analyse globale peut alors être résumé comme suit : tester s'il existe une combinaison de toutes les variables X_{Di} et X_{Gk} satisfaisant simultanément toutes les contraintes LMI générées à chaque fréquence dans $\mathbf{\Omega_s}$. Si toutes les

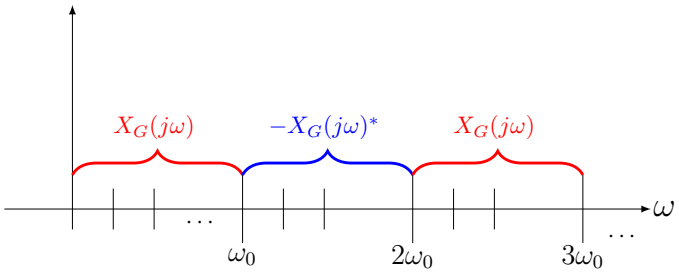

FIGURE F.3: Construction of $X_G(j\omega)$

contraintes sont satisfaites, alors le système est stable de manière robuste par rapport à l'ensemble des fonctions harmoniques.

Solution dans l'espace d'état

Le lemme suivant propose une paramétrisation pour une version partielle des multiplicateurs dans l'ensemble (F.20), c'est-à-dire en considérant $X_G(j\omega) = 0_{n_q \times n_q}$. On définit alors le sous-ensemble $\underline{\boldsymbol{\Pi}}_{\boldsymbol{\theta}} \subset \boldsymbol{\Pi}_{\boldsymbol{\theta}}$.

Lemma F.3. *Soit l'ensemble $\boldsymbol{\Delta}_{\boldsymbol{H}}^{\boldsymbol{\omega_0}}$, défini dans (F.13) avec $\theta^{\omega_0}(t)$ donné par (F.14). Soit $\boldsymbol{M_D} = \{M_D | M_D \in \mathbb{S}^\bullet, \Psi(j\omega)^* M_D \Psi(j\omega) \succ 0 \; \forall \; \omega\}$, et soit la fonction de base Ψ qui appartient à $\mathcal{RH}_\infty^{(v+1)n_q \times n_q}$. Alors, l'IQC (F.7) tient avec Π appartenant au sous-ensemble $\underline{\boldsymbol{\Pi}}_{\boldsymbol{\theta}}$ défini par*

$$\underline{\boldsymbol{\Pi}}_{\boldsymbol{\theta}} = \left\{ \Pi \;\middle|\; \begin{array}{c} \exists\, M_D \in \boldsymbol{M_D}, \\ \Pi(j\omega) = \left[\begin{array}{c} \star \\ \star \\ \star \end{array}\right]^* \left[\begin{array}{cc|c} \frac{1}{2}M_D & 0 & 0 \\ 0 & \frac{1}{2}M_D & 0 \\ \hline 0 & 0 & -2M_D \end{array}\right] \left[\begin{array}{c|c} \Psi_+ + \Psi_- & 0 \\ -j(\Psi_+ - \Psi_-) & 0 \\ \hline 0 & \Psi \end{array}\right], \\ \text{avec } \Psi_+(j\omega) := \Psi(j(\omega+\omega_0)),\ \Psi_-(j\omega) := \Psi(j(\omega-\omega_0)), \end{array} \right\}. \tag{F.23}$$

La démonstration se trouve dans chapter 3.

Afin d'obtenir un test de stabilité efficace en dimension finie grâce au lemme F.1, il est nécessaire de trouver une réalisation appropriée de l'espace d'état pour les éléments de (F.23). Introduisons alors le lemme auxiliaire suivant.

Lemma F.4. *Soit $\Psi \in \mathcal{RH}_\infty^{n_y \times n_u}$ avec la réalisation minimale*

$$\left[\begin{array}{c|c} A_\Psi & B_\Psi \\ \hline C_\Psi & D_\Psi \end{array}\right]$$

où $A_\Psi \in \mathbb{R}^{n \times n}$, $B_\Psi \in \mathbb{R}^{n \times n_u}$, $C_\Psi \in \mathbb{R}^{n_y \times n}$, $D_\Psi \in \mathbb{R}^{n_y \times n_u}$. Alors

$$\left[\begin{array}{c} \Psi(s+j\omega_0) + \Psi(s-j\omega_0) \\ -j(\Psi(s+j\omega_0) - \Psi(s-j\omega_0)) \end{array}\right] \tag{F.24}$$

a la représentation dans l'espace d'état

$$\left[\begin{array}{cc|c} A_\Psi & \omega_0 I & B_\Psi \\ -\omega_0 I & A_\Psi & 0 \\ \hline 2C_\Psi & 0 & 2D_\Psi \\ 0 & 2C_\Psi & 0 \end{array}\right]. \tag{F.25}$$

La démonstration se trouve dans chapter 3.

Compte tenu de la paramétrisation précédente, nous pouvons énoncer la condition de stabilité LMI suivante.

Theorem F.5. *Soit G_{qp} un système LTI stable admettant la réalisation de l'espace d'état (A, B, C, D). Soit $\mathbf{\Delta_H^{\omega_0}}$ l'ensemble défini par (F.13), avec θ^{ω_0} donné par (F.14). Soit l'ensemble de multiplicateurs $\underline{\mathbf{\Pi}}_{\boldsymbol{\theta}}$ donné par (F.23) avec Ψ admettant une réalisation minimale de l'espace d'état $(A_\Psi, B_\Psi, C_\Psi, D_\Psi)$.*

Alors, l'interconnexion $(G_{qp}, \mathbf{\Delta_H^{\omega_0}})$ est stable de manière robuste s'il existe $M_D \in \boldsymbol{M_D}$, $P \in \mathbb{S}^\bullet$ et $\epsilon > 0$ tels que

$$\begin{bmatrix} I & 0 \\ \tilde{A} & \tilde{B} \\ \tilde{C} & \tilde{D} \end{bmatrix}^T \begin{bmatrix} 0 & P & 0 \\ P & 0 & 0 \\ 0 & 0 & \tilde{M}_D \end{bmatrix} \begin{bmatrix} I & 0 \\ \tilde{A} & \tilde{B} \\ \tilde{C} & \tilde{D} \end{bmatrix} \preceq -\epsilon I \tag{F.26}$$

avec $\tilde{M}_D = diag(\frac{1}{2}M_D, \frac{1}{2}M_D, -2M_D)$, et

$$\tilde{A} = \begin{bmatrix} A_\Psi & \omega_0 I & 0 & B_\Psi C \\ -\omega_0 I & A_\Psi & 0 & 0 \\ 0 & 0 & A_\Psi & 0 \\ 0 & 0 & 0 & A \end{bmatrix}, \tilde{B} = \begin{bmatrix} B_\Psi D \\ 0 \\ B_\Psi \\ B \end{bmatrix},$$
$$\tilde{C} = \begin{bmatrix} 2C_\Psi & 0 & 0 & 2D_\Psi C \\ 0 & 2C_\Psi & 0 & 0 \\ 0 & 0 & C_\Psi & 0 \end{bmatrix}, \tilde{D} = \begin{bmatrix} 2D_\Psi D \\ 0 \\ D_\Psi \end{bmatrix}.$$

La démonstration se trouve dans chapter 3.

F.5.3 Multiplieur pour des paramètres harmoniques couplés

Les paramètres harmoniques couplés sont définis par deux paramètres HTV répétés de même fréquence ω_0 mais avec un déphasage particulier ψ entre eux, ce qui inclut le cas des systèmes contenant des modules de démodulation synchrones. Cet opérateur appartient à l'ensemble $\mathbf{\Delta_H^{\omega_0}}$, donné par (F.13), avec $\theta^{\omega_0}(t)$ défini par (F.15). Le multiplicateur (F.20) considère que $\theta(t, \omega_0)$ est borné, ainsi que sa nature harmonique. La question est maintenant de savoir si ce résultat peut être étendu au cas de deux paramètres harmoniques qui sont en quelque sorte couplés, comme c'est le cas des fonctions cosinus et sinus par rapport au déphasage constant entre eux. Le théorème suivant propose une nouvelle classe de multiplicateurs qui sont spécialement dérivés pour les opérateurs temps-variants harmoniques et contenant simultanément des fonctions cosinus et sinus.

Theorem F.6. *Soit l'ensemble* $\mathbf{\Delta_H^{\omega_0}}$*, défini dans* (F.13) *avec* $\theta^{\omega_0}(t)$ *donné par* (F.15)*. Alors, l'IQC* (F.7) *tient avec* Π *appartenant à l'ensemble des multiplicateurs*

$$\mathbf{\Pi_{\theta SD}^{\omega_0}} = \left\{ \Pi \;\middle|\; \begin{array}{c} \exists\, X_D(j\omega) \;/\; X_D(j\omega) = X_D(j\omega)^* \succ 0, \\ \\ \exists\, X_G(j\omega) \;/ \\ X_G(j(\omega+\omega_0)) = -\begin{bmatrix} I & 0 \\ 0 & e^{j\psi} I \end{bmatrix} X_G(j\omega)^* \begin{bmatrix} I & 0 \\ 0 & e^{-j\psi} I \end{bmatrix} \\ \\ \Pi(j\omega) = \begin{bmatrix} \tilde{X}_{D+}(j\omega) + \tilde{X}_{D-}(j\omega) & X_G(j\omega) \\ X_G(j\omega)^* & -2X_D(j\omega) \end{bmatrix}, \\ \\ \textit{with} \\ \\ \tilde{X}_{D+}(j\omega) = \begin{bmatrix} I & 0 \\ 0 & e^{-j\psi} I \end{bmatrix} X_D(j(\omega+\omega_0)) \begin{bmatrix} I & 0 \\ 0 & e^{j\psi} I \end{bmatrix}, \\ \\ \tilde{X}_{D-}(j\omega) = \begin{bmatrix} I & 0 \\ 0 & e^{j\psi} I \end{bmatrix} X_D(j(\omega-\omega_0)) \begin{bmatrix} I & 0 \\ 0 & e^{-j\psi} I \end{bmatrix}, \end{array} \right\}. \quad \text{(F.27)}$$

La démonstration suit une procédure similaire à celle de Theorem F.3, et elle est détaillée dans Appendix A.

Similaire à l'ensemble des multiplicateurs pour un paramètre harmonique unique répété, ce multiplicateur prend en compte les informations sur la fréquence d'oscillation ω_0. De plus, il inclut les matrices de phase $\mathrm{diag}(I, e^{+/-j\psi})$ permettant de vérifier comment le déphasage peut affecter la stabilité du système en boucle fermée. La procédure pour les solutions du domaine fréquentiel et de l'espace d'état sont très similaires à celles d'un paramètre HTV répété, avec la différence de l'inclusion des matrices de phase. Comme les deux procédures sont similaires, la solution dans le domaine fréquentiel n'est pas présentée et la solution dans l'espace d'état peut être trouvée dans chapter 3.

F.6 Conclusion du chapitre

Dans ce chapitre, nous introduisons les concepts nécessaires à l'étude de la stabilité et à la validation des performances des gyroscopes MEMS. Nous présentons la représentation LFT qui est utilisée pour la modélisation des systèmes incertains, suivie par l'introduction des notions de stabilité robuste et de performance robuste. Notre travail se concentre sur l'utilisation du cadre IQC. L'accent a été mis sur les ensembles de multiplieurs IQC pour réduire le conservatisme de l'analyse. Nous discutons de deux approches pour obtenir des conditions de stabilité et de performance traçables : une solution dans le domaine fréquentiel et une solution dans l'espace d'état. Dans la deuxième partie, nous introduisons l'analyse des systèmes incertains à variation temporelle harmonique dans le cadre de l'IQC. Nous y présentons un catalogue de multiplieurs dépendant de la fréquence pour plusieurs types d'éléments HTV. Les multiplieurs dérivés exploitent plus d'informations sur les paramètres harmoniques que tout autre multiplieur existant dans la littérature. Pour compléter ces résultats, nous avons proposé des approches pour les solutions dans le domaine fréquentiel et dans l'espace d'état.

Appendix G

Résumé étendu : Chapitre 4. Analyse du Biais et de la Non-linéarité du Facteur d'Échelle

Dans ce chapitre, nous étudions les spécifications qui sont liées à la précision et à la sensibilité des gyroscopes MEMS. L'objectif principal de ce chapitre est de proposer un ensemble d'outils permettant d'évaluer les différentes spécifications de performance en utilisant une approche basée sur le modèle. Cela nécessite de reformuler les spécifications de performance en tant que critères mathématiques qui sont liés au modèle du système et qui peuvent être analysés formellement. Ceci est fait sous la forme de problèmes d'optimisation robuste.

G.1 Spécifications standard et tests des MEMS

G.1.1 Spécifications de précision

L'entrée du gyroscope est la vitesse angulaire Ω_z et la sortie est la mesure obtenue z. Énonçons ensuite la définition du biais nominal.

Definition G.1 (Biais nominal)**.** *Le biais est la valeur mesurée à la sortie du gyroscope z, à l'état d'équilibre, sans rotation, c'est-à-dire pour $\Omega_z = 0$. La mesure doit être obtenue aux conditions nominales, notamment en ce qui concerne la température.*

$$B(T) = z \qquad for \;\; \Omega_z = 0, \qquad T = T_0$$

où T désigne la température, et T_0 indique la température nominale.

Ensuite, en suivant les spécifications de performance aux conditions nominales, introduisons la non-linéarité du facteur d'échelle (SFNL).

Definition G.2 (Non-linéarité du facteur d'échelle (SFNL))**.** *Soit z la sortie mesurée à l'état d'équilibre pour une vitesse angulaire d'entrée donnée Ω_z. Soit $z^{fit}(\Omega_z)$ la sortie ajustée donnée par* (E.11).

La non-linéarité du facteur d'échelle est alors définie comme l'erreur maximale normalisée, sur tout l'intervalle $[\underline{\Omega}_z, \overline{\Omega}_z]$, entre la sortie mesurée z et la sortie ajustée $z^{fit}(\Omega_z)$, à savoir

$$SFNL(T) = \sup_{\Omega_z \in [\underline{\Omega}_z, \overline{\Omega}_z]} \left(\frac{|z^{fit}(\Omega_z) - z(\Omega_z)|}{SF^{fit}\Omega^{fs}} \right) \;\; for \;\; T = T_0, \tag{G.1}$$

où $\Omega^{fs} = (\overline{\Omega}_z - \underline{\Omega}_z)/2$, T désigne la température, et T_0 indique la température nominale.

La SFNL est alors calculée comme la valeur absolue pire cas de l'erreur de sortie

$$\varepsilon_z = z^{fit}(\Omega_z) - z(\Omega_z),$$

pour toutes les vitesses angulaires d'entrée possibles Ω_z dans l'intervalle $[\underline{\Omega}_z, \overline{\Omega}_z]$.

Spécifications de sensibilité

Les exigences suivantes concernent la sensibilité thermique du gyroscope, qui est une mesure de la dégradation des spécifications de performance lorsque la température varie par rapport à la valeur nominale.

Definition G.3 (Sensibilité thermique du biais)**.** *La sensibilité thermique du biais est le biais maximal sur la plage de température spécifiée, c'est-à-dire*

$$B_{ts} = \max_{T \in [\underline{T}, \overline{T}]} |B(T)|$$

avec

$$B(T) = z(T) \qquad for\ \ \Omega_z = 0,$$

où T désigne la température, tandis que $\underline{T}$ et $\overline{T}$ indiquent les températures minimale et maximale.

Definition G.4 (Sensibilité thermique du facteur d'échelle)**.** *La sensibilité thermique du facteur d'échelle est la SFNL maximale sur la plage de température spécifiée, à savoir*

$$SFNL_{ts} = \sup_{T \in [\underline{T}, \overline{T}]} SFNL(T)$$

avec

$$SFNL(T) = \sup_{\Omega_z \in [\underline{\Omega}_z, \overline{\Omega}_z]} \left(\frac{|z^{fit}(\Omega_z) - z(\Omega_z)|}{SF^{fit} \Omega^{fs}} \right),$$

et $T \in [\underline{T}, \overline{T}]$ désignant la température.

Nous pouvons alors énoncer l'objectif général de ce chapitre.

Sachant les mesures de performance et les conditions de test dans lesquelles elles sont obtenues, comment garantir un certain niveau de performance dans ces conditions en utilisant le modèle du système et certaines informations sur l'incertitude du système.

G.2 Des spécifications standard aux critères d'analyse

L'objectif de cette section est de proposer une méthode basée sur un modèle pour calculer efficacement la SFNL. Selon les protocoles et les conditions de test pour évaluer la SFNL, la sortie du gyroscope z est mesurée pour une vitesse angulaire fixe Ω_z et lorsque l'état d'équilibre est atteint. Dans ce cas, la vitesse angulaire peut être modélisée comme un paramètre du système qui est constant et prend des valeurs dans la plage $[\underline{\Omega}_z, \overline{\Omega}_z]$. Sans perte de généralité, dans ce chapitre, nous considérons une commande directe en boucle fermée LTI. Le modèle dépend du paramètre Ω_z $[\underline{\Omega}_z, \overline{\Omega}_z]$. Alors, le système en boucle fermée H_{Ω_z} est donné par un système LTI avec une entrée harmonique et dont la sortie dépend du paramètre Ω_z. Nous déterminons d'abord comment la sortie du gyroscope z peut être calculée à partir du modèle du système lorsqu'elle est obtenue par démodulation synchrone idéale. Le signal de

consigne étant un signal harmonique $x_r(t) = \sin(\omega_{exc}t)$, l'estimation de la force de Coriolis est donnée par la réponse harmonique du système en boucle fermée H_{Ω_z} :

$$\tilde{f}_c(t) = |H_{\Omega_z}(j\omega_{exc})| \sin(\omega_{exc}t + \arg(H_{\Omega_z}(j\omega_{exc}))),$$

qui est un signal modulé qui peut être décomposé comme suit

$$\tilde{f}_c(t) = z_i(t)\cos(\omega_{exc}t) - z_q(t)\sin(\omega_{exc}t)$$

où $z_i(t)$ et $z_q(t)$ sont respectivement les composantes en phase et en quadrature, données par

$$\begin{cases} z_i(t) &= |H_{\Omega_z}(j\omega_{exc})| \sin(\arg(H_{\Omega_z}(j\omega_{exc})), \\ z_q(t) &= |H_{\Omega_z}(j\omega_{exc})| \cos(\arg(H_{\Omega_z}(j\omega_{exc})) \end{cases}.$$

Ensuite, l'application d'une démodulation synchrone idéale, comme illustré dans Figure G.1, permet d'extraire la composante en phase contenant l'amplitude de la force de Coriolis, la sortie est alors donnée par

$$\begin{aligned} z = z_i &= |H_{\Omega_z}(j\omega_{exc})| \sin(\arg(H_{\Omega_z}(j\omega_{exc}))) \\ &= \Im\{H_{\Omega_z}(j\omega_{exc})\} \end{aligned}$$

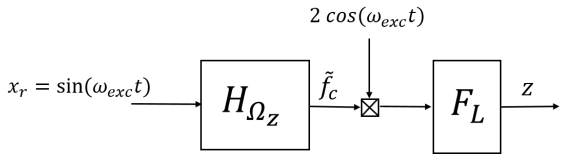

FIGURE G.1: Extraction of the in-phase component

L'étape suivante consiste à dériver un critère mathématique qui exprime explicitement la sortie z en fonction de Ω_z. Puisque le système en boucle fermée H_{Ω_z} dépend linéairement de la vitesse angulaire Ω_z, le système peut alors être reconfiguré pour obtenir le modèle LFT :

$$H_{\Omega_z} = \Omega_z I_2 \star M_H.$$

Nous avons alors $z = \Im\{\Omega_z I_2 \star M_H(j\omega_{exc})\}$. L'extraction de la partie imaginaire d'une interconnexion LFT conduit à une autre interconnexion LFT qui double la taille des répétitions de paramètres (subsection B.1.1). De même, z^{fit} est une fonction qui dépend linéairement de Ω_z. Par conséquent, étant donné que z et z^{fit} peuvent tous deux être obtenus à partir d'interconnexions LFT de Ω_z, l'erreur de sortie $\varepsilon_z(\Omega_z) = z^{fit}(\Omega_z) - z(\Omega_z)$ peut également être obtenue à partir d'une LFT, exprimée ici comme suit :

$$\varepsilon_z = (\Omega_z I_5 \star M_\varepsilon).$$

Enfin, la SFNL basé sur le modèle est donné par la plus grande valeur absolue de l'erreur de sortie ε_z sur l'intervalle $[\underline{\Omega}_z, \overline{\Omega}_z]$ divisé par $(SF^{fit}\ \Omega^{fs})$, c'est-à-dire,

$$SFNL = \sup_{\Omega_z \in [\underline{\Omega}_z, \overline{\Omega}_z]} \left(\frac{|\Omega_z\ I_5 \star M_\varepsilon|}{SF^{fit}\ \Omega^{fs}} \right). \tag{G.2}$$

Un tel cas peut être naturellement traité comme une analyse pire-cas avec un objectif de performance ε_z et dépendant du paramètre Ω_z. Dans la section suivante,

nous proposons une méthode d'analyse basée sur le modèle qui permet de calculer exactement la SFNL à travers un problème d'optimisation LMI.

G.3 Condition LMI de la nonlinearité du facteur d'échelle

Puisque la sortie du gyroscope z et la sortie ajustée z^{fit} peuvent être obtenues à partir d'interconnexions LFT. Ensuite, l'erreur de sortie ε_z peut être calculée à partir d'une LFT écrite comme suit

$$\varepsilon_z = \Omega_z \; I_5 \star \tilde{M}_H = D_\varepsilon + C_\varepsilon \Omega_z (I - A_\varepsilon \Omega_z)^{-1} B_\varepsilon, \tag{G.3}$$

Comme nous l'avons vu précédemment, le SFNL est donné par la plus grande valeur absolue pire-cas de l'erreur de sortie ε_z. Son calcul peut être exprimé comme suit

$$SFNL = \frac{\sqrt{\eta_{SF}}}{SF^{fit}\Omega^{fs}}$$

où η_{SF} est la solution du problème d'optimisation

$$\begin{array}{c} \min\limits_{\eta} \quad \eta \\ \\ \text{such that} \\ \\ \forall \Omega_z \in [\underline{\Omega}_z, \overline{\Omega}_z], \quad \left[\begin{array}{c} \Omega_z I \star \left[\begin{array}{cc} A_\varepsilon & B_\varepsilon \\ C_\varepsilon & D_\varepsilon \end{array} \right] \\ 1 \end{array} \right]^T \left[\begin{array}{cc} I & 0 \\ 0 & -\eta \end{array} \right] \left[\begin{array}{c} \Omega_z I \star \left[\begin{array}{cc} A_\varepsilon & B_\varepsilon \\ C_\varepsilon & D_\varepsilon \end{array} \right] \\ 1 \end{array} \right] \prec 0 \end{array}. \tag{G.4}$$

Il s'agit d'un problème d'optimisation convexe sous contraintes LMI. Malheureusement, le nombre de contraintes LMI est infini, ce qui empêche la résolution du problème. Le théorème suivant permet de montrer que nous pouvons remplacer la condition LMI de dimension infinie (dépendant d'un paramètre dans un ensemble continu) (G.4) par une condition LMI équivalente avec un nombre fini de variables de décision.

Theorem G.1. *Soit $\Omega_z \in [\underline{\Omega}_z, \overline{\Omega}_z]$ et soit l'interconnexion LFT*

$$\Omega_z I_n \star \left[\begin{array}{cc} A_\varepsilon & B_\varepsilon \\ C_\varepsilon & D_\varepsilon \end{array} \right].$$

Soit $\boldsymbol{W}$ l'ensemble

$$\boldsymbol{W} = \left\{ W = W^T \;\middle|\; \begin{array}{c} \exists \;\; X_D \in \mathbb{R}^{n \times n}, \;\; X_D \succ 0, \;\; \exists X_G = -X_G^T \in \mathbb{R}^{n \times n}, \\ \\ W = \left[\begin{array}{cc} -2(\underline{\Omega}_z \overline{\Omega}_z) X_D & (\underline{\Omega}_z + \overline{\Omega}_z) X_D + X_G \\ (\underline{\Omega}_z + \overline{\Omega}_z) X_D + X_G^T & -2 X_D \end{array} \right] \end{array} \right\}. \tag{G.5}$$

Alors, les deux affirmations suivantes sont équivalentes :

1. *la contrainte quadratique*

$$\left[\begin{array}{c} \Omega_z I \star \left[\begin{array}{cc} A_\varepsilon & B_\varepsilon \\ C_\varepsilon & D_\varepsilon \end{array} \right] \\ 1 \end{array} \right]^T \left[\begin{array}{cc} I & 0 \\ 0 & -\eta \end{array} \right] \left[\begin{array}{c} \Omega_z I \star \left[\begin{array}{cc} A_\varepsilon & B_\varepsilon \\ C_\varepsilon & D_\varepsilon \end{array} \right] \\ 1 \end{array} \right] \prec 0 \tag{G.6}$$

   est satisfaite pour tous les $\Omega_z \in [\underline{\Omega}_z, \overline{\Omega}_z]$;

2. *il existe* $W \in \boldsymbol{W}$ *tel que*

$$\begin{bmatrix} C_\varepsilon & D_\varepsilon \\ 0 & 1 \end{bmatrix}^T \begin{bmatrix} I & 0 \\ 0 & -\eta \end{bmatrix} \begin{bmatrix} C_\varepsilon & D_\varepsilon \\ 0 & 1 \end{bmatrix} + \begin{bmatrix} A_\varepsilon & B_\varepsilon \\ I_n & 0 \end{bmatrix}^T W \begin{bmatrix} A_\varepsilon & B_\varepsilon \\ I_n & 0 \end{bmatrix} \prec 0 \quad \text{(G.7)}$$

La démonstration est une application directe du théorème 1.1 de la page 28 et du lemme 1.6 de la page 41 de [Din05], avec de légères adaptations à notre cas particulier.

Par conséquent, le calcul de la SFNL est reformulé comme suit

$$SFNL = \frac{\sqrt{\eta_{SF}}}{SF^{fit}\Omega^{fs}}$$

avec η_{SF} la solution de

$$\min_{\eta} \quad \eta$$

$$\text{such that}$$

$$\begin{cases} \exists\, W \in \boldsymbol{W}, \\ \begin{bmatrix} C_\varepsilon & D_\varepsilon \\ 0 & 1 \end{bmatrix}^T \begin{bmatrix} I & 0 \\ 0 & -\eta \end{bmatrix} \begin{bmatrix} C_\varepsilon & D_\varepsilon \\ 0 & 1 \end{bmatrix} + \begin{bmatrix} A_\varepsilon & B_\varepsilon \\ I_n & 0 \end{bmatrix}^T W \begin{bmatrix} A_\varepsilon & B_\varepsilon \\ I_n & 0 \end{bmatrix} \prec 0 \end{cases}, \quad \text{(G.8)}$$

avec $\boldsymbol{W}$ donnée par (G.5).

Veuillez noter que le biais peut être facilement déterminé comme le cas particulier du calcul de la sortie z pour $\Omega_z = 0$ dans (G.3), ayant directement l'égalité $B = D_\varepsilon - B^{fit}$.

G.4 SFNL pire-cas pour les modèles obtenus par identification en utilisant la méthode des erreurs de prédiction de modèle

Dans le cadre du projet NEXT4MEMS, les modèles de gyroscope MEMS sont obtenus en utilisant des méthodes d'identification de système (basées sur les données). Plus précisément, la modélisation est basée sur le cadre d'erreur de prédiction de modèle [Col20, Lju98]. Ces méthodes délivrent un modèle paramétrique du système $G(z, \theta)$. Cependant, en raison de la présence de bruit, et étant donné que le nombre et la durée des expériences sont finis, les paramètres obtenus ne sont que des estimations des vrais paramètres du modèle. L'ensemble des paramètres identifiés sont regroupés dans le vecteur de paramètres identifiés $\widehat{\theta}$ qui appartient à un ensemble incertain $\boldsymbol{U}$. Introduisons ensuite la définition de la SFNL pire-cas des systèmes incertains.

Definition G.5 (Nonlinearité du facteur d'échelle pire-cas)**.** *Soit le gyroscope MEMS modélisé par un modèle paramétrique dépendant du vecteur paramètre incertain* θ*, qui appartient à l'ensemble* $\boldsymbol{U}$*. Alors, la non-linéarité du facteur d'échelle pire-cas est la SFNL maximale sur toute la région d'incertitude* $\boldsymbol{U}$*, à savoir*

$$SFNL_{wc} = \sup_{\theta \in \boldsymbol{U}} (SFNL(\theta))$$

avec

$$SFNL(\theta) = \max_{\Omega_z \in [\underline{\Omega}_z, \overline{\Omega}_z]} \left(\frac{|z^{fit}(\Omega_z) - z(\Omega_z, \theta)|}{SF^{fit}\Omega^{fs}} \right).$$

L'objectif est alors de déterminer une condition LMI permettant de calculer une borne supérieure du module maximal de l'erreur de sortie ε_z, pour toutes les vitesses angulaires $\Omega_z \in [\underline{\Omega}_z, \overline{\Omega}_z]$ et pour tous les $\theta \in \boldsymbol{U}$.

Par conséquent, ε_z peut être obtenu à partir d'une LFT de la forme :

$$\varepsilon_z = \Delta \star \left[\begin{array}{cc} A_\varepsilon & B_\varepsilon \\ C_\varepsilon & D_\varepsilon \end{array} \right], \tag{G.9}$$

avec Δ appartenant à l'ensemble $\boldsymbol{\Delta}$, donné par

$$\boldsymbol{\Delta} = \left\{ \Delta \;\middle|\; \begin{array}{c} \exists\, \Omega_z \in [\underline{\Omega}_z, \overline{\Omega}_z] \\ \forall i = 1, ...n,\ \exists\, \Delta_i = I_{n_i} \otimes \delta_{\theta i},\ \delta_{\theta i} \in \mathbb{R}^{n_{\theta_i}},\ \delta_{\theta i}^T \delta_{\theta i} \leq 1 \\ \Delta(\theta) = \mathrm{diag}(\Omega_z I, \delta_{\theta 1}, ...\delta_{\theta n}) \end{array} \right\}. \tag{G.10}$$

Ensuite, un problème d'optimisation de dimension finie pour calculer la SFNL du pire-cas peut être dérivé en utilisant un résultat similaire à celui de Theorem G.1, en introduisant cette fois, en plus de l'ensemble $\boldsymbol{W_\Omega}$ de (G.5), un ensemble $\boldsymbol{W_\delta}$ caractérisant les vecteurs incertains, donné par

$$\boldsymbol{W_\delta} = \left\{ W = W^T \;\middle|\; \begin{array}{c} \exists\, X_D \in \mathbb{C}^{n \times n},\ X_D = X_D^*,\ X_D \succ 0 \\ \exists\, X_{Gi} \in \mathbb{C}^{n \times n},\ \forall\, i = \{1, ..., n_\delta\},\ X_{Gi} = -X_{Gi}^* \\ W = \left[\begin{array}{c|c} X_D & \sum_{k=1}^{n_\theta} X_{Gi} \otimes e_k^{n_\theta T} \\ \hline \sum_{k=1}^{n_\theta} X_{Gi}^* \otimes e_k^{n_\theta} & -X_D \bigotimes I_{n_\theta} \end{array} \right] \end{array} \right\}.$$

Cependant, cette fois-ci, la condition obtenue est seulement suffisante. Le résultat est une application du théorème 1.1 de la page 28 et du lemme 1.8 de la page 44 de [Din05], combinée à une version adaptée du lemme 3.1 de [SBBF07].

La borne supérieure sur la SFNL pire-cas peut alors être calculée comme suit :

$$SFNL_{wc} \leq \frac{\sqrt{\eta_{wc}}}{SF^{fit} \Omega^{fs}}$$

avec η_{wc} la solution de

$$\begin{array}{c} \min\limits_{\eta} \quad \eta \\ \text{such that} \\ \left\{ \begin{array}{c} \exists\, W \in \boldsymbol{W}, \\ \left[\begin{array}{cc} C_\varepsilon & D_\varepsilon \\ 0 & 1 \end{array} \right]^T \left[\begin{array}{cc} I & 0 \\ 0 & -\eta \end{array} \right] \left[\begin{array}{cc} C_\varepsilon & D_\varepsilon \\ 0 & 1 \end{array} \right] + \left[\begin{array}{cc} A_\varepsilon & B_\varepsilon \\ I_n & 0 \end{array} \right]^T W \left[\begin{array}{cc} A_\varepsilon & B_\varepsilon \\ I_n & 0 \end{array} \right] \prec 0 \end{array} \right. \end{array}.$$

G.5 Cas d'application : étude de la SFNL expérimentale

Présentons maintenant un cas d'application, où nous appliquons les outils d'analyse proposés dans un contexte qui met en relation les résultats obtenus à partir des différents travaux menés dans le cadre du projet Next4MEMS. Tout d'abord, les modèles sont obtenus à partir de données expérimentales sur un gyroscope MEMS et

en utilisant les méthodes d'identification développées dans le projet. Ensuite, les correcteurs sont synthétisés à partir d'une version simplifiée du modèle en utilisant également les méthodes développées dans ce projet. Les gyroscopes MEMS et les kits de développement qui ont permis l'implémentation des méthodes développées ont été fournis par nos partenaires industriels.

L'objectif de cette section est d'évaluer les performances obtenues avec l'un des correcteurs qui a été testé expérimentalement. L'incertitude des modèles obtenus a été intégrée dans l'analyse afin de déterminer une borne supérieure de la performance pire-cas. Ensuite, ces résultats sont comparés aux résultats observés expérimentalement.

G.5.1 Résultat

Nous intégrons le modèle, le correcteur conçu et les incertitudes dans l'outil d'analyse pour déterminer la limite supérieure de la SFNL pire-cas. Différents tests ont été effectués à des vitesses angulaires d'entrée dans l'intervalle $[-300, 300]^\circ/s$. Les résultats sont présentés en Figure G.2. Les erreurs de mesure sont données en unités de vitesse angulaire ($^\circ/s$). Nous comparons les résultats expérimentaux, les erreurs obtenues par les simulations de Monte Carlo et la borne supérieure de la SFNL pire-cas obtenue en résolvant le problème d'optimisation LMI (G.4).

Commençons par comparer l'erreur pire-cas, obtenue par l'approche de Monte Carlo (200 tests aléatoires) et l'approche LMI. Puisque le calcul de la SFNL pire-cas ne donne qu'une condition suffisante, l'approche LMI permet d'obtenir une borne supérieure sur l'erreur pire-cas, égale à 12.063, alors que l'erreur maximale obtenue par Monte Carlo est égale à 8.391. Cela montre que l'approche LMI offre en fait une borne supérieure à l'erreur pire-cas. En ce qui concerne les résultats expérimentaux, la borne supérieure de l'approche LMI est également validée par rapport au résultat expérimental maximal $(9, 159)$.

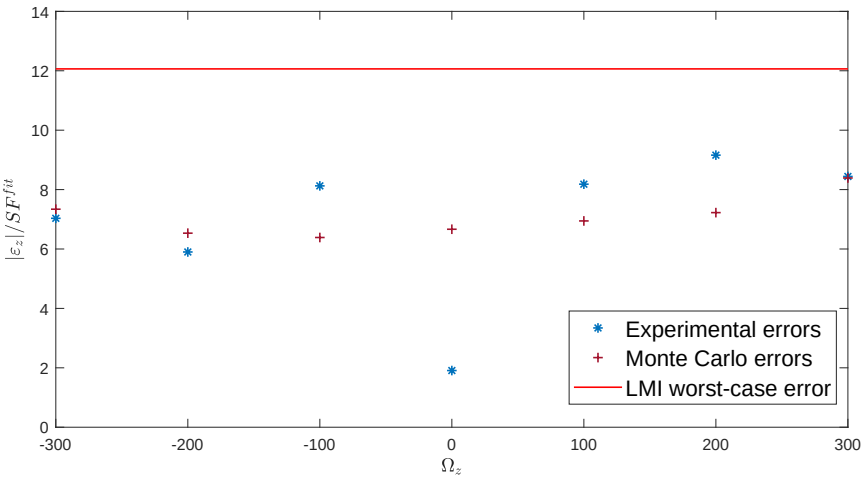

FIGURE G.2: Comparaison des erreurs expérimentales, de Monte Carlo et de LMI pire-cas

G.6 Conclusion du chapitre

Dans ce chapitre, nous abordons l'analyse des spécifications de performance liées aux erreurs de mesure, à savoir le biais et la non-linéarité du facteur d'échelle (SFNL). Nous montrons que le calcul de la SFNL est lié à un problème d'optimisation robuste avec un nombre infini de contraintes LMI. Le problème peut être résolu en remplaçant le problème original par un problème d'optimisation de dimension finie dont les conditions sont suffisantes et nécessaires. Le résultat de la SFNL est ensuite étendu au calcul de la SFNL pire-cas pour les modèles obtenus par identification du système.

Appendix H

Résumé étendu : Chapitre 5. Analyse du Niveau de Bruit de Sortie

Pour mesurer la qualité d'un signal affecté par le bruit, nous pouvons envisager une comparaison entre le signal désiré et le bruit en utilisant le rapport signal sur bruit (SNR), ou en mettant le signal d'intérêt à zéro et en évaluant la puissance du bruit, également connu sous le nom de bruit RMS. Dans les deux cas, il est nécessaire de quantifier la puissance du signal de bruit.

Dans le cas particulier des capteurs MEMS, l'évaluation de la performance du bruit de sortie a été standardisée, en utilisant comme outil principal la méthode de la variance d'Allan. Basé sur l'étude de cette méthode particulière, notre objectif dans ce chapitre est de proposer des outils alternatifs basés sur des modèles pour calculer la variance d'Allan des gyroscopes MEMS.

H.1 Le bruit dans les gyroscopes MEMS et la méthode de la Variance d'Allan

La procédure standard pour évaluer la performance du bruit de sortie des capteurs inertiels MEMS (accéléromètres et gyroscopes) est la méthode de la variance d'Allan. La variance d'Allan a été introduite en 1966 par David W. Allan [All66]. La variance d'Allan est une caractérisation dans le domaine temporel qui permet d'identifier les propriétés d'un signal aléatoire dont le contenu fréquentiel est plus riche que celui qui peut être détecté, par exemple, en utilisant l'identification du bruit efficace.

La variance d'Allan étant une caractéristique d'un signal, la première étape pour appliquer cette méthode aux gyroscopes MEMS consiste à effectuer une longue mesure, généralement de quelques heures, de la sortie bruitée du gyroscope $\Omega(t)$, avec l'entrée mise à zéro (pas de mouvement angulaire). Ensuite, on calcule la variance d'Allan, définie comme suit.

Definition H.1 (Variance d'Allan)**.** *Soit $y(t)$ la réalisation d'un signal aléatoire ergodique. Alors, la variance d'Allan $\sigma_y^2(T)$ est définie comme suit*

$$\sigma_y^2(T) = \frac{1}{2}\left\langle \left(\overline{y}_T(t+T) - \overline{y}_T(t)\right)^2 \right\rangle \tag{H.1}$$

avec $\langle\rangle$ désignant l'opération de moyennage donnée par

$$\langle f(t)\rangle = \lim_{T_e\to\infty} \frac{1}{T_e}\int_{-T_e/2}^{T_e/2} f(t)dt,$$

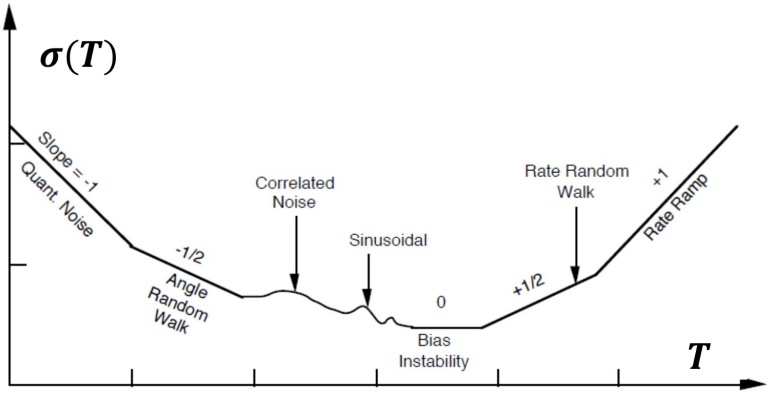

FIGURE H.1: Tracé de l'écart d'Allan (adapté de [IEE06])

et $\overline{y}_T(t)$ *la moyenne locale de* $y(t)$ *sur un intervalle* T*, définie comme suit*

$$\overline{y}_T(t) = \frac{1}{T}\int_t^{t+T} y(\tau)d\tau. \tag{H.2}$$

Enfin, nous obtenons l'écart d'Allan $\sigma_y(T)$ en calculant la racine carrée de la variance d'Allan. Les valeurs sont représentées sur un graphique à échelle semi-logarithmique de l'écart d'Allan en fonction du temps de moyennage local T, qui est affiché sur Figure 5.3.

Dans Figure H.1, nous pouvons observer que le tracé de l'écart d'Allan présente des lignes droites de différentes pentes, chacune d'entre elles caractérisant différentes composantes de fréquence dans la Densité Spectrale de Puissance (DSP) du signal mesuré. Il existe deux principaux types de bruit qui présentent un intérêt pour les normes des gyroscopes MEMS. Premièrement, dans le Figure H.1, nous pouvons observer un intervalle où l'écart d'Allan $\sigma_y(T)$ a un comportement linéaire avec une pente de -1/2. Cela indique la présence d'une composante de bruit blanc dans la sortie du capteur et est généralement appelé *Angle Random Walk* dans la communauté MEMS. Deuxièmement, l'*instabilité du biais* est défini comme le point le plus bas du tracé de l'écart d'Allan, qui peut parfois apparaître comme une ligne de pente nulle. L'instabilité du biais peut être causée par un bruit de scintillement (bruit $1/f$) ou par des changements lents du biais sur des mesures de longue durée.

Notre objectif dans ce chapitre est donc de proposer une approche complémentaire qui, au lieu de calculer la variance d'Allan à partir d'une mesure expérimentale, permet d'estimer le même indicateur de performance en utilisant une approche basée sur le concept de filtre générateur, appelée ci-après estimation de la variance d'Allan basée sur le modèle. Pour ce faire, nous allons d'abord établir formellement la relation entre l'indicateur de performance (variance d'Allan) et les caractéristiques du signal à évaluer. Ensuite, nous déterminons comment calculer la variance d'Allan en utilisant une approche par filtre générateur : pour le cas nominal et pour le cas incertain. Enfin, on étend le résultat en incluant la démodulation synchrone.

H.2 Variance d'Allan dans le domaine fréquentiel

Afin de fournir une estimation de mesure équivalente, la première étape consiste à comprendre quelles sont les propriétés d'un signal bruité que la variance d'Allan décrit. À cette fin, nous présentons ci-dessous un résultat qui relie la densité spectrale de puissance du signal d'intérêt à sa variance d'Allan : [BCC+71, Hou04].

Theorem H.1. *Soit y un signal aléatoire stationnaire et ergodique dont la densité spectrale de puissance est S_y. Alors, la variance d'Allan $\sigma_y^2(T)$ est donnée par*

$$\sigma_y^2(T) = \int_{-\infty}^{+\infty} |H_{All_T}(\nu)|^2 S_y(\nu) d\nu \tag{H.3}$$

avec

$$H_{All_T}(\nu) = \sqrt{2}\frac{\sin^2(\pi T\nu)}{\pi T\nu}. \tag{H.4}$$

La démonstration se trouve dans le chapter 5.

H.3 Variance d'Allan basée sur le modèle LTI

Afin de calculer la variance d'Allan basée sur modèle, nous proposons une approche par filtre générateur. Cette approche consiste à modéliser les principales caractéristiques d'un signal donné comme la sortie du modèle d'un système (ou filtre générateur) qui est excité par un signal d'entrée bien connu (bruit blanc, impulsion de Dirac). Dans ce cas, nous avons besoin d'un cadre qui permette de modéliser les signaux aléatoires : on utilise alors une entrée du type bruit blanc. Le bruit blanc est caractérisé par une DSP constante, c'est-à-dire que pour un bruit blanc d'entrée w, on a $S_w(\nu) = \sigma_w^2$. Ensuite, la DSP $S_n(\nu)$ des bruits corrélés n peut être modélisée avec précision en introduisant des filtres fictifs tels que $S_n(\nu) = |N_n(\nu)|^2\sigma_w^2$, qui sont généralement intégrés dans le modèle du système. Ainsi, comme illustré dans Figure H.2, il est possible de construire un système étendu G_e qui contient à la fois les modèles du système et du bruit qui, excités par un vecteur de bruit blanc w, génèrent le signal de sortie à évaluer. Ensuite, en appliquant le filtre d'Allan à la sortie, on a

$$d_T = H_{All_T}(s)G_e(s)w. \tag{H.5}$$

Pour être cohérent avec l'application au gyroscope MEMS, supposons que ce modèle est un système MISO (Multi-Input Single-Output).

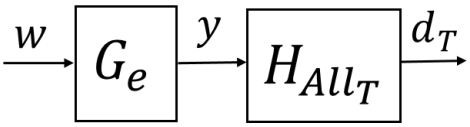

FIGURE H.2: Système étendu G_e

Disposant d'un modèle de système pour caractériser le signal de sortie bruité, nous devons déterminer une mesure de performance (basée modèle) appropriée pour estimer la variance d'Allan. Un tel résultat est présenté dans la sous-section suivante.

H.3.1 La variance d'Allan et la performance $\mathcal{H}_2$ des systèmes.

Dans cette section, nous présentons comment, en utilisant une approche de filtre générateur pour modéliser un signal bruité y, nous pouvons calculer la variance d'Allan de ce signal en utilisant les propriétés du modèle du système et du signal d'entrée. Introduisons le théorème suivant qui établit une relation entre la variance d'Allan d'un signal de sortie aléatoire et la norme $\mathcal{H}_2$ du système MISO, excité par un bruit blanc, qui génère un tel signal.

Theorem H.2. *Soit $G_e(s)$ un système de convolution MISO, $G_e(s) = \begin{bmatrix} G_{e_1}(s) & \cdots & G_{e_{n_w}}(s) \end{bmatrix}$, et soit l'entrée du système w un vecteur de bruit blanc normalisé avec une matrice de spectre $\Phi(\nu) = \sigma_w^2 I_{n_w}$. Alors, avec $y = G_e(s)w$, la variance d'Allan $\sigma_{G_e w}(T)$ de y est donnée par*

$$\sigma_{G_e w}(T) = \sigma_w^2 \|H_{All_T} G_e\|_2^2$$

avec $\|H_{All_T} G_e\|_2^2$ le carré de la norme $\mathcal{H}_2$ de $H_{All_T}(s)G_e(s)$, écrite comme suit

$$\|H_{All_T} G_e\|_2^2 = \frac{1}{2\pi} \int_{-\infty}^{+\infty} |H_{All_T}(j\omega)|^2 \left(|G_{e_1}(j\omega)|^2 + |G_{e_2}(j\omega)|^2 + ... + |G_{e_{n_w}}(j\omega)|^2 \right) d\omega. \tag{H.6}$$

La démonstration se trouve au chapter 5.

En outre, en supposant que le système $H_{All_T} G_e$ admet une représentation d'état (A, B, C, D), nous pouvons énoncer le théorème suivant adapté du résultat classique pour calculer la norme $\mathcal{H}_2$ des systèmes LTI [ZD98].

Theorem H.3. *Soit G_e un système LTI MISO, soit le système $H_{All_T} G_e$ qui admet la représentation de d'état (A, B, C, D) avec $D = 0$, et que l'entrée du système w soit un vecteur de signaux de bruit blanc normalisé avec une matrice de spectre $\Phi(\nu) = \sigma_w^2 I_{n_w}$. Alors, avec $y = G_e(s)w$, la variance d'Allan $\sigma_{G_e w}(T)$ de y est donnée par*

$$\sigma_{G_e w}^2(T) = \sigma_w^2 Tr\left(B^T G_O B\right) \tag{H.7}$$

où Tr désigne la trace d'une matrice et G_O est une solution de l'équation

$$A^T G_O + G_O A + C^T C = 0.$$

La démonstration se trouve au chapter 5.

Le filtre d'Allan, dont la réponse en fréquence $H_{All_T}(\nu)$ est définie dans (H.4), est donnée par une fonction de transfert non rationnelle, elle n'admet donc pas de représentation d'état (A, B, C, D), ce qui ne permet pas d'appliquer directement Theorem H.3 pour déterminer la variance d'Allan.

Par conséquent, afin de transformer le calcul de la variance d'Allan en un problème calculable, nous proposons de remplacer le filtre d'Allan par un filtre d'Allan approximé dont la fonction de transfert est rationnelle.

H.4 Variance d'Allan des signaux démodulés basée sur un modèle

Le système étudié dans ce mémoire demande de déterminer la variance d'Allan d'un signal provenant d'une opération de démodulation synchrone. Ainsi, ce dernier problème peut être résumé comme suit : étant donné un signal modulé y qui peut être décomposé en ses deux composantes, une composante en phase y_i et une composante en quadrature y_q, comment calculer la variance d'Allan de la composante en phase en utilisant les caractéristiques du modèle du système ? En considérant ce problème comme une extension des précédents, le signal en phase peut être modélisé comme suit

$$y_i = F_L(s) \cos(\omega_0 t) G_e(s) w \tag{H.8}$$

où $G_e(s)$ et w sont respectivement le système étendu et le bruit blanc d'entrée, tandis que $F_L(s)$ est un filtre passe-bas associé à la démodulation synchrone. Nous proposons ensuite deux approches différentes pour effectuer une telle analyse.

1. Une approche IQC utilisant le catalogue de multiplicateurs harmoniques introduit dans Appendix F.

2. Une approche stochastique utilisant les propriétés des signaux aléatoires et modulés afin d'établir un système LTI tel que sa variance d'Allan soit équivalente à la variance d'Allan du système contenant la démodulation synchrone.

H.4.1 Approche 1 : Approche IQC avec multiplieurs harmoniques

L'approche IQC peut être considérée comme une simple extension du théorème IQC pour la performance $\mathcal{H}_2$ combinée avec l'ensemble de multiplieurs pour un paramètre harmonique proposé dans le Appendix F. Introduisons un théorème, utilisant la résolution de l'espace d'état, pour calculer la performance $\mathcal{H}_2$ d'un système temps-variant harmonique.

Theorem H.4 (Borne supérieure de la variance d'Allan pour les systèmes TV harmoniques)**.** *Soit H_T un système LTI stable dont la représentation d'état est la suivante*

$$\left[\begin{array}{c|cc} A & B_p & B_w \\ \hline C_q & D_{qp} & 0 \\ C_z & D_{zp} & 0 \end{array}\right].$$

Soit l'ensemble harmonique $\mathbf{\Delta}_{\boldsymbol{H}}^{\boldsymbol{\omega_0}}$ défini par (3.27), avec θ^{ω_0} donné par (3.28). Soit l'ensemble des multiplieurs $\underline{\mathbf{\Pi}}_{\boldsymbol{\theta}}$ donné par (3.43) avec $\Psi \in \mathcal{RH}_\infty^{\bullet\times\bullet}$ ayant la réalisation minimale d'état $(A_\Psi, B_\Psi, C_\Psi, D_\Psi)$.

Alors, $\mathbf{\Delta}_{\boldsymbol{\theta}}^{\boldsymbol{\omega_0}} \star H_T$ est robustement stable et garantit une norme $\mathcal{H}_2$ inférieure à γ si elle est bien posée et s'il existe $M_D \in \boldsymbol{M_D}$ et $P \in \mathbb{S}^\bullet$ satisfaisant

$$\begin{bmatrix} I & 0 \\ A & B_1 \\ C_1 & D_{11} \\ C_2 & D_{21} \end{bmatrix}^T \begin{bmatrix} 0 & P & 0 & 0 \\ P & 0 & 0 & 0 \\ 0 & 0 & \tilde{M}_D & 0 \\ 0 & 0 & 0 & I \end{bmatrix} \begin{bmatrix} I & 0 \\ A & B_1 \\ C_1 & D_{11} \\ C_2 & D_{21} \end{bmatrix} \prec 0 \tag{H.9}$$

et

$$Tr(B_w P B_w) < \gamma^2 \tag{H.10}$$

avec $\tilde{M}_D = diag(\frac{1}{2}M_D, \frac{1}{2}M_D, -2M_D)$ et

$$A = \begin{bmatrix} A_\Psi & \omega_0 I & 0 & B_\Psi C_q \\ -\omega_0 I & A_\Psi & 0 & 0 \\ 0 & 0 & A_\Psi & 0 \\ 0 & 0 & 0 & A \end{bmatrix}, B_1 = \begin{bmatrix} B_\Psi D_{qp} \\ 0 \\ B_\Psi \\ B_p \end{bmatrix},$$
$$C_1 = \begin{bmatrix} 2C_\Psi & 0 & 0 & 2D_\Psi C_q \\ 0 & 2C_\Psi & 0 & 0 \\ 0 & 0 & C_\Psi & 0 \end{bmatrix}, D_{11} = \begin{bmatrix} 2D_\Psi D_{qp} \\ 0 \\ D_\Psi \end{bmatrix}.,$$
$$C_2 = \begin{bmatrix} 0 & 0 & 0 & C_z \end{bmatrix} \qquad , D_{21} = D_{zp}.$$

De plus, l'entrée étant un vecteur de bruit blanc, nous garantissons une variance d'Allan pire-cas $\sigma_{(\mathbf{\Delta}\star H_T)w}(T)$ bornée par

$$\sigma_{(\mathbf{\Delta}\star H_T)w}(T) \leq \gamma^2 \sigma_w^2.$$

H.4.2 Approche 2 : Système LTI équivalent

Cette deuxième approche exploite les caractéristiques des signaux aléatoires modulés. En effet, les signaux des systèmes MEMS en boucle fermée ont généralement un spectre fortement concentré autour d'une fréquence de résonance ω_0. Ainsi, la sortie du système, avant démodulation, a une DSP qui permet de la modéliser comme un signal aléatoire modulé. La définition des signaux modulés purs est introduite dans subsection E.1.4, où l'hypothèse de signaux modulés purs permet de dériver certains des principaux résultats concernant la démodulation synchrone. Une telle hypothèse est également nécessaire pour modéliser y comme un signal modulé. De plus, dans ce cas, y doit également être supposé être un signal aléatoire stationnaire à sens large (WSS). Adoptons alors une hypothèse adaptée au contexte des signaux aléatoires.

Assumption H.1. *Supposons que la sortie y d'un modèle de système soit un signal modulé aléatoire, défini comme un signal stationnaire au sens large (WSS) dont la densité spectrale de puissance S_y a une largeur de bande limitée $2W$ autour d'une fréquence ω_0, avec $W < \omega_0$,*

$$S_y(\omega) = 0 \quad \forall\, \omega \ \in]-\omega_0 + W, \omega_0 - W[\cup]\omega_0 + W, \infty[\cup]-\infty, -\omega_0 - W[, \tag{H.11}$$

Sous l'hypothèse 5.1, nous pouvons prouver que y peut être exactement décomposé en ses composantes en phase y_i et en quadrature y_q. De plus, l'expression de la densité spectrale de puissance S_y permet dans la suite de reformuler le calcul de la variance d'Allan de y_i comme le calcul de la norme $\mathcal{H}_2$ d'un système LTI fictif. A cette fin, nous devons introduire quelques résultats relatifs aux signaux aléatoires modulés, qui seront utiles pour le théorème final, ce résultat est tiré de [Lat70] (Chapitre 5, page 326), complété par quelques résultats de [Pap83].

Theorem H.5. *Soit y un signal aléatoire modulé à sens large de largeur de bande $2W$ centré à ω_0.*

Alors, il existe des signaux stationnaires à sens large y_i et y_q de largeur de bande $2W$ centrés sur 0 tels que

$$y(t) = y_i(t)\cos(\omega_0 t) + y_q(t)\sin(\omega_0 t).$$

En outre,

- $$\begin{cases} y_i(t) &= y(t)\cos(\omega_0 t) + \check{y}(t)\sin(\omega_0 t) \\ y_q(t) &= y(t)\sin(\omega_0 t) - \check{y}(t)\cos(\omega_0 t) \end{cases}, \tag{H.12}$$

  avec $\check{y}(t) = \frac{1}{\pi t} * y(t)$ étant la transformée de Hilbert de $y(t)$.

- $$S_{y_i}(\omega) = \begin{cases} S_y(\omega + \omega_0) + S_y(\omega - \omega_0) & |\omega| < W \\ 0 & |\omega| \geq W \end{cases} \tag{H.13}$$

Ensuite, selon subsection E.1.4, y_i peut être obtenu en adoptant l'hypothèse E.1 qui considère une démodulation synchrone idéale, c'est-à-dire une multiplication par $2\cos(\omega_0)$ suivie d'un filtre passe-bas idéal de la forme

$$F_L(j\omega) = \text{rect}\left(\frac{\omega}{2W}\right). \tag{H.14}$$

Ensuite, sous les hypothèses précédentes, la variance d'Allan de y_i peut être calculée en utilisant la norme $\mathcal{H}_2$ d'un système LTI, comme l'indique le théorème suivant.

Theorem H.6. *Soit $y = G_e w$, avec w étant un vecteur de signaux de bruit blanc normalisé, et supposons que y satisfait l'hypothèse H.1. Soit y_i la composante en phase de y utilisant la démodulation sous l'hypothèse E.1. La variance d'Allan de la composante en phase y_i est donnée par la formule suivante*

$$\sigma_{y_i}(T) = \sigma_w^2 \| \left(F(s + j\omega_0) + F(s - j\omega_0)\right) G_e(s) \|_2^2 \tag{H.15}$$

avec $F(s) = H_{All_T}(s) F_L(s)$, H_{All_T} donné par (5.4) et $F_L(s)$ donné par (5.37).

De plus, si l'on suppose que $F(s)$ a une représentation de d'état avec des matrices réelles, alors $F^{\omega_0}(s) = (F(s + \omega_0) + F(s - \omega_0))$ en a également une, et nous pouvons énoncer le théorème suivant qui permet de calculer la variance d'Allan de y_i en utilisant la représentation d'état d'un système LTI particulier.

Theorem H.7. *Soit $y = G_e w$, avec w étant un vecteur de bruit blanc normalisé, et supposons que y satisfait l'hypothèse H.1. Soit y_i le signal en phase de y, obtenu par démodulation selon l'hypothèse E.1. Soit G_e un système de convolution MISO admettant la réalisation de l'espace d'état (A_G, B_G, C_G, D_G) avec $D_G = 0$, et soit le système $F = H_{All_T} F_L$ avec la représentation d'état (A_F, B_F, C_F, D_F). Alors, la variance d'Allan de y_i est donnée par*

$$\sigma_{y_i}(T) = \sigma_w^2 Tr\left(B^T G_O B\right) \tag{H.16}$$

où Tr désigne la trace d'une matrice, G_O est une solution de l'équation

$$A^T G_O + G_O A + C^T C = 0$$

and

$$A = \begin{bmatrix} A_F & \omega_0 I & B_F C_G \\ -\omega_0 I & A_F & 0 \\ 0 & 0 & A_G \end{bmatrix}, B = \begin{bmatrix} B_F D_G \\ 0 \\ B_G \end{bmatrix},$$
$$C = \begin{bmatrix} 2C_F & 0 & 2D_F C_G \end{bmatrix}.$$

H.5 Application au gyroscope MEMS

Dans cette dernière section, nous présentons un cas d'application où nous appliquons les outils d'analyse proposés à un gyroscope MEMS testé expérimentalement. En Figure H.3, nous illustrons une représentation schématique du système étendu utilisé pour calculer la variance d'Allan de la sortie du gyroscope z_i. Les principaux éléments du système sont les modèles de bruit N_{in}, le modèle MEMS en boucle fermée G_s, la fonction cosinus représentant l'extraction du signal en phase, le filtre passe-bas de la démodulation F_L et enfin le filtre d'Allan H_{All_T}.

Ensuite, nous comparons la variance d'Allan obtenue par deux approches. Premièrement, nous calculons la variance d'Allan en appliquant directement la définition H.1 sur la sortie mesurée z_i, implémentée en temps discret. Ensuite, nous appliquons Theorem H.7 pour calculer la variance d'Allan basée sur le modèle. Les résultats sont présentés dans Figure H.4, où l'on peut observer une grande similitude sur les deux variances d'Allan calculées. Comme l'approche LTI n'est pas celle du pire-cas, il est possible dans ce cas d'obtenir un résultat qui n'est pas supérieur au résultat expérimental. Les erreurs d'estimation peuvent alors être provoquées par les non-idéalités induisant d'autres processus non-stochastiques (petites dérives de biais), des erreurs de modélisation, l'hypothèse de modulation pure, les filtres non-idéaux, entre autres phénomènes.

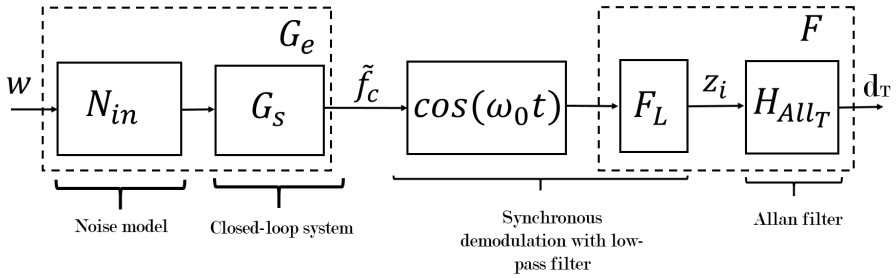

FIGURE H.3: Système équivalent

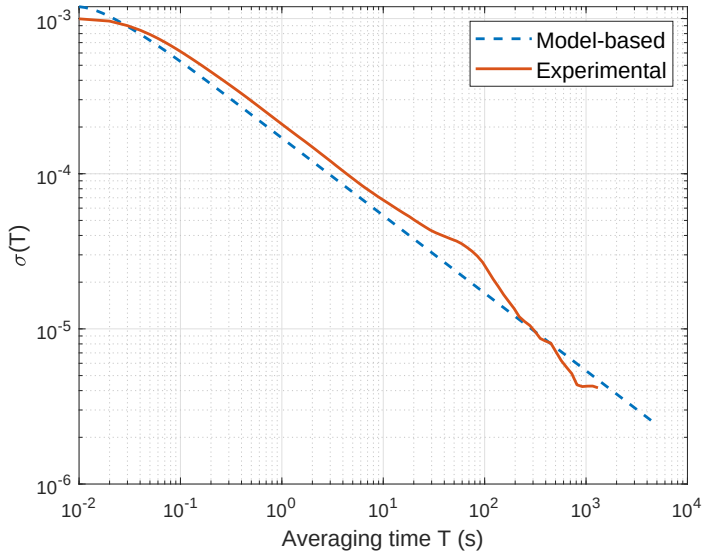

FIGURE H.4: Comparaison des résultats de l'écart d'Allan

H.6 Conclusion du chapitre

Dans ce chapitre, nous abordons l'analyse du bruit de sortie. La méthode standard pour évaluer le bruit dans les gyroscopes MEMS est la méthode de la variance d'Allan. Afin de traduire la méthode de la variance d'Allan en une méthode basée sur un modèle, plusieurs problèmes sont abordés. Tout d'abord, la variance d'Allan peut être interprétée comme le calcul de la puissance de la sortie d'un système filtré par un filtre dit d'Allan. Ensuite, en utilisant la notion de filtre générateur, nous trouvons une relation entre la variance d'Allan du signal de sortie et la performance $\mathcal{H}_2$ du système générateur. Enfin, nous abordons le problème du calcul de la variance d'Allan d'un système contenant une démodulation synchrone.

Appendix I

Résumé étendu : Chapitre 6. Méthodes d'analyse pour des stratégies de commande alternatives

Dans ce dernier chapitre, nous introduisons des techniques d'analyse adaptées à des techniques de commande des gyroscopes MEMS qui vont au delà du cadre de la commande LTI. D'abord, nous traitons le cas de la commande par phaseurs. D'un point de vue du problème d'analyse, dans le cas où la démodulation synchrone est non-idéale, nous sommes naturellement amenés à un problème d'analyse d'un système LHTV (Appendix F). Deuxièment, nous proposons un outil d'analyse pour une commande adaptative dont le correcteur est dépendant de la fréquence de resonance du resonateur MEMS. Ce problème implique l'analyse d'un système incertain qui n'a pas une dépendance rationnelle aux incertitudes.

I.1 Analyse de stabilité d'une commande basée-phaseurs avec démodulation non-idéale

L'objectif de la commande basée sur les phaseurs est que, étant donné un procédé LTI, le correcteur permette de suivre les signaux de consigne et de rejeter les perturbations qui sont des signaux modulés purs au sens de la définition E.1. Commençons par introduire la définition du phaseur associé à un signal modulé.

Definition I.1. *Soit le signal modulé $z(t)$ donné par*

$$z(t) = Z(t)\cos(\omega_{exc}t + \Phi_z(t),$$

où ω_{exc} est la fréquence harmonique, ici supposée constante, tandis que $Z(t)$ et $\Phi_z(t)$ sont respectivement l'amplitude et la phase instantanées du signal modulé. Ensuite, le phaseur associé au signal z est défini comme le couple (Z, ϕ_z) et il est généralement exprimé sous la forme du phaseur complexe :

$$\underline{z}(t) = Z(t)e^{j\Phi_z(t)}$$

.

Soit les modes du résonateur MEMS modélisés comme un système LTI avec une représentation réelle de l'espace d'état

$$G : \begin{cases} \dot{x}(t) = Ax(t) + Bu(t) \\ y(t) = Cx(t) + Du(t) \end{cases}, \tag{I.1}$$

où l'entrée u et la sortie y sont des signaux modulés purs.

La sortie du procédé y, étant un signal modulé, s'écrit comme suit

$$y(t) = Y(t)\cos(\omega_{exc}t + \Phi_y(t),$$

peut être exprimé de manière équivalente comme

$$y(t) = y_R(t)\cos(\omega_{exc}t) - y_I(t)\sin(\omega_{exc}t). \tag{I.2}$$

Ensuite, selon la stratégie de [SSK20], le correcteur basé sur le phaseur est un correcteur LTI qui fonctionne avec la partie réelle et imaginaire du phaseur associé aux signaux modulés. Ce correcteur a la représentation suivante de l'espace d'état :

$$K : \left\{ \begin{array}{ll} \dot{x}_k(t) & = A_k x_k(t) + B_k\, s2p(y(t)) + B_k^r y_r(t) \\ u(t) & = p2s(C_k x_k(t) + D_k s2p(y(t)) + D_k^r y_r(t)) \end{array} \right. , \tag{I.3}$$

où $s2p$ et $p2s$ sont respectivement les transformations du signal en phaseur et du phaseur en signal. Plus précisément, étant donné le signal modulé (I.2), l'opération $s2p$ extrait les parties réelle et imaginaire du phaseur associé, à savoir

$$s2p(y(t)) = \left[\begin{array}{c} y_R(t) \\ y_I(t) \end{array} \right].$$

D'autre part, l'opération $p2s$ construit un signal modulé pur u à partir des parties réelle et imaginaire de son phaseur, soit

$$p2s\left(\left[\begin{array}{c} u_R(t) \\ u_I(t) \end{array} \right] \right) = u_R(t)\cos(\omega_{exc}t) - u_I(t)\sin(\omega_{exc}t).$$

Les transformations $s2p$ et $p2s$ impliquent d'introduire dans la boucle de rétroaction certaines opérations qui ne sont pas LTI. Néanmoins, dans le cas d'un fonctionnement idéal de $s2p$ et $p2s$, la méthode de conception de la commande basée sur les phaseurs qui calcule les matrices de l'espace d'état (A_k, B_k, C_k, D_k) est reformulée comme un problème standard H_∞. La méthode de conception de la commande est basée sur le fait que le procédé G, du point de vue du correcteur, peut être vue comme suit

$$G : \left\{ \begin{array}{ll} \dot{x}(t) & = Ax(t) + B\; p2s\left(\left[\begin{array}{c} u_R(t) \\ u_I(t) \end{array} \right] \right) \\ \left[\begin{array}{c} y_R(t) \\ y_I(t) \end{array} \right] & = s2p\left(Cx(t) + D\; p2s\left(\left[\begin{array}{c} u_R(t) \\ u_I(t) \end{array} \right] \right) \right) \end{array} \right. , \tag{I.4}$$

Ensuite, G peut être réécrit comme un système LTI équivalent G_{cp} dont l'entrée et la sortie sont les parties réelles et imaginaires des signaux modulés [SACKS20]. Ce système a la représentation d'état :

$$G_{cp} : \left\{ \begin{array}{ll} \left[\begin{array}{c} \dot{x}_R(t) \\ \dot{x}_I(t) \end{array} \right] & = \left[\begin{array}{cc} A & \omega_{exc} I \\ -\omega_{exc} I & A \end{array} \right] \left[\begin{array}{c} x_R(t) \\ x_I(t) \end{array} \right] + \left[\begin{array}{cc} B & 0 \\ 0 & B \end{array} \right] \left[\begin{array}{c} u_R(t) \\ u_I(t) \end{array} \right] \\ \left[\begin{array}{c} y_R(t) \\ y_I(t) \end{array} \right] & = \left[\begin{array}{cc} C & 0 \\ 0 & C \end{array} \right] \left[\begin{array}{c} x_R(t) \\ x_I(t) \end{array} \right] + \left[\begin{array}{cc} D & 0 \\ 0 & D \end{array} \right] \left[\begin{array}{c} u_R(t) \\ u_I(t) \end{array} \right] \end{array} \right. . \tag{I.5}$$

En ce qui concerne l'implémentation, la transformation $p2s$ peut être mise en œuvre de manière directe en multipliant respectivement u_R et u_I par des fonctions

cosinus et sinus (modulation). Or, comme indiqué dans subsection E.1.4, l'opération $s2p$ est mise en œuvre en utilisant la démodulation synchrone, où

$$\begin{cases} y_c(t) &= y_R(t) + \underbrace{y_R(t)\cos(2\omega_{exc}t) - y_I(t)\sin(2\omega_{exc}t)}_{\delta_{y_R}} \\ y_s(t) &= y_I(t) \underbrace{-y_R(t)\sin(2\omega_{exc}t) - y_I(t)\cos(2\omega_{exc}t)}_{\delta_{y_I}} \end{cases} \tag{I.6}$$

Le filtre passe-bas de démodulation F_{LP} étant un filtre idéal avec une fréquence de coupure $\omega_c < \omega_0$, nous avons que :

$$\begin{cases} y_c^{LP}(t) &= y_R(t) \\ y_s^{LP}(t) &= y_I(t) \end{cases} . \tag{I.7}$$

Or, si F_{LP} n'est plus un filtre passe-bas idéal, l'égalité (I.7) n'est plus valide. Par conséquent, notre objectif est d'analyser si le système en boucle fermée reste stable lorsque F_{LP} n'est pas un filtre idéal. Notez que les équations (I.6) peuvent être exprimées comme suit :

$$\begin{bmatrix} y_c(t) \\ y_s(t) \end{bmatrix} = \left(I_2 + \underbrace{\begin{bmatrix} \cos(2\omega_{exc}t) & -\sin(2\omega_{exc}t) \\ -\sin(2\omega_{exc}t) & -\cos(2\omega_{exc}t) \end{bmatrix}}_{R(t)} \right) \begin{bmatrix} y_R(t) \\ y_I(t) \end{bmatrix}, \tag{I.8}$$

où $R(t)$ est une fonction harmonique en bloc dont la structure est similaire à une matrice de rotation temps-variant. Puis, avec F_{LP} étant un filtre passe-bas non idéal, les signaux démodulés sont donnés par

$$\begin{bmatrix} \widehat{y}_R(t) \\ \widehat{y}_I(t) \end{bmatrix} = \begin{bmatrix} F_{LP}(y_c)(t) \\ F_{LP}(y_s)(t) \end{bmatrix}. \tag{I.9}$$

Ensuite, la démodulation synchrone non-idéale est, comme illustré dans Figure I.1, modélisée par la transformation idéale $s2p$, suivie d'une interconnexion avec un opérateur de rotation temps-variant $R(t)$ qui représente les composantes restantes à $2\omega_{exc}$, puis suivie du F_{LP}. Les composantes qui sont contenues dans $R(t)$ vont se propager dans la boucle fermée. C'est un phénomène qui ne peut pas être pris en compte dans le processus de conception du correcteur, pourtant il peut avoir un effet sur la stabilité du système.

Maintenant, étant donné que le modèle, le correcteur et les filtres F_{LP} sont tous linéaires, le système de commande du phaseur non idéal peut être modélisé comme un système (LHTV) $(M, R(t))$, défini dans (F.16), où M représente la partie LTI du système en boucle fermée, donnée par

$$M = G_{cp}KF_{LP}(I - G_{cp}KF_{LP})^{-1},$$

tandis que la fonction $R(t)$ est donnée par

$$R(t) = \begin{bmatrix} \cos(2\omega_{exc}t) & -\sin(2\omega_{exc}t) \\ -\sin(2\omega_{exc}t) & -\cos(2\omega_{exc}t) \end{bmatrix}.$$

Ensuite, l'évaluation de la stabilité du système en boucle fermée basé sur les phaseurs avec démodulation synchrone non-idéale peut être considérée comme l'analyse

de stabilité d'un système linéaire temps-variant harmonique (LHTV). Par conséquent, ce problème peut être analysé en utilisant le catalogue de multiplieurs proposé dans Appendix F.

L'interconnexion peut être réarrangée comme le système LHTV équivalent $(\tilde{M}_{SD}, \theta_{SD}^{2\omega_{exc}}(t))$, avec

$$\theta_{SD}^{2\omega_{exc}}(t) = \begin{bmatrix} \cos(2\omega_{exc}t)I_2 & 0 \\ 0 & \sin(2\omega_{exc}t)I_2 \end{bmatrix} q(t).$$

and

$$\tilde{M}_{SD} = \begin{bmatrix} 1 & 0 \\ 0 & 1 \\ 0 & 1 \\ 1 & 0 \end{bmatrix} M \begin{bmatrix} 1 & 0 & -1 & 0 \\ 0 & -1 & 0 & -1 \end{bmatrix}.$$

Cette deuxième représentation permet de tester la stabilité en employant trois ensembles de multiplieurs harmoniques : 1) multiplieurs pour des paramètres HTV répétées simples $\boldsymbol{\Pi}_{\boldsymbol{\theta}}^{\boldsymbol{2\omega_{exc}}}$, donnés par (F.20) ; 2) multiplieurs pour les paramètres HTV couplées $\boldsymbol{\Pi}_{\boldsymbol{\theta SD}}^{\boldsymbol{2\omega_{exc}}}$, (F.27) ; 3) multiplieurs pour les paramètres temps-variant de façon arbitrairement rapide $\boldsymbol{\Pi_{TV}}$, (F.17).

Afin de quantifier le conservatisme des différents ensembles de multiplieurs, nous remplaçons θ^{ω_0} par $\alpha\theta^{\omega_0}$, $\alpha > 0$. Nous évaluons ensuite l'amplitude maximale des oscillations α pour laquelle chaque ensemble de multiplieurs peut assurer la stabilité. Plus la valeur de α est grande, plus le conservatisme observé est faible. Les résultats sont résumés dans le Table I.1. Tout d'abord, l'ensemble de multiplieurs qui conduit aux meilleurs résultats est l'ensemble des paramètres HTV couplées $\boldsymbol{\Pi_{\theta SD}}$, donné par (F.27). En comparant avec les ensembles de multiplieurs pour un paramètre HTV répété $\boldsymbol{\Pi_{\theta}}$, comme prévu, l'ensemble $\boldsymbol{\Pi_{\theta SD}}$ est moins conservateur puisque le premier inclut des informations sur le déphasage entre les oscillations harmoniques. Dans les deux cas, l'inclusion des fonctions non diagonales X_G réduit radicalement le conservatisme, confirmant sa pertinence. À l'autre extrême, l'ensemble de multiplieurs pour des paramètres variant arbitrairement dans le temps $\boldsymbol{\Pi_{TV}}$ est de loin l'ensemble de multiplieurs le plus conservateur, ce qui est attendu étant donné que ces multiplieurs ne dépendent pas de la fréquence.

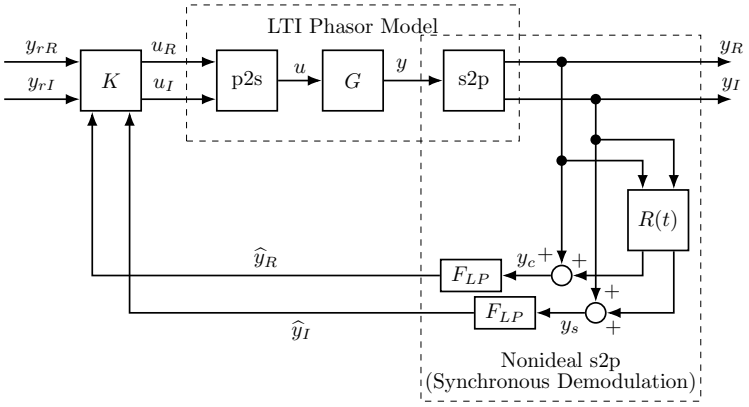

FIGURE I.1: Boucle de commande par phaseurs non-idéale

Ensemble	α max (que avec X_D)	α max (avec X_D et X_G)
$\mathbf{\Pi}_{\theta}^{2\omega_{esx}}$: param. HTV répété	1.1621	3.5156
$\mathbf{\Pi}_{\theta SD}^{2\omega_{exc}}$: HTV couplés	1.1719	4.7656
$\mathbf{\Pi}_{TV}$: arbitrairement TV	0.2891	0.2891
Simulation	≈ 5.1	≈ 5.1

TABLE I.1: Résultats de l'analyse de la commande basée phaseur non-idéale

I.2 Analyse de l'implémentation en temps discret d'un correcteur adaptatif dépendant d'un paramètre

L'objectif général de cette section est de proposer une méthode permettant d'évaluer si une commande en temps discret dépendant d'un paramètre assure la stabilité et la performance de suivi de consigne du système en boucle fermée.

Le mode drive est modélisé par un système à temps discret avec représentation d'état :

$$G_{\omega_0}^d : \begin{cases} x((k+1)T_s) &= e^{\omega_0} e^{AT_s} x(kT_s) + (e^{\omega_0} e^{AT_s} - I)A^{-1}Bu(kT_s) \\ y(kT_s) &= Cx(kT_s) + Du(kT_s) \end{cases}, \tag{I.10}$$

où ω_0 est la fréquence de résonance du mode primaire, T_s la fréquence d'échantillonnage et A, B, C, D les matrices d'état du modèle du mode primaire à temps continu et normalisé, voir [SACKS20]. Étant donné que les variations de la fréquence de résonance sont lentes, ω_0 est supposé être un paramètre incertain time-invariant, c'est-à-dire

$$\omega_0 \in [\underline{\omega}_0, \overline{\omega}_0].$$

Le correcteur dépendant d'un paramètre $K_{\tilde{\omega}_0}^c$ est conçu dans un espace à temps continu, lié à l'espace à temps discret via la transformée bilinéaire. Le correcteur est synthétisé en utilisant un modèle du système fictif simplifié ayant des caractéristiques similaires à celles de $G_{\omega_0}^d$ [SACKS20]. Le correcteur obtenu a la représentation d'état

$$K_{\tilde{\omega}_0}^c : \begin{cases} \dot{x}_K(t) &= g(\tilde{\omega}_0)A_K x_K(t) + g(\tilde{\omega}_0)B_{Kr} y_r(t) + g(\tilde{\omega}_0)B_K y(t) \\ u(t) &= C_K x_K(t) + D_{Kr} y_r(t) + D_K y(t) \end{cases}. \tag{I.11}$$

où $\tilde{\omega}_0$ est la mesure de la fréquence de résonance ω_0 et

$$g(\omega) = \frac{2}{T_s} \tan\left(\frac{\omega T_s}{2}\right).$$

Dans la suite, l'erreur entre la fréquence de résonance mesurée $\tilde{\omega}_0$ et la fréquence de résonance réelle ω_0 est notée ω_m, que l'on suppose appartenir à l'intervalle $[-\overline{\omega}_m, \overline{\omega}_m]$. Le problème d'analyse est alors énoncé comme suit.

Problem I.1. *Soit un système en boucle fermée, constitué de l'interconnexion du correcteur à temps continu $K_{\tilde{\omega}_0}^c$ et du procédé à temps continu $G_{\omega_0}^c$, obtenue en appliquant la transformée bilinéaire à $G_{\omega_0}^d$. Tester si le système en boucle fermée est stable et atteint un certain niveau de performance de poursuite*

$$|T_{y_r \to \varepsilon}^c(j\, g(\omega_0 + \omega_m))| \leq \eta, \tag{I.12}$$

pour tout $\omega_0 \in [\underline{\omega}_0, \overline{\omega}_0]$ *et pour tout* $\omega_m \in [-\overline{\omega}_m, \overline{\omega}_m]$, *avec* $T^c_{y_r \to \varepsilon}$ *désignant la fonction de transfert associant le signal de consigne à l'erreur de poursuite.*

Nous pouvons observer, dans (I.10), que le procédé à temps discret $G^d_{\omega_0}$ a une dépendance linéaire de la fonction exponentielle e^{ω_0}, qui contient le paramètre d'intérêt. De plus, tout système LTI à temps discret peut être exprimé comme l'interconnexion LFT d'une matrice constante et de l'opérateur de retard du domaine Z, ce qui permet de représenter le système sous forme LFT. Ensuite, l'application de la transformée bilinéaire pour passer le système en temps continu revient à remplacer Z par $\frac{1+\frac{sT_s}{2}}{1-\frac{sT_s}{2}}$. On obtient alors le modèle LFT en temps continu donnée par

$$G^c_{\omega_0} = e^{\omega_0} I \star \left(\frac{1 - \frac{sT_s}{2}}{1 + \frac{sT_s}{2}} I \star M^d_G \right) = e^{\omega_0} I \star M^c_G(s), \tag{I.13}$$

Or, l'évaluation de la performance du suivi présente une difficulté. En effet, la condition de performance (I.12) demande à être testée à la fréquence $g(\omega_0 + \omega_m)$, pour tout $\omega_0 \in [\underline{\omega}_0, \overline{\omega}_0]$ et pour tout $\omega_m \in [-\overline{\omega}_m, \overline{\omega}_m]$, ce qui implique un nombre infini de contraintes. Cependant, notez que (I.12) peut être radicalement simplifié en considérant une normalisation de fréquence de $T^c_{y_r \to \varepsilon}$, c'est-à-dire en prenant $\omega_n = \omega / g(\omega_0 + \omega_m)$, obtenant alors la condition de performance de poursuite suivante :

$$|T^c_{(y_r \to \varepsilon)_n}(j \cdot 1)| \leq \eta. \tag{I.14}$$

où $T^c_{(y_r \to \varepsilon)_n}$ désigne la version normalisée du système $T^c_{y_r \to \varepsilon}$.

Par conséquent, le correcteur et le procédé doivent être normalisés. Notez que, puisque le correcteur $K^c_{\omega_0}$ est linéairement paramétré par $g(\omega_0 + \omega_m)$, alors sa version normalisée K^c_n est directement obtenue :

$$K^c_n : \left\{ \begin{array}{rcl} \dot{x}_K(t_n) & = & A_K x_K(t_n) + B_{Kr} y_r(t_n) + B_K y(t_n) \\ u(t_n) & = & C_K x_K(t_n) + D_{Kr} y_r(t_n) + D_K y(t_n) \end{array} \right. . \tag{I.15}$$

D'autre part, la normalisation du procédé à temps continu est une transformation qui implique une dépendance linéaire de la fonction $\frac{1}{g(\omega_0+\omega_m)} I$, le procédé normalisé peut alors être exprimée comme le système LFT

$$G^c_n(s_n) = \text{diag}\left(\frac{1}{g(\omega_0 + \omega_m)} I, e^{\omega_0} I \right) \star M^c_{Gn}(s_n). \tag{I.16}$$

avec

$$M^c_{Gn}(s_n) : \left\{ \begin{bmatrix} \dot{\zeta}(t_n) \\ q_e(t_n) \\ q_g(t_n) \\ y(t_n) \end{bmatrix} = \begin{bmatrix} 0 & 0 & I & 0 \\ e^{AT_s} & -e^{AT_s} & 0 & 2e^{AT_s} A^{-1} B \\ -\frac{2}{T_s} I & \frac{4}{T_s} I & 0 & -\frac{4}{T_s} A^{-1} B \\ C & -C & 0 & CA^{-1}B + D \end{bmatrix} \begin{bmatrix} \zeta(t_n) \\ p_e(t_n) \\ p_g(t_n) \\ u(t_n) \end{bmatrix} \right.$$

Enfin, le système global en boucle fermée $T^c_{(y_r \to \varepsilon)_n}$ peut être représenté comme un système LFT, illustré dans Figure 6.5, donné par :

$$T^c_{(y_r \to \varepsilon)_n}(s_n) = \text{diag}\left(\frac{1}{g(\omega_0 + \omega_m)} I, e^{\omega_0} I \right) \star M_\mu(s_n). \tag{I.17}$$

Ensuite, nous pouvons tester la stabilité robuste des systèmes modélisés comme des interconnexions LFT en utilisant Theorem F.1. Si la stabilité robuste est vérifiée,

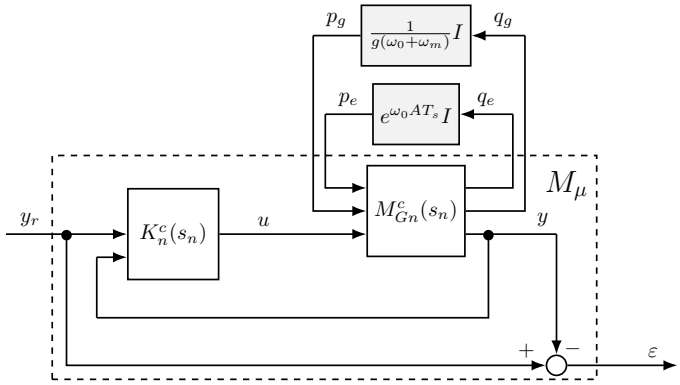

FIGURE I.2: Analysis model in normalized pseudo-continuous time

alors le test de la performance robuste, défini par la contrainte (I.14), est une version particulière de Theorem F.2 qui consiste à tester (F.10) à une seule fréquence échantillonnée $\omega = 1$ rad/s. Cependant, afin d'appliquer Theorem F.1 et la version particulière de Theorem F.2 est possible si la dépendance de la fonction vis-à-vis des paramètres incertains est rationnelle. Cependant, ce n'est pas réellement le cas puisque la dépendance de e^{ω_0} et de $1/g(\omega_0+\omega_m)$ n'est pas rationnelle par rapport à ω_0 et ω_m. Afin d'établir un modèle LFT qui puisse être analysé, nous proposons d'approximer les fonctions non rationnelles e^{ω_0} et $1/g(\omega_0+\omega_m)$ par des fonctions rationnelles des paramètres incertains. L'approche proposée est basée sur une série d'approximations de Taylor. Cependant, toute approximation produit une erreur entre la fonction originale et la fonction approximée. Il est donc important de prendre en compte cette erreur d'approximation afin de ne pas négliger son impact sur la stabilité et les performances du système.

Introduisons le lemme suivant qui permet d'intégrer une fonction non rationnelle d'un paramètre incertain dans une représentation LFT dont le bloc incertain contient le paramètre d'intérêt, ainsi que les erreurs d'approximation sous forme d'incertitudes additionnelles.

Lemma I.1. *Soit une fonction matricielle non rationnelle $F(\theta) \in \mathbb{R}^{n_q \times n_q}$ dépendant d'un paramètre θ, avec θ prenant des valeurs dans un intervalle fini $[\underline{\theta}, \overline{\theta}]$ et avec une valeur nominale $\theta_c = (\overline{\theta}+\underline{\theta})/2$. Si $F(\theta)$ est dérivable $(d+1)$ fois, alors : $\forall\, \theta \in [\underline{\theta}, \overline{\theta}]$, $\exists\, \Delta_{RF} \in \mathbb{R}^{n_q \times n_q}$, $\overline{\sigma}(\Delta_{RF}) \leq R_{maxF}$ tel que $F(\theta) = diag(\delta_\theta I_{(d\times n_q)}, \Delta_{RF}) \star N_F$ avec $\delta_\theta = \theta - \theta_c$,*

$$N_F = \begin{bmatrix} 0 & \dots & 0 & 0 & I_{n_q} \\ I_{(d\times n_q)-1} & & 0 & 0 & 0 \\ 0 & \dots & 0 & 0 & I_{n_q} \\ F_1 & \dots & F_d & I_{n_q} & F_0 \end{bmatrix}, \tag{I.18}$$

$F_0 = F(\theta_c)$, $F_k = \frac{1}{k!}\frac{d^k F}{d\theta^k}(\theta_c)\ \forall\, k \in \{1,\dots,d\}$, *et*

$$R_{maxF} = \frac{D}{(d+1)!}\,(\delta_{max\theta})^{d+1}$$

avec $D \geq \|\frac{d^{(d+1)}F}{d\theta^{(d+1)}}(\theta_\xi)\|\ \forall\, \theta_\xi \in [\underline{\theta}, \overline{\theta}]$, *et* $\delta_{max\theta} = \frac{(\overline{\theta}-\underline{\theta})}{2}$.

La démonstration se trouve au chapter 6.

En utilisant le Lemme I.1, le système original avec dépendance non rationnelle peut être reformulé comme en un système avec dépendance rationnelle. Ce nouveau

système peut alors être exploité pour l'analyse en utilisant les résultats classiques du cadre d'analyse de la robustesse. Introduisons ensuite le théorème suivant qui permet de tester la stabilité et la performance de poursuite données par le transfert $T^c_{(y_r\to\varepsilon)_n}$, impliquant la performance de suivi de $T^c_{y_r\to\varepsilon}$.

Theorem I.1. *Soit le système LFT donné par (I.17). Soit* $\mathbf{\Delta}$ *l'ensemble défini par :*

$$\mathbf{\Delta} = \left\{ \Delta \;\middle|\; \begin{array}{c} \exists\, \delta_{\omega_0} \in [\underline{\omega}_0, \overline{\omega}_0],\ \exists\, \delta_{\omega_m} \in [-\overline{\omega}_m, \overline{\omega}_m], \\ \exists\, \delta_{Rg} \in [-R_{maxg}, R_{maxg}],\ \exists\, \delta_{R_e} \in [-R_{maxe}, R_{maxe}] \\ \\ \Delta = diag(\delta_{\omega_0} I_{(d\times n_{qg})+(d\times n_{qe})}, \delta_{\omega_m} I_{d\times n_{qg}}, \delta_{Rg} I_{n_{qg}}, \delta_{Re} I_{n_{qe}}) \end{array} \right\}. \tag{I.19}$$

Soit N donnée par :

$$\left[\begin{array}{cccccccccccc}
0 & \dots & 0 & 0 & \dots & 0 & 0 & \dots & 0 & 0 & 0 & I_{n_{qg}} & 0 \\
I_{(d\times n_{qg})-1} & & 0 & 0 & \dots & 0 & 0 & \dots & 0 & 0 & 0 & 0 & 0 \\
0 & \dots & 0 & 0 & \dots & 0 & 0 & \dots & 0 & 0 & 0 & 0 & I_{n_{qe}} \\
0 & \dots & 0 & I_{(d\times n_{qe})-1} & & 0 & 0 & \dots & 0 & 0 & 0 & 0 & 0 \\
0 & \dots & 0 & 0 & \dots & 0 & 0 & \dots & 0 & 0 & 0 & I_{n_{qg}} & 0 \\
0 & \dots & 0 & & 0 & & 0 & I_{(d\times n_{qg})-1} & 0 & 0 & 0 & 0 & 0 \\
0 & \dots & 0 & 0 & \dots & 0 & 0 & \dots & 0 & 0 & 0 & I_{n_{qg}} & 0 \\
0 & \dots & 0 & & 0 & & 0 & I_{(d\times n_{qg})-1} & 0 & 0 & 0 & 0 & 0 \\
0 & \dots & 0 & 0 & \dots & 0 & 0 & \dots & 0 & 0 & 0 & I_{n_{qg}} & 0 \\
0 & \dots & 0 & 0 & \dots & 0 & 0 & \dots & 0 & 0 & 0 & 0 & I_{n_{qe}} \\
g_1 I_{n_{qg}} & \dots & g_d I_{n_{qg}} & & 0 & & 0 & g_1 I_{n_{qg}} \dots & g_d I_{n_{qg}} & I_{n_{qg}} & 0 & g_0 I_{n_{qg}} & 0 \\
0 & \dots & 0 & e_1 I_{n_{qe}} & \dots & e_d I_{n_{qe}} & 0 & \dots & 0 & 0 & I_{n_{qe}} & 0 & e_0 I_{n_{qe}}
\end{array}\right], \tag{I.20}$$

dont les paramètres sont données dans le chapter 6, Theorem 6.1.

Alors, si le système LFT $\Delta \star (N \star M_\mu)$ *est stable et garantit*

$$|\Delta \star (N \star M_\mu(j\times 1))| \le \eta, \tag{I.21}$$

pour tout $\Delta \in \mathbf{\Delta}$*, alors,* $T^c_{(y_r\to\varepsilon)_n}$ *et* $T^c_{y_r\to\varepsilon}$ *sont stables et satisfont aux conditions (6.13) et (6.16)* $\forall\ \omega_0 \in [\underline{\omega}_0, \overline{\omega}_0]$ *et* $\forall\ \omega_m \in [-\overline{\omega}_m, \overline{\omega}_m]$.

La démonstration se trouve au chapter 6

La stabilité robuste du système LFT (I.21), pour l'ensemble structuré $\mathbf{\Delta}$ donné par (I.19), peut être testée en utilisant Theorem F.1 et en construisant des multiplieurs dans l'ensemble (F.18) pour les différentes incertitudes paramétriques. Ensuite, si la stabilité robuste est garantie pour tous les $\Delta \in \mathbf{\Delta}$, on peut évaluer la condition de performance robuste, donnée par (I.14), en testant la condition (3.15) de Theorem 3.2, pour $\omega = 1$.

I.3 Conclusion du chapitre

Dans ce chapitre, nous proposons des outils d'analyse pour les stratégies de commande qui induisent intrinsèquement dans le système certaines propriétés allant au-delà d'un système LTI. D'abord, nous étudions stabilité d'une commande basée sur les phaseurs avec démodulation synchrone non-idéale. Ce type de système est un banc d'essai naturel pour l'analyse des systèmes LHTV. Ensuite, nous abordons l'analyse des performances de l'implémentation en temps discret d'un correcteur

dépendant d'un paramètre. Du point de vue de l'analyse, ce problème conduit à l'analyse d'un système incertain qui ne dépend pas rationnellement des incertitudes paramétriques. Pour y faire face, nous proposons une approximation des fonctions non-rationnelles basée sur Taylor.

Appendix J

Résumé étendu : Chapitre 7. Conclusions et perspectives

J.1 Conclusions

L'objectif principal de ce travail est le développement de méthodes efficaces et systématiques pour la validation pré-expérimentale des performances des gyroscopes MEMS. Trois grandes classes de problèmes sont abordées : l'analyse des systèmes LHTV, le calcul basé sur un modèle des principales spécifications de performance des MEMS et la validation des stratégies de commande au-delà du cadre LTI.

Analyse des systèmes LHTV. Nous définissons un système LHTV comme un système linéaire contenant un ou plusieurs paramètres temps-variants harmoniques (HTV). Pour l'analyse, nous adoptons l'approche IQC. Une étape clé consiste à vérifier si tous les éléments de l'ensemble incertain satisfont un IQC défini par un ensemble de multiplieurs. L'ensemble des multiplieurs choisis joue un rôle central dans le conservatisme des résultats de l'analyse. Dans le cas d'un paramètre HTV répété, un multiplieur du domaine fréquentiel a été introduit dans le catalogue des multiplieurs de [MR97]. Nous en déduisons que la construction d'ensembles de multiplieurs pour les paramètres HTV est possible en utilisant une propriété de modulation-commutation. Une contribution majeure de notre travail a consisté à rechercher et construire une fonction hors diagonale harmonique (G scaling) qui réduit significativement le conservatisme de l'analyse. Ce résultat est ensuite étendu au cas des systèmes LHTV contenant plusieurs paramètres HTV qui oscillent à la même fréquence mais avec un déphasage entre eux, couvrant le cas de la démodulation synchrone. L'innovation de cette deuxième classe de multiplieurs est que, en plus de la fréquence et de l'amplitude, elle intègre également l'information sur le déphasage entre les oscillations harmoniques.

Calcul des spécifications de performance basé sur un modèle. La SFNL est définie comme la plus grande erreur de mesure sur toute la gamme des vitesses angulaires d'entrée. Le calcul de la SFNL basé sur le modèle est réduit à un problème d'optimisation robuste. Ensuite, en appliquant les résultats de la commande robuste de [Din05], le calcul basé sur le modèle de la SFNL fournit une condition suffisante et nécessaire, qui est illustrée par un exemple numérique. Les résultats sont ensuite étendus à l'étude de la SFNL pire cas des modèles identifiés. Le calcul basé sur le modèle de la SFNL pire cas d'un modèle identifié a été comparé aux résultats expérimentaux, montrant que le calcul basé sur le modèle permet d'établir une performance pire cas dans un cas d'application réel, avec un léger conservatisme.

La variance d'Allan est la méthode standard pour classifier et quantifier les processus stochastiques du bruit de sortie. Pour dériver des méthodes de calcul de

la variance d'Allan basées sur un modèle, nous adoptons une approche de filtre générateur. Nous abordons d'abord le problème du calcul de la variance d'Allan en considérant que le signal de sortie est généré par un système LTI, montrant que la variance d'Allan peut être reformulée comme la performance $\mathcal{H}_2$ d'un système étendu. Le résultat est ensuite étendu aux gyroscopes MEMS, modélisés comme un système LTI en boucle fermée dont la sortie est ensuite appliquée à un démodulateur synchrone. Pour résoudre ce problème, nous proposons deux approches : une approche basée sur l'IQC et une approche LTI équivalente basée sur l'hypothèse d'un signal modulé aléatoire. Enfin, l'approche LTI équivalente a été testée dans un cas d'application, montrant l'importante précision de la variance d'Allan basée sur le modèle par rapport aux résultats expérimentaux.

Validation des stratégies de commande alternatives. Comme ces classes de stratégies de commande sont conçues en adoptant certaines hypothèses appropriées mais fortes, des outils d'analyse spéciaux ont été développés pour vérifier la stabilité et les performances de ces solutions de commande dans un scénario plus réaliste. Le premier cas concerne l'analyse de stabilité d'une commande à base de phaseurs avec démodulation synchrone non-idéale, qui peut être directement modélisée comme un système LHTV. Ensuite, en utilisant l'ensemble des outils IQC développés pour l'analyse de cette classe de systèmes, nous avons pu vérifier la stabilité de cette stratégie de commande. Le deuxième cas concerne l'implémentation en temps discret d'une stratégie de commande dépendant d'un paramètre, en considérant une estimation non-idéale de la fréquence de résonance. Ce problème nous conduit à l'analyse d'un système incertain avec une dépendance non rationnelle à l'incertitude. Ensuite, en utilisant une approximation de Taylor de la fonction non-rationnelle, et en modélisant l'erreur d'approximation comme une incertitude supplémentaire, il a été possible de valider les performances de suivi de cette stratégie de commande, ainsi que de déterminer la relation entre l'erreur d'estimation et les performances obtenues.

J.2 Travaux futurs

J.2.1 Évaluation des gyroscopes MEMS basée sur des modèles

Sur l'extension de la variance d'Allan basée sur un modèle à l'étude de l'instabilité du biais

Les méthodes proposées pour le calcul de la variance d'Allan à partir d'un modèle fournissent des résultats satisfaisants pour l'étude du bruit de sortie des gyroscopes MEMS. Cependant, dans la communauté MEMS, la variance d'Allan est également utilisée pour évaluer la dérive du biais sur une longue échelle de temps. La variation du biais dans le temps est un phénomène non stochastique qui a une contribution importante sur la variance d'Allan observée, principalement pour de longs temps de moyennage. Une question ouverte est donc le développement d'une approche basée sur un modèle pour le calcul de la variance d'Allan pire cas sur une longue échelle de temps.

Sur l'analyse de la performance de la commande basée sur les phaseurs.

Le calcul basé sur le modèle des principales spécifications de performance a été dérivé en considérant une configuration en série du système en boucle fermée et

du démodulateur synchrone. Ensuite, nous abordons l'analyse de stabilité de la commande basée sur les phaseurs, basée sur un système LHTV à rétroaction. Par conséquent, compte tenu de la structure modulaire de l'approche IQC, tous les outils d'analyse obtenus peuvent être combinés pour étendre l'analyse de la commande basée sur les phaseurs à l'évaluation des spécifications de performance.

Sur l'intégration des phénomènes non linéaires

L'analyse de certains des phénomènes non linéaires les plus pertinents des gyroscopes MEMS n'a pas été explorée dans ce travail. Des modèles complets dans la littérature [EKT+11, ST17] montrent que le spring-hardening et sprng softening sont causés par des phénomènes parasites électrostatiques et de grandes déflexions dans les poutres en silicium. Dans ces modèles, ils apparaissent comme le carré ou le cube de la position du mode drive. Il est alors nécessaire de déterminer l'outil d'analyse approprié. Ensuite, parmi les architectures de commande qui ont été exploitées au cours du projet, nous avons une approche basée sur une commande $\Sigma - \Delta$, intégrant le correcteur et le convertisseur analogique-numérique dans un seul système. Ce type d'architecture introduit un relais dans la boucle fermée, qui peut être modélisé comme la fonction de signe. Ensuite, l'analyse d'une telle architecture demande l'utilisation d'outils d'analyse non linéaire tels que l'analyse des systèmes affines par morceaux [Wai18].

J.2.2 Analyse des systèmes LHTV

Sur l'étude du conservatisme des multiplieurs harmoniques

Il a été prouvé que les multiplieurs dépendant de la fréquence pour une incertitude paramétrique répétée permettent d'obtenir des conditions d'analyse nécessaires et suffisantes. En examinant le cas d'un multiplieur pour un seul paramètre HTV répété, nous pouvons observer que les multiplieurs pour une incertitude paramétrique sont un cas particulier des multiplieurs pour un paramètre HTV. La construction des multiplieurs harmoniques permet de déterminer directement les conditions suffisantes. En revanche, l'observation des conditions nécessaires est beaucoup moins intuitive. Une revue de la nécessité des multiplieurs classiques pour une incertitude paramétrique dans différents cas pourrait permettre une meilleure compréhension du conservatisme des multiplieurs harmoniques, ainsi que des idées pour des améliorations possibles.

Sur la recherche de meilleures solutions dans l'espace d'état

Afin d'obtenir des conditions d'analyse qui peuvent être résolues, une option efficace consiste à dériver des solutions dans l'espace d'état pour les systèmes LHTV. L'application du lemme de KYP pour obtenir la solution dans l'espace d'état nécessite des ensembles de multiplieurs qui admettent une paramétrisation appropriée. Ce problème est partiellement résolu en trouvant une paramétrisation des multiplieurs harmoniques contenant uniquement les fonctions sur la diagonale X_D. Néanmoins, ce sous-ensemble de multiplieurs est considérablement plus conservateur que les multiplieurs harmoniques complets, contenant également les fonctions hors diagonale X_G. Le principal défi consiste à trouver une paramétrisation pour le multiplieur complet. En effet, les fonctions hirs diagonale sont des fonctions périodiques particulières de la fréquence, alors des fonctions de dimension infinie qui

n'admettent pas de réalisation dans l'espace d'état. Il faut alors rechercher les relaxations, approximations ou modifications possibles des fonctions hors diagonale X_G afin d'obtenir un multiplieur harmonique complètement paramétrable et optimisant mieux le compromis entre efficacité et conservatisme.

Bibliography

[ACSKS19] Jorge Ayala-Cuevas, Fabrício Saggin, Anton Korniienko, and Gerard Scorletti. Stability analysis of time-varying systems with harmonic oscillations using iqc frequency domain multipliers. In *Proceedings of the 58th IEEE Conference on Decision and Control, Nice, France*. IEEE, 2019.

[AGB95] Pierre Apkarian, Pascal Gahinet, and Greg Becker. Self-scheduled H_∞ control of linear parameter-varying systems: a design example. 31(9):1251–1261, September 1995.

[All66] David W. Allan. Statistics of atomic frequency standards. *Proceedings of the IEEE*, 54(2):221–230, 1966.

[ALM99] Valerio Annovazzi-Lodi and Sabina Merlo. Mechanical-thermal noise in micromachined gyros. *Microelectronics journal*, 30(12):1227–1230, 1999.

[AOPB09] Riccardo Antonello, Roberto Oboe, Luciano Prandi, and Fabio Biganzoli. Automatic mode matching in MEMS vibrating gyroscopes using extremum-seeking control. *IEEE Transactions on Industrial Electronics*, 56(10):3880–3891, 2009.

[Apo06] Vladislav Apostolyuk. Theory and Design of Micromechanical Vibratory Gyroscopes. pages 161–175. Springer Science+Business Media, 2006.

[ApS19] Mosek ApS. Mosek optimization toolbox for Matlab. *User's Guide and Reference Manual, version*, 4, 2019.

[AS05] Cenk Acar and Andrei Shkel. An Approach for Increasing Drive-Mode Bandwidth of MEMS Vibratory Gyroscopes. *J. Microelectromechanical Syst.*, 14(3):520–528, 2005. doi:10.1109/JMEMS.2005.844801.

[AS08] Cenk Acar and Andrei Shkel. *MEMS vibratory gyroscopes: structural approaches to improve robustness*. Springer Science & Business Media, 2008.

[Bau71] Richard A Baugh. Frequency modulation analysis with the hadamard variance. In *25th Annual Symposium on Frequency Control*, pages 222–225. IEEE, 1971.

[BC88] Paolo Bolzern and Patrizio Colaneri. The periodic lyapunov equation. *SIAM Journal on Matrix Analysis and Applications*, 9(4):499–512, 1988.

[BC09] Sergio Bittanti and Patrizio Colaneri. *Periodic systems: filtering and control*, volume 5108985. Springer Science & Business Media, 2009.

[BCC+71] James A Barnes, Andrew R Chi, Leonard S Cutler, Daniel J Healey, David B Leeson, Thomas E McGunigal, James A Mullen, Warren L Smith, Richard L Sydnor, Robert FC Vessot, et al. Characterization of frequency stability. *IEEE transactions on instrumentation and measurement*, (2):105–120, 1971.

[BEGFB94] Stephen Boyd, Laurent El Ghaoui, Eric Feron, and Venkataramanan Balakrishnan. *Linear matrix inequalities in system and control theory*. SIAM, 1994.

[BGSA01] Xavier Bombois, Michel Gevers, Gérard Scorletti, and Brian DO Anderson. Robustness analysis tools for an uncertainty set obtained by prediction error identification. *Automatica*, 37(10):1629–1636, 2001.

[BLA12] Christoph Böhm, Mircea Lazar, and Frank Allgöwer. Stability of periodically time-varying systems: Periodic Lyapunov functions. *Automatica*, 48(10):2663–2669, 2012.

[BP92] Bassam A Bamieh and J Boyd Pearson. A general framework for linear periodic systems with applications to H-infinity sampled-data control. *IEEE transactions on automatic control*, 37(4):418–435, 1992.

[CG98] Michael Cantoni and Keith Glover. Robustness of linear periodically-time-varying closed-loop systems. In *Proceedings of the 37th IEEE Conference on Decision and Control, Tampa FL, USA*, volume 4, pages 3807–3812. IEEE, 1998.

[CG00] Michael Cantoni and Keith Glover. Gap-metric robustness analysis of linear periodically time-varying feedback systems. *SIAM Journal on Control and Optimization*, 38(3):803–822, 2000.

[Col20] Kevin Colin. *Data informativity for the prediction error identification of MIMO systems: identification of a MEMS gyroscope*. PhD thesis, Université de Lyon, 2020.

[Cor35] Gaspard Gustave Coriolis. *Mémoire sur les équations du mouvement relatif des systèmes de corps*. Bachelier, 1835.

[CS15] Joaquin Carrasco and Peter Seiler. Integral quadratic constraint theorem: A topological separation approach. In *2015 54th IEEE Conference on Decision and Control (CDC)*, pages 5701–5706. IEEE, 2015.

[CSL+12] Sheng-Ren Chiu, Chung-Yang Sue, Chih-Hsiou Lin, Li-Tao Teng, Lu-Pu Liao, Yu-Wen Hsu, and Yan-Kuin Su. Active thermal compensation of MEMS based gyroscope. In *SENSORS, 2012 IEEE*, pages 1–4. IEEE, 2012.

[CSLB+19] Kévin Colin, Fabrício Saggin, Christophe Le Blanc, Xavier Bombois, Anton Korniienko, and Gérard Scorletti. Identification-Based Approach for Electrical Coupling Compensation in a MEMS Gyroscope. In *2019 IEEE International Symposium on Inertial Sensors and Systems (INERTIAL)*, pages 1–4. IEEE, 2019.

[CT95] Yung-Shan Chou and André Tits. On robust stability under slowly-varying memoryless uncertainty. In *IEEE Conference on Decision and Control*, volume 4, pages 4321–4326. IEEE, 1995.

[DA09] Lili Dong and David Avanesian. Drive-Mode Control for Vibrational MEMS Gyroscopes. *IEEE Trans. Ind. Electron.*, 56(4):956–963, April 2009. doi:10.1109/TIE.2008.2010088.

[Dev20] Yole Developpement. Status of the MEMS Industry 2020. *IEEE Transactions on Automatic Control*, 2020.

[Din05] Marc Dinh. *Synthèse dépendant de paramètres par optimisation LMI de dimension finie: application à la synthèse de correcteurs reréglables*. PhD thesis, 2005.

[DM10] Thierry Dutoit and Ferran Marques. *Applied Signal Processing: A MATLABTM-based proof of concept*. Springer Science & Business Media, 2010.

[Doy82] John Doyle. Analysis of feedback systems with structured uncertainties. In *IEE Proceedings D-Control Theory and Applications*, volume 129, pages 242–250. IET, 1982.

[DS81] John Doyle and Gunter Stein. Multivariable feedback design: Concepts for a classical/modern synthesis. *IEEE transactions on Automatic Control*, 26(1):4–16, 1981.

[DV75] Charles A Desoer and Mathukumalli Vidyasagar. *Feedback systems: input-output properties*, volume 55. Siam, 1975.

[DVS+17] Antonino D'Alessandro, Giovanni Vitale, Salvatore Scudero, Roberto D'Anna, Antonio Costanza, Adriano Fagiolini, and Luca Greco. Characterization of mems accelerometer self-noise by means of psd and allan variance analysis. In *2017 7th IEEE International workshop on advances in sensors and interfaces (IWASI)*, pages 159–164. IEEE, 2017.

[DZG07] Lili Dong, Qing Zheng, and Zhiqiang Gao. A novel oscillation controller for vibrational mems gyroscopes. In *American Control Conference, 2007. ACC'07*, pages 3204–3209. IEEE, 2007.

[EKT+11] Amro M. Elshurafa, Kareem Khirallah, Hani H. Tawfik, Ahmed Emira, Ahmed K. S. Abdel Aziz, and Sherif M. Sedky. Nonlinear Dynamics of Spring Softening and Hardening in Folded-MEMS Comb Drive Resonators. *J. Microelectromechanical Syst.*, 20(4):943–958, 2011. doi:10.1109/JMEMS.2011.2148162.

[ES98] David S Eddy and Douglas R Sparks. Application of MEMS technology in automotive sensors and actuators. *Proceedings of the IEEE*, 86(8):1747–1755, 1998.

[Far94] Miklos. Farkas. *Periodic Motions*. Springer New York, 1994.

[FB98] Gilles Ferreres and Jean-Marc Biannic. A μ analysis technique without frequency gridding. In *Proceedings of the 1998 American Control Conference. ACC (IEEE Cat. No. 98CH36207)*, volume 4, pages 2294–2298. IEEE, 1998.

[FB01] Gilles Ferreres and Jean-Marc Biannic. Reliable computation of the robustness margin for a flexible aircraft. *Control Engineering Practice*, 9(12):1267–1278, 2001.

[Fer99] Gilles Ferreres. *A practical approach to robustness analysis with aeronautical applications*. Springer Science & Business Media, 1999.

[FF17] J. Micah Fry and Mazen Farhood. Robustness analysis of eventually periodic systems using integral quadratic constraints with periodic multipliers. In *2017 IEEE 56th Annual Conference on Decision and Control (CDC)*, pages 2967–2972. IEEE, 2017.

[FKP+05] Michael I. Ferguson, Didier Keymeulen, Chris Peay, Karl Yee, and Daliang Leon Li. Effect of temperature on MEMS vibratory rate gyroscope. *IEEE Aerospace Conference Proceedings*, 2005, 2005. doi:10.1109/AERO.2005.1559561.

[FLW11] Yongzhen Fan, Bing Luo, and Ancheng Wang. Analysis of temperature adaptability for frequency control loop for silicon micromechanical gyroscope. *Proceedings - IEEE 2011 10th International Conference on Electronic Measurement and Instruments, ICEMI 2011*, 4(4):346–349, 2011. doi:10.1109/ICEMI.2011.6038012.

[FTD91] Michael KH Fan, Andre L Tits, and John C Doyle. Robustness in the presence of mixed parametric uncertainty and unmodeled dynamics. *IEEE Transactions on Automatic Control*, 36(1):25–38, 1991.

[Gab93] Thomas B. Gabrielson. Mechanical-thermal noise in micromachined acoustic and vibration sensors. *IEEE transactions on Electron Devices*, 40(5):903–909, 1993.

[Gag98] Jean-Jacques Gagnepain. La variance de B. Picinbono. *TS. Traitement du signal*, 15(6):477–482, 1998.

[GBKN91] P Greiff, B Boxenhorn, T King, and L Niles. Silicon monolithic micromechanical gyroscope. In *TRANSDUCERS'91: 1991 International Conference on Solid-State Sensors and Actuators. Digest of Technical Papers*, pages 966–968. IEEE, 1991.

[GHL+15] Rui Guan, Chunhua He, Dachuan Liu, Qiancheng Zhao, Zhenchuan Yang, and Guizhen Yan. A temperature control system used for improving resonant frequency drift of MEMS gyroscopes. *2015 IEEE 10th International Conference on Nano/Micro Engineered and Molecular Systems, NEMS 2015*, pages 397–400, 2015. doi:10.1109/NEMS.2015.7147452.

[Gre98] Charles A Greenhall. Spectral ambiguity of allan variance. *IEEE Transactions on Instrumentation and Measurement*, 47(3):623–627, 1998.

[GS97] Tryphon T Georgiou and Malcolm C Smith. Robustness analysis of nonlinear feedback systems: An input-output approach. *IEEE Transactions on Automatic Control*, 42(9):1200–1221, 1997.

[GVL96] Gene H Golub and Charles Van-Loan. *Matrix Computations*. Johns Hopkins University Press, 1996.

[HO10] Tomomichi Hagiwara and Yasuhiro Ohara. Noncausal linear periodically time-varying scaling for robust stability analysis of discrete-time systems: Frequency-dependent scaling induced by static separators. *Automatica*, 46(1):167–173, 2010.

[Hou04] Haiying Hou. *Modeling inertial sensors errors using Allan variance*. University of Calgary, Department of Geomatics Engineering, 2004.

[IEE04] IEEE Standard Specification Format Guide and Test Procedure for Coriolis Vibratory Gyros. *IEEE Std 1431-2004*, pages 1–78, 2004.

[IEE06] IEEE Standard Specification Format Guide and Test Procedure for Single-Axis Laser Gyros. *IEEE Std 647-2006 (Revision of IEEE Std 647-1995)*, pages 1–83, 2006.

[IEE18] IEEE Standard for Sensor Performance Parameter Definitions. *IEEE Std 2700-2017 (Revision of IEEE Std 2700-2014)*, pages 1–64, 2018.

[JKM99] Ulf T Jonsson, C-Y Kao, and Alexandre Megretski. Robustness analysis of periodic systems. In *Proceedings of the 38th IEEE Conference on Decision and Control, Phoenix AZ, USA*, volume 2, pages 1839–1844. IEEE, 1999.

[KBP06] Jongrae Kim, Declan G. Bates, and Ian Postlethwaite. Robustness analysis of linear periodic time-varying systems subject to structured uncertainty. *Systems and Control Letters*, 55(9):719–725, 2006. doi:10.1016/j.sysconle.2006.02.005.

[Kem11] Volke Kempe. *Inertial MEMS - Principles and Practice*. Cambridge University Press, Cambridge, 2011.

[KHC+08] Bongsang Kim, Matthew A. Hopcroft, Rob N. Candler, Chandra Mohan Jha, Manu Agarwal, Renata Melamud, Saurabh A. Chandorkar, Gary Yama, and Thomas W. Kenny. Temperature dependence of quality factor in MEMS resonators. *Journal of Microelectromechanical Systems*, 17(3):755–766, 2008. doi:10.1109/JMEMS.2008.924253.

[KJCT12] Martti Kirkko-Jaakkola, Jussi Collin, and Jarmo Takala. Bias prediction for MEMS gyroscopes. *IEEE Sensors Journal*, 12(6):2157–2163, 2012.

[KM13] Dennis Kim and Robert Thomas M'Closkey. Spectral analysis of vibratory gyro noise. *IEEE Sensors Journal*, 13(11):4361–4374, 2013.

[KMJ01] Chung Yao Kao, Alexandre Megretski, and Ulf T. Jönsson. A cutting plane algorithm for robustness analysis of periodically time-varying systems. *IEEE Transactions on Automatic Control*, 46(4):579–592, 2001. doi:10.1109/9.917659.

[KWB05] Peter Y Kwok, Marc S Weinberg, and Kenneth S Breuer. Fluid effects in vibrating micromachined structures. *Journal of Microelectromechanical systems*, 14(4):770–781, 2005.

[Lat70] Bhagawandas P Lathi. *Introduction to Random Signals and Communication Theory*. International Textbook Company, 1970.

[Lel06] R. P. Leland. Adaptive Control of a MEMS Gyroscope Using Lyapunov Methods. *IEEE Trans. Control Syst. Technol.*, 14(2):278–283, 2006. doi:10.1109/TCST.2005.860514.

[Lib06] M. R. Liberzon. Essays on the absolute stability theory. *Automation and remote control*, 67(10):1610–1644, 2006.

[Lju98] Lennart Ljung. *System Identification: Theory for the User*. Pearson Education, 2nd edition, 1998.

[Lof04] Johan Lofberg. YALMIP: A toolbox for modeling and optimization in MATLAB. In *2004 IEEE international conference on robotics and automation (IEEE Cat. No. 04CH37508)*, pages 284–289. IEEE, 2004.

[LR02] Philip W. Loveday and Craig A. Rogers. The Influence of Control System Design on the Performance of Vibratory Gyroscopes. *J. Sound and Vibration*, 255(3):417–432, 2002. doi:10.1006/jsvi.2001.4163.

[LR03] Bernhard P Lampe and Efim N Rosenwasser. Operational Description and Statistical Analysis of Linear Periodic Systems on the Unbounded Interval $-\infty< t<\infty$. *European journal of control*, 9(5):512–525, 2003.

[LS09] Josh E-Y Lee and Ashwin A. Seshia. Parasitic feedthrough cancellation techniques for enhanced electrical characterization of electrostatic microresonators. *Sensors and Actuators A: Physical*, 156(1):36–42, 2009.

[LTVD00] Craig T Lawrence, André L Tits, and Paul Van Dooren. A fast algorithm for the computation of an upper bound on the μ-norm. *Automatica*, 36(3):449–456, 2000.

[MCZ+10] Gaoyin Ma, Wenyuan Chen, Weiping Zhang, Feng Cui, and Kai Li. Compact $\mathcal{H}_\infty$ Robust Rebalance Loop Controller Design for a Micromachined Electrostatically Suspended Gyroscope. *ISA Trans.*, 49(2):222–228, April 2010. doi:10.1016/j.isatra.2009.11.003.

[MG99] Karen W Markus and Kaigham J Gabriel. MEMS: The systems function revolution. *Computer*, 32(10):25–31, 1999.

[MIF00] Gjerrit Meinsma, Tetsuya Iwasaki, and Minyue Fu. When is (D, G)-scaling both necessary and sufficient. *IEEE Transactions on Automatic Control*, 45(9):1755–1759, 2000.

[Mor21] Federico Morelli. *Optimal identification experiment design : contributions to its robustification and to its use for dynamic network identification. Resonance Frequency Tracking.* PhD thesis, Université de Lyon, 2021.

[MR97] Alexandre Megretski and Anders Rantzer. System analysis via integral quadratic constraints. *IEEE Transactions on Automatic Control*, 42(6):819–830, 1997.

[MVG01] Robert T. M'Closkey, Alex Vakakis, and Roman Gutierrez. Mode Localization Induced by a Nonlinear Control Loop. *Nonlinear Dyn.*, 25(1/3):221–236, 2001. doi:10.1023/A:1012934112137.

[MYKPT15] Ehsan Maani Miandoab, Aghil Yousefi-Koma, Hossein Nejat Pishkenari, and Farid Tajaddodianfar. Study of nonlinear dynamics and chaos in MEMS/NEMS resonators. *Communications in Nonlinear Science and Numerical Simulation*, 22(1-3):611–622, 2015.

[NN94] Yurii Nesterov and Arkadii Nemirovskii. *Interior-point polynomial algorithms in convex programming*, volume 13. Siam, 1994.

[NYAR] Ali H Nayfeh, Mohammad I Younis, and Eihab M Abdel-Rahman. Dynamic pull-in phenomenon in MEMS resonators.

[OAL+05] R. Oboe, R. Antonello, E. Lasalandra, G. Spinola Durante, and L. Prandi. Control of Z-Axis MEMS Vibrational Gyroscope. *IEEE/ASME Trans. Mechatronics*, 10(4):364–370, August 2005. doi:10.1109/TMECH.2005.852437.

[OP19] Daniel Ossman and Harald Pfifer. Robustness analysis of continuous periodic systems using integral quadratic constraints. In *Proceedings of the 58th IEEE Conference on Decision and Control, Nice, France*. IEEE, 2019.

[O'S67] R. P. O'Shea. An improved frequency time domain stability criterion for autonomous continuous systems. *IEEE Transactions on Automatic Control*, 12(6):725–731, 1967.

[Pag96] Fernando Paganini. A set-based approach for white noise modeling. *IEEE Transactions on Automatic Control*, 41(10):1453–1465, 1996.

[Pag99] Frequency domain conditions for robust H/sub 2 performance, author=Paganini, Fernando. *IEEE Transactions on Automatic Control*, 44(1):38–49, 1999.

[Pap83] Athanasios Papoulis. Random modulation: A review. *IEEE Transactions on Acoustics, Speech, and Signal Processing*, 31(1):96–105, 1983.

[PB16] Michael Perlmutter and Stephen Breit. The future of the mems inertial sensor performance, design and manufacturing. In *2016 DGON intertial sensors and systems (ISS)*, pages 1–12. IEEE, 2016.

[PD93] Andrew Packard and John Doyle. The complex structured singular value. *Automatica*, 29(1):71–109, 1993.

[Ped80] PAULI Pedersen. Stability of the solutions to mathieu-hill equations with damping. *Ingenieur-Archiv*, 49(1):15–29, 1980.

[PH03] Sungsu Park and Roberto Horowitz. Adaptive Control for the Conventional Mode of Operation of MEMS Gyroscopes. *J. Microelectromechanical Syst.*, 12(1):101–108, February 2003. doi:10.1109/JMEMS.2002.807468.

[Pop61] Vasile-Mihai Popov. Absolute stability of nonlinear systems of automatic control. *Automation and Remote Control*, 22(8):857–875, 1961.

[PS02] Chris C Painter and Andrei M Shkel. Identification of anisoelasticity for electrostatic trimming of rate-integrating gyroscopes. In *Smart Structures and Materials 2002: Smart Electronics, MEMS, and Nanotechnology*, volume 4700, pages 157–168. International Society for Optics and Photonics, 2002.

[PS10] Petko Petkov and Tsonyo Slavov. Stochastic modeling of mems inertial sensors. *Cybernetics and information technologies*, 10(2):31–40, 2010.

[PTS12] I. P. Prikhodko, A. A. Trusov, and A. M. Shkel. Achieving Long-Term Bias Stability in High-Q Inertial MEMS by Temperature Self-Sensing with a 0.5 m°C Precision. *Solid-State Sensors, Actuators, Micosystems Work. Hilt. Head*, 2012.

[PTS13] Igor P Prikhodko, Alexander A Trusov, and Andrei M Shkel. Compensation of drifts in high-Q MEMS gyroscopes using temperature self-sensing. *Sensors and Actuators A: Physical*, 201:517–524, 2013.

[Ran96] Anders Rantzer. On the Kalman—Yakubovich—Popov lemma. *Systems & Control Letters*, 28(1):7 – 10, 1996. doi:https://doi.org/10.1016/0167-6911(95)00063-1.

[RCRW09] Johan Raman, Edmond Cretu, Pieter Rombouts, and Ludo Weyten. A Closed-Loop Digitally Controlled MEMS Gyroscope with Unconstrained Sigma-Delta Force-Feedback. *IEEE Sens. J.*, 9(3):297–305, March 2009. doi:10.1109/JSEN.2008.2012237.

[Roz67] Yurii A Rozanov. *Stationary Random Processes*. Holden-Day, 1967.

[SACKS20] Fabrício Saggin, Jorge Ayala-Cuevas, Anton Korniienko, and Gérard Scorletti. *On the Parameter-dependent H-infinty control for MEMS gyroscopes: synthesis and analysis*. PhD thesis, Ecole Centrale Lyon; Laboratoire Ampère, 2020.

[Saf80] Michael George Safonov. *Stability and robustness of multivariable feedback systems*. MIT press, 1980.

[Sag21] Fabrício Saggin. *Robust Control for MEMS gyroscopes*. PhD thesis, Université de Lyon, 2021.

[SAH08] Mikko Saukoski, Lasse Aaltonen, and Kari AI Halonen. Effects of synchronous demodulation in vibratory mems gyroscopes: A theoretical study. *IEEE Sensors Journal*, 8(10):1722–1733, 2008.

[San64] I. W. Sandberg. On the L2-Boundedness of Solutions of Nonlinear Functional Equations. *Bell System Technical Journal*, 43(4):1581–1599, 1964.

[Sau08a] Mikko Saukoski. *System and circuit design for a capacitive MEMS gyroscope*. PhD thesis, Helsinski University of Technology, 2008.

[Sau08b] Mikko Saukoski. *System and Circuit Design for a Capacitive MEMS Gyroscope*. PhD thesis, 2008.

[SBBF07] Gérard Scorletti, Xavier Bombois, Marta Barenthin, and Vincent Fromion. Improved efficient analysis for systems with uncertain parameters. In *IEEE Conference on Decision and Control*, pages 5038–5043. IEEE, 2007.

[SEGT00] Kirill Shcheglov, Christopher Evans, Roman Gutierrez, and Tony K Tang. Temperature dependent characteristics of the JPL silicon MEMS gyroscope. In *2000 IEEE Aerospace Conference. Proceedings (Cat. No. 00TH8484)*, volume 1, pages 403–411. IEEE, 2000.

[Sei14] Peter Seiler. Stability analysis with dissipation inequalities and integral quadratic constraints. *IEEE Transactions on Automatic Control*, 60(6):1704–1709, 2014.

[SF06] Gérard Scorletti and Vincent Fromion. Further results on the design of robust $\mathcal{H}_\infty$ feedforward controllers and filters. In *Decision and Control, 2006 45th IEEE Conference on*, pages 3560–3565. IEEE, 2006.

[SHC+12] Jaw-Kuen Shiau, Chen-Xuan Huang, Ming-Yu Chang, et al. Noise characteristics of mems gyro's null drift and temperature compensation. *Journal of Applied Science and engineering*, 15(3):239–246, 2012.

[SHS+99] Andrei M. Shkel, Roberto Horowitz, Ashwin A. Seshia, Sungsu Park, and Roger T. Howe. Dynamics and Control of Micromachined Gyroscopes. In *Proc. 1999 Am. Control Conf. (Cat. No. 99CH36251)*, volume 3, pages 2119–2124. IEEE, 1999. doi:10.1109/ACC.1999.786303.

[SKP+20] Fabrício Saggin, Anton Korniienko, Guillaume Papin, Eva Markiewicz, Y. David, Anthony El Hajj, and Gérard Scorletti. H_∞ Design of an EM-ΣΔ Feedback for MEMS Gyroscopes. In *2020 DGON Inertial Sensors and Systems (ISS)*, pages 1–20. IEEE, 2020. URL: https://hal.archives-ouvertes.fr/hal-03091684, doi:10.1109/ISS50053.2020.9244916.

[SP01] Sigurd Skogestad and Ian Postlethwaite. *Multivariable Feedback Control - Analisys and Design*. John Wiley & Sons, second edition, 2001.

[SSK20] Fabrício Saggin, Gérard Scorletti, and Anton Korniienko. A novel phasor control design method: application to MEMS gyroscopes. In *2020 American Control Conference (ACC)*, pages 3236–3241. IEEE, 2020.

[SSP+06] A. Srikantha Phani, Ashwin A. Seshia, Moorthi Palaniapan, Roger T. Howe, and John A. Yasaitis. Modal coupling in micromechanical vibratory rate gyroscopes. *IEEE Sensors Journal*, 6(5):1144–1152, 2006. doi:10.1109/JSEN.2006.881432.

[ST17] Srinivasan Sabarathinam and K Thamilmaran. Implementation of analog circuit and study of chaotic dynamics in a generalized Duffing-type MEMS resonator. *Nonlinear Dynamics*, 87(4):2345–2356, 2017.

[Stu99] Jos F Sturm. Using SeDuMi 1.02, a MATLAB toolbox for optimization over symmetric cones. *Optimization methods and software*, 11(1-4):625–653, 1999.

[SV18] Carsten W Scherer and Joost Veenman. Stability analysis by dynamic dissipation inequalities: On merging frequency-domain techniques with time-domain conditions. *Systems & Control Letters*, 121:7–15, 2018.

[Teh83] Masoud Masih Tehrani. Ring laser gyro data analysis with cluster sampling technique. In *Fiber Optic and Laser Sensors I*, volume 412, pages 207–220. International Society for Optics and Photonics, 1983.

[TSS09] Alexander A Trusov, Adam R Schofield, and Andrei M Shkel. Performance characterization of a new temperature-robust gain-bandwidth improved mems gyroscope operated in air. *Sensors and Actuators A: Physical*, 155(1):16–22, 2009.

[TWY17] Qijian Tang, Xiangjun Wang, and Qingping Yang. Scale factor model analysis of mems gyroscopes. *Microsystem Technologies*, 23(5):1215–1219, 2017.

[VBH12] Martin Vagner, Petr Beneš, and Zdeněk Havránek. Experience with allan variance method for mems gyroscope performance characterization. In *2012 IEEE International Instrumentation and Measurement Technology Conference Proceedings*, pages 1343–1347. IEEE, 2012.

[VSK16] Joost Veenman, Carsten W Scherer, and Hakan Köroğlu. Robust stability and performance analysis based on integral quadratic constraints. *European Journal of Control*, 31:1–32, 2016.

[Wai18] *A piecewise-affine approach to nonlinear performance, author=Waitman, Sergio*. PhD thesis, Université de Lyon, 2018.

[WHGS16] Oliver Willers, Christopher Huth, Jorge Guajardo, and Helmut Seidel. Mems gyroscopes as physical unclonable functions. In *Proceedings of the 2016 ACM SIGSAC Conference on Computer and Communications Security*, pages 591–602, 2016.

[Wil72] Jan C Willems. Dissipative dynamical systems part i: General theory. *Archive for rational mechanics and analysis*, 45(5):321–351, 1972.

[WK06] Marc S Weinberg and Anthony Kourepenis. Error sources in in-plane silicon tuning-fork MEMS gyroscopes. *Journal of Microelectromechanical systems*, 15(3):479–491, 2006.

[XCWL09] Dunzhu Xia, Shuling Chen, Shourong Wang, and Hongsheng Li. Micrgyroscope Temperature Effects and Compensation-Control Methods. *Sensors*, 9(12):8349–8376, 2009. doi:10.3390/s91008349.

[Yak65] Vladimir A. Yakubovich. Frequency conditions for the absolute stability and dissipativity of control systems with a single differentiable nonlinearity. In *Soviet Mathematics Doklady*, volume 6, page 101, 1965.

[Yak67] Vladimir A. Yakubovich. Frequency conditions for the absolute stability of control systems with several nonlinear or linear nonstationary blocks. *Avtomatika i telemekhanika*, 6:5–30, 1967.

[Yak71] Vladimir A. Yakubovich. S-procedure in nonlinear control theory. *Vestnick Leningrad Univ. Math.*, 1:62–77, 1971.

[YAN98] Navid Yazdi, Farrokh Ayazi, and Khalil Najafi. Micromachined Inertial Sensors. *Proc. IEEE*, 86(8):1640–1659, 1998. doi:10.1109/5.704269.

[You11] Mohammad I. Younis. *MEMS Linear and Nonlinear Statics and Dynamics*, volume 20 of *Microsystems*. Springer US, 2011. doi:10.1007/978-1-4419-6020-7.

[Zam66a] George Zames. On the input-output stability of time-varying nonlinear feedback systems–part ii: Conditions involving circles in the frequency plane and sector nonlinearities. *IEEE transactions on automatic control*, 11(3):465–476, 1966.

[Zam66b] George Zames. On the input-output stability of time-varying nonlinear feedback systems part one: Conditions derived using concepts of loop gain, conicity, and positivity. *IEEE transactions on automatic control*, 11(2):228–238, 1966.

[ZD98] Kemin Zhou and John Comstock Doyle. *Essentials of robust control*, volume 104. Prentice hall Upper Saddle River, NJ, 1998.

[ZF68] George Zames and PL Falb. Stability conditions for systems with monotone and slope-restricted nonlinearities. *SIAM Journal on Control*, 6(1):89–108, 1968.

[ZHA02] Jun Zhou, Tomomichi Hagiwara, and Mituhiko Araki. Stability analysis of continuous-time periodic systems via the harmonic analysis. *IEEE Transactions on Automatic Control*, 47(2):292–298, 2002. doi:10.1109/9.983361.

[ZTSL10] Hao Zhou, Hailin Tang, Wei Su, and Xianxue Liu. Robust design of a MEMS gyroscope considering the worst-case tolerance. In *2010 IEEE 5th International Conference on Nano/Micro Engineered and Molecular Systems*, pages 1012–1016. IEEE, 2010.